First-Principles Study on Pyrites and Marcasites for Photovoltaic Application

Timo Schena

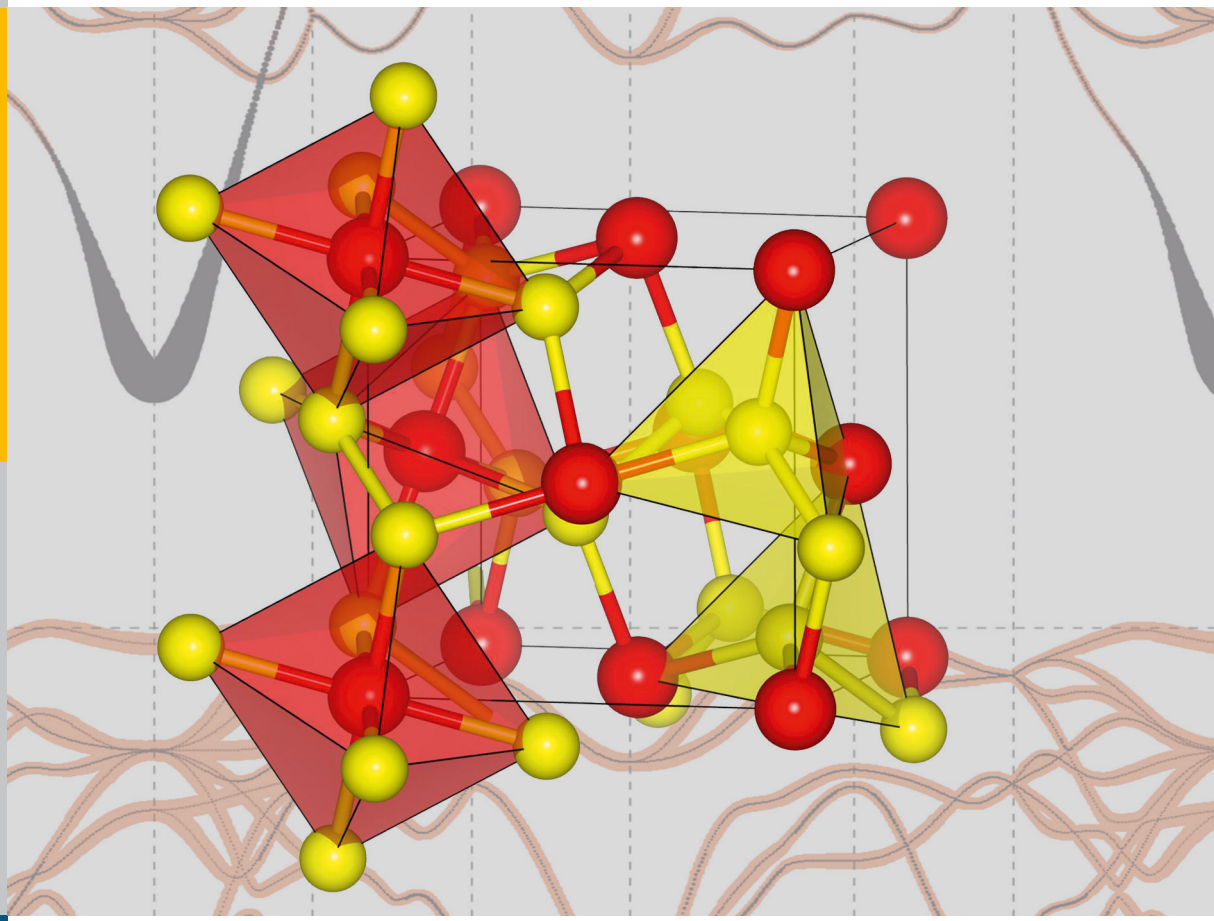

Energie & Umwelt / Energy & Environment
Band / Volume 254
ISBN 978-3-95806-041-8

JÜLICH
FORSCHUNGSZENTRUM

Schriften des Forschungszentrums Jülich
Reihe Energie & Umwelt / Energy & Environment Band / Volume 254

Forschungszentrum Jülich GmbH
Peter Grünberg Institute (PGI)
Quantum Theory of Materials (PGI-1/IAS-1)

First-Principles Study on Pyrites and Marcasites for Photovoltaic Application

Timo Schena

Schriften des Forschungszentrums Jülich
Reihe Energie & Umwelt / Energy & Environment Band / Volume 254

ISSN 1866-1793 ISBN 978-3-95806-041-8

Bibliographic information published by the Deutsche Nationalbibliothek.
The Deutsche Nationalbibliothek lists this publication in the Deutsche Nationalbibliografie; detailed bibliographic data are available in the Internet at http://dnb.d-nb.de.

Publisher and Distributor: Forschungszentrum Jülich GmbH
Zentralbibliothek
52425 Jülich
Tel: +49 2461 61-5368
Fax: +49 2461 61-6103
Email: zb-publikation@fz-juelich.de
www.fz-juelich.de/zb

Cover Design: Grafische Medien, Forschungszentrum Jülich GmbH

Printer: Grafische Medien, Forschungszentrum Jülich GmbH

Schriften des Forschungszentrums Jülich
Reihe Energie & Umwelt / Energy & Environment, Band / Volume 254

D 82 (Diss. RWTH Aachen University, 2015)

ISSN 1866-1793
ISBN 978-3-95806-041-8

The complete volume is freely available on the Internet on the Jülicher Open Access Server (JuSER) at www.fz-juelich.de/zb/openaccess.

Abstract

This thesis deals with first-principles calculations for pyrite and marcasite compounds, with a particular focus on their suitability for photovoltaic applications. Their electronic structure and their optical properties are thoroughly investigated within density-functional theory (DFT) using various exchange-correlation functionals, among them sophisticated hybrid functionals. To account for electronic excitations the many-body perturbation theory in the GW approximation has also been exploited.

The investigation of the electronic and optical properties of iron pyrite (FeS_2) covers an essential part of this thesis, since iron pyrite is reported to be a promising material for photovoltaic applications due to its large optical absorption, a suitable band gap and large photocurrents. Furthermore, iron pyrite consists of abundant elements, and thus would allow for a large-scale and long-term utilization. However, iron pyrite solar cells exhibit only an open-circuit voltage of merely 200 mV, leading to a small conversion efficiency of 3%, which disqualifies iron pyrite for photovoltaic applications at present.

This thesis exposes that the question about the size of the fundamental and optical band gap of iron pyrite, both, theoretically and experimentally, might not be settled yet. Low-intensity contributions in the optical absorption might complicate the determination of the optical band gap, and the GW results show that the fundamental band gap might be much smaller than expected. Therefore, the small fundamental band gap of pristine iron pyrite in the bulk phase might be already responsible for the low open-circuit voltage.

Since interfaces and surfaces play an important role for the photovoltaic performance, the electronic structure of the most stable iron pyrite surfaces is also discussed, revealing that surface states of Fe $3d$ character might act as charge recombination centers. First attempts to passivate these surface states indicate that heavier adatoms are more suitable than light adatoms.

The application of the GW approximation on iron pyrite yields an unconventional reduction of the band gap compared to the "plain" DFT results, whereas largely overestimated band gaps are obtained using hybrid functionals. By extending the calculations to other pyrite compounds (RuS_2, OsS_2, NiP_2 and ZnS_2) and to the structurally closely related marcasite compounds (FeS_2, $FeSe_2$ and $FeTe_2$), it is shown that the interplay of transitions between p and d states and the screening caused by the d states is responsible for this peculiar behavior.

Finally, a particular focus is set on FeS_2 marcasite, which is reported to coexist with the pyrite phase, but is presumed to degrade the photovoltaic performance. However, the results in this thesis indicate that iron marcasite might be better suited for photovoltaic applications than iron pyrite.

Contents

Conventions and Abbreviations

In this thesis the following conventions in mathematical expressions are used:

Symbol	Attribute	Quantity
$\boldsymbol{r}$	bold	vector
$\hat{\boldsymbol{r}}$	bold and hat	normalized vector
$\underline{\boldsymbol{H}}$	bold and underline	matrix

The following abbreviations are used frequently in this thesis:

Abbr.	Meaning
a.u.	atomic unit
CBM	conduction band minimum
c-RPA	constrained random phase approximation
DFT	density-functional theory
FLAPW	full potential linearized augmented plane-wave
GGA	generalized gradient approximation
HELO	higher-energy local orbital
HF	Hartree-Fock
HSE	Heyd-Scuseria-Ernzerhof
IR	interstitial region
LDA	local density approximation
LO	local orbital
MT	muffin tin
PBE	Perdew-Burke-Ernzerhof
QSGW	quasiparticle selfconsistent GW
VBM	valence band maximum

1. Introduction

The world demands for an expanding or at least stable energy supply. Fossil energies are not going to be a solution, since they are running out within the next centuries. The "oil-peak" is probably almost passed or will take place within the next decades [1]. The situation will become even more severe, when Asia technologically closes up to Europe and North America. And even if another large fossil fuel depot will be discovered, which is able to delay a resource shortage, there is still the problem with global warming. By burning fossil fuels the concentration of greenhouse gases in the earth's atmosphere increases.[1] Hence, if we want to sustain or even improve the standard of living for the future, we have to fundamentally restructure our energy production.

In the year 2013 57% of the energy production in Germany was based on fossil fuels like coal, oil or petroleum gas, whereas 15% of the power originated from nuclear power plants and only 24% from renewable energies such as wind, water, solar and biomass [2]. Although nuclear energy contributes relatively little to the CO_2 augmentation, the accidents in Tschernobyl and Fukushima demonstrate the high risk to rely on that branch. Renewable energies or so-called "green energies" are the cleanest energy source, and practically they are infinitely available, and thus are the only option on a long-term scale so far.

Although we are aware of the energy problem, the fraction of renewable energies in Germany is only about 25%, which is already quite high as compared to many other countries. This fraction might be much larger, if the energy production costs using renewable energy sources were comparable or even lower than those exploiting fossil energies. In particular the photovoltaics with about 0.08-0.14 €/kWh are still to expensive to compete against 0.04 €/kWh using brown coal [3], which explains that photovoltaics makes for only a small fraction of merely 5% to the energy production in Germany. Though, the solar energy is one of the most promising energy sources. The nature itself has made use of solar energy in every ordinary plant via the photosynthesis, and all life on the planet depends on that energy. The earth is radiated with $1.74 \cdot 10^{17}$ W solar power [4]. To get a feeling for this number, let me mention, if we were able to convert all of this to electrical energy, we would be able to generate the annual world energy demand of the year 2013 of $1.5 \cdot 10^{14}$ kWh [5] in less than one hour.

There are two major reasons that the production costs for photovoltaics are high, although solar energy is vastly existent. First, the amount of extractable solar energy of an area fluctuates with weather conditions and the day-night cycle, which demands for a well-developed energy network and suitable energy storage, which is a challenging task.

[1] Here, I would like to quote James Hansen, a researcher in the field of climatology: "What has become clear from the science is that we cannot burn all of the fossil fuels without creating a very different planet."

Second, the production costs of solar panels play a crucial role, and in the following I will focus on that. In the coming paragraph, the currently most prominent commercial solar cell materials with their advantages and disadvantages are briefly introduced.

The market for solar cells has been always dominated by Si with most cells consisting of mono-crystalline or poly-crystalline Si (c-Si), since technological know-how about processing Si has been already assimilated in the silicon-based computer chip production. The absorption layers of this cells have to be quite thick with hundreds of μm and exhibit a (solar-grade) purity of 99.999%, which is less than electronic-grade purity of 99.9999999%, but still quite cost-intensive in production. After growing high-purity Si using the Czochralski-process [6], there is a quite cost-intense step of cutting the crystal into thin wafers, since it leads to a substantial waste of pure Si material. Production processes via chemical vapor deposition (CVD) or physical vapor deposition (PVD), as they are used for thin-film solar cells, are much simpler and cost-efficient. In addition, a significantly thinner absorber layer is needed for thin-film solar cell materials like amorphous Si (a-Si). Thus, in the recent years the application range of thin-film photovoltaics, with a focus on a-Si or micro-crystalline Si (μc-Si), has been extended from only small-scale applications like hand calculators to large-scale devices. However, problems with up to 30% degradation of the conversion efficiency within some months to typical values of about 5-7% efficiency as well as a shorter lifetime than the c-Si solar cells, make them mostly only attractive for applications demanding for a mechanically flexible device. For comparison, note that the energy conversion efficiency of single-stack c-Si solar cells in research can reach up to 25%, which is already quite close to the maximal theoretical value of about 32% for single-stack cells predicted by the Shockley-Queisser limit [7].[2] Thin-film solar cells made of CdTe or CIGS (Copper-Indium-Gallium-Diselenide) suffer less from degradation than a-Si and exhibit promising efficiencies of above 10%, exceeding even 20% for solar cells in research. However, a major drawback of the CdTe and CIGS cells is the scarcity of Te, In and Ga [8, 9]. These materials can be mined only as a by-product making it difficult to mine large amounts. For Te all known deposits are insufficient to guarantee photovoltaics on large-scale. Furthermore, Cd is poisonous and carcinogenic, which might pose some serious complications regarding the recycling of CdTe cells. In the case of Ga and In the supply is regarded to be critical, in particular for In, since the growing market of liquid crystal displays tightens the resource shortage. Hence, CdTe and CIGS solar cells are most probably not a long-term solution for the energy problem. Finally, there are also commercially produced multi-junction GaAs solar cells with astonishing 30% efficiency,[3] but they are so expensive, that the application is limited to space missions, where weight and size of the devices is more important than the costs.

Overall, to guarantee a long-term and large-scale supply of solar energy on an environmentally sustainable basis, the materials are restricted to abundant, non-toxic materials. Si already fulfills these conditions, but there are other materials, which might be better suited for photovoltaic applications. For instance, the optical absorption of Si with 10^3-

[2] Commercial c-Si solar cells show a maximum efficiency of about 20%.

[3] The world-record solar cell is based on GaAs using a multi-junction and concentrator buildup, exhibiting an efficiency of more than 40%.

10^4 cm^{-1} [10] is only mediocre compared to other semiconductors. This is caused by the nature of the indirect band gap in Si, and thus it demands for quite thick absorption layers to obtain a reasonably large quantum efficiency. Hence, the search for alternative materials might be very promising. Copper sulfides, copper oxides, pyrites, chalcopyrites and kesterites are regarded to be good candidates [11, 12]. This thesis is concerned with the pyrite compounds and the structurally related marcasite compounds, in particular the most prominent compound FeS_2 lies in its focus.

FeS_2 pyrite is a mineral, which is quite common in the earth's crust. The compound is so abundant that it has been used in flintlock guns to ignite the gunpowder in the 16th and 17th century. It is also referred to as fool's gold due to its shiny luster of its surfaces, similar in appearance to gold. However, iron pyrite is much harder than gold, which makes it easy to distinguish them. Due to a large optical absorption coefficient of about 6×10^5 cm^{-1} for photon energies $E > 1.3$ eV, large photocurrent densities of 40 mA/cm^2 and a band gap of 0.95 eV measured via optical absorption and photoconductivity measurements [13], FeS_2 is believed to be a promising photovoltaic material for the last 20-30 years. This large optical absorption leads to a high quantum efficiency of about 90% by using only 10 nm thick absorption layers, whereas for comparison μm-thick layers have to be used for thin-film a-Si solar cells. Doping the material with As, Ni or Co leads to n- as well as p-type conductivity in FeS_2 [14], which might be of importance to assemble a p-n junction purely consisting of iron pyrite. However, all attempts using iron pyrite as absorber material in a solar cell led to a disappointing maximal conversion efficiency of around 3% [13] or even much lower, as it has been observed recently in pyrite nanocrystal solar cells [15]. These low efficiencies are caused by a low photovoltage with an open-circuit voltage being maximal 200 mV, corresponding only to about 20% of the measured band gap size.

Many publications focus on the possible reasons for that low open-circuit voltage in pyrite, since all other relevant properties for photovoltaic applications are really promising. However, there is no agreement on one or a few possible sources yet. The suggested reasons cover intrinsic and extrinsic point-defects [16, 17], intrinsic surface states [18–21], conductive conversion layers [22], metallic FeS-precipitates [23], bulk phase impurities [24] and a small fundamental band gap of pyrite bulk itself [25, 26]. In the following I will briefly discuss each of these possible sources and draw connections between them, showing that in some cases the conclusions are contradictory, and thus the results on iron pyrite are still not well understood.

The very first attempts to explain the low photovoltage are based on defects in the material. Electrical resistivity measurements yield large free charge carrier densities of 10^{14}-10^{18} cm^{-3} in undoped pyrite [14, 27], whereas for clean pyrite free charge carrier densities of 10^{10} cm^{-3} are expected at room temperature, comparable to those in solar-grade Si. The much larger densities are attributed to defects. Since exclusively sulfur-deficient pyrite crystals have been observed in studies [28], Birkholz *et al.* report of a model in which sulfur vacancies in bulk pyrite lead to defect states in the band gap acting as charge recombination centers, and thus reducing the open-circuit voltage [16]. These defect states are formed due to the breaking of the octahedral symmetry. The same symmetry-breaking appears also on the S-terminated (100)-surface, which might lead to intrinsic surface states located in the band gap giving rise to a Fermi level pinning [18]. Sun *et al.* claim both

causes to be unlikely to explain the low open-circuit voltage, since their calculations show no intragap surface states of the (100)-surface [29] and the formation energy of sulfur vacancies in pyrite bulk is large with about 2.4-2.7 eV [17]. Since the sulfur vacancies are the dominant intrinsic defects, bulk pyrite should be essentially intrinsically stoichiometric. Instead, Sun *et al.* propose oxygen impurities acting as substitutional defects for sulfur as a possible cause of the low open-circuit voltage, which might be in addition responsible for the unintentional p-type conductivity of pyrite samples [17]. However, Hu *et al.* come to a different conclusion, showing that oxygen-doped pyrite might improve the carrier mobilities and lifetimes, and thus lead also to an improvement of the device performance [30, 31]. The same group also suggests to synthesize pyrite thin films under sulfur-poor conditions, because the sulfur-rich (100)-surfaces possess a considerably smaller band gap than the sulfur-poor surfaces [19]. The S-terminated (100)-surface, which has been examined in many other studies, and has been made responsible for the low performance in some cases, is categorized into the S-poor surfaces in this study and exhibits a spin-polarization. Another recent study on the (100)-surface of pyrite using scanning tunneling microscopy measurements and simulations reports a band gap decrease to 0.4 ± 0.1 eV due to intrinsic surface states, which are overlapping with the bulk bands of the band edges [20, 21]. A similar argument has been reported by Limpinsel *et al.*, who make a p-type inversion layer on top of an n-type pyrite surface responsible for the low performance [22].

Furthermore, the accumulation of metallic sulfur-poor FeS_x precipitates at the surface [23], as well as the formation of bulk phase impurities like the Marcasite phase [24] have been also offered as a cause of the low open-circuit voltage. In the synthesis of pyrite the structurally closely related marcasite structure might be produced, which has been reported to have a much smaller band gap with 0.34 eV than pyrite [32]. Such a small band gap might have a crucial influence on the performance of a solar cell for already very small traces of that phase impurity. The band gap of FeS_2 marcasite has been obtained using electrical resistivity measurements, and since then there had been no reports about further experimental investigations on this band gap to my knowledge. Hence, the marcasite phase of FeS_2 has been considered to be critical for photovoltaic applications. However, recent studies indicate an at least as large band gap of the marcasite phase and a similar strong optical absorption as compared to pyrite [29, 33].

While most studies focus on the presence of defects, phase impurities or surface-related phenomena to investigate the low photovoltage in iron pyrite, there are also electronic structure calculations showing that already in the ideal bulk structure the question of the size of the fundamental band gap is still not settled. Although the band gap size of 0.95 eV is widely accepted, there is a quite large spread of reported experimentally measured band gap sizes and transition types for iron pyrite, comprised in the work of Ferrer *et al.* [34]. The authors indicate that this large spread is caused mainly due to the purity of the samples and the differences in the experimental techniques and the post-treatment of the measured data. Eyert *et al.* have demonstrated in calculations a rather sensitive dependence of the band gap of pyrite on the Wyckoff parameter, which is a structural parameter controlling the distance of the sulfur atoms in the sulfur dimers [35]. They claim that the large optical absorption in FeS_2 pyrite is a consequence of the transitions between the Fe $3d$ states at the valence band edge and the S $3p$ state at the conduction

band edge around the Γ point. However, recent results of the pseudodielectric function by Choi *et al.* indicate that the optical transitions from the valence band maximum to this S $3p$-state are strongly suppressed [36]. Therefore, optical measurements might not be able to detect this low-intensity conduction band minimum in iron pyrite, and thus the fundamental band gap might be significantly smaller than the measured 0.95 eV. This is supported by a theoretical study of Lazić *et al.* [26] and one of my publications [25]. Most of the experimental data could be also correctly interpreted by considering a small fundamental band gap in iron pyrite, which is difficult to detect due to its low optical activity and the small contribution to the density of states of this S $3p$ band. For instance, the low temperature activation energy of 0.2 eV obtained within electrical resistivity measurements [37, 38] might be caused by defects as it is proposed in these references, but a low-intensity bulk band might explain it as well.

Now it should be apparent that there are many works trying to explain the low open-circuit voltage in iron pyrite with both experimental as well as theoretical approaches, which come to a variety of conclusions. Since the results in this thesis are obtained within theoretical approaches only, let me throw in a short interlude, broaching in the issue of the importance of simulations and theory. Although a large part of this work was stimulated by experiment, simulations and theory are as well essential to understand the underlying mechanisms of physical phenomena. Experiment and simulation approach the problem from different sides. In experiment relevant quantities are measured, but to constrain the measurement to the essential effects might be difficult. For instance, finite temperature or unknown impurities in the material might have a considerable influence on the results. In simulations we know exactly the system and the underlying conditions, though we have to capture the essential physics with our model in the right way. If this is the case, simulations are not only able to help in understanding, but they might even have predictive power. Furthermore, with increasing computational resources we are able to treat larger system sizes and more complex systems with more sophisticated approaches and thereby we are able to model more realistic systems, while experimentalists strive to obtain pure samples and work at lower temperatures. Hence, there is a slow but steady diminution of the gap between experiment and simulation.

After this short interlude, let me focus on the pyrite results obtained within simulations now. Most of the theoretical results in the aforementioned publications are based on density-functional theory (DFT) [39, 40] in the local density approximation (LDA) [41, 42] or the generalized gradient approximation (GGA) proposed by Perdew-Burke-Ernzerhof (PBE) [43]. Density-functional theory has earned and still earns a lot of merits in various applications, where the electronic structure is needed, which also expresses in an increasing number of publications with this topic [44]. The reported band gap of iron pyrite within DFT using the LDA or GGA functional varies from metallic (*i.e.* 0 eV) to about 1 eV [29, 45–50] depending strongly on the value of the Wyckoff parameter [35]. The most recent results state a band gap of 0.6 eV for the structural parameters taken from experiment [51] and 0.4 eV using optimized structural parameters [19, 25, 29]. These values are consistent with the conventional band gap underestimation of DFT calculations within local exchange-correlation functionals [52, 53], exhibiting an about 50% smaller band gap than the widely accepted experimentally measured value of 0.95 eV. Since the band gap has a crucial

influence on the electronic and optical properties of semiconductors, an improvement of the band gap description is necessary to guarantee a reliable analysis for photovoltaic applications. One possibility to correct for that underestimation is the DFT+U method with a local Hubbard-U correction, which considers for correlation effects, and thereby enhances the band gap size. By applying this method to FeS_2 pyrite, the band gap is reported to increase to about 1 eV for a Hubbard-U of about 2 eV [29, 30]. However, aside the rigidity of this approach and the discussion whether the DFT+U method is not fully *ab-initio* any more due to the introduction of U, there is a recent study by Choi *et al.*, in which a considerable worsening of the optical absorption compared to experiment is found for the DFT+U results of pyrite compared to the "plain" DFT results [36].

Hence, more sophisticated methods like hybrid functional approaches or the GW approximation within many-body perturbation theory [54] might be needed to describe the electronic and optical properties of iron pyrite. The GW approximation has been a great success in the prediction of band gaps of various semiconductors [55], and also the hybrid functional HSE06 is reported to improve the prediction of band gaps [56, 57]. To my knowledge there is not much literature containing systematic investigations for pyrite or marcasite compounds using these methods. The application of the HSE06 functional is touched in [29, 30], reporting of a much too large band gap of iron pyrite and iron marcasite compared to experiment, and in [36], there is one sentence reporting about a quite unconventional reduction of the band gap of iron pyrite to about 0.4 eV when applying single-shot GW on top of GGA-PBE results. Both, the drastic overestimation of the band gap within HSE06, as well as the reduction of the band gap size using GW is very surprising and remarkable. It also seems that the single-shot GW results of iron pyrite exhibit a strong starting-point dependence as reported for several other systems [58–60], since the starting-point independent quasiparticle selfconsistent GW (QSGW) method [61, 62] yields a quite different result with a band gap of 0.81 eV compared to the single-shot GW approach [63]. It would be highly interesting to understand the reason, why single-shot GW and QSGW predict these different results. For instance, it is not clear how far the reported overestimation of band gap sizes within selfconsistent GW methods [64] affects the results for iron pyrite. There is no comparison between those approaches in reference [63], and additionally, an examination of the optical absorption is absent, making it difficult to compare the results to experiment.

Thus, iron pyrite behaves quite exotic when applying these more sophisticated approaches, and although there are plenty of publications about iron pyrite, it seems not even to be clear which method is most suitable to describe this compound. Much less is even known about the electronic structure of other pyrite compounds, as well as the structurally related marcasite compounds, within these more sophisticated methods.

In this thesis I am going to deal with two major topics: first I would like to shed some light on the electronic structure and the optical properties of several pyrite and marcasite compounds in the bulk structure (FeS_2, RuS_2, OsS_2, NiP_2 and ZnS_2 pyrite and FeS_2, $FeSe_2$ and $FeTe_2$ marcasite), and thus interpret the photovoltaic performance of these materials.[4]

[4] Note that some of the results regarding the electronic structure and optical properties of iron pyrite and iron marcasite are already published in one of my references [25].

Secondly, since interfaces play a crucial role for the photovoltaic performance of solar cells, I examine the thermodynamic stability and the role of surface states in iron pyrite by using free-standing iron pyrite films of (001), (111) and (210) orientation as a simplified model. Furthermore, first attempts to passivate surface states by placing adatoms on top of the surface are also discussed. For the calculations a full-potential linearized augmented plane-wave (FLAPW) method [65] as implemented in the Jülich DFT code FLEUR [66] has been exploited, which also features a hybrid functional framework [67, 68]. For the GW calculations the Jülich SPEX code [69] has been used, which also allows for QSGW calculations in the most recent version. Both codes are highly efficient and very accurate.

This thesis is structured as follows: in chapter 2 the density-functional theory (DFT) is established and the most basic approximations for the exchange-correlation functional, *i.e.* the local density approximation and the generalized gradient approximation are depicted. The more sophisticated exchange-correlation functionals like hybrid functionals or the DFT+U model are explained in chapter 3. The GW approximation is briefly introduced in chapter 4, including a discussion of its most important characteristic quantities and the difference between the single-shot approaches and the quasiparticle selfconsistent GW method. Chapter 5 is about the basics of the full potential linearized augmented plane-wave method as implemented in the DFT code FLEUR [66]. In particular the numerical parameters, which are important for the convergence of the results, are addressed. The fundamental mechanism of solar cells and the basic quantities to evaluate their performance are covered in chapter 6.

The DFT results of the electronic structure and the optical properties of iron pyrite are presented in chapter 7. In particular the dependence on the exchange-correlation functional and on the structural parameters is investigated. In chapter 8 the calculations for iron pyrite are extended to the GW approximation, and finally a possible cause for the low open-circuit voltage in iron pyrite solar cells is discussed.

The DFT and GW results for the iron marcasite compound, which is structurally closely related to iron pyrite, are presented in chapter 9. There I try to shed some light on the question, whether iron marcasite might be suitable for photovoltaic applications.

In chapter 10 the electronic structure of the pyrite compounds FeS_2, RuS_2, OsS_2, NiP_2 and ZnS_2, and the marcasite compounds FeS_2, $FeSe_2$ and $FeTe_2$ are calculated within DFT and GW to allow for a thorough comparison, and thereby understand the unconventional results of iron pyrite when applying hybrid functionals or the GW approximation.

The next two chapters cover iron pyrite surfaces, where in chapter 11 the thermodynamic stability of the iron pyrite (001), (111) and (210) surfaces is discussed and in chapter 12 the electronic structure of the most stable iron pyrite surfaces (001)-S, (111)-3S and (210)-2S is presented. Finally, the thesis is concluded in chapter 13.

2. Density-Functional Theory

2.1. Introduction

We scientists working in the large field of condensed matter physics are in the fortunate situation that we know exactly which problem needs to be solved. The Coulomb interaction of the cores and electrons is well known in its form and we have to deal at most with two-particle interactions. The corresponding Hamilton operator of the full problem including cores and electrons looks as follows:

$$\mathcal{H} = \mathcal{T}_e + \mathcal{T}_c + \mathcal{V}_{e-c} + \mathcal{V}_{e-e} + \mathcal{V}_{c-c}, \tag{2.1}$$

where[1]

$$\mathcal{T}_e = -\sum_i \frac{1}{2}\nabla_i^2 \tag{2.2}$$

is the kinetic energy of the electrons,

$$\mathcal{T}_c = -\sum_\alpha \frac{1}{2M_\alpha}\nabla_\alpha^2 \tag{2.3}$$

is the kinetic energy of the nuclei with masses M_α,

$$\mathcal{V}_{e-c} = -\sum_\alpha \sum_i \frac{Z_\alpha}{|\boldsymbol{r}_i - \boldsymbol{R}_\alpha|} \tag{2.4}$$

is the Coulomb interaction between the electrons and the nuclei with the atomic number Z_α,

$$\mathcal{V}_{e-e} = \frac{1}{2}\sum_i \sum_{j\neq i} \frac{1}{|\boldsymbol{r}_i - \boldsymbol{r}_j|} \tag{2.5}$$

is the Coulomb interaction between the electrons and

$$\mathcal{V}_{c-c} = \frac{1}{2}\sum_\alpha \sum_{\beta\neq\alpha} \frac{Z_\alpha Z_\beta}{|\boldsymbol{R}_\alpha - \boldsymbol{R}_\beta|} \tag{2.6}$$

is the Coulomb interaction between the nuclei. The spatial coordinates of the electrons are denoted by $\boldsymbol{r}_i$ and those of the cores as $\boldsymbol{R}_\alpha$.

[1] In my thesis atomic units with $\hbar = e = m_e = 4\pi\epsilon_0 = 1$ are used for all equations, unless something else is said. Here, $\hbar$ is the Planck constant, e is the elementary charge, m_e is the mass of an electron and ϵ_0 is the vacuum permittivity.

Knowing the problem, we could now ask why we have not solved the time-dependent or time-independent Schrödinger equation of this simple-looking Hamiltonian to obtain the general result for all possible condensed matter systems yet. First of all, although the Hamiltonian does not look very complicated, the Coulomb interaction between the particles makes it rather tough to solve. Already for three particles the problem can not be solved analytically and numerical approaches are needed. For many particles it is a necessity to exploit suitable approximations for the full Coulomb interaction to even succeed with numerical approaches.

However, there is an even more fundamental restriction based on the dimensionality of our problem, that we can not solve the Schrödinger equation of the Hamiltonian (2.1). Let us assume we would like to use a spatial grid for the full-particle wave function $\Psi(\boldsymbol{r}_1, .., \boldsymbol{r}_N, \boldsymbol{R}_1, .., \boldsymbol{R}_A)$ of the problem of N electrons and A cores, either to numerically approach the problem or only to display the wave function. Then, a grid consisting of 10 grid points for each coordinate is a rather typical choice, which leads to in total 10^{3N+3A} grid points which need to be processed and saved. Even for atoms ($A = 1$) with a few electrons this becomes impracticable [70]. To demonstrate the severeness of this problem, let me mention that the total number of electrons in our universe is estimated to be about 10^{80}, which is approximately the number of grid points when using an Fe atom as system ($N = 26$, $A = 1$). Hence, we are never able to even save the full wave function Ψ for the problem of an Fe atom.[2]

Therefore, approximations are indispensable to process with the Hamiltonian (2.1). The first common step to tackle it is to decouple the electronic motion from the motion of the cores via the Born-Oppenheimer approximation [71]. Since the mass of the cores is much larger than the mass of the electrons, the electrons can be assumed to adiabatically react to the movement of the cores. Then, we are left with two separate Schrödinger equations, one for the cores and one for the electrons. The electronic Schrödinger equation looks as follows:

$$\begin{aligned} \mathcal{H}_e &= \mathcal{T}_e + \mathcal{V}_{e-c} + \mathcal{V}_{e-e} && (2.7) \\ &= -\sum_i \frac{1}{2}\nabla_i^2 - \sum_\alpha \sum_i \frac{Z_\alpha}{|\boldsymbol{r}_i - \boldsymbol{R}_\alpha|} + \frac{1}{2}\sum_i \sum_{j\neq i} \frac{1}{|\boldsymbol{r}_i - \boldsymbol{r}_j|}, && (2.8) \end{aligned}$$

where the same definitions for the kinetic energy of the electrons, the electron-core interaction and the electron-electron interaction have been inserted as for Hamiltonian (2.1).[3] A major difference to the terms in (2.1) is that the spatial coordinates of the cores enter only as parameters and not as variables. But also the pure electronic problem is too difficult to solve without approximations due to the electron-electron interaction. Basically all approximations try to derive equations for a system with non-interacting particles.

[2] This example demonstrating the impossibility of ever solving the full Hamiltonian (2.1) has been presented in the lecture "Theoretische Festkörperphysik I" of E. Koch in the winter semester 2007/2008 at the RWTH Aachen. I found it so astonishing and convincing, that I needed to include it into this thesis.

[3] More precisely I have skipped the core-core interaction in eq. (2.1). Since it is only an additive constant, this term does not play a significant role except for some special cases as in the Madelung sum.

There are many approximations based on the many-particle wave function as a basic quantity. However, a large increase of the dimensionality with increasing particle number is a general problem of all wave-function based methods in condensed matter physics. Of course quantum-chemical methods such as Hartree-Fock, Configuration Interaction (CI) or Coupled Clusters (CC) are able to calculate the approximated wave function of an Fe atom quite easily, thus there are not as severe problems as for the full Hamiltonian (2.1). Nevertheless, the computational effort of those wave-function based methods scales in most cases with at least the 4th power in the number of atoms, drastically increasing for higher-order calculations, making them practical only for smaller and medium-sized molecules, whereas they are not useful for large molecules and also solids. For those interested to learn more about wave-function based quantum-mechanical methods I recommend the reference [72].

Instead of using the wave function as central quantity, the density-functional theory (DFT) makes the electronic density to the central quantity of the calculations. At the heart of DFT lies the mapping of the interacting electron system to a non-interacting electronic system with the same electronic density. Interestingly, the typical electronic densities look rather featureless, but still they contain the essential physics of the system. The reduction from $3N$ dimensions for the wave function to only 3 dimensions for the electronic density allows to treat larger systems as compared to the wave-function based methods, and in addition the framework of DFT is well suited to describe periodical systems, *i.e.* solids. Although DFT has been not well-accepted in the community of the chemists for a long time, since early DFT implementations had problems in predicting the bonding states of simple molecules [73], nowadays DFT is a standard tool for calculating electronic structures. The number of new annual publications using DFT is increasing almost every year [44, 74], demonstrating the large influence and the success of this method.

In this chapter I will present the very basics of DFT without going into detail. I recommend to read the articles by R. Jones about DFT [44, 75] and the references within for the interested reader. This chapter starts with the Hohenberg-Kohn theorem and then focuses on the various descriptions of the exchange-correlation energy. In the conclusions I point out a couple of advantages and drawbacks using DFT for electronic structure calculations to summarize the chapter.

2.2. The Electronic Density as Fundamental Variable

The ancestor of DFT goes back to the years 1927 and 1928, where the Thomas-Fermi method has been presented [76, 77]. This method inspired the development of DFT, since it focuses on the electronic density as basic variable instead of the wave function. However, in particular the approximated description of the kinetic energy in this model leads to severe shortcomings, like the inability to capture chemical bondings in molecules or shell structures in atoms. From there it took more than 30 years before Hohenberg and Kohn published their theorems based on the variational principle on the energy [39], which are

the basis for DFT. The theorems are as follows:

(a) The ground-state properties of a system are uniquely determined by an electron density $n = n(\boldsymbol{r})$. Hence, the ground-state wave function is a unique functional of the electron density: $\Psi_0 = \Psi_0[n]$.

(b) The ground-state electronic density n_0 is the unique density, which minimizes the total energy of the system.

Hence, all ground-state quantities are functionals of the electronic density via $O[n] = \langle\Psi_0[n]|\hat{\mathcal{O}}|\Psi_0[n]\rangle$ for an observable $\hat{\mathcal{O}}$. In particular the total energy $E = E[n]$ is of interest, since its minimization yields the ground-state density.[4]

Thus, if we find a system of non-interacting electrons with the same ground-state density as the system with interacting electrons, the ground-state properties of both systems would be the same and we would have solved the problem of the interacting system, supposed that we know the functionals. Kohn and Sham did this by connecting the total energy of the interacting system to the following total energy of a non-interacting system [40]:

$$E[n] = T_S[n] + E_{\text{ext}}[n] + E_H[n] + E_{\text{xc}}[n], \tag{2.9}$$

where

$$T_S[n] = -\frac{1}{2}\sum_i \langle\phi_i|\nabla_i^2|\phi_i\rangle \tag{2.10}$$

is the kinetic energy of the non-interacting system with ϕ_i the one-electron wave functions,

$$E_{\text{ext}}[n] = \int d^3r\ n(\boldsymbol{r})V_{\text{ext}}(\boldsymbol{r}) \tag{2.11}$$

is the energy originating from an external potential $V_{\text{ext}}(\boldsymbol{r})$,

$$E_H[n] = \frac{1}{2}\int\int d^3r d^3r'\ \frac{n(\boldsymbol{r})n(\boldsymbol{r'})}{|\boldsymbol{r}-\boldsymbol{r'}|} \tag{2.12}$$

is the Hartree energy comprising the "classical" Coulomb interaction between the electrons and $E_{\text{xc}}[n]$ is the exchange-correlation energy, which is sometimes divided separately into an exchange and a correlation term. The exchange term is a non-classical Coulomb contribution, which can be derived within the Hartree-Fock theory. Everything beyond that is put into a correlation term, which for example contains the difference between the kinetic energy of the interacting and non-interacting electron system.

Since the one-electron wave functions ϕ_i enter the energy directly via T_S and in all other terms via the electronic density

$$n(\boldsymbol{r}) = \sum_i |\phi_i(\boldsymbol{r})|^2, \tag{2.13}$$

[4] The ground-state density is only unique for a non-degenerate ground state. The extension to degenerate ground states has been done by Levy [78].

the minimization of the energy functional with respect to those ϕ_i (thereby also with respect to the density) leads to the so-called Kohn-Sham equations for these one-electron wave functions:

$$\left(-\frac{1}{2}\nabla^2 + V_{\text{eff}}(\boldsymbol{r})\right)\phi_i(\boldsymbol{r}) = \varepsilon_i\phi_i(\boldsymbol{r}), \tag{2.14}$$

where

$$V_{\text{eff}}(\boldsymbol{r}) = V_{\text{ext}}(\boldsymbol{r}) + \int d^3r' \, \frac{n(\boldsymbol{r'})}{|\boldsymbol{r} - \boldsymbol{r'}|} + V_{\text{xc}}(\boldsymbol{r}) \tag{2.15}$$

is the effective one-particle potential of our non-interacting system. The Kohn-Sham eigenenergies ε_i are the Lagrange parameters of the minimization, which enter through the constraint that the Kohn-Sham wave functions need to be normalized. They have no direct physical meaning except of the highest occupied Kohn-Sham energy, which is the negative value of the ionization energy. The quantity $V_{\text{xc}}(\boldsymbol{r}) = \frac{\delta E_{\text{xc}}[n]}{\delta n}$ is the exchange-correlation potential, comprising the complicated many-body effects. Numerically, the Kohn-Sham equations allow us to calculate the ground-state electronic density in a selfconsistent scheme. After choosing a reasonable starting-point density, the calculated Kohn-Sham orbitals ϕ_i can be used to recalculate a new density via eq. (2.13), which then again can be inserted into the Kohn-Sham equations. This process can be iterated till convergence of the density, yielding the ground-state density of the system.

Formally the Kohn-Sham DFT scheme is exact, thus we really could obtain the ground-state properties of the interacting electron system. Hence, as long as we are not interested in excited electrons we have formally solved the electronic Hamiltonian (2.8). However, the exact functional form of V_{xc} is not known and only approximations can be used. There is a whole zoo of forms and approximations for the exchange-correlation term, and in the next section I will briefly introduce the two most basic implementations, which are the local density approximation (LDA) and the generalized gradient approximation (GGA).

2.3. The Exchange-Correlation Functionals

In principle density-functional theory gives the exact ground-state solution of the fully interacting electron system, but in practice approximations for the exchange-correlation energy have to be used. There are many scientists trying to improve the description of the exchange-correlation by inventing new functionals. Nowadays there is a vast amount of functionals, which can be (non-)empirical, (non-)local, even orbital-dependent and they can be classified into much more properties I am not going to discuss in this thesis. More information about the zoo of functionals can be found for instance in [79]. In this section I focus on the most prominent local exchange-correlation functionals in use, which are the exchange correlation functionals within the local density approximation (LDA) [41, 42] and the generalized gradient approximation (GGA) [43].[5] The property 'local' means that the spatial dependence of the exchange-correlation potential is solely on $\boldsymbol{r}$ and no

[5] The functionals within GGA are sometimes also denoted as semi-local functionals. In this thesis I will not make this distinction.

additional other spatial vectors. The locality of the LDA and GGA functional makes it relatively simple to use them in computations and since they already provide good results for a variety of systems, they are the backbone of most DFT calculations.

In the LDA the exchange-correlation term of the homogeneous electron gas $\varepsilon_{\mathrm{xc}}^{\mathrm{hom}}$ enters via

$$E_{\mathrm{xc}}[n] = \int d^3r \; n(\boldsymbol{r}) \varepsilon_{\mathrm{xc}}^{\mathrm{hom}}(n(\boldsymbol{r})). \tag{2.16}$$

The pure exchange term of the homogeneous electron gas is proportional to $n(\boldsymbol{r})^{1/3}$, whereas an exact expression for the correlation term in the homogeneous electron gas is not known up to now. Instead, there are different approaches within the LDA using approximations for the correlation energy of the homogeneous electron gas, as for instance the functionals by Vosko-Wilk-Nusair [42] or by Perdew-Zunger [80].

The local density approximation has led to successful predictions of physical quantities in various systems, which at first glance is quite surprising. It is hardly imaginable that the formal expressions of the exchange-correlation terms of the homogeneous electron gas can be used to obtain reasonable results for solids, since the electrostatic potential, and thus also the electronic density is very different between those two systems. That the LDA leads to such surprising good results can be contributed to a reasonable description of the spherical average of the exchange- and correlation-hole due to a cancellation of systematical errors [81].

The generalized gradient approximation (GGA) is an attempt to improve the LDA functional by including the spatial derivative of the electron charge density $\nabla n(\boldsymbol{r})$. Hence, the exchange-correlation energy is of following form:

$$E_{\mathrm{xc}}[n] = \int d^3r \; n(\boldsymbol{r}) \varepsilon_{\mathrm{xc}}(n(\boldsymbol{r}), \nabla n(\boldsymbol{r})). \tag{2.17}$$

One could think the idea behind this approach is motivated by a typical Taylor expansion, where higher-order derivatives enhance the accuracy of a result. However, there is no simple way to improve the results in DFT. This is very well observable when using higher derivatives than $\nabla n(\boldsymbol{r})$ in a GGA-like approach, since the results usually become worse as compared to the experiment. Here, the GGA functional by Perdew-Burke-Ernzerhof [43] is used, which improves the results as compared to the experiment in some cases. In particular the geometrical structure optimization and the binding energies are improved for many systems [82]. For all the pyrite and marcasite compounds investigated in this thesis, I used the GGA functional instead of the LDA functional, since it leads to better results.

2.4. Conclusions

In this section the basics of density-functional theory (DFT) have been introduced. Compared to wave-function based methods, DFT shows a much more benign scaling with the system size. Formally, DFT yields the exact solution of the ground state of the many-electron system. But, since the exact expression for the exchange-correlation functional is unknown, approximations have to be used. As a major drawback of DFT there is no

simple way to systematically improve the results. Hence, there are functionals which might work well for a class of systems, but not for another class. In addition, DFT is suited to calculate ground-state properties, whereas it has only a limited predictability for excited electronic states.

The most basic exchange-correlation functionals are based on the LDA and the GGA, which both are local functionals in the spatial coordinates. These two approximations lead to good results for various systems and due to the simplicity of these approaches they have become the backbone of nowadays calculations within DFT. However, the local exchange-correlation functionals suffer of a systematical underestimation of band gaps in semiconductors and insulators due to a wrong description of the derivative discontinuity of the exchange-correlation energy with respect to the particle number [52]. Additionally, the self-interaction error caused by the missing cancellation of the self-interaction in the Hartree-term with the local exchange-correlation functionals might lead to a wrong prediction of localized states [80]. Hence, methods beyond LDA and GGA might be necessary to remedy these shortcomings. In the next chapter a couple of those methods will be introduced.

3. Density-Functional Theory beyond the LDA and the GGA

3.1. Introduction

The local exchange-correlation functionals within the LDA and the GGA in density-functional theory suffer of several shortcomings, which I have already mentioned in the last section of the previous chapter. In particular the underestimation of band gap sizes poses a problem for my investigations of the pyrite and marcasite compounds. Hence, methods beyond the LDA and the GGA are necessary to remedy these shortcomings.

There are plenty of methods, which improve the description of semiconductors compared to "conventional" LDA and GGA calculations. Here, I am going to focus only on a handful of them, namely DFT+U, and the hybrid functionals PBE0 and HSE06. The GW approximation of the many-body perturbation theory is derived in a different spirit and will be discussed in the next chapter. All methods discussed here need the "conventional" DFT calculations as a starting point. The simplest and fastest of those methods is DFT+U, which might shift and change the bandwidth of a subset of electronic bands. The hybrid functionals act on all bands and no input parameter U is needed. Furthermore, they can lead to changes in the character or the curvature of the bands, which is of importance in several cases as for instance in EuO [83]. However, the computational effort is largely increased compared to "conventional" DFT and DFT+U. An expensive, but state-of-the-art method to calculate band gaps is the GW approximation, since it is the only approach of those discussed here, which comprises electronic excitations.

For most semiconductors the predicted band gap size considerably improves with respect to the experimental values by using these methods. I will now give more details in the specific sections of this chapter.

3.2. The DFT+U Method

Despite the increasing number of other existing more sophisticated methods, which become more feasible with growing computational power, the DFT+U method is still a popular approach to overcome some of the shortcomings of "conventional" DFT calculations. The popularity is based on the simplicity of DFT+U, allowing easily implementations into existing frameworks, as well as the low computational demand comparable to "conventional" DFT calculations. "Conventional" DFT calculations tend to an over-delocalization of the electrons, *i.e.* they lack an accurate description of localized electrons, which might be important for transition-metal compounds and is important for rare-earth compounds.

Inspired by the single-band Hubbard model, in DFT+U a Hubbard-U parameter accounts for the strong Coulomb interaction of the localized electrons. This Hubbard-U parameter is usually applied only to d- or f-electrons, thereby introducing an orbital-dependence of the energy functional into the DFT scheme:

$$E_{\mathrm{DFT}+U}[n(\boldsymbol{r})] = E_{\mathrm{DFT}}[n(\boldsymbol{r})] + E_U[\{n_i\}] - E_{\mathrm{dc}}[\{n_i\}], \tag{3.1}$$

where n_i are the electron occupation numbers for the orbitals i,[1] E_{DFT} is the total energy of the "conventional" DFT calculation, E_U is the Hubbard-U contribution to the total energy and E_{dc} accounts for the double counting of the former two terms. For a simplified DFT+U approach with only one U parameter, E_U and E_{dc} look as follows:

$$E_U = \frac{U}{2}\sum_{i\neq j} n_i n_j, \tag{3.2}$$

$$E_{\mathrm{dc}} = \frac{U}{2}N(N-1), \tag{3.3}$$

with $N = \sum_i n_i$ the total number of electrons. Hence, the Hubbard-term E_U only adds a plus of Coulomb repulsion, if both states i and j are occupied.

In the Jülich DFT code FLEUR [66] a more elaborate DFT+U scheme is used, involving not only a Hubbard-U, but also a Hund-exchange parameter J and higher terms. Moreover, the full electronic density matrix depending on the atom and the angular momentum quantum number l is treated in a multiband Hubbard model. The Hund-exchange parameter J considers for an energy difference between singlet and triplet spin-configurations for two electrons in two different states i and j. It is common to introduce an effective Hubbard-U parameter $U_{\mathrm{eff}} = U - J$. The energy functionals E_U and E_{dc} look more complicated using U_{eff}, U and J. Furthermore, the double counting term is not unique and the two most prominent limits are the fully-localized limit and the around-mean field limit. The former is suited for quite localized electron systems, whereas the latter is better suited for systems exhibiting weak orbital polarizations. I will not present the expressions for E_U and E_{dc} in this thesis, but for the interested reader I recommend to take a look into [84].

The Coulomb repulsion mediated via the Hubbard-U term essentially shifts the orbital energies of the corresponding states; usually these are the d- or f-states. This can be seen by taking the derivative of the total energy (3.1) with respect to the occupation number n_i, which leads to

$$\varepsilon_i^{\mathrm{DFT}+U} = \frac{\partial E_{\mathrm{DFT}+U}}{\partial n_i} = \varepsilon_i^{\mathrm{DFT}} + U(1/2 - n_i), \tag{3.4}$$

where $\varepsilon_i^{\mathrm{DFT}}$ and $\varepsilon_i^{\mathrm{DFT}+U}$ are the orbital energies for the "conventional" DFT calculation and the DFT+U calculation, respectively. The occupied orbital energies are shifted by $-U/2$, whereas the unoccupied orbital energies are shifted by $+U/2$. Note that the expressions for the orbital energies become more complicated for the DFT+U method accounting U

[1] The notation i for the orbitals is an abbreviation for the angular momentum quantum number, the magnetic quantum number and the electron spin, *i.e.* $i = l, m, \sigma$.

and J. Nevertheless, the main feature remains, which is a shift of the localized bands to lower or higher energies depending on their occupation status. As a consequence this might lead to larger band gap sizes as compared to the DFT calculation within the LDA or GGA, whenever the band edges are defined by those localized states.

The Hubbard-U parameter might have a crucial influence on the size of the band gap, whenever the gap is formed by states affected by U. This parameter can either be fitted to experimental data or it can be determined via approaches like the constrained random-phase approximation (c-RPA) [84–86]. In the first case DFT+U becomes an empirical method and the results should be regarded with caution, in particular if only the size of the band gap has been used as a fitting parameter. The DFT+U method might have a considerable influence on the structural stability, optical properties, and more. Those results might become worse compared to the experiment when applying DFT+U in an empirical sense. Of course the same might be the case when calculating the Hubbard-U parameter via c-RPA, but then the approach is in some sense *ab-initio* and thereby in itself consistent.

In DFT+U not only the size of the band gap might change, but also the band character and the curvature can be slightly altered due to changes in the orbital hybridization. However, for some systems the curvature of the bands is described poorly within "conventional" DFT, which might demand for more sophisticated methods than DFT+U to significantly improve the description. In the next section I will introduce two prominent hybrid functionals, which can satisfy those demands.

3.3. Hybrid Functionals

The fundamental Kohn-Sham band gap $\varepsilon_{\mathrm{gap}}^{\mathrm{KS}}$, *i.e.* the band gap determined by the highest occupied and lowest unoccupied Kohn-Sham energy, is not the real fundamental band gap of the semiconductor. The real fundamental band gap $\varepsilon_{\mathrm{gap}}$ can be obtained via the total energy differences $E(N+1)+E(N-1)-2E(N)$, thereby DFT calculations with $N+1$, N and $N-1$ electrons need to be conducted. Taking the limit of infinitesimal particle number changes ΔN we obtain

$$\varepsilon_{\mathrm{gap}} = \varepsilon_{\mathrm{gap}}^{\mathrm{KS}} + \left.\frac{\delta E}{\delta n}\right|_{N+\Delta N} - \left.\frac{\delta E}{\delta n}\right|_{N-\Delta N}, \tag{3.5}$$

where $\left.\frac{\delta E}{\delta n}\right|_{N+\Delta N} - \left.\frac{\delta E}{\delta n}\right|_{N-\Delta N}$ is the derivative discontinuity of the exchange-correlation energy with respect to the particle number. The underestimation of band gap sizes in "conventional" DFT calculations is mainly caused by an inadequate description of this derivative discontinuity. Local exchange-correlation functionals as for instance the LDA and GGA functionals do not describe the derivative discontinuity, usually leading to underestimated band gaps due to $\varepsilon_{\mathrm{gap}}^{\mathrm{KS}} < \varepsilon_{\mathrm{gap}}$. However, the self-interaction error, and additional shortcomings in the description of the exchange energy, as well as in the correlation energy might have also considerable influence on the size of the band gap. Hence, the systematic underestimation of the band gap size for local exchange-correlation functionals is more a rule of thumb than a fact.

On the other hand, the Hartree-Fock (HF) approximation yields no self-interaction error, the exchange energy is treated exactly and the derivative discontinuity is not zero. But due to missing electron correlation, the HF approximation is not able to produce reasonable results for molecules or solids. At the heart of hybrid functionals lies the mixing of a fraction local exchange-correlation with a fraction non-local HF-exchange. Thus, there is the hope to remedy the shortcomings of the local exchange-correlation for solids without loosing the ability to describe solids reasonably. The mixing factor for the HF-exchange has been determined to 25% by Becke *et al.* [87], leading to the PBE0 functional with the following exchange-correlation energy:

$$E_{\mathrm{xc}}^{\mathrm{PBE0}} = E_{\mathrm{xc}}^{\mathrm{PBE}} + \frac{1}{4}\left(E_{\mathrm{x}}^{\mathrm{HF}} - E_{\mathrm{x}}^{\mathrm{PBE}}\right), \tag{3.6}$$

where $E_{\mathrm{x}}^{\mathrm{PBE}}$ and $E_{\mathrm{xc}}^{\mathrm{PBE}}$ is the exchange and exchange-correlation energy of the PBE (GGA) functional [43], and $E_{\mathrm{x}}^{\mathrm{HF}}$ is the exchange energy in HF.

Since the HF-exchange introduces a non-local potential $V_x(\boldsymbol{r}, \boldsymbol{r'})$ into the Kohn-Sham scheme, the effort to solve the equations is drastically increased as compared to "conventional" DFT. Typically, the calculations need about an order of magnitude more computational time. Additionally, PBE0 treats both the exchange and correlation as a long-range interaction, which consumes a lot of time. However, in reality, polarization, thus correlation effects, screen the long-range exchange, reducing a bit the band gap size of the system, explaining why the band gaps predicted within PBE0 are usually too large compared to experiment. Hence, the screened hybrid functional HSE by Heyd, Scuseria and Ernzerhof [88, 89] has been constructed, which separates the exchange energy of PBE into a long-range (LR) and a short-range (SR) contribution, whereas the HF-exchange is only accounted within short-range.[2] For this the Coulomb interaction $\nu(r)$ is divided into a long- and short-range part $\nu^{\mathrm{LR}}(r)$ and $\nu^{\mathrm{SR}}(r)$ via the Gaussian error-function $\mathrm{erf}(\omega r)$:

$$\nu(r) = \frac{1}{r} = \frac{\mathrm{erf}(\omega \mathrm{r})}{r} + \frac{1 - \mathrm{erf}(\omega \mathrm{r})}{r} =: \nu^{\mathrm{LR}}(r) + \nu^{\mathrm{SR}}(r). \tag{3.7}$$

Thus, the screening is introduced in an artificial way via the Gaussian error-function with an optimized screening parameter $\omega = 0.11$ in HSE06 [89]. The exchange-correlation energy within the HSE functional looks as follows:

$$E_{\mathrm{xc}}^{\mathrm{HSE}} = E_{\mathrm{xc}}^{\mathrm{PBE}} + \frac{1}{4}\left(E_{\mathrm{x}}^{\mathrm{HF,SR}} - E_{\mathrm{x}}^{\mathrm{PBE,SR}}\right). \tag{3.8}$$

Although the screening is artificial, the results for the band gaps considerably improve as compared to PBE and PBE0 [56, 57]. The HSE functional also improves the predicted lattice parameters compared to PBE, which is also already the case for the PBE0 functional. As a rule of thumb the screened hybrid functional is well adapted for semiconductors with moderate band gap sizes. For large band gap semiconductors the screening is overestimated in HSE leading to smaller band gaps as compared to experiment, and for small band gap

[2] Historically, the HSE functional has been constructed for computational convenience first. Then it turned out that also the band gaps are improved due to the implemented screening.

semiconductors and metals the situation is the contrary with an underestimated screening. There are modified screened-exchange approaches with other mixing parameters than 25% to improve the description for small band gap and large band gap semiconductors [90, 91]. Most of them use the inverse of the static dielectric constant as mixing parameter due to a straight connection between polarizability and screening effects. In other cases the mixing parameter is empirically determined in the spirit of the DFT+U approach.

For more details about hybrid functionals, in particular about the screened hybrid functional HSE, I recommend to read the PhD thesis of M. Schlipf [83]. More information on orbital-dependent functionals in general is given in reference [92]. The implementation into the Jülich DFT code FLEUR is explained in the references [68, 93].

3.4. Conclusions

In this chapter I have briefly discussed the DFT+U method and the hybrid functionals PBE0 and HSE, which both have earned their merits to overcome the shortcomings of local functionals like the LDA or GGA functionals. For most semiconductors the band gap prediction is systematically improved, although there are cases where it might become worse.

The DFT+U method is simple and allows for fast computation, but the determination of the Hubbard-U parameter is a potential problem. Empirical fittings should be regarded critically and exploiting methods like c-RPA to determine the U parameter are costly.

On the other hand, hybrid functionals are a much more sophisticated approach to attenuate the problems of local functionals. With hybrid functionals the lattice parameters for some systems are improved compared to "conventional" DFT calculations, *e.g.* for Perovskites or in the Europium chalcogenides series as shown in the references [83, 94]. When accounting for an (artificially incorporated) electron screening as it is done in the HSE functional, the prediction of band gaps becomes also better. However, due to the inclusion of the Hartree-Fock exchange the potential becomes non-local, which makes the calculations very costly.

A point of debate is the value of the mixing parameter of the Hartree-Fock exchange, which is chosen to be 25% for "conventional" PBE0 and HSE calculations. With this choice of the mixing parameter small band gap and large band gap semiconductors might be described poorly. Therefore, there are approaches combining the static dielectric function with the mixing parameter and thus controlling the screening to improve the description for these semiconductors as well. Since the choice of the mixing parameter is not unique, critics might point out that this is alike a more complicated DFT+U method.

In the next chapter I will introduce an additional method beyond the LDA and GGA, namely the GW approximation to many-body perturbation theory. It is the only method discussed in this thesis, which is even beyond DFT, since it is designed to accurately calculate electronic excitations. Hence, it became the state-of-the-art tool to predict band gaps.

4. GW Approximation

4.1. Introduction

Density-functional theory (DFT) is an electronic ground state theory, and thus it is not the method of choice to predict accurate results about excited states. Furthermore, in difference to, for instance the total energy, the Kohn-Sham energies and wave functions are only mathematical tools and except of the highest occupied Kohn-Sham energy do not have a physical meaning. Hence, strictly speaking the whole electronic band structure calculated via DFT can not be directly related to the "real" band structure of the fully interacting electron system, *i.e.* the excitation energies of all quasiparticles of the system. Although in many cases the band structure within DFT already gives a nice qualitative understanding, explaining the enormous amount of references focusing on the analysis of those band structures, a theory beyond DFT is vital to predict accurate electronic band structures. The many-body perturbation theory is such a framework.

I will focus on the GW approximation to the many-body perturbation theory [54], which corrects the Kohn-Sham energies (or others, *e.g.* Hartree-Fock energies) and in the case of a selfconsistent approach also the Kohn-Sham wave functions, and thus remedies a couple of shortcomings caused by the description of DFT. In particular the sizes of the band gaps are considerably improved, making the GW approximation a state-of-the-art method to describe band gaps. Within the GW approximation, additional to the N-electron system already described in DFT, an $(N+1)$- and $(N-1)$-electron system can be calculated, modeling the experimental situation of photoemission and inverse photoemission spectroscopy. That explains the success in predicting band gaps within GW. Essential to the GW approximation is the introduction of a screened Coulomb interaction, originating from electrons, which are screened by their oppositely charged Coulomb holes, leading to an effective reduction of the charge of those electrons. While the electrostatic screening is introduced in a purely mathematical way in the hybrid functional HSE as demonstrated in the last chapter, it enters in a physical sense in the GW approximation.

The electron and its Coulomb hole form a quasiparticle and these quasiparticles are independent particles to a good approximation.[1] Hence, also the GW approximation leads to a set of equations for non-interacting (quasi-)particles. The so-called self energy Σ acts as potential for those quasiparticles. Since Σ is a non-local and energy-dependent quantity, GW calculations are computationally very demanding. Typically, the calculations take about 1-2 orders of magnitude more computational time as compared to "conventional" DFT calculations. Due to this huge computational effort, single-shot GW calculations are still the standard, whereas selfconsistent GW approaches like for instance quasiparticle

[1] At least that is true close to the Fermi energy, since there is a finite lifetime otherwise.

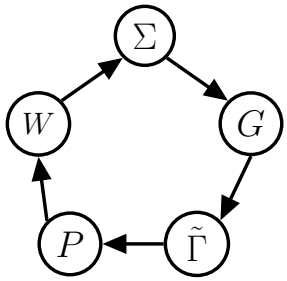

Figure 4.1.: Hedin's equations [54] comprise five characteristic quantities, the self energy Σ, the Green's function G, the vertex function $\tilde{\Gamma}$, the polarizability P and the screened Coulomb interaction W into a highly-complicated set of integro-differential equations. This flow chart symbolizes the connection of those quantities and the sequence of their calculation.

selfconsistent GW (QSGW) [61, 62] slowly catch up with increasing computer power.

In this chapter I will introduce the most important characteristic quantities of the GW approach, followed by a brief discussion about single-shot GW versus selfconsistent GW.

4.2. Characteristic Quantities in the GW Approach

The many-body problem can be formally solved by a set of five integro-differential equations, the so-called Hedin's equations [54]. These equations are rather complicated and up to now could only be solved for simple systems under additional approximations. There is one equation for the self energy Σ, the Green's function G, the vertex function $\tilde{\Gamma}$, the polarizability P and the screened Coulomb interaction W. In Fig. 4.1 an approach to solve Hedin's equations is displayed, showing the order in which these five quantities need to be solved iteratively. Since those quantities are also essential for the GW approximation, I will briefly discuss them and show the connection between the Hedin's equations and the GW approximation. I will not present Hedin's equations or corresponding derivations in this thesis and refer the interested reader to the literature and the references within [54, 95].

First let me introduce the one-particle Green's functions $G(\boldsymbol{r}, t; \boldsymbol{r'}, t')$, which are also called one-particle propagators, since they describe the propagation of one additional electron or hole in the system from the space-time coordinate $(\boldsymbol{r}, t)$ to another coordinate $(\boldsymbol{r'}, t')$. Thus, we describe not only an N-electron system, but also the $(N+1)$- and $(N-1)$-electron system, allowing to model the situation of (inverse) photoemission experiments. Hence, we are also able to calculate the "real" band gap of the system. The one-particle Green's function contains much less information than the full many-body wave function, but still it allows to calculate all expectation values of single-particle operators and it comprises all possible single electron excitations. The applications of Green's functions are very diverse and I recommend the book by G. F. Roach [96] to the interested reader.

The next quantity I would like to introduce is the polarizability $P(\boldsymbol{r}, \boldsymbol{r'}, \varepsilon)$, which is closely related to the dielectric function $\epsilon(\boldsymbol{q}, \omega)$ describing the response of the system to electrical fields. The injection of an additional electron into the system leads to an accumulation of positive charge around this electron, which is called the Coulomb hole of that electron. The Coulomb hole leads to a reduction of the effective charge of each electron. The response of the system on the additional electron, *i.e.* the creation of the Coulomb hole, is described via P. The Coulomb hole and the electron always coexist, and thus they can be described as a quasiparticle. The screened Coulomb interaction $W(\boldsymbol{r}, \boldsymbol{r'}, \varepsilon)$ is the interaction between those quasiparticles, similar to the bare Coulomb interaction being the interaction between the "naked" electrons. Since the screened Coulomb interaction W is significantly smaller than the bare Coulomb interaction, those quasiparticles can be described in a non-interacting particle picture in good approximation. Therefore, treating W and the Green's function of the interacting electron system G in perturbation theory as it is done in Hedin's equations is much more promising than using the bare Coulomb interaction and the non-interacting Green's function G_0 as basic quantities for many-body perturbation theory as it has been done before Hedin [97]. The screened Coulomb interaction is essential for the description of electronic excitations and can be tagged as the most important additional physical effect in the GW approximation as compared to the Hartree-Fock approximation.

The self energy $\Sigma(\boldsymbol{r}, \boldsymbol{r'}, \varepsilon)$ acts as a potential connecting the non-interacting electron system to the interacting electron system. The role as potential becomes clear in the Dyson equation, which couples the Green's functions of the interacting and non-interacting system via $G = G_0 + G_0 \Sigma G$, where G_0 is the Green's function of a non-interacting electron system in the same external potential. The diagonal elements of Σ contain the quasiparticle energy corrections.[2] The quasiparticle energies are complex and their imaginary part is related to the lifetime of the quasiparticle. Typically, the lifetime is smaller the larger the excitation energy is. Since the self energy $\Sigma(\boldsymbol{r}, \boldsymbol{r'}, \varepsilon)$ is non-local and energy-dependent, calculations including this quantity are rather time-consuming and complicated.

The vertex function $\tilde{\Gamma}(\boldsymbol{r}, t; \boldsymbol{r'}, t'; \boldsymbol{r''}, t'')$ is the most complicated quantity of these five, having a dependence on three spatial vectors and making it difficult to find a simple physical interpretation. From the perspective of the GW approximation, all the many-body effects beyond GW are comprised in the vertex corrections. These are for instance excitonic effects or strongly correlated electronic phenomena. However, the vertex function is still elusive and is known even for simple systems up to now only approximately.

After explaining the most basic quantities in Hedin's equation, let me indicate the connection between these equations and the GW approximation. In the GW approximation the vertex function is approximated to $\tilde{\Gamma}(\boldsymbol{r}, t; \boldsymbol{r'}, t'; \boldsymbol{r''}, t'') = \delta(\boldsymbol{r}, t; \boldsymbol{r'}, t') \delta(\boldsymbol{r}, t; \boldsymbol{r''}, t'')$ making the four remaining equations of Hedin much less complicated. Hence, all many-body effects beyond the GW approximation are hidden in those elusive vertex corrections. With that simplified vertex function the equation for the self energy Σ turns out to be

[2] To be more precise, the quasiparticle energy corrections to a DFT result can be calculated from the quantity $\Sigma - V_{\mathrm{xc}}$. Depending on the calculation scheme, either only the diagonal elements or the full matrix in the basis of the Kohn-Sham orbitals can be used.

formally $\Sigma = \mathrm{i}GW$, explaining the name GW approximation. The eigenvalue equation for the quasiparticle energies and wave function looks similar to the Kohn-Sham equations, but note that they are non-linear in the quasiparticle energies $\varepsilon_i^{\mathrm{QP}}$:

$$\left(-\frac{1}{2}\nabla^2 + V_{\mathrm{ext}}(\boldsymbol{r}) + V_{\mathrm{H}}(\boldsymbol{r})\right)\phi_i(\boldsymbol{r}) + \int d^3r'\ \Sigma(\boldsymbol{r}, \boldsymbol{r'}, \varepsilon_i^{\mathrm{QP}})\phi_i(\boldsymbol{r'}) = \varepsilon_i^{\mathrm{QP}}\phi_i(\boldsymbol{r}), \quad (4.1)$$

where $\varepsilon_i^{\mathrm{QP}}$ are the complex quasiparticle energies, $\phi_i(\boldsymbol{r})$ are the corresponding wave functions, $V_{\mathrm{ext}}(\boldsymbol{r})$ is the external potential and $V_{\mathrm{H}}(\boldsymbol{r})$ is the Hartree potential as introduced in the chapter 2 about DFT. The self energy takes over the role to determine the exchange energy and correlation energy of the electron system. Due to the energy dependence of the self energy Σ, this exchange-correlation potential is different for each state. In addition the non-locality of the self energy leads to long-range interaction effects, which make the calculations even more complicated. For instance, for the description of surfaces and thin films in many DFT codes a vacuum layer has to be defined, which needs to be thick enough to prevent a mirror interaction due to periodic boundary conditions (see chapter 5). Within GW the long-range interaction makes it very tough to reduce these mirror interaction effects.

The numerical implementation of the GW approximation is highly complicated and I would like to point out only a few points. For more details I refer to the references [69, 98–100] and to some extent I will discuss it in more detail in the chapter 5. For the most basic quantities within GW, as for instance the polarization function, one has to sum over unoccupied states. In practice the sum only goes over a finite amount of unoccupied bands and it turns out that in some cases the convergence with the number of those bands might be rather slow. For instance, in the case of ZnO about 3000 bands are necessary to converge the fundamental band gap, whereas only a small fraction of those are occupied bands [101, 102]. When accounting for such high-lying band energies, it is also highly non-trivial to guarantee reasonably described wave functions. It is quite common within the GW approximation to approximate the quasiparticle wave functions by those of the converged Kohn-Sham system within DFT, at least when performing single-shot GW calculations. To get a correct description of these wave functions for high-lying energies, it might be that the standard DFT basis set has to be extended, *e.g.* many higher-derivative local orbitals (HELOs) and semi-core local orbitals need to be included into the basis representation. In addition, the plane-wave cutoff k_{max} might have to be increased, which on the other hand might lead to an over-complete basis leading to numerical problems. I will talk about these numerical parameters and the difficulties in more detail in the next chapter in the context of the full-potential linearized augmented plane-wave (FLAPW) method. Hence, you can consider this paragraph as an "appetizer" to those numerical difficulties.

4.3. Single-Shot and Selfconsistency

Nowadays, there exist plenty of different GW approximation schemes. First of all, they can be distinguished into the single-shot GW schemes and the selfconsistent approaches.

The single-shot GW schemes are very common and were the only feasible approaches in earlier days due to the required computational effort of the GW calculations. They are also denoted as G_0W_0 to emphasize that the Green's function G and the screened Coulomb interaction W are both not treated selfconsistently and are instead calculated from the DFT results. The G_0W_0 calculations are in general starting-point dependent, in which the starting point is indicated by the notation G_0W_0@starting-point, *e.g.* G_0W_0@PBE or G_0W_0@HSE06. The degree of starting-point dependence depends on the type of system. A good test for the starting-point dependence is offered by the DFT+U method, where the starting point can be changed in a controllable way via the Hubbard-U parameter. There are plenty of references in which the starting-point dependence of the single-shot GW calculations is discussed [58–60, 103]. In this thesis it will be discussed for iron pyrite in chapter 8.

In single-shot GW the Kohn-Sham energies are corrected by the quasiparticle energy corrections, but the wave functions are usually not altered, *i.e.* in the representation of the Kohn-Sham wave functions, only diagonal matrix elements $\langle\phi_i|\Sigma|\phi_i\rangle$ are included in eq. (4.1). However, there are approaches accounting for the non-diagonal elements of the self energy (and the exchange-correlation potential in DFT) in the basis of the Kohn-Sham orbitals, which might have a considerable influence on the hybridization of the wave function predicted within G_0W_0. In the case of the tetradymites, Aguilera *et al.* have shown that the treatment of those non-diagonal elements of Σ is crucial to obtain a good agreement of the band gaps with the experiment [104].

To reduce the starting-point dependence significantly or even dispose of it, selfconsistent GW methods can be exploited. There are plenty of selfconsistent GW schemes, in some cases G is determined selfconsistently, in others W or even both quantities. However, the up to date most accepted selfconsistent GW method is the quasiparticle selfconsistent GW (QSGW) approach [61, 62], since most selfconsistent GW methods tend to a large overestimation of the band gaps, whereas QSGW tends only to a slight overestimation. This overestimation of band gaps within selfconsistent GW methods is believed to be caused by the missing description of excitonic effects and other many-body effects comprised in the vertex corrections. The extraordinary well predicted band gaps of main group semiconductors within single-shot GW might be caused by fortuitous error-cancellation, since the missing vertex corrections might cancel against the overestimated screening effects. A more detailed discussion on the single-shot GW and QSGW results of simple semiconductors is presented in appendix A.

In this thesis I will focus only on QSGW as selfconsistent GW method. In Fig. 4.2 the scheme of the QSGW method is depicted, starting with the mean-field solution for the exchange-correlation potential V_{xc} obtained in a DFT calculation. From there a single-shot GW calculation yields the self energy, which is an energy-dependent and in general not hermitian quantity. By integrating over the energy and "hermitianizing" the self energy, which then can be used as effective potential in a DFT calculation, we obtain a new non-local mean-field solution. With this new mean-field solution a single-shot GW calculation allows to obtain again the self energy. This process is iterated till the mean-field solution within DFT and the "hermitianized" self energy converge to the same value. With other words in each iteration of QSGW the potential for the quasiparticle in

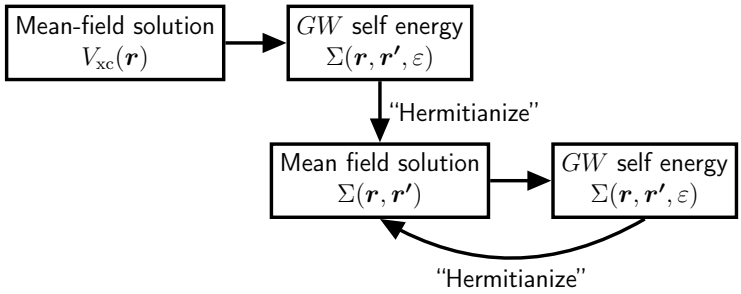

Figure 4.2.: The calculation scheme of the quasiparticle selfconsistent GW (QSGW) method [61, 62]. After obtaining a mean-field solution for the exchange-correlation potential V_{xc} within DFT, a single-shot GW calculation yields the self energy $\Sigma(\boldsymbol{r},\boldsymbol{r'},\varepsilon)$. By "hermitianizing" this quantity and using it as effective potential for another DFT calculation, another mean-field solution $\Sigma(\boldsymbol{r},\boldsymbol{r'})$ can be obtained, which again leads to a self energy when applying single-shot GW. This process can now be iterated till convergence.

GW is mapped to an effective potential within DFT. The QSGW method yields not only the corrected quasiparticle energies, but also the wave functions are corrected. The biggest advantage of the QSGW calculations is the strongly reduced starting-point dependence as compared to single-shot GW. In some cases this might be essential to even predict the correct electronic condition, *i.e.* metallic or semiconducting. A system wrongly predicted to be metallic within "conventional" DFT might not become a semiconductor after a single GW step, since the wave functions might need to change significantly. In such cases QSGW might be a remedy.

4.4. Conclusions

The GW approximation is a powerful beyond-DFT method based on many-body perturbation theory allowing to accurately predict electronic excitation energies, and thus also band gaps. In contrast to DFT, many-body perturbation theory describes the process of adding an electron to the system or removing one electron from the system. The formation of Coulomb holes around the electrons, forming together with the electrons so-called quasiparticles, which then interact via a screened Coulomb interaction, is the essential ingredient to obtain reasonable excitation energies. However, GW calculations require about 1-2 orders more computational time as compared to "conventional" DFT calculations. That is why for a long time GW calculations have been restricted to single-shot GW calculations essentially. Although the band gaps within single-shot GW have been in excellent agreement with experiment for many systems and material classes, the method suffers from a dependence on the starting point, which can lead to completely wrong predictions of the electronic state in some cases. The quasiparticle selfconsistent GW

(QSGW) method helps to significantly reduce this starting-point dependence. The band gaps within QSGW are usually slightly overestimated with respect to experiment, which is believed to be coming from the missing vertex corrections. On the other hand, the single-shot GW method seems to profit from a fortuitous error-cancellation of the missing vertex corrections and an overestimated screening. However, both methods have earned their merits in the prediction of band gaps and beyond.

In general the GW approximation is not adapted to describe optical properties, since a two-particle Green's function is necessary to describe electron-hole interaction. Therefore, also excitonic effects are not included in the theory of the GW approximation, which might be a problem for some systems if we compare to optical absorption spectra. However, for most systems the excitonic effects are negligible and the optical properties can be already approximately described within the GW approximation.

In this chapter I gave only a brief introduction into the topic of the many-body perturbation theory and the GW approximation. In particular, the numerical difficulties of those methods have been only sketched. Some more information on the numerical difficulties can be found in the next chapter 5 about the FLAPW method. The interested reader might find the references [61, 93, 100, 105] useful in this context.

5. Full-potential linearized augmented plane-wave (FLAPW) method

5.1. Introduction

In the previous chapters I have introduced the density functional theory (DFT) and the GW approximation, which both lead to equations for non-interacting particles. In the case of DFT these are the Kohn-Sham equations (2.14), whereas the quasiparticle equations (4.1) are obtained within the GW approximation. The numerical solution of these eigenvalue equations can be performed via a transformation to matrix equations (linear algebra problems) by choosing proper basis functions. Then, there are plenty of well-known algorithms to diagonalize the matrix.

The choice of the basis has a crucial influence on the further numerical approaches. An intuitive and simple choice are plane-wave functions. For instance the Laplace-operator from the kinetic energy is transformed into a simple multiplication within a plane-wave basis. However, there is a major disadvantage of a pure plane-wave basis, which is the necessity to introduce pseudopotentials to describe the behavior of the wave functions close to the nuclei [106, 107]. Without pseudopotentials the oscillations of the wave functions close to the nuclei require an unfeasible large amount of plane-waves to be described. A pseudopotential has a much softer gradient close to the core than the "real" potential, but still captures the essential physics, and thus the wave function close to the core can already be described with a reasonable amount of plane-waves. There are plenty of pseudopotentials for each chemical element in- or excluding the effects of semicore states. The transferability of these pseudopotentials might be quite limited in some cases.[1] In addition, the accuracy of most pseudo-potential methods is usually worse than that of the full-potential linearized augmented plane-wave (FLAPW) method, which is explained in this chapter.

Another prominent choice for a basis are localized functions as for instance atomic orbitals [109–111].[2] Although those functions are conceptually more complicated than the plane-waves, the matrices become thinly occupied for large systems, for which specific

[1] A pseudopotential is usually obtained from a specific system, and thus it might not be adapted for a different system. This adaptability of the pseudopotential is referred to as transferability in the text. For instance a pseudopotential for Fe atoms calculated from bcc-Fe might be too inaccurate to describe Fe atoms in a chain-like structure. For more details see also [108].

[2] Tight-binding models are usually also based on a basis of atomic orbitals (*c.f.* [112, 113]).

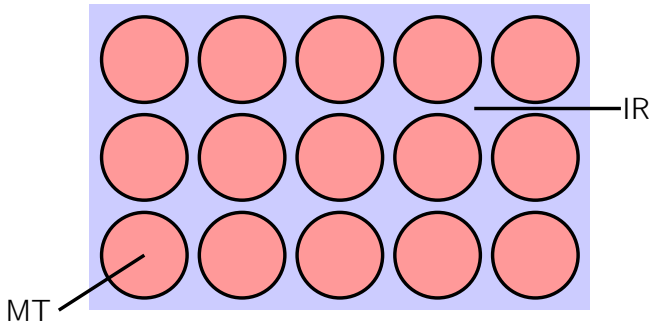

Figure 5.1.: The space is divided into muffin tins (MT) and the interstitial region (IR) in the (L)APW method. The muffin tins are centered around the atomic core positions.

algorithms might save a considerable amount of computational time. However, the convergence of the results with respect to that basis is far from trivial, since it is difficult to expand the basis in a systematical way.

For the calculations in this thesis the linearized augmented plane-wave (LAPW) basis has been used, which most important concept is the division of space into spheres around the positions of the nuclei, referred to as muffin-tins in the following, and the interstitial region in between (see Fig. 5.1). In the interstitial region plane-waves are used for the basis, whereas radial functions obtained from the solution of an atomic-like problem and spherical harmonics are exploited in the muffin tins. Thus, the basis is already suited to the physical conditions of a system consisting of atoms. For instance, the oscillations close to the nuclei are already captured in the basis, and thus the introduction of pseudopotentials is not necessary. This choice of a basis is very efficient, considerably reducing the necessary amount of basis functions for a given accuracy. However, it is no "beginner's basis", both being conceptually and from the point of view of convergence quite difficult.

In this chapter I will introduce the (L)APW basis and the important numerical issues behind this approach. The modifications if using hybrid functionals or using a film-geometry will be also discussed. In this chapter I will only present the very basic mathematical expressions behind the FLAPW approach. For more details I refer to the following references [65, 114–116].

5.2. The Basics of the FLAPW Method

5.2.1. The LAPW Basis

The Kohn-Sham equations (2.14) can be transformed into matrix equations by choosing a basis with basis functions $\varphi_{j\boldsymbol{k}}(\boldsymbol{r})$. The Kohn-Sham orbitals $\phi_{i\boldsymbol{k}}$ can be written as linear

combination of these basis functions:

$$\phi_{i\boldsymbol{k}}(\boldsymbol{r}) = \sum_j c_{ij}(\boldsymbol{k})\varphi_{j\boldsymbol{k}}(\boldsymbol{r}), \tag{5.1}$$

where the $c_{ij}(\boldsymbol{k})$ are the expansion-coefficients of the linear combination. Here, I have already introduced a $\boldsymbol{k}$-dependence originating from the translational symmetry of the system.[3] Inserting the expansion of $\phi_{i\boldsymbol{k}}$ into the Kohn-Sham equations and multiplying with $\varphi_{j'\boldsymbol{k}}(\boldsymbol{r})$ from the left side leads to following generalized eigenvalue problem:

$$\underline{\boldsymbol{H}}(\boldsymbol{k})\boldsymbol{c_i}(\boldsymbol{k}) = \varepsilon_i(\boldsymbol{k})\underline{\boldsymbol{S}}(\boldsymbol{k})\boldsymbol{c_i}(\boldsymbol{k}), \tag{5.2}$$

where $\underline{\boldsymbol{H}}(\boldsymbol{k})$ is the Hamilton matrix and $\underline{\boldsymbol{S}}(\boldsymbol{k})$ the overlap matrix in representation of the basis, *i.e.*

$$[\underline{\boldsymbol{H}}(\boldsymbol{k})]_{j'j} = \int d^3r\ \varphi^*_{j'\boldsymbol{k}}(\boldsymbol{r})\left(-\frac{1}{2}\nabla^2 + V_{\text{eff}}(\boldsymbol{r})\right)\varphi_{j\boldsymbol{k}}(\boldsymbol{r}) \tag{5.3}$$

$$[\underline{\boldsymbol{S}}(\boldsymbol{k})]_{j'j} = \int d^3r\ \varphi^*_{j'\boldsymbol{k}}(\boldsymbol{r})\varphi_{j\boldsymbol{k}}(\boldsymbol{r}) \tag{5.4}$$

are the elements of the matrices. In the case of an orthonormal basis the overlap matrix becomes the unity matrix. The coefficients $c_{ij}(\boldsymbol{k})$ build the vectors $\boldsymbol{c_i}(\boldsymbol{k})$, which are the Kohn-Sham orbitals in representation of the basis. Now that the (generalized) eigenvector equation is written in matrices, it can be solved with a variety of well-known algorithms to obtain the Kohn-Sham orbitals ϕ_i and Kohn-Sham energies ε_i.

I have already discussed in the introduction of this chapter that the choice of the basis has a crucial influence on the simplicity of the Hamiltonian $\underline{\boldsymbol{H}}(\boldsymbol{k})$ and the numerics of the eigenvalue problem.

Before discussing the linearized augmented plane-wave (LAPW) basis, I follow the historical course and start with the related augmented plane-wave (APW) basis. The APW basis yields a good accuracy of the results by using a reasonable amount of basis function. In Fig. 5.1 the division of space for the APW method is shown, and the basis functions are defined in the muffin-tins (MT) and interstitial region (IR) separately:

$$\varphi_{\boldsymbol{k}+\boldsymbol{G}}(\boldsymbol{r}) = \begin{cases} \frac{1}{\sqrt{\Omega}}\mathrm{e}^{\mathrm{i}(\boldsymbol{k}+\boldsymbol{G})\boldsymbol{r}}, & \boldsymbol{r} \in \text{IR} \\ \sum_{lm} a^{\boldsymbol{k}+\boldsymbol{G}}_{\mu lm} u_{\mu l}(r_\mu, \varepsilon) Y_{lm}(\hat{\boldsymbol{r}}_{\boldsymbol{\mu}}), & \boldsymbol{r} \in \text{MT}(\mu) \end{cases} \tag{5.5}$$

where Ω is the volume of the unit cell, $\boldsymbol{G}$ is a reciprocal lattice vector, l and m denote the angular and magnetic quantum numbers, μ is an index for the μ-th muffin tin, $a^{\boldsymbol{k}+\boldsymbol{G}}_{\mu lm}$ is a coefficient, $\boldsymbol{r}_{\boldsymbol{\mu}} = \boldsymbol{r} - \boldsymbol{R}_{\boldsymbol{\mu}}$ is the spatial vector centered around the muffin tin at $\boldsymbol{R}_{\boldsymbol{\mu}}$, $u_{\mu l}(r_\mu, \varepsilon)$ is a radial-dependent function, and $Y_{lm}(\hat{\boldsymbol{r}}_{\boldsymbol{\mu}})$ are the spherical harmonic functions

[3] A system exhibiting translational symmetry obeys the Bloch theorem, which states that the electronic wave function can be expressed as a lattice periodical function multiplied with a plane wave $\mathrm{e}^{\mathrm{i}\boldsymbol{k}\boldsymbol{r}}$. Therefore, those $\boldsymbol{k}$-vectors of the reciprocal space fulfilling the periodicity conditions of the chosen supercell are good quantum numbers of the system.

depending on the angular part of the spatial vector $\boldsymbol{r_\mu}$. The radial-dependent functions are constructed such that they fulfill the radial, spherical Schrödinger-type equation:

$$\left(-\frac{1}{2}\frac{\partial^2}{\partial r^2} + \frac{l(l+1)}{2r^2} + V^{\mu}_{\mathrm{sph}}(r)\right) r u_{\mu l}(r,\varepsilon) = \varepsilon r u_{\mu l}(r,\varepsilon), \tag{5.6}$$

where ε is an energy parameter and $V^{\mu}_{\mathrm{sph}}(r)$ is the spherical part of the potential inside the μ-th muffin tin.

Note that the $u_{\mu l}(r,\varepsilon)$ depend on an energy ε, and it turns out that a fixed energy parameter in the radial Schrödinger equation is not accurate enough to guarantee reasonable results from the Kohn-Sham equations. The Kohn-Sham energies themselves have to be used as energy parameters for the radial functions to construct an accurate basis. However, this leads to non-linear eigenvalue equations, which are computationally very demanding. Additionally, there are some other minor disadvantages of the APW basis, which are discussed in reference [117]. Therefore, a linearized approach of the augmented plane-wave method has been developed to avoid the non-linearity in the eigenvalue equations.

The central difference between the linearized augmented plane-wave (LAPW) basis to the APW basis refers to the energy-dependence of the radial function $u_{\mu l}(r,\varepsilon)$. Instead of using the Kohn-Sham energies for ε, a Taylor expansion at a reasonably chosen energy parameter $E_{\mu l}$ can be used for the radial functions $u_{\mu l}$, describing an l-like state at atom μ:

$$u_{\mu l}(r,\varepsilon) = u_{\mu l}(r,E_{\mu l}) + (\varepsilon - E_{\mu l})\dot{u}_{\mu l}(r,E_{\mu l}) + \mathcal{O}\left((\varepsilon - E_{\mu l})^2\right), \tag{5.7}$$

where $\dot{u}_{\mu l}$ is the energy derivative of $u_{\mu l}$. This expansion allows to separate valence states from core states. It is common to consider only terms up to linear order in the Taylor expansion of u. With that the basis functions look as follows:

$$\varphi_{\boldsymbol{k}+\boldsymbol{G}}(\boldsymbol{r}) = \begin{cases} \frac{1}{\sqrt{\Omega}} \mathrm{e}^{\mathrm{i}(\boldsymbol{k}+\boldsymbol{G})\boldsymbol{r}}, & \boldsymbol{r} \in \mathsf{IR} \\ \sum_{lm}\left(a^{\boldsymbol{k}+\boldsymbol{G}}_{\mu lm} u_{\mu l}(r_\mu, E_{\mu l}) + b^{\boldsymbol{k}+\boldsymbol{G}}_{\mu lm}\dot{u}_{\mu l}(r_\mu, E_{\mu l})\right) Y_{lm}(\hat{\boldsymbol{r}}_{\boldsymbol{\mu}}), & \boldsymbol{r} \in \mathsf{MT}(\mu) \end{cases}, \tag{5.8}$$

where the coefficients $a^{\boldsymbol{k}+\boldsymbol{G}}_{\mu lm}$ and $b^{\boldsymbol{k}+\boldsymbol{G}}_{\mu lm}$ are determined via the boundary conditions between the interstitial region and the muffin tins. The coefficients are determined such that the basis functions are continuous and continuously differentiable at the muffin tin boundary. Since we only go up to linear order in the Taylor expansion of the radial function u, the LAPW results suffer of a so-called linearization error, which should be kept as minimal as possible. In some cases the linearization error needs to be reduced by the inclusion of so-called local orbitals (LOs) into the basis. The local orbitals are only defined in the muffin tins with the following definition:

$$\varphi^{\mathrm{LO}}_{\boldsymbol{k}+\boldsymbol{G}}(\boldsymbol{r}) = \sum_{lm}\left(a^{\boldsymbol{k}+\boldsymbol{G}}_{\mu lm} u_{\mu l}(r_\mu, E_{\mu l}) + b^{\boldsymbol{k}+\boldsymbol{G}}_{\mu lm}\dot{u}_{\mu l}(r_\mu, E_{\mu l}) + c^{\boldsymbol{k}+\boldsymbol{G}}_{\mu lm} u_{\mu l}(r_\mu, E^{\mathrm{LO}}_{\mu l})\right) Y_{lm}(\hat{\boldsymbol{r}}_{\boldsymbol{\mu}}), \tag{5.9}$$

where $E^{\mathrm{LO}}_{\mu l}$ is the energy parameter for this local orbital. More information about the LOs and the energy parameters $E^{\mathrm{LO}}_{\mu l}$ is presented in the next sections.

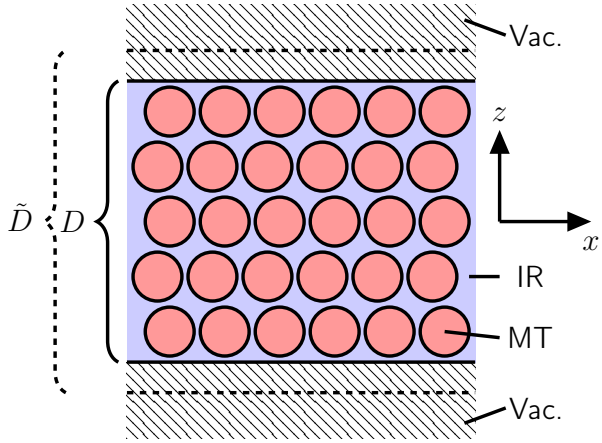

Figure 5.2.: For film calculations within FLEUR the space is divided into the muffin tins (MT) and the interstitial region (IR) within the slab, and additionally two vacuum regions (Vac.) are defined. For the treatment of the vacuum two parameters D and $\tilde{D}$ are needed to obtain sufficient flexibility to describe the exponential decay of the wave functions into the vacuum. Note that no periodicity along the z-direction is required, therefore in the FLEUR code a "real" two-dimensional periodic system is calculated.

5.2.2. LAPW Basis in Film Calculations

A film can be modeled by imposing periodic boundary conditions within the plane of the film and perpendicular to the film and choosing a suitable supercell. However, the Jülich FLAPW code FLEUR [66] allows for the calculation of films, without the need of periodic boundary conditions along the out-of-plane axis of the film. Hence, there is no need to construct a thick enough vacuum region between periodically repeated film structures to prevent spurious mirror interactions between these films. Nevertheless, a vacuum region needs to be defined in which the wave functions are able to exponentially decay to zero.

The Fig. 5.2 displays the three different regions, which are used for the definition of the LAPW basis in a film geometry. As before the space is divided into muffin tins (MT) and the interstitial region (IR) within the film, but additionally there is a vacuum region on the upper and lower side of the film. The parameter D defines the borderline between the IR and the vacuum, whereas the parameter $\tilde{D} > D$ is used to avoid numerical problems. The wave function forms a standing wave in between the boundaries defined by $\tilde{D}$ and thus we avoid numerical difficulties adjusting those standing waves at the edges of the IR.

The LAPW basis for the film geometry looks as follows:

$$\varphi_{\boldsymbol{k}_{||}+\boldsymbol{G}_{||},G_\perp}(\boldsymbol{r}) = \begin{cases} \frac{1}{\sqrt{\Omega}} \mathrm{e}^{\mathrm{i}(\boldsymbol{k}_{||}+\boldsymbol{G}_{||})\boldsymbol{r}_{||}} \mathrm{e}^{\mathrm{i}G_\perp z}, & \boldsymbol{r} \in \mathrm{IR} \\ \sum_{lm} \left(a_{\mu lm}^{\boldsymbol{k}+\boldsymbol{G}} u_{\mu l}(r_\mu, E_{\mu l}) + b_{\mu lm}^{\boldsymbol{k}+\boldsymbol{G}} \dot{u}_{\mu l}(r_\mu, E_{\mu l}) \right) Y_{lm}(\hat{\boldsymbol{r}}_{\boldsymbol{\mu}}), & \boldsymbol{r} \in \mathrm{MT}(\mu) \\ \left(a_{\boldsymbol{G}_{||}G_\perp}^{\boldsymbol{k}_{||}} u_{\boldsymbol{G}_{||}}^{\boldsymbol{k}_{||}}(z, E_{\mathrm{vac}}) + b_{\boldsymbol{G}_{||}G_\perp}^{\boldsymbol{k}_{||}} \dot{u}_{\boldsymbol{G}_{||}}^{\boldsymbol{k}_{||}}(z, E_{\mathrm{vac}}) \right) \mathrm{e}^{\mathrm{i}(\boldsymbol{G}_{||}+\boldsymbol{k}_{||})\boldsymbol{r}_{||}}, & \boldsymbol{r} \in \mathrm{Vac.} \end{cases} , \tag{5.10}$$

where $\boldsymbol{G}_{||}$ and $\boldsymbol{k}_{||}$ are a 2-dimensional reciprocal lattice vector and the Bloch vectors in the plane of the film, $\boldsymbol{r}_{||}$ is the parallel component of $\boldsymbol{r}$ projected on the plane of the film and $G_\perp$ is an out-of-plane reciprocal lattice vector, defined in terms of $\tilde{D}$. The radial dependent functions $u_{\boldsymbol{G}_{||}}^{\boldsymbol{k}_{||}}(z)$ in the vacuum region have to fulfill the one-dimensional Schrödinger equation

$$\left(-\frac{1}{2}\frac{\partial^2}{\partial z} + V_0(z) + \frac{1}{2}(\boldsymbol{k}_{||} + \boldsymbol{G}_{||})^2 \right) u_{\boldsymbol{G}_{||}}^{\boldsymbol{k}_{||}}(z, E_{\mathrm{vac}}) = E_{\mathrm{vac}} u_{\boldsymbol{G}_{||}}^{\boldsymbol{k}_{||}}(z, E_{\mathrm{vac}}), \tag{5.11}$$

in which $V_0(z)$ is the planar averaged part of the vacuum potential and E_{vac} is a suitably chosen vacuum energy parameter.[4] The coefficients $a_{\boldsymbol{G}_{||}G_\perp}^{\boldsymbol{k}_{||}}$ and $b_{\boldsymbol{G}_{||}G_\perp}^{\boldsymbol{k}_{||}}$ are both determined such that the basis functions are continuous and continuously differentiable at the boundary between the vacuum and the IR. For more details I refer to the reference [118].

5.2.3. Full-Potential Treatment

Early APW and LAPW methods have used a shape-approximated potential $V(r)$ for the Kohn-Sham equations to simplify the computation. Within the shape-approximation the potential has been considered constant in the interstitial region and spherical in the muffin tins. For many systems this approximation works fine, however, in particular systems with an open structure need a more accurate description of the potential.

Within the FLEUR code a full-potential linearized augmented plane-wave (FLAPW) method is implemented, including non-spherical contributions to the potential inside the muffin tins and using the warped potential instead of a constant one in the interstitial region:

$$V(\boldsymbol{r}) = \begin{cases} \sum_{\boldsymbol{G}} V_{\mathrm{IR}}^{\boldsymbol{G}} \mathrm{e}^{\mathrm{i}\boldsymbol{G}\boldsymbol{r}}, & \boldsymbol{r} \in \mathrm{IR} \\ \sum_{lm} V_{\mathrm{MT}}^{lm} Y_{lm}(\hat{\boldsymbol{r}}), & \boldsymbol{r} \in \mathrm{MT} \end{cases} . \tag{5.12}$$

For more details I refer to the reference [119].

5.2.4. Numerical Parameters in the FLAPW Method

Now that I have briefly introduced the LAPW basis, I would like to draw the attention to the most important numerical parameters. Some of these parameters need to be converged for each system in the FLEUR code, which means the parameters are increased to values,

[4] More precisely there are two different vacuum regions on the top and the bottom of the film, which exhibit in general different radial-dependent functions. In the case of a symmetric film, both vacuum regions are equivalent.

where the examined physical properties such as the total energy or band gaps are within the desired accuracy.

First, there is the plane-wave cutoff parameter $k_{\max}$ controlling the maximal $(\boldsymbol{k}+\boldsymbol{G})$-vectors used within the LAPW basis description, and thus it has a crucial influence on the number of basis functions. On the one hand, more basis functions improve the accuracy of the description, but a too large $k_{\max}$ might lead to linear dependencies in the basis, which then causes numerical problems. Typical values for $k_{\max}$ are about 3.5-4.5 a.u.$^{-1}$ in the case of "conventional" DFT calculations.

Then, there is the angular momentum cutoff parameter $l_{\max}$, which determines the maximum angular momentum quantum number in the sum of eq. (5.8) for the calculation of the LAPW basis functions in the muffin tins. The cutoff parameter can be rather large with values around 8-10.[5]

The calculations should be almost independent of the chosen muffin tin radii R_{MT}, however there is always a slight dependence on the radii. The muffin tin radii are usually chosen such that they nearly touch each other, except of the case where a structural relaxation needs to be done, in which the radii are chosen a bit smaller. A typical radius of the muffin tin is about 2-3 a.u. A much smaller radius leads to numerical problems, since we approach the limit, where the clear separation between core and valence states vanishes.

The FLAPW method is based on equations in the reciprocal space, and thus we also need to define a proper $\boldsymbol{k}$-point mesh to guarantee convergence. The $\boldsymbol{k}$-points enter both the Kohn-Sham equations in eq. (5.2) as well as the basis functions in eq. (5.8). For semiconductors about 100 $\boldsymbol{k}$-points in the full Brillouin zone are in most cases sufficient, but several orders of magnitude more $\boldsymbol{k}$-points might be necessary to converge metallic or magnetic systems.

Finally, let me briefly discuss the inclusion of local orbitals (LOs) into the basis to improve convergence. The purpose of the LOs is to expand the range of energy in which the wave functions are accurately described, and thus to decrease the linearization error. The LOs are defined only in the muffin tin via eq. (5.9). The energy parameters of the LOs need to be chosen reasonably, and here atomic energy levels are used.

In this thesis I will distinguish two kind of local orbitals, which are semicore LOs and higher-energy LOs. It might become necessary to include so-called semicore LOs, whenever the energy of a core state is close to the energy of the valence states [120].[6] With other words that means that the overlap between these core states and the LAPW basis is too large, since preferably they should be orthogonal to each other. If those (semi-)core states

[5] The large l-numbers ensure an adequate flexibility of the LAPW basis functions at the muffin tin borders for fulfilling the boundary conditions. Therefore, it is recommended to satisfy the condition $k_{\max}R_{\mathrm{MT}} = l_{\max}$.

[6] The FLAPW method is an all-electron method, which means both the valence electrons as well as the core electrons are treated within the presented Kohn-Sham scheme. In the case of the core electrons even full-relativistic effects are considered for a spherical potential. The LAPW basis is only used for the description of the valence states and the core states are (approximately) orthogonal on those LAPW basis functions. However, those core states, which are close in energy to the valence energy window are called semicore states and might need to be included into the LAPW basis to prevent numerical problems.

are not included into the basis, they might lead to "ghost" bands in the electronic structure, messing up the calculation or leading to wrong results. Another purpose to include LOs is to improve the description of the unoccupied wave functions by adding additional energy parameters $E_{\mu l}^{\mathrm{LO}}$ at higher energies. These higher-energy LOs (HELOs) are usually not needed for "conventional" DFT calculations, but they might become essential for hybrid functional calculations or beyond-DFT methods like the GW approximation. In this thesis only semicore LOs and HELOs are used via eq. (5.9), but there exist several other definitions for LOs. The interested reader is referred to [121], where more details are presented.

5.2.5. FLAPW for Hybrids and GW

Hybrid functional calculations and to an even greater extent GW calculations are much more difficult to converge with respect to the numerical parameters of FLAPW introduced in subsection 5.2.4. In the GW approximation we need a reasonable description of the wave functions and eigenenergies from the unoccupied energy spectrum, since they enter in the determination of the polarization function and of the self energy. Depending on the system one has to account for a large amount of unoccupied bands to converge the results. For instance, in the case of ZnO almost 3000 bands have been used for the calculations and the results were still not fully converged [101, 102], although only a small fraction of those bands are occupied. A large plane-wave cutoff parameter $k_{\max}$ and an adjusted $l_{\max}$ might be necessary to allow for a reasonable description of those high-lying energy states. Additionally, many high-energy local orbitals (HELOs) might be needed to reduce the linearization error for the unoccupied energy spectrum. In many systems semicore states need to be included into the basis via local orbitals to converge the results. In "conventional" DFT calculations this has to be done only for the most important semicore states to avoid "ghost" bands in the valence window, but in hybrid functional calculations and GW even semicore states at quite low energies might have an influence on the results. An important part of my thesis deals with the convergence of the pyrite systems in the GW approximation, showing the considerable increase in difficulty to converge the results compared to "conventional" DFT calculations.

But not only the convergence becomes more complicated within hybrid functional and GW calculations, also conceptually there are some extensions to the LAPW basis. For both methods the implementation of a mixed product basis is useful [83, 122]. The basis helps whenever a product of Kohn-Sham wave functions occurs, which is the case in the evaluation of the non-local potential contributions in the hybrid calculations and for the determination of the polarization function and the exchange part of the self energy in the GW approximation. Even so the mixed product basis is conceptually more complicated than the LAPW basis, it can be reduced to a minimal size basis, which is optimized and separately defined for the muffin tins and the interstitial region to allow for an efficient computation. I will not present the expressions for the mixed product basis in this thesis and advise the reader to the references [83, 99] for more details. But let me mention that there is also some freedom in creating this mixed product basis and the basis needs to be converged as well. However, the experience shows that the results do not depend much

on the choice of the mixed product basis, if it is only chosen reasonably.

5.3. Conclusions

I have briefly discussed the full-potential linearized augmented plane-wave (FLAPW) method as implemented in the Jülich DFT code FLEUR [66]. Within the LAPW basis we can treat the wave functions in the full potential of the nuclei, and thus no pseudopotentials need to be used as it is the case in pure plane-wave approaches. The basis is systematically expandable and accurate results can be obtained for various systems. In the FLEUR code a specifically adapted LAPW basis for film geometries allows to calculate "real" two-dimensional systems without the necessity to separate periodically repeated film structures via thick layers of vacuum.

However, the LAPW basis is no "beginner's basis", *i.e.* implementations are rather non-trivial and the convergence of results depends on a couple of parameters and might be cumbersome in particular for hybrid functional or GW calculations.

In this chapter I have discussed the basics of FLAPW without focusing too much on the mathematics. I recommend the references [65, 119, 123] to the readers interested in more details.

6. Basics of Photovoltaics

6.1. Introduction

Photovoltaics probably will become the most important energy production branch in the future, even if it might take a long time. The earth is radiated with $1.74 \cdot 10^{17}$ W by the sun [4], which is much more than sufficient to cover the world annual energy demand. The practically unlimited amount of energy produced by the sun allows to solve the energy problems without running into resource shortages as it is the case for the fossil energy sources. Hence, it is clear that there is a lot of potential in photovoltaics.

The hardest challenges are to establish a well-structured network to conduct and store the electric energy, as well as to increase the efficiency and decrease the costs of solar cells, in order to compete with the energy production costs of fossil energies. For instance, within the branches of organic photovoltaics a "printing" technique makes the construction of solar cells very cost efficient, and thus organic photovoltaics is a quite popular research topic, although the efficiencies of those solar cells are not particularly large and they suffer of a low stability. However, anorganic materials are still used in the most concepts for solar cells. But instead of dealing with thick absorption layers, the research focuses more and more on thin layer systems or nano-structures, by this hoping to significantly reduce the costs of solar cells. Within the project group, in which I had the possibility to work on in this thesis, the focus has been on nano-particles of abundant anorganic materials.[1] The size of the nano-particles can be tuned in their creation process and this size is usually closely connected to the size of the band gap, and thus also to the absorption spectrum. By embedding those nano-particles into a Si-matrix, a high optical absorption in a wide range of the solar spectrum might be reached by the combination of differently sized nano-particles. Additionally, there might be also the possibility to use "printing" techniques to construct future solar cells of nano-particles, and by this significantly reduce the production costs.

Despite the variegated amount of approaches, the main material of a solar cell is in any case a semiconductor, in which the type and the size of the band gap has a crucial influence on the performance of the solar cell. In the studies of this thesis I will focus mainly on the band gap, whereas surface recombination, defects or even the geometry of the solar cell are only briefly discussed. In this chapter I start with an explanation of the basic mechanism of a solar cell, *i.e.* the light-generated exciton and the separation and

[1] The project code has been NADNuM 03SF0402A, registered as a BMBF project. The abbreviation NADNuM stands for "Neue Absorbermaterialien für Dünnschichtsolarzellen mit Nanopartikeln aus unbegrenzt verfügbaren Materialien", which is german and means translated "New absorber materials for thin film solar cells with nanoparticles from infinitely available materials".

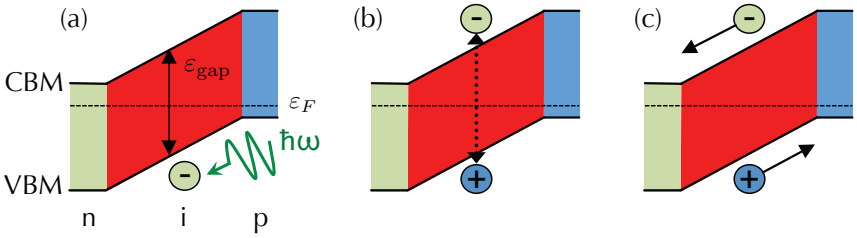

Figure 6.1.: The basic principle of a solar cell is based on the sequence of the following steps. The vertical direction in the figure can be interpreted as an energy axis and from left to right we show the different materials the solar cell is made: the p- and n-doped semiconducting layers and the undoped intrinsic (i) one. The location of the Fermi energy ε_F is indicated by the dashed line. (a) A photon is absorbed in the intrinsic semiconducting layer. (b) An electron from the valence band (VBM - valence band maximum) is excited into the conduction bands (CBM - conduction band minimum). The remaining hole in the valence band is coupled to the electron. Both together form a so-called exciton. (c) An internal electric field caused by the space-charges in the p- and n-doped semiconducting layers separates the charge carriers.

collection of the single charges.

To evaluate the performance of a solar cell many quantities are of interest. For instance, a very basic quantity is the efficiency η comprising some other quantities like the open-circuit voltage, V_{oc}, the short-circuit current, I_{sc}, or the fill-factor, FF. In this chapter I will briefly discuss all those quantities and some effects which might have a considerable influence on those quantities. Finally, a brief overview over some existing solar cell types is presented to get a feeling for typical values of the solar cell parameters.

6.2. Fundamental Mechanism of a Solar Cell

First of all, I will discuss the basic mechanism in a solar cell, which is based on quantum mechanical effects. That explains why density-functional theory (DFT) and beyond-DFT approaches are crucial to describe the physics in solar cells. The basic mechanism is depicted in Fig. 6.1, which I will discuss bit by bit in the following.

A semiconducting material with a band gap $\varepsilon_{\mathrm{gap}}$ is used as absorber material. The valence states are fully occupied by electrons, whereas the conduction bands are unoccupied.[2] An impinging light quantum of a specific energy $\hbar\omega$ might excite an electron from the valence bands into the conduction bands, leaving a positively charged hole in the valence bands. The probability of this electron excitation depends on various conditions, *e.g.* the size and

[2] Of course thermal energy leads to a very small occupation of the conduction states with electrons, but this will be neglected in the following.

type of the energy transition compared to the energy of the photon or the thickness of the absorber layer. The energy of the photon has to be at least as large as the band gap size to excite an electron, but a photon with a considerably larger energy than the energy of visible light quantums is less probable to scatter with an electron of the semiconductor. If a photon is absorbed, the excited electron and the remaining hole are (weakly) coupled, and the thus formed quasiparticle is the so-called exciton. Not every absorbed photon yields such a "stable" exciton, since the electron and the hole might recombine in a very short time leaving no free charge carriers in the system. On the other hand, in some systems multiple excitons are generated, *i.e.* a single photon excites more than one electron or an excited electron excites other electrons, possibly leading to many excitons.

After having obtained an exciton, the next step is to separate the majority and minority charge carriers by an electric field in the material. Since we want to generate an electrical current without applying an external electrical field, the solar cell should exhibit an own internal electrical field. A p-n junction (diode) creates such an internal electrical field. How is this internal field created? - The p-doped and n-doped semiconducting material are both electrical neutral, but the majority charge carriers are holes in the first case and electrons in the latter.[3] At the interface of this junction electrons and holes recombine due to the concentration gradient of the charge carriers, leaving a depletion region. In this depletion region the p-doped area becomes negatively charged, whereas the n-doped area becomes positively charged, and thus an internal electric field is created by those space-charge areas, which acts against the charge carrier diffusion. In thermodynamic equilibrium the electric field is large enough to stop the charge carrier diffusion. If new charge carriers are now created in the depletion region, the electron will flow to the n-doped and the hole to the p-doped side of the p-n junction.[4] An intrinsic semiconducting layer between the p-doped and n-doped semiconductor materials does not change this basic concept. The intrinsic layer acts like a capacitor elongating the electric field generated by the p-n-junction, and thus increasing the volume in which newly generated excitons can be separated into free charge carriers by the internal electric field. Hence, most solar cell concepts are based on a p-i-n structure of a semiconducting material, where the i stands for the intrinsic layer sandwiched by the p-doped and n-doped layer.

Let me summarize the most important steps of the physics in a solar cell with respect to Fig. 6.1:

(a) An impinging photon is absorbed by an electron in the valence states inside the intrinsic semiconducting layer.
(b) An exciton is created, which is a (weakly) coupled electron in the conduction band and a hole in the valence band.

[3] As an example consider Si in one case doped with B and in another case with P atoms. In the first case the system lacks of electrons compared to the pure Si material, whereas in the latter case it exhibits a surplus of electrons. Note that both systems are still charge neutral. Since there will be holes in the valence bands in the first case, the majority charge carrier are holes, whereas in the P-doped Si the surplus of electrons is located in donator levels nearby the conduction band edge, leading to electrons as majority charge carriers.

[4] This direction of flow seems to be against the first intuition, but the formation of the depletion region explains this behavior (cf. Fig. 6.1).

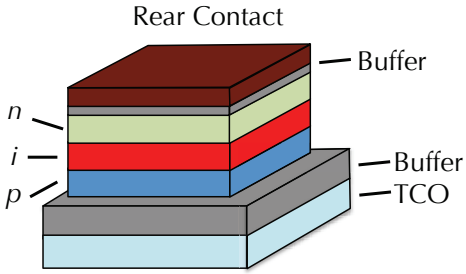

Figure 6.2.: A schematic figure of a typical p-i-n thin-film solar cell, consisting of the intrinsic absorber layer i sandwiched by a p- and n-doped semiconducting layer. The two buffer layers are usually needed to improve the growth conditions and to increase the performance of the solar cell. On the side where the light enters, a transparent conductive oxide (TCO) collects the charges, whereas a nontransparent metallic contact is used on the rear side.

(c) An internal electric field caused by the space-charges in the depletion region of the p- and n-doped layers separates the charge carriers, *i.e.* the electron and hole. The electron travels to the n-doped and the hole to the p-doped site.

(d) The majority charge carrier is collected at the contact causing a photocurrent. This last step is not visualized in Fig. 6.1.

This sequence takes place in an ideal solar cell, but in a real material in each step something can go wrong, and thus a much smaller or no photocurrent can occur. In the next section I will talk in detail about some possible causes of a small photocurrent.

I would like to finish this section by discussing a typical buildup of a p-i-n thin-film solar cell as it is displayed in Fig. 6.2. The most essential part of the solar cell is the absorber layer, which is the intrinsic semiconductor layer. This layer is sandwiched by a p- and n-doped layer to create an external electric field. Instead of growing the contact layers directly on top of the p- and n-doped layer, in many cases buffer layers are used to facilitate the growth process and to decrease stress-induced degradation or transient effects. On top of the buffer layer is located a transparent and conductive layer, *e.g.* a transparent conductive oxide like indium-tin-oxide, for both to allow the light to pass through and to collect charge carriers. On the backside a non-transparent contact layer is deposited to reflect the light and to collect the charge carriers. The interfaces between the layers look very smooth in the figure, but in reality those can be quite rough. This can be of disadvantage, since charge carriers could recombine at surface defects, but there are also approaches to use the rough surfaces for light-trapping and by this increasing the probability to absorb the photons in the material [124].

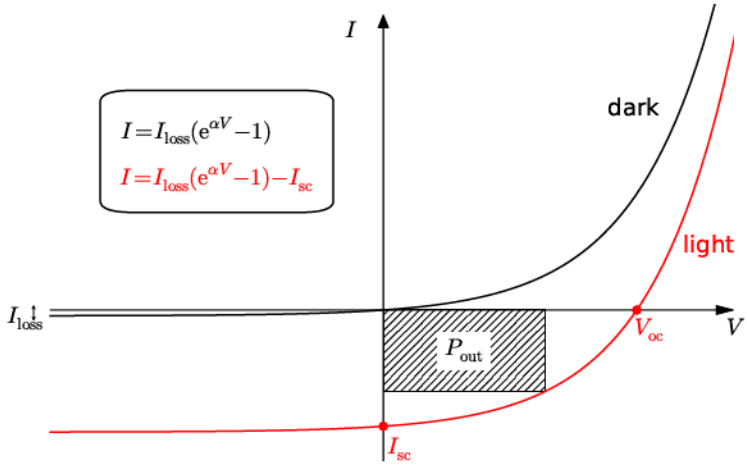

Figure 6.3.: The I-V characteristic of a solar cell under illumination (red curve) and under dark conditions (black curve). The loss current I_{loss}, the short-circuit current I_{sc} and the open-circuit voltage V_{oc} are also indicated in the figure. The hatched box indicates the power output P_{out}, which is the maximally obtainable power $I_{\text{mp}}V_{\text{mp}}$ of the cell.

6.3. Important Quantities of a Solar Cell

In this section I will talk about the most important quantities of a solar cell and I will point out the requirements for an ideal solar cell material. At the beginning of the process depicted in Fig. 6.1 is the absorption of a photon, and thus materials with a high optical absorption for a wide range of wavelengths are preferred. For materials with an "average" optical absorption there is the possibility to increase the thickness of the absorption layers to increase the probability to absorb the photons. However, in thick absorption layers the collection of the charge carriers might be more of a problem and an ideal solar cell should consist of a minimum amount of absorber material to decrease the production costs. The optical absorption delicately depends on the type and the size of the transition, *e.g.* usually the absorption of a photon for direct band transitions are much more probable to occur compared to indirect transitions.

To separate the charge carriers and obtain a photocurrent, an internal or external electric field is needed. The current-voltage characteristic of a typical solar cell is displayed in Fig. 6.3. Under dark conditions the solar cell behaves like a normal p-n junction, which means in one direction the electric current I is blocked, whereas the other direction shows (initially) an exponential increase with the potential V. In equations the I-V characteristic of a solar cell under dark conditions looks as follows:

$$I(V) = I_{\text{loss}}(e^{\frac{eV}{k_B T}} - 1), \tag{6.1}$$

where $k_B T$ is the thermal energy for temperature T and I_{loss} is the loss current caused by

imperfections in the p-n junction. Not shown in the figure is the breakthrough area, which occurs for large negative voltages leading to an exponentially decreasing negative current. An illuminated solar cell behaves to a good approximation like a p-n junction in which an additional light-induced current is present,

$$I(V) = I_{\mathrm{loss}}(\mathrm{e}^{\frac{eV}{k_B T}} - 1) - I_{\mathrm{sc}}. \tag{6.2}$$

Here, I_{sc} is the short-circuit current, which is the electric current in the solar cell under short-circuit conditions, *i.e.* $V = 0$. The light-induced current and the short-circuit current are approximately the same for good solar cells. Another important quantity for the solar cell, which can be extracted from the I-V characteristic is the open-circuit voltage V_{oc}, which is the required voltage to exactly compensate the light-induced current, *i.e.* $I = 0$. In an ideal solar cell without recombination losses reducing the photocurrent, the negative value of the open-circuit voltage corresponds to the voltage produced by the internal electric field caused by the space charges in the p-n junction. The open-circuit voltage can be maximally as large as $\varepsilon_{\mathrm{gap}}/e$, since a larger voltage will promote electrons from the valence band directly into the conduction band, and thus over-compensating the photocurrent. A too small short-circuit current or open-circuit voltage can have various reasons. Although the solar cell might absorb a high amount of the incident light and a sufficiently large number of excitons is created, the majority and minority charge carriers might recombine at surfaces, interfaces or defects. A calculation of the electronic structure shows surface- or defect-states within the band gap, which might act as recombination centers for the charge carriers.

Another quantity classifying the amount of collected charge carriers with respect to the number of absorbed photons is the (internal) quantum efficiency. It is common to display it in percent. For instance, a quantum efficiency of 50% means that half of the absorbed photons are transformed into charge carriers, which could be collected at the contacts. For the ideal solar cell material the absorbed photons should create as many excitons as possible, and thus in the case of multi-exciton generation quantum efficiencies above 100% might be achieved.

Finally, there is the conversion efficiency η, which is often used as "the" quality criterion for a solar cell. It is the ratio between the power output of the solar cell and the power of the incident light, thus

$$\eta = \frac{P_{\mathrm{out}}}{P_{\mathrm{in}}} = \frac{V_{\mathrm{oc}} I_{\mathrm{sc}} FF}{P_{\mathrm{in}}} = \frac{V_{\mathrm{mp}} I_{\mathrm{mp}}}{P_{\mathrm{in}}}, \tag{6.3}$$

where FF is the fill-factor. The fill-factor is the ratio between the maximum obtainable power of the solar cell and the product of I_{sc} and V_{oc}:

$$FF = \frac{I_{\mathrm{mp}} V_{\mathrm{mp}}}{I_{\mathrm{sc}} V_{\mathrm{oc}}}, \tag{6.4}$$

where the index mp stands for maximum power. If we only consider the subspace of positive voltages V and of negative photocurrents of Fig. 6.3, the short-circuit current is the maximum possible current of the solar cell, whereas the open-circuit voltage is the

	η (%)	V_{oc} (V)	J_{sc} (mA/cm^2)	FF (%)	$\varepsilon_{\mathrm{gap}}$ (eV)	Ref.
c-Si	25.0	0.71	42.7	82.8	1.11	[125, 126]
a-Si	10.1	0.89	16.8	67.8	1.75	[125, 127]
CIGS (cell)	19.8	0.72	34.9	79.2	1.1-1.7[e]	[125, 128]
CdTe (cell)	19.6	0.86	28.6	80.0	1.44	[125, 126]
GaAs (thin film)	28.8	1.12	29.7	86.5	1.43	[125, 126]
FeS_2	3	0.2	40	-	0.95	[13]

Table 6.1.: The top-values for the conversion efficiency η, the open-circuit voltage V_{oc}, the short-circuit current density J_{sc}, the fill-factor FF and the band gap are displayed for a couple of solar cells. Except of the iron pyrite cell, all other cells have been already heavily optimized in research and most of them are even commercially available (but then with lower efficiencies). The solar cell parameters have been extracted from the references indicated in the last column. The efficiency, the open-circuit voltage, the short-circuit current density and the fill-factor have been measured under 25 °C and AM 1.5 conditions, *i.e.* 1000 W/m^2.

largest possible voltage. At both points in the I-V diagram the corresponding power output of the solar cell is zero and in between it reaches a maximum. The fill-factor can be interpreted as the quantity classifying the possible maximum power output of the solar cell. For given I_{sc} and V_{oc} the more "rectangular" the I-V curve is the larger is this fill-factor.

The Shockley-Queisser limit [7] describes the maximally possible conversion efficiency of a (single-stack) solar cell depending on the band gap of the absorber material. For that limit radiative recombination and spectral losses have been considered, but the influence of defects or surfaces are not included. Due to the characteristics of the solar spectrum the largest conversion efficiencies are expected for materials with a band gap between 1-1.5 eV, since materials with a larger band gap exhibit large spectral losses, whereas materials with a smaller band gap suffer of radiative recombination. The Shockley-Queisser limit can be used to search for specific semiconductors, which might provide a reasonable efficiency if used in a solar cell. However, it can be only seen as a first check and a further detailed analysis of those materials is indispensable.

6.4. A Brief Overview of Existing Solar Cells

To get a feeling for the typical sizes of the quantities in a solar cell, some data is collected in the table 6.1. There the conversion efficiency η, the open-circuit voltage V_{oc}, the short-circuit current density J_{sc}, the fill-factor FF and the band gap are shown for crystalline silicon (c-Si), amorphous silicon (a-Si), a copper-indium-gallium-(di)selenide (CIGS) cell, CdTe, a GaAs thin film and finally iron pyrite, which I will focus on in this thesis. All these values are up to date the best values measured for a solar cell consisting of those

[e]The band gap depends on the In and Ga content in the cell.

materials [125]. For the band gaps in the table the reference [126] and the references within have been used. In the case of iron pyrite, the data has been recorded more than 20 years ago [13] and no significant optimization has been achieved since. Partly this can be explained by a low interest in the community to investigate this system, which changed just within the last few years.

First of all, it is noticeable that the size of the band gaps are all more or less in the energetic region, which is predicted to be optimal within the Shockley-Queisser limit [7]. Only iron pyrite has a bit smaller band gap with 0.95 eV and a-Si exhibits a larger band gap with 1.7 eV. The best efficiencies for crystalline Si solar cells are not far off from the maximum possible value of about 30% predicted by the Shockley-Queisser limit. For the other systems there is still a lot of room for improvement. The open-circuit voltage is in most cases considerably smaller than the size of the band gap, but a value of 0.7 V or more is usually sufficient to guarantee a good charge carrier separation. Optimally, short-circuit current densities of about 40-60 mA/cm^2 can be achieved. Although iron pyrite exhibits a small open-circuit voltage, the short-circuit current is large enough. For the fill-factors values of 80-90% are desirable.

The optical absorption coefficient and the (internal) quantum efficiency are not displayed in the table, since these two quantities depend delicately on the wavelength of the incident light. Typically, an average optical absorption coefficient of 10^5-10^6 cm^{-1} for the visible spectrum of light is a rather large value. Then, already very thin absorption layers are able to absorb most of the photons, usually also leading to large internal quantum efficiencies. The absorption coefficient depends also on the type of transition, which usually leads to larger values for direct (optical) transitions, whereas indirect transitions exhibit much smaller values. For instance, due to the indirect band gap the optical absorption in c-Si is "only" 10^3-10^4 cm^{-1}, and thus thick absorption layers need to be used for this solar cells. In CdTe, GaAs and FeS_2 the optical absorption is 1-2 orders of magnitude larger. For the internal quantum efficiency values around 80-90% are large enough for a good solar cell material.

6.5. Conclusions

To understand and predict the suitability of materials for photovoltaics, electronic structure calculations need to be conducted, since the essential physics in a solar cell are based on electronic excitations. An impinging photon is absorbed and an electron is excited from the valence bands into the conduction bands, leaving a positively charged hole. The electron and the hole are coupled and an internal electric field, which is usually caused by the space charges of the p-n junction, has to separate the charge carriers. Those are finally collected at the contacts and a photo current flows.

To evaluate the performance of solar cells a couple of quantities, *e.g.* the conversion efficiency or the open-circuit voltage are used. I have introduced them in this chapter and typical values have been presented for a couple of solar cells. Additionally, I briefly discussed effects, which might lower the performance of solar cells. For the interested reader, I recommend the references [126, 129] for more details.

7. Iron Pyrite Bulk within DFT

7.1. Introduction

Iron pyrite or FeS_2 pyrite is a quite abundant mineral in the earth's crust and most people know it by the name "fool's gold". The origin of this name comes from the shiny gloss of the pyrite crystal surface, reminding of gold. The degree of hardness can be used to distinguish gold nuggets from pyrite crystals, since pyrite is much harder than gold. Iron pyrite is a semiconductor with a measured band gap of 0.95 eV and a large optical absorption of about $6 \cdot 10^5$ cm^{-1} for visible light [13]. Hence, it is not surprising that iron pyrite has drawn attention as possible promising photovoltaic material. Solar cell prototypes using FeS_2 pyrite as optical absorber yield large quantum efficiencies of above 90 % and sufficiently high photocurrents of 40 mA/cm^2, but they suffer of a too low open-circuit voltage of only 200 mV leading to conversion efficiencies smaller than 3 %. There are plenty of possible explanations for the low open-circuit voltage, which I have already addressed in the introduction of this thesis (see chapter 1).

To understand the origin of the low open-circuit voltage, electronic structure calculations within density-functional theory (DFT) can be of great help. First, the electronic structure of the "simple" bulk system should be understood, before approaching more realistic scenarios like surfaces or interfaces. This chapter is dedicated to this topic. There are already many publications focusing on the DFT results of iron pyrite with which I will compare my results, and thus, this chapter can be also seen as a benchmark of my results.

I will start by introducing the lattice structure of iron pyrite bulk followed by a detailed discussion of its electronic structure within "conventional" DFT. The strong connection between the geometrical characteristics and the electronic structure will be exposed, including results of the structural optimization. Finally, the dependence of the results on different exchange-correlation functionals and methods, *e.g.* LDA, GGA-PBE, DFT+U, hybrid functionals, within the DFT framework is examined.

Parts of the results presented in this chapter are already published in the reference [25].

7.2. The Pyrite Structure

Iron pyrite is only one compound crystallizing in the pyrite structure. The whole row of transition-metal dichalcogenides MS_2 with M=Fe, Co, Ni, Cu and Zn crystallize in the pyrite structure and they exhibit a broad spectrum of physical properties ranging from "normal" semiconductors, ferromagnets to Mott insulators [46]. This variety is directly connected to the electronic occupation and the geometry of the pyrite structure, which is

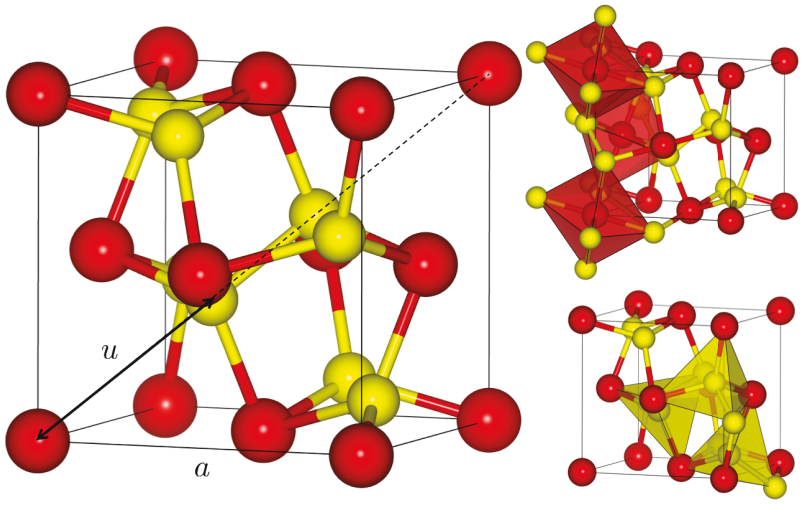

Figure 7.1.: The iron pyrite structure with the S atoms as yellow spheres and the Fe atoms as red spheres. The lattice parameter a controls the size of the cubic unit cell and the Wyckoff parameter u determines the position of the S atoms within the cell. In the right panel the (almost) octahedral and tetrahedral surrounding of the Fe and S atoms are displayed. In the tetrahedrons, the characteristic S dimers are clearly visible. This figure has been created with the help of the program VESTA [130].

displayed in Fig. 7.1. In the next section I will in detail discuss the connection between the geometrical structure and the electronic structure.

The pyrite unit cell is simple cubic with a lattice parameter a and it consists of 4 Fe atoms and 8 S atoms, where the S atoms form characteristic S dimers. The position of the S atoms in the unit cell are described by the Wyckoff parameter u. The pyrite structure can be seen as NaCl structure with the Fe atoms located at the Na positions and the centers of the S dimers occupying the Cl positions. The S dimers are orientated along the space diagonals. The S atoms are almost octahedrally arranged around the Fe atoms, whereas each S atom is tetrahedrally surrounded by 3 Fe atoms and one additional S atom with which it forms the S dimer. The distance between the two S atoms is smaller than the nearest S-Fe distance in most pyrite systems, which is a consequence of the strong covalent bond between those S atoms. Although the octahedrons and tetrahedrons are slightly distorted[1], they lead to a good approximation to the common crystal-field splitting of the d states into t_{2g} and e_g states, which has a crucial influence on the electronic structure.

The positions of the basis atoms are as follows, where Fe^i with $i = 1, .., 4$ and S^j with

[1] A perfect octahedral and tetrahedral coordination exists for a Wyckoff parameter of $u = 0.25$.

$j = 1, .., 8$ denote the Fe and S atoms in the unit cell:

$$\begin{aligned}
\boldsymbol{B}_{\mathrm{Fe}^1} &= (0,0,0), & \boldsymbol{B}_{\mathrm{Fe}^2} &= (0,\tfrac{1}{2},\tfrac{1}{2}),\\
\boldsymbol{B}_{\mathrm{Fe}^3} &= (\tfrac{1}{2},0,\tfrac{1}{2}), & \boldsymbol{B}_{\mathrm{Fe}^4} &= (\tfrac{1}{2},\tfrac{1}{2},0),\\
\boldsymbol{B}_{\mathrm{S}^1} &= (u,u,u), & \boldsymbol{B}_{\mathrm{S}^2} &= (-u,-u,-u),\\
\boldsymbol{B}_{\mathrm{S}^3} &= (\tfrac{1}{2}+u,\tfrac{1}{2}-u,-u), & \boldsymbol{B}_{\mathrm{S}^4} &= (-\tfrac{1}{2}-u,u-\tfrac{1}{2},u),\\
\boldsymbol{B}_{\mathrm{S}^5} &= (-u,\tfrac{1}{2}+u,\tfrac{1}{2}-u), & \boldsymbol{B}_{\mathrm{S}^6} &= (u,-\tfrac{1}{2}-u,u-\tfrac{1}{2}),\\
\boldsymbol{B}_{\mathrm{S}^7} &= (\tfrac{1}{2}-u,-u,\tfrac{1}{2}+u), & \boldsymbol{B}_{\mathrm{S}^8} &= (u-\tfrac{1}{2},u,-\tfrac{1}{2}-u).
\end{aligned} \tag{7.1}$$

The distance between the S atoms in a S dimer, $d_{\mathrm{S-S}}$, is directly controlled by the Wyckoff parameter u. In Fig. 7.1 it becomes clear that the relation is as follows:

$$d_{\mathrm{S-S}} = \sqrt{3}a(1-2u). \tag{7.2}$$

The distance of the S dimers has a strong influence on the electronic structure, and thus also the Wyckoff parameter has a strong influence, as it will be discussed in the next sections.

The experimentally determined lattice parameter taken from reference [51] with $a = 5.418$ Å and a Wyckoff parameter of $u = 0.385$ (both measured at room temperature) are used in several calculations of this thesis for the iron pyrite structure, and they are from now on referred to as the structural parameters taken from experiment. The lattice parameters and Wyckoff parameters of natural and synthetic iron pyrite crystals show variations of about 0.5 %, probably due to defects. The structural optimization presented in another section of this chapter leads to an additional set of structural parameters, denoted as the optimized structural parameters in the thesis.

The iron pyrite structure belongs to the $Pa\bar{3}$ group, and thus exhibits 24 symmetries, including the inversion-symmetry, which significantly simplifies and speeds up calculations. However, a total number of 12 atoms in the unit cell poses a challenge for DFT calculations using more sophisticated schemes like hybrid functionals.

7.3. Computational Details

We used the FLEUR code [66] to perform the calculations, which is based on the full-potential linearized augmented plane-wave (FLAPW) method within the framework of density-functional theory (DFT). I refer the interested reader to the theory chapters about DFT and FLAPW in this thesis (chapters 2 and 5) and the references within for more details on the methods. The FLEUR code has a couple of computational parameters discussed in chapter 5, which need to be carefully converged. For our purposes sufficiently converged

are a plane-wave cutoff parameter $k_{\max} = 4.0$ a.u.$^{-1}$, an angular momentum cutoff of $l_{\max} = 8$ for both the Fe and the S atoms, and muffin tin radii with $R^{\mathrm{Fe}}_{\mathrm{MT}} = 2.23$ a.u. and $R^{\mathrm{S}}_{\mathrm{MT}} = 1.98$ a.u. A rather dense $\boldsymbol{k}$-mesh of 10×10×10 $\boldsymbol{k}$-points in the full Brillouin zone via Monkhorst-Pack has been chosen to guarantee convergence in all cases, although I am quite sure a less dense $\boldsymbol{k}$-mesh would have worked too. Since all 24 symmetries of the pyrite structure are exploited, the calculations can be restricted to an irreducible wedge of the Brillouin zone only containing 45 $\boldsymbol{k}$-points. In the appendix D a more detailed convergence analysis of the DFT calculations for iron pyrite is presented, in which my choice of parameters is justified.

The results of the "conventional" DFT calculations are rather insensitive to the inclusion of local orbitals into the LAPW basis. The energetically highest-lying core states are the Fe 3s and 3p states, which are located about -2.8 Htr and -1.6 Htr below the valence states. These semicore states do not lead to "ghost" bands in the DFT description and an inclusion as LOs into the LAPW basis has no significant influence. The inclusion of additional higher-energy local orbitals leads also to no significant change of the "conventional" DFT results, and thus no local orbitals are included in the calculations.

The DFT+U calculations of iron pyrite have been performed based on the GGA-PBE functional. The effective Hubbard-U has been calculated to an optimal value of $U_{\mathrm{eff}} = 2.4$ eV using constrained RPA within the SPEX code [85]. More precisely the Hubbard-U is 3.3 eV and the Hund-exchange parameter $J = 0.9$ eV, adding up to the mentioned effective Hubbard-U. The U parameter has been applied to the Fe 3d states. For the double counting the around mean-field limit has been used.

For the hybrid functional calculations the same parameter set has been used, except that the $\boldsymbol{k}$-points needed to be reduced to a Γ-centered 4×4×4 $\boldsymbol{k}$-mesh. Since the calculations also demand for a number of unoccupied electronic bands, I have included 800 total bands. Since hybrid functional calculations are more sensitive to the inclusion of LOs, I have tested the effect of the inclusion of the Fe 3s and 3p semi-core states as LOs into the FLAPW basis and no considerable change in the results was observable. The same is true for the inclusion of high-energy LOs.

Iron pyrite is non-magnetic in experiment and also the calculations indicate a stable non-magnetic ground state. As a test I have started a magnetic calculation of iron pyrite with finite magnetic moments of about 2 μ_B, which finally converged to a non-magnetic calculation. Therefore, all following calculations of iron pyrite bulk have been treated non-magnetically. Additionally, no spin-orbit coupling (SOC) has been considered, since Fe and S are quite light elements, and thus the size of the band gap of iron pyrite changes less than 0.01 eV on inclusion of SOC. For the structural relaxation and the determination of the atomic forces a Broyden-Fletcher-Goldfarb-Shanno algorithm has been exploited and the forces have been converged to the order 10^{-5} Htr/a.u.

The optical absorption of iron pyrite has been calculated using the SPEX code.[2] A detailed discussion about the theoretical basics of the calculation of the (orbital-resolved)

[2] Although I use the SPEX code also for the GW calculations, please note that for the calculation of the optical absorption we used in this chapter only the Kohn-Sham energies and Kohn-Sham wave functions, and thus we deal only with the optical absorption calculated within DFT.

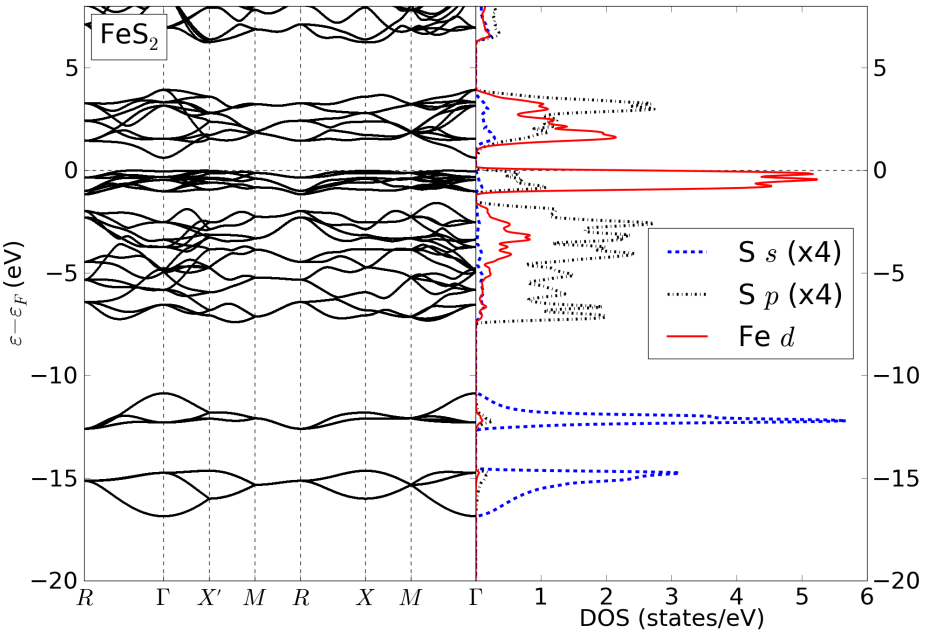

Figure 7.2.: The electronic band structure of iron pyrite for the structural parameters taken from experiment using the GGA-PBE functional (left panel) and the corresponding density of states (right panel) decomposed into S $3s$- (blue dashed), S $3p$- (black pointed), and Fe $3d$-orbital contributions (red solid). To improve the visibility the LDOS of the S $3s$- and S $3p$-orbital contributions are enhanced by a factor of 4. The Fermi energy ε_F is located at 0. The high-symmetry points of the $\boldsymbol{k}$-path are denoted according to Bradley and Cracknell [131], where X' is equivalent to X.

optical absorption is presented in the appendix B. A $\boldsymbol{k}$-mesh of 20×20×20 $\boldsymbol{k}$-points and an artificial broadening with the Lorentzian functions with 50 meV full-width at half-maximum (FWHM) has been used. For the determination of the orbital-resolved optical absorption see appendix B.

7.4. First Glimpse on the Electronic Structure of Iron Pyrite

The electronic band structure and the corresponding density of states (DOS) of iron pyrite calculated within the GGA-PBE functional are displayed in Fig. 7.2. The DOS is decomposed into the most important orbital contributions in the observed energy range,

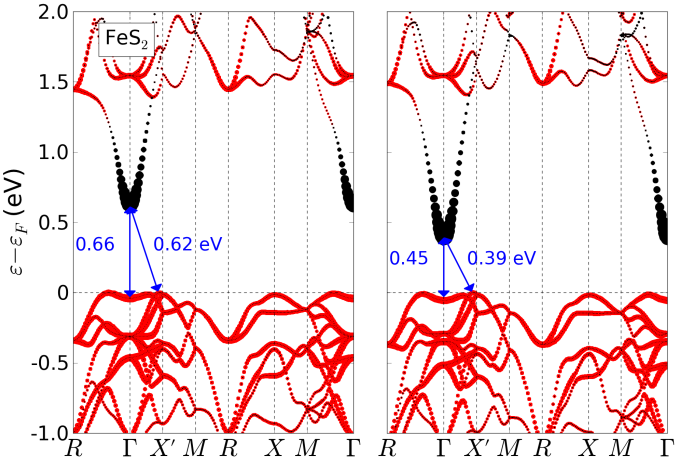

Figure 7.3.: The orbital-resolved band structure of iron pyrite for the structural parameters taken from experiment (left panel, $a = 5.418$ Å and $u = 0.385$) and for the optimized structural parameters (right panel, $a = 5.403$ Å and $u = 0.383$) obtained within GGA-PBE. The Fe $3d$ orbital contributions are indicated in red, whereas the S $3p$ character is displayed in black color. The size of the points is connected to the content of the corresponding orbital character. The high-symmetry $\boldsymbol{k}$ points of the $\boldsymbol{k}$-path are denoted according to Bradley and Cracknell [131] (X' equivalent to X). The direct band transition at Γ and the smallest indirect transition, *i.e.* the fundamental band gap, are indicated as blue arrows.

which are the S $3s$-, the S $3p$-, and the Fe $3d$-orbital contributions. The LDOS of the S contributions are enhanced by a factor of 4 to improve the visibility. The electronic structure can be simply analyzed according to the geometry of the pyrite structure. On the one hand, there is the strong covalent bond of the S dimers, and then for the Fe atoms there is the crystal field splitting into t_{2g}- and e_g states caused by the octahedral symmetry of the structure.[3]

The covalent bond of the S dimers leads to bonding and anti-bonding states of the S $3s$- and S $3p$-orbitals. The S $ss\sigma$ and $ss\sigma^*$ states are located at about -15 and -12 eV, and thus are split by about 3 eV. These states are quite separated from all other states only weakly hybridizing with the rest, and thus do not play a significant role for the states around the Fermi energy, which are essential for the band gap. The bonding and

[3]The pyrite structure exhibits only approximately an octahedral symmetry (see Fig. 7.1), leading to a bit more complicated crystal field splitting than assumed. However, for the purpose of a first understanding of the electronic structure the assumption of a perfect octahedral symmetry is adequate. Additionally, note that the splitting into t_{2g} and e_g states relate to the principal axes of the octahedrons in the crystal and not the global z axis.

anti-bonding S $3p$ states $pp\sigma$, $pp\pi$, $pp\pi^*$ and $pp\sigma^*$ range from -7 to 5 eV and hybridize strongly with the Fe $3d$ states depending on their energy. The closer these states are to the Fermi energy the more they hybridize with the Fe $3d$ states. From -7 to -2 eV the S $pp\sigma$, $pp\pi$ and $pp\pi^*$ are the major contributions to the DOS exhibiting more hybridization with the Fe $3d$ t_{2g} states for the larger energies. From -2 eV to the Fermi energy the t_{2g} states are quite flat and localized, and thus they lead to large contributions in the DOS dominating this energy range. These states hybridize weakly with the S $3p$ states.

In the conduction bands ranging from about 0.6 to 4 eV the Fe $3d$ e_g states dominate the lower energies, whereas the S $pp\sigma^*$ contributions become more important for larger energies. The hybridization between the e_g and the S $pp\sigma^*$ states is quite strong for the whole energy range. For energies larger than 5 eV the orbital contributions from S $4s$ and Fe $4p$ states gain influence, which is not shown in the figure. In the appendix E the orbital contributions are discussed with the help of charge density isosurfaces, confirming the above statements.

The density of states in Fig. 7.2 indicates that the band edges around the Fermi energy are mostly dominated by Fe $3d$ states, but a closer look into the orbital contributions at the conduction band edge reveals that there are significant contributions from S $3p$ states. The orbital-resolved band structure in Fig. 7.3 allows more insight into the orbital contributions at the Fermi edge. The valence states at the Fermi edge, and thus also the valence band maximum (VBM) are quite localized and have mostly Fe $3d$ orbital character. The highest occupied state at Γ is even of pure Fe $3d$ character. The conduction bands are also dominated by Fe $3d$ states, except of the lowest unoccupied band around Γ, which exhibits an increasing S $3p$ orbital contribution the closer it gets to Γ. The conduction band minimum (CBM) is located at Γ, and it is of pure S $3p$ orbital character. But also in the vicinity of Γ the orbital character of the band is very pure. This single S $3p$ rich band appears at lower energies than the Fe $3d$ states in the conduction band due to the larger bandwidth of the $pp\sigma^*$ compared to the quite localized d states. Interestingly, it becomes only evident around Γ at the band-bottom. In difference to the localized Fe $3d$ states this S $3p$ band is delocalized, leading to a quite remarkable type of transition in the fundamental band gap in iron pyrite. It is predicted to be 0.62 eV within PBE, and it is defined between a rather localized band of Fe $3d$ character and a delocalized band at Γ of S $3p$ character. Hence, not only the orbital character of the VBM and CBM are different, but they are also located on different atoms and the corresponding bands exhibit a very different localization. This has considerable consequences on the optical absorption of iron pyrite as it is discussed in section 7.7. Due to the flatness of the valence bands, the direct transition at Γ is only slightly larger in energy with 0.66 eV than the fundamental band gap, and thus the direct transition can also be used to analyze the dependence of the band gap on the structural parameters or the chosen exchange-correlation functional.

The Fig. 7.4 shows a charge density slice for the energies close to the VBM and CBM at Γ projected on the plane spanned by the (111) and $(1\bar{1}0)$ direction. It indicates that the relevant contributions to the states arise from Fe d_{z^2} and S $pp\sigma^*$ orbitals.[4] The Fe d_{z^2}

[4] Note that the spherical harmonics are expressed with respect to the (111) direction as global quantization axis. The rotational behavior of the spherical harmonics is determined by the Wigner matrices.

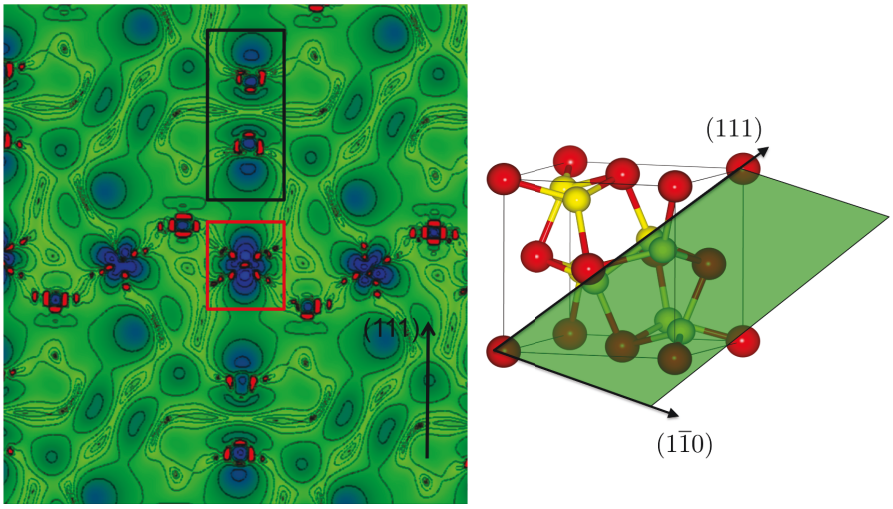

Figure 7.4.: The projected charge density of FeS_2 pyrite onto the plane spanned by the directions (111) and $(1\bar{1}0)$ is presented for an energy range only containing the highest occupied band and the lowest unoccupied band at Γ. The RGB (Red-Green-Blue) color code follows a logarithmic scale with red (blue) indicating minimal (maximal) charge density contribution. The black box contains two S atoms forming the S dimer orientated along the (111) direction and the red box enframes an Fe atoms along the same direction. The figure on the right side visualizes the position of the projection plane in the iron pyrite structure.

orbital character comes from the valence band, whereas the S $pp\sigma^*$ character arises in the conduction states. The charge density is quite localized to the Fe and S atom positions, whereas it shows less structure between those atoms. In particular no sp^3d^2 hybridization can be observed, and thus a more ionic bonding between the Fe and S atoms is present.

The calculated electronic structure of iron pyrite is in excellent agreement with the most recent publications, *e.g.* [29, 30]. The band gap size of 0.62 eV within GGA-PBE is about 35% smaller than the experimentally measured value of 0.95 eV. This underestimation is quite typical also for some simple semiconductors. However, in many simple semiconductors the band gap underestimation is considerably larger, and thus it is still surprising how well the GGA-PBE result agrees with the experimental band gap size regarding the absolute values.

7.5. Structural Optimization of Iron Pyrite and Dependence on the Structural Parameters

In particular for later examinations of the iron pyrite surfaces, the bulk structure has been structurally optimized. First the optimized lattice constant a has been calculated by energy minimization, and then a first guess for the Wyckoff parameter u has been determined via energy minimization using the optimized lattice constant. In the energy minimization the optimized structure parameters can be extracted via parabolic fits, which are presented in the Fig. 7.5.[5] The optimized lattice constant is determined to about 5.40 Å within the PBE functional,[6] which is in nice agreement with the experimentally measured lattice constant of 5.418 Å [51].

With the first guess for the optimized Wyckoff parameter and the optimized lattice constant a the iron pyrite structure has been structurally relaxed, which leads to an optimized value of $u = 0.3826$ for the Wyckoff parameter (experimental value: $u = 0.385$). The corresponding forces have been already quite small using the first guess Wyckoff parameter, explaining the small difference between the first guess u and the relaxed value. These parameters lead to a distance between the S atoms in the S dimer of 2.16 Å for the structure parameters from experiment and 2.20 Å for the optimized structural parameters.

In the right panel of Fig. 7.3 the electronic band structure of structurally optimized iron pyrite is displayed. Despite a difference in the size of the band gap, which is smaller (0.4 eV) than the band gap for the structural parameters taken from experiment (0.6 eV), the band structure shows similar characteristics regarding the orbital contributions. But still it is astonishing that a relative difference of less than 1% in the structural parameters leads to a change in the band gap size of about 50%. That is owed less to the change in the lattice constant a, but much more to the difference in the Wyckoff parameter. A change of a few percent in the lattice constant has almost no influence on the electronic structure around the Fermi energy, since not only the distance between the S atoms in the S dimer is altered, but also the distance between the Fe atoms and the Fe-S bondings are altered leading to insignificantly small relative shifts between the Fe $3d$ and S $3p$ rich bands. On the other hand, the Wyckoff parameter mostly controls the distance between the S atoms in the S dimer, which has a crucial influence on the bonding anti-bonding splitting between the S $3p$ states, and thus alters the relative position of the Fe $3d$ and S $3p$ states.

This can be observed in Fig. 7.6, where the orbital-resolved band structure of iron pyrite is displayed for four different Wyckoff parameters. The smaller the Wyckoff parameter is the larger is the distance of the S atoms in the S dimer, and thus the smaller is the splitting between the bonding and anti-bonding S $3p$ states leading to a smaller fundamental band

[5] In addition to the quite straight-forward way to determine the optimized lattice constant as presented in this thesis, I tried also the Birch-Murnaghan equation of state for the optimization, revealing no significant changes.

[6] To be more precise, the optimized lattice constant is 5.403 Å within GGA, however I found that the lattice constant has not such a significant influence on the electronic structure and the band gap of iron pyrite, and thus I calculated the optimized lattice constants of iron pyrite within all other functionals only up to two digits behind the comma.

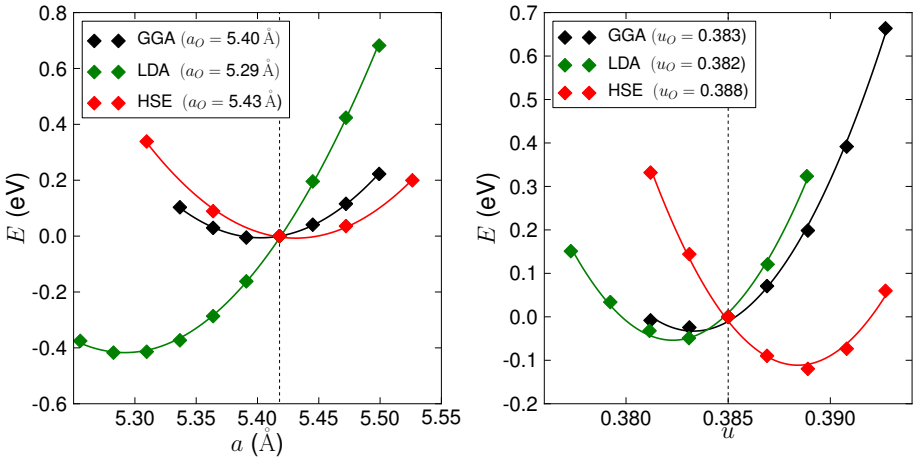

Figure 7.5.: The optimized lattice constant a_O (left panel) and the first guess for the optimized Wyckoff parameter u_O (right panel) has been calculated via energy minimization using a parabolic fit. For the determination of the first guess Wyckoff parameter the optimized lattice constant has been used. The structural parameters have been determined within the GGA-PBE (black), the LDA and the HSE06 (red) functional. The dashed lines indicate the structural parameters taken from experiment of 5.418 Å and $u = 0.385$. We used the Harris-Foulkes approximation for the HSE06 calculations to save computational time [132, 133].

gap. For too small Wyckoff parameters this can even lead to metallicity in iron pyrite as it can be observed in the case of $u = 0.375$. There are also reports in the literature predicting a metallic electronic structure, since the structural optimization led to small Wyckoff parameters [49]. The strong connection between the Wyckoff parameter and the band gap has been already examined by Eyert *et al.* [35]. Since natural crystals of iron pyrite show slight deviations in the structural parameters [51], most probably caused by defects, some deviations in the band gap are expected. The large spread of the reported band gaps in the literature (cf. [34]) might be at least partially attributed to this fact.

Let me compare the results to literature on the optimized structural parameters of iron pyrite. Zeng *et al.* [49] report a lattice constant of $a = 5.455$ Å and a Wyckoff parameter $u = 0.379$ after structural relaxation using the GGA-PBE functional leading to an almost metallic electronic band structure. In a quite recent publication of Sun *et al.* [29] an optimized lattice constant of $a = 5.403$ Å is reported, leading to a band gap size of 0.39 eV using the GGA-PBE functional, which is in excellent agreement to the results reported in this thesis. Unfortunately, no information about the value of the optimized Wyckoff parameter is presented, which is crucial for the band gap size as pointed out in the last paragraph.

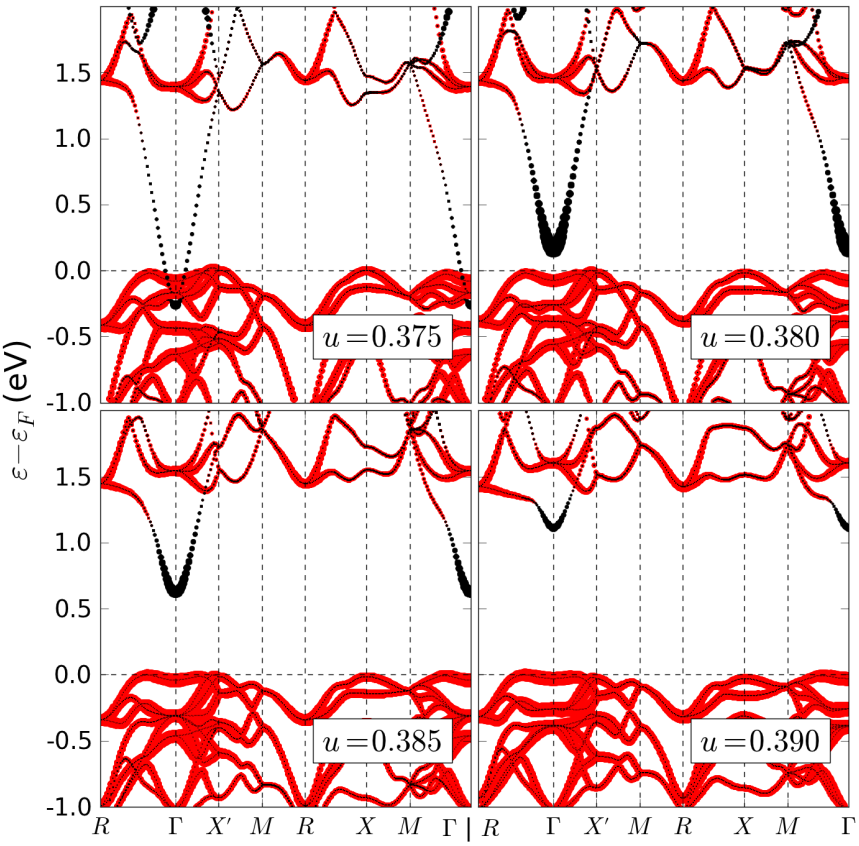

Figure 7.6.: The electronic band structures of iron pyrite within the GGA-PBE functional for four different Wyckoff parameters $u = 0.375$ (upper left), $u = 0.380$ (upper right), $u = 0.385$ (lower left) and $u = 0.390$ (lower right). In all those cases the lattice constant has been chosen to $a = 5.418$ Å. The orbital character of the bands is indicated in red for Fe $3d$ and in black for S $3p$ states. The fatness of the points corresponds to the orbital contribution.

FeS_2	exp.	LDA	PBE	PBE+U	PBE0	HSE06	EXX-OEP
$\varepsilon_{\mathrm{gap}}$ (eV)	0.95	0.65	0.62	0.90	2.98*	2.24	2.70*

Table 7.1.: The size of the fundamental band gap of iron pyrite for the structural parameters from experiment, *i.e.* $a = 5.418$ Å and $u = 0.385$, is listed using different exchange-correlation functionals for the DFT calculations. The local functionals LDA and GGA-PBE, the DFT+U result for $U_{\mathrm{eff}} = 2.4$ eV and the hybrid functionals PBE0, HSE06 and EXX-OEP are compared to the experimentally measured band gap size. For the PBE0 and EXX-OEP result only the Γ-Γ transition has been calculated (indicated by a "*"), which might be not the smallest energy transition, and thus the fundamental band gap might be smaller in these cases.

7.6. Dependence on the Exchange-Correlation Functional

I have discussed the electronic structure of iron pyrite calculated within the GGA-PBE functional so far. In this section the dependence of the electronic structure on the choice of the exchange-correlation functional is examined. I used local functionals like the LDA functional, but also more sophisticated hybrid functionals like PBE0, HSE06 and EXX-OEP. Additionally, I discuss the application of the DFT+U method on iron pyrite.

In table 7.1 the size of the fundamental band gaps of iron pyrite are listed using these exchange-correlation functionals. There is a quite large variation in the band gap size, with slightly smaller band gaps than the experimental one for the LDA and GGA-PBE functional, a very nice agreement for the PBE+U calculation and drastically overestimated band gaps for the hybrid functionals. In the following I will discuss each of these cases separately:

7.6.1. LDA/GGA Result

The GGA-PBE results have been already discussed in detail in the previous sections, and thus I will focus on the results of the LDA functional. Using the structural parameters from the experiment, the band gap size and the orbital character of the bands (not shown) does not significantly change compared to the PBE results. However, the structural optimization within the LDA yields quite different results for iron pyrite with an optimized lattice constant $a = 5.29$ Å and an optimized Wyckoff parameter $u = 0.381$, which leads to an almost metallic system due to the small u. The parabolic fits for the determination of the optimized structural parameters within the LDA are displayed in Fig. 7.5. The GGA-PBE results are in much better agreement with the experimentally measured structural parameters, showing for one system more that the GGA functional tends to an improvement of the description of bond lengths and lattice constants. From here on all results in this thesis using a local exchange-correlation functional are calculated within GGA-PBE.

In the literature Opahle *et al.* [50] report a metallic electronic band structure of iron

pyrite using the LDA functional and after structural relaxation, since they obtain an optimized lattice constant of about $a = 5.30$ Å and a Wyckoff parameter of 0.377. These values are both in reasonable agreement with the results reported in the last paragraph.

7.6.2. DFT+U Result

In Fig. 7.7 the orbital-resolved electronic band structure of iron pyrite calculated within the DFT+U method (the GGA-PBE functional has been used as basis) is presented. For comparison also the GGA-PBE band structure is displayed. An effective Hubbard-U parameter of 2.4 eV, which has been calculated using the constrained RPA method [85], has been applied to the localized Fe $3d$ states, in order to improve their description. The theory behind the DFT+U approach is discussed in chapter 3.

The DFT+U results exhibit no major changes in the orbital character and the effective masses, except of the increased band gap size to about 0.9 eV and small changes of the valence bands around Γ, which are most probably caused by slight changes in the hybridization with the S $3p$ states. The agreement of the band gap size with the experiment is rather satisfying, although the DFT+U method worsens the description of the optical properties of iron pyrite as I will discuss in the following section. Due to the nice agreement of the experimental and calculated band gap size, the DFT+U method is used in a couple of publications dealing with defects or surfaces in iron pyrite [19, 29]. Their DFT+U band structure agrees well with the results in this thesis.

7.6.3. Hybrid Functional Results

The band gap size of iron pyrite calculated within the hybrid functionals is much larger than the experimentally determined 0.95 eV and the about 0.6 eV predicted within the local exchange-correlation functionals. With the PBE0 functional [87] a band gap of about 2.9 eV is obtained, which is more than 200% larger than the experimental band gap. Since the PBE0 functional uses unscreened exchange, the band gap sizes tend to be too large compared to the experiment. Due to the (artificially) incorporated screening the HSE06 functional (see chapter 3 for theory) is reported to predict reliable band gaps for semiconductors with not too large band gaps [56, 57]. However, for iron pyrite also the HSE06 functional tends to a large overestimation of the band gap size with about 2.2 eV (almost 150% larger than the experimental value).

The electronic band structure calculated within the HSE06 functional is presented in Fig. 7.8. Since the $\boldsymbol{k}$-mesh within a HSE calculation can not be chosen arbitrary, and thus no direct calculation of the band structure along a high-symmetry $\boldsymbol{k}$-path is possible, the Wannier interpolation technique [134, 135] has been used to obtain an interpolated band structure.[7] There are no major changes regarding the orbital character of the bands (not shown), but the Fe $3d$ t_{2g} and e_g states at the edges of the Fermi energy are shifted

[7] A coarse $\boldsymbol{k}$-mesh of 4×4×4 and the first 52 bands have been used to obtain maximally localized Wannier functions of iron pyrite. The first 40 bands are the occupied bands, whereas the last 12 are unoccupied bands. Fortunately, there is no overlap between the first 52 bands and bands at higher-energies, which considerably simplifies the determination of the Wannier functions.

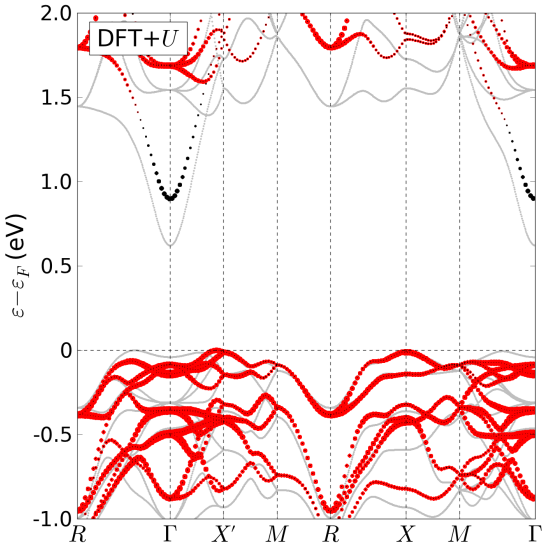

Figure 7.7.: The orbital-resolved band structure of iron pyrite for the structural parameters from experiment is presented using DFT+U. The Fe $3d$ orbital character is displayed in red and the S $3p$ orbital character in black. The size of the points is connected to the value of the corresponding orbital character. The gray thin lines represent the GGA-PBE band structure for comparison.

considerably. In GGA-PBE the band gap between the Fe $3d$ states is about 1.5 eV, whereas in HSE06 the gap is increased to about 3.5 eV. Consequently also the S $3p$ band at the conduction band edge around Γ is shifted together with the Fe $3d$ bands due to hybridization, leading to a fundamental band gap size of about 2.2 eV. The character of the fundamental band gap changes compared to the PBE calculation from an indirect to a direct one due to slight changes in the hybridization between the S $3p$ and Fe $3d$ orbitals in the quite flat valence bands.

The structural optimization of iron pyrite within the HSE06 functional yields an optimized lattice constant of $a = 5.43$ Å and an optimized Wyckoff parameter $u = 0.388$. The parabolic fits for the determination of the optimized structural parameters are displayed in Fig. 7.5. Using the optimized structural parameters from the HSE calculation the fundamental band gap of iron pyrite is predicted to be 2.66 eV. Due to the larger Wyckoff parameter compared to the u from experiment, a band gap larger than the 2.2 eV determined with the structural parameters taken from experiment is quite expected. Using the optimized structural parameters calculated within the GGA-PBE functional, *i.e.* $a = 5.40$ Å and $u = 0.383$, leads to a fundamental band gap of 1.91 eV, which is still about 100% larger than the experimental value.

There are two references in the literature, in which there is briefly reported about the band gap size of iron pyrite using the HSE06 functional [29, 30]. In both cases the same

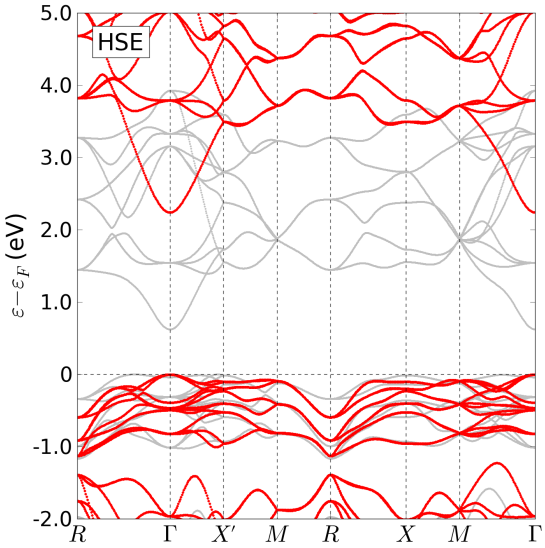

Figure 7.8.: The electronic band structure of iron pyrite for the structural parameters from experiment using the HSE06 functional is presented in red. The Wannier interpolation technique has been used to obtain the band structure. In gray the GGA-PBE band structure is indicated for comparison.

code has been used, yielding a fundamental band gap of about 2.7-2.8 eV. They use the same experimental lattice constant as I did, however it is not clear from the references, whether they relaxed the structure within HSE, and thus used a Wyckoff parameter different to the experimental one. Considering the values of the band gaps, I assume they performed a structural relaxation, since the values correspond to the reported band gap of 2.66 eV of this thesis using the optimized structural parameters within HSE.

The reason for the quite surprising strong overestimation of the band gap size within hybrid functionals is discussed in more detail in chapter 10.

For completeness let me me mention that calculations using the EXX-OEP approach[8] have been also performed, yielding a band gap of 2.7 eV.

[8]The EXX-OEP method stands for an exact exchange treatment within an optimized effective potential. I have not introduced this method in the theory part of my thesis, since the band gap of iron pyrite is the only results in the thesis, where the EXX-OEP method has been used. The corresponding calculation has been carried out by Markus Betzinger. More details on the approach can be found in the literature [136, 137].

7.7. Optical Absorption

GGA-PBE In Fig. 7.9 the orbital-resolved optical absorption, α, of iron pyrite calculated within GGA-PBE is displayed. The computational details, how the orbital-resolved optical absorption has been calculated, can be found in the appendix B. Within photon energies of maximally 6 eV the major contributions to the transitions are coming from Fe $3d$-Fe $3d$ (red dashed), Fe $3d$-S $3p$ (blue dotted), S $3p$-Fe $3d$ (green dashed-dotted) and S $3p$-S $3p$ (yellow striped) transitions. All other transitions are negligible in the observed energy range and become important only for larger energies. Hence, also the sum of these four orbital-resolved transition rates approximately yields the total transition rate as it can be seen in the appendix. The term Fe $3d$-Fe $3d$ or S $3p$-S $3p$ transitions refers to transitions between Fe $3d$-rich or S $3p$-rich states, but they also need an admixture of other orbital character via hybridization or p and d electrons at different atoms to fulfill the dipole selection rule. An exact definition is given in Eq. (B.22) of the appendix B.

The total optical absorption exhibits two major peaks, one located at about $\omega = 2.1 \pm 0.2$ eV (marked with A in Fig. 7.9) and another one at about 3.6 ± 0.1 eV (B). Since the peaks are rather broad, even when reducing the broadening of the Lorentzian functions, energy ranges rather than energy values are given here for the peak positions. More precisely, peak A seems to consist of two peaks, where one is at about 2.0 eV and the other at around 2.2 eV. However, in the following I will treat it as one peak at 2.1 eV with an error bar of ± 0.2 eV. The optical absorption exhibits quite large maximal values of $12 \cdot 10^5$ cm^{-1} and an average value of more than $9 \cdot 10^5$ cm^{-1} for energies between 2-6 eV.

The major transitions contributing to peak A are the Fe $3d$-Fe $3d$ transitions, which are more precisely the transitions between the Fe $3d\,t_{2g}$ states of the valence band and the Fe $3d\,e_g$ states of the conduction bands, whereas the Fe $3d$-S $3p$ transitions contribute much less. At first sight that is quite surprising, since the fundamental band gap of iron pyrite is defined by a VBM of Fe $3d$ orbital character and a CBM dominated by S $3p$ character, and thus the dipole selection rule with $\Delta l = \pm 1$ is clearly fulfilled, which is expected to lead to a large optical absorption, as it is also stated by Eyert *et al.* [35]. Hence, one might expect that the transitions between Fe $3d$-S $3p$ states should be strongly favored and the first peak should depend on them. However, the wave functions of the valence states are quite localized at the Fe atoms, whereas the S $3p$ band at the CBM is essentially localized at the S atoms, and thus the overlap between the wave functions entering in the computation of the dipole matrix elements (see appendix B) is very small for the Fe $3d$-S $3p$ transitions around the band edge. Along the high-symmetry $\boldsymbol{k}$-path $\Gamma \to X$ the dipole matrix elements vanish even completely for the transitions between the highest valence band and the S $3p$ band, whereas along $\Gamma \to R$ they are three orders of magnitude smaller than the Fe $3d$-Fe $3d$ transitions contributing to the first peak. The large optical absorption is rather caused by the large LDOS of Fe $3d$ states hybridized with a bit of S $3p$ at the band edges.

The second major peak B comprises mostly of Fe $3d$-S $3p$ and S $3p$-Fe $3d$ transitions, since for transition energies of more than 3 eV the electrons from the Fe $3d\ t_{2g}$ valence states can be excited to the higher-lying S $pp\sigma^*$ states, or electrons from the S $pp\pi^*$ can be excited to the Fe $3d\ e_g$ states. For larger transition energies up to 6 eV the S $3p$-Fe $3d$

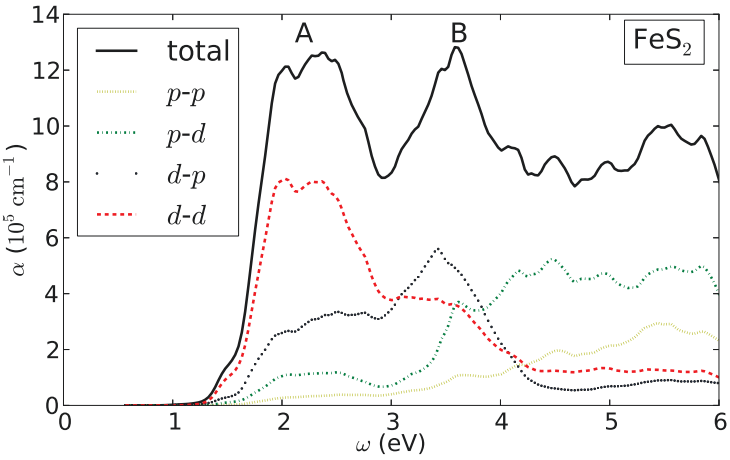

Figure 7.9.: The optical absorption of iron pyrite for the structural parameters from experiment within the GGA-PBE functional for photon energies up to 6 eV. The total optical absorption (black solid) is mainly the sum of the Fe $3d$-Fe $3d$ (red dashed), the Fe $3d$-S $3p$ (blue dotted), the S $3p$-Fe $3d$ (green dashed-dotted) and the S $3p$-S $3p$ (yellow striped) orbital contributions to the optical absorption. The two main peak positions are indicated by A and B.

and the S $3p$-S $3p$ transitions play the major role. Only for completeness let me mention that for larger energies than 6 eV the S $4s$ or Fe $4p$ states contribute also to the optical absorption.

To accurately determine the size of the optical band gap, it is common in experiment to analyze the tail of the first peak in detail by applying a linear regression to the function $(\alpha\omega)^n$ vs. ω with a power n depending on the type of transition.[9] However, for these fits a parabolic behavior of the highest valence band and the lowest conduction band (or equivalently a $\sqrt{E}$ behavior of the density of states at the band edges) is assumed, which is clearly not the case in iron pyrite. Nevertheless, in Fig. 7.10 $(\alpha\omega)^n$ is displayed within the energy range of the tail of peak A from 0.7 to 1.9 eV for $n = 1/2$ assuming an allowed indirect transition and $n = 1/3$ assuming a forbidden indirect transition for the optical band gap, as it is also done in the reference [34]. The curves show a pronounced non-linear behavior, which is most probably caused by the non-parabolic behavior of the localized Fe $3d$ states at the band edges. It is not quite clear how to apply a linear regression to these curves, since there are three distinct regions per curve, which all show a more or less

[9] Since I will not focus on the determination of the optical band gap using these fits beyond this and the next chapter, I refer the interested reader to the reference [34] and the references within for more details about the theory. I would like also to point out that no indirect transitions are considered in the calculated optical absorption, and thus these fits are solely used to investigate their effect on the tail of the absorption.

linear behavior, as it is indicated in the figure. Probably it is most consistent to perform a linear regression to the low-intensity tail for the small energies leading to an optical band gap of about 0.8 eV for $n = 1/2$ and 0.75 eV for $n = 1/3$. This low-intensity tail comprises of mostly Fe $3d$-Fe $3d$ and Fe $3d$-S $3p$ transitions (not shown). However, due to the difference in the magnitude of the optical absorption between the tail and peak A, it might be very difficult to measure the "correct" optical band gap in iron pyrite. Thus, not only the fundamental band gap might be smaller than the size of the optical band gap in iron pyrite due to suppressed or even forbidden transitions between the states at the band edges, but also the measured size of the optical band gap might be larger than the correct optical band gap due to the low intensity of the tail. Hence, optical measurements might be not able to obtain the limiting band gap in iron pyrite, which determines the maximally obtainable open-circuit voltage.

Using the optimized structural parameters of iron pyrite does not significantly change the position of the first peak (not shown), since the energy gap between the Fe $3d$ states at the band edges is not very different (cf. Fig. 7.3). The position of the peak B is slightly shifted to lower transition energies due to the smaller bonding anti-bonding splitting of the S $3p$ states. Therefore, it is sufficient to only compare the optical absorption calculated within the structural parameters from experiment with the literature.

A comparison of the calculated optical absorption to the literature [33, 34, 138, 139] reveals that there are two major peaks in the optical absorption for energies lower than 6 eV and that the position of the first peak is reported to be at about 2.1-2.2 eV, which is in quite good agreement with the result in this thesis. The peak position of the second peak deviates from the result in the thesis (3.6 eV), but also the reported values of the three references are different with values ranging from about 4.0-4.7 eV. Hence, the calculated position of peak B is located at smaller transition energies than the experimentally measured one. However, it is not clear how much this peak might be influenced by excitonic effects, which are not included in the calculations. The optical absorption is reported to have maximal values of about 5-$7 \cdot 10^5$ cm^{-1} in the range of visible light, and thus the calculated optical absorption is about 70% larger. It might be that defects in the material lead to a reduction of the experimentally measured optical absorption. The optical band gap has been determined to about 0.9-1.2 eV in the references. The problem of applying the linear regression to curves showing non-linear behavior due to the non-parabolicity of the states at the band edges in iron pyrite has been also discussed in [34]. In addition, the low-intensity tail of the optical absorption due to the small dipole matrix elements of the transitions between Fe $3d$ and S $3p$ states might be interpreted in an optical experiment purely as an effect caused by defects in the material, and thus the optical band gap might be actually smaller. For instance the linear curve fitting in [34] has been not applied to the linear regime of the lowest transition energies at about 0.7-1 eV, which is interpreted to originate from defects, but to the linear regime at larger transition energies. However, I still observe those low-intensity contributions from Fe $3d$-S $3p$ transitions for these low energies in pristine iron pyrite. A similar argument has been also reported in a recent theoretical investigation by Lazić *et al.* [26].

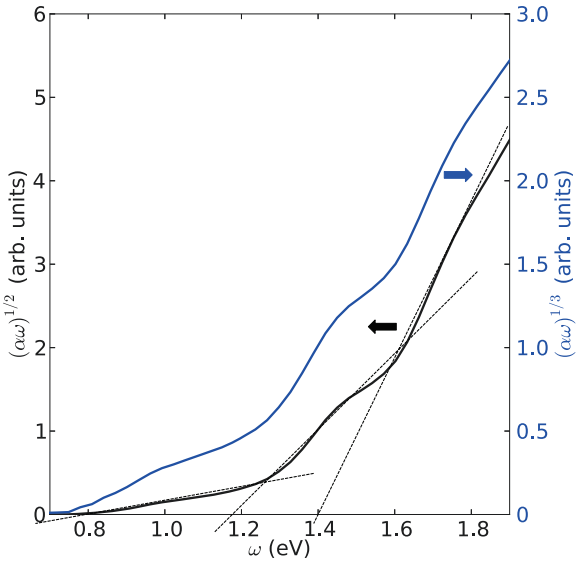

Figure 7.10.: The tail of the optical absorption of Fig. 7.9 in the range of 0.7 to 1.9 eV has been examined in case of an allowed indirect transition ($n = 1/2$, black curve) and in case of a forbidden indirect transition ($n = 1/3$, blue curve) for the optical band gap as it is presented in the reference [34]. The left y-axis corresponds to the black curve, whereas the right y-axis is valid for the blue curve. For the case of $n = 1/2$ linear fits are indicated for the three distinct regions of pronounced linear behavior by the thin, dashed black lines.

DFT+U Since the DFT+U method yields a fundamental band gap size of 0.90 eV (cf. Fig. 7.7), and thus leads to nice agreement to the reported measured band gap of 0.95 eV, it is interesting to also investigate the optical absorption calculated within the DFT+U method using $U_{\text{eff}} = 2.4$ eV (see Fig. 7.11).[10] It exhibits also two major peaks and the composition and the absolute values of the optical absorption from the orbital-resolved contributions is similar to the plain GGA-PBE result. However, the position of the first major peak (and also the tail of the first peak, which is not shown magnified here, and thus is barely visible) is shifted by about 0.3-0.4 eV to a larger energy with 2.5 ± 0.2 eV compared to the plain GGA-PBE result and the experimentally determined position. This shift directly corresponds to the enhanced energy gap between the Fe $3d$ t_{2g} and e_g states due to the inclusion of the Hubbard-U (cf. Fig. 7.7). The second major peak is slightly shifted to larger energies, now located at about 3.8 ± 0.2 eV. From the shift of the first

[10] For the calculation of the optical absorption within DFT+U only a 10×10×10 $\boldsymbol{k}$-mesh has been used, instead of the 20×20×20 for plain GGA-PBE. However, already a 10×10×10 $\boldsymbol{k}$-mesh is sufficiently dense to predict the positions of the two major peaks.

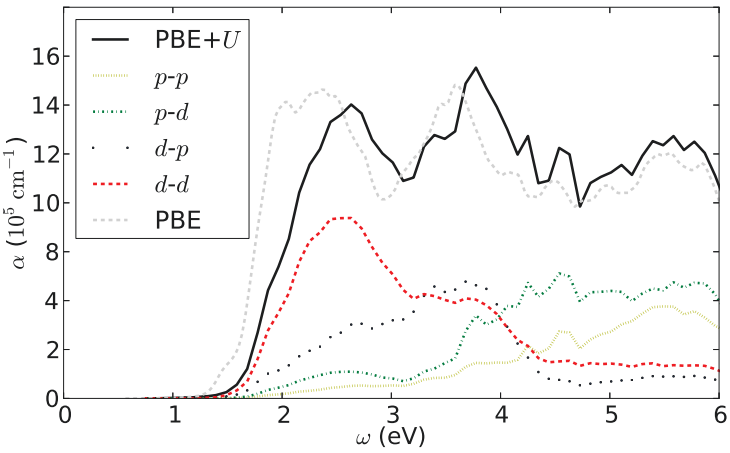

Figure 7.11.: The optical absorption of iron pyrite for the structural parameters from experiment within the DFT+U method using $U_{\text{eff}} = 2.4$ eV for photon energies up to 6 eV. The DFT+U method has been applied to a GGA-PBE calculation. The total optical absorption (black solid) comprises of the Fe $3d$-Fe $3d$ (red dashed), the Fe $3d$-S $3p$ (blue dotted), the S $3p$-Fe $3d$ (green dashed-dotted) and the S $3p$-S $3p$ (yellow striped) orbital contributions to the optical absorption. The optical absorption of the plain GGA-PBE calculation is displayed for comparison (gray dashed curve).

peak, it seems the DFT+U method is not suited to describe the optical properties of iron pyrite, and the excellent agreement between the measured band gap and the calculated one might be a deception. It might be that the experimentally determined band gap is larger than the fundamental band gap, and even the measured optical band gap might be overestimated due to the low-intensity contributions, as stated previously, and thus the fundamental band gap can not be easily compared to the size of the optically measured band gap. Hence, the DFT+U method might even not capture the right electronic band structure.

For completeness let me mention that the optical absorption within the hybrid functionals leads to completely different peak positions as compared to the experiment due to the strong overestimation of the energy gap between the Fe $3d$ t_{2g} and e_g states, and thus the electronic band structure as well as the optical properties of iron pyrite are not captured by hybrid functionals.

Dielectric Function The dielectric function $\epsilon(\omega)$ is closely related to the optical absorption $\alpha(\omega)$,[11] and since there are a couple of references, which report about $\epsilon(\omega)$, instead

[11] The optical absorption can be calculated from the dielectric function via the following equation: $\frac{\omega}{cn}\text{Im}\left(\epsilon(\omega)\right)$. The dielectric function describes the (linear) response of the system to an electric field.

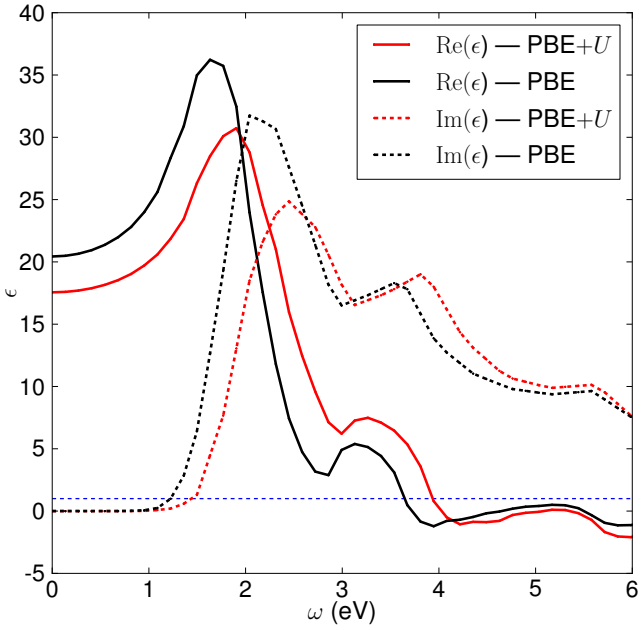

Figure 7.12.: The dielectric function $\epsilon(\omega)$ of iron pyrite depending on the energy $\hbar\omega$ ($\hbar$ is omitted in the figure) and calculated within GGA-PBE (black curves) and DFT+U (red curves) using the structural parameters from experiment is shown. The real part $\mathrm{Re}\,(\epsilon)$ is presented as solid curve, whereas the imaginary part $\mathrm{Im}\,(\epsilon)$ is displayed as dashed curve. The blue dashed line indicates the vacuum dielectric constant of 1.

of $\alpha(\omega)$, for iron pyrite, I present the results on the dielectric function calculated within GGA-PBE and DFT+U in Fig. 7.12.

The dielectric function is a complex quantity, where the real part $\mathrm{Re}\,(\epsilon)$ is related to a stored energy in the medium exposed to an electric field, whereas the imaginary part $\mathrm{Im}\,(\epsilon)$ describes the energy dissipation via absorption. Both quantities are related to each other via the Kramers-Kronig relation, and thus only one component needs to be calculated directly from DFT. The real part of the dielectric function for $\omega = 0$ corresponds to the static dielectric function, which is calculated to be about 20 within GGA-PBE and 17 within DFT+U. The imaginary part of the dielectric function is closely related to the optical absorption, and thus there are also two major peaks, one at about 2 eV and another one at about 3.5 eV. The peaks are also shifted by 0.3-0.4 eV for the DFT+U result compared to plain GGA-PBE.

Since the light wave exposes the material to an external, oscillating electric field, there is a close connection between α and ϵ.

A comparison with a recent publication reporting about the dielectric function experimentally measured and calculated via DFT within GGA-PBE yields a very nice agreement [36]. They report also that the critical points of the dielectric function are considerably shifted using DFT+U, leading to a worse agreement with experiment. The peak positions and their orbital decomposition reported in this thesis correspond nicely to results predicted by Vadkhiya *et al.* [140] and Antonov *et al.* [141]. An experimental study by Schlegel *et al.* [142] reports the two major peaks of the dielectric function to be located at around 1.7-1.8 eV and 3.7-3.9 eV, respectively, which is in reasonable agreement to the reported values of Suga *et al.* [143] with 1.6-1.8 eV and 3.9-4.1 eV.[12] Again, the location of the first peak is in nice agreement with the theoretical predictions, whereas the second peak is a bit off. In all mentioned references the static dielectric constant $\epsilon(\omega = 0)$ is reported to be about 20, which matches the calculated value in this thesis.

7.8. Conclusions

The electronic structure and the optical properties of iron pyrite have been examined within DFT using the local exchange-correlation functionals LDA and GGA-PBE, as well as more sophisticated hybrid functionals and the DFT+U method. The results have been also compared to the literature, leading to an overall nice agreement.

The electronic structure of iron pyrite can be understood easily in terms of the geometrical structure, since a complex hybridization between Fe $3d$ states and S $3p$ states is formed around the Fermi energy due to the crystal field splitting of the Fe $3d$ states and the bonding anti-bonding splitting of the S $3p$ states caused by the octahedral symmetry and the covalent bonding of the S atoms in the S dimers, respectively. The fundamental band gap has a size of about 0.6 eV within GGA-PBE and is defined by a VBM exhibiting a strong Fe $3d$ t_{2g} orbital character and a CBM comprised of pure S $3p$ orbital character. This has eminent consequences on the dependence of the band gap on the Wyckoff parameter u, which controls the distance of the S atoms in the S dimer, and for the optical absorption. The first one can be explained due to the dependence of the bonding anti-bonding splitting on the Wyckoff parameter, leading to smaller band gap sizes for smaller u. For instance the band gap size is about 0.4 eV for the optimized structural parameters, although u changes only 0.5% compared to the structural parameters from experiment. That explains also the large deviations in the reported band gap results from computations [29, 45–50] and from experiments [34], which might be caused by slight differences of a few percent in u. The difference in u for different crystals is most probably not related to intrinsic defects, since the formation energy for these defects is reported to be quite large [17]. This is unlike the situation in CuIn(S,Se)$_2$, where a strong dependence of the band gap on the internal parameter is observed, which on the other hand is strongly influenced by the Cu vacancy concentration in the material [144].

The band gap size depends also significantly on the choice of the exchange-correlation functional, where the local functionals LDA and GGA-PBE predict a band gap size, which

[12] Since the references do not report the exact value of the peaks, but rather show figures of the dielectric function, these values have been estimated by eye from the figures.

is about 35% smaller than the experimentally determined one. However, regarding only the absolute difference of the band gaps, the agreement can be identified as surprisingly good, since the local functionals usually tend to a large underestimation also in terms of the absolute value of the band gap. The more sophisticated hybrid functionals yield drastically overestimated band gap sizes, which are about 150-200% larger than the experimental value. A possible explanation of this behavior is presented in the chapter 10. The DFT+U method for $U_{\text{eff}} = 2.4$ eV yields with about 0.9 eV the best result for the band gap compared to the experiment.

However, where the optical absorption within GGA-PBE is in nice agreement with experiment, the optical absorption within DFT+U is considerably worse. The optical absorption consists of two major peaks within the range of transition energies up to 6 eV, one located at about 2.1 eV and the second at 3.5 eV, whereas these values are shifted by 0.3-0.5 eV to larger energies within DFT+U. The first peak is caused mainly by transitions between Fe $3d$ t_{2g} and Fe $3d$ e_g states and the second peak comprises of Fe $3d$ t_{2g} and S $3p$ transitions. The orbital composition of the first peak is quite surprising, since the band edges in iron pyrite are of Fe $3d$ character at the valence bands and S $3p$ character at the conduction states, and thus one might expect a large optical absorption for low energies coming from Fe $3d$-S $3p$ transitions. However, the wave functions of the highest valence states are quite localized at the Fe atoms, whereas the wave functions of the lowest conduction p state is located almost entirely on the S atoms, leading to small dipole matrix elements. The first peak is in very nice agreement to experiment [34, 138, 139], whereas the second peak is shifted by about 0.5 eV to smaller energies, which might change if excitonic effects were included in the calculations.

The tail of the optical absorption at the first peak determines the size of the optical band gap and most of the experimentally determined band gaps of iron pyrite are based on optical measurements. Interestingly, the tail is quite long exhibiting a quite untypical behavior due to the non-parabolic valence states in iron pyrite, the Fe $3d$-S $3p$ transitions become more eminent and the magnitude of the optical absorption is much smaller compared to the magnitude of the peaks. Therefore, it might be that optical experiments measure the energy gap between the Fe $3d$ states at the band edges instead of the optically suppressed Fe $3d$-S $3p$ transitions, and thus the "real" optical band gap might be smaller. In addition, the transitions along $\Gamma \rightarrow X$ between the VBM and the CBM exhibit even zero dipole matrix elements, which might lead even to a considerable difference between the fundamental and the optical band gap in iron pyrite.

Hence, optical experiments might not obtain the limiting band gap of iron pyrite for photovoltaic applications. A smaller band gap as the measured one could be a quite natural explanation for the low open-circuit voltage in iron pyrite solar cells. A more detailed discussion about a possible interpretation of the characteristic photovoltaic quantities of iron pyrite by comparing to the results of this thesis follows in the next chapter in the context of the GW calculations.

8. Iron Pyrite Bulk within GW

8.1. Introduction

Essential to the GW approximation is the introduction of an electrostatic screening, *i.e.* an electron is screened by an oppositely charged Coulomb hole reducing the effective charge of this electron, which then leads to a screened Coulomb interaction between the electrons instead of a bare Coulomb interaction. Therefore, since there are quasiparticles that can be added or removed, GW describes the physics of a (inverse) photoemission experiment, and thus this usually leads to an improvement of the calculated band gap sizes compared to "conventional" DFT. More details about the theory and the most important characteristic quantities have been presented in chapter 4.

As discussed in the previous chapter, the fundamental band gap of iron pyrite calculated within DFT strongly depends on the choice of the exchange-correlation functional. Due to the special orbital character of the corresponding band edges, it might be that the optical experiments do not obtain the "real" band gap, which limits the photovoltaic performance of an iron pyrite solar cell. Thus, it is quite interesting to investigate iron pyrite within the GW approximation, which is known for a reliable band gap prediction for a wide range of materials.

The GW calculations are classified into single-shot GW calculations on top of a DFT calculation (denoted as G_0W_0@DFT) and a quasiparticle selfconsistent GW (QSGW) approach. First the electronic structure and the optical properties of iron pyrite are investigated within G_0W_0@PBE. Then the starting-point dependence of G_0W_0 in the case of iron pyrite is investigated, which is followed by results on the (almost) starting-point independent QSGW calculations.

Some of the presented results in this chapter are already published in [25].

8.2. Computational Details

In GW calculations usually much more effort is needed to converge the results compared to "conventional" DFT calculations, since in GW also a reasonably accurate description of the unoccupied energy spectrum and wave functions is necessary. For some systems many electronic bands might be needed for the calculation, which demands for large plane-wave cutoff parameters $k_{\max}$, large angular momentum cutoffs $l_{\max}$ as well as the inclusion of many higher-energy local orbitals. In addition the inclusion of semicore states as local orbitals (LOs) into the LAPW basis is essential to not only avoid "ghost bands" in the occupied energy spectrum, but also to improve the unoccupied spectrum.

For the GW calculations the SPEX code [69] has been employed and the FLEUR code [66] has been used to obtain the starting point for the GW approximation. A plane-wave cutoff of $k_{\max} = 6.0$ a.u.$^{-1}$ and an angular momentum cutoff $l_{\max} = 12$ has been used. Although it is a considerably large value for $k_{\max}$, the LAPW basis shows no problems with linear dependencies yet. The problematic behavior starts not before using values of about 6.5 a.u.$^{-1}$. To reduce the linearization error of the FLAPW method in the unoccupied energy spectrum five full sets of s, p, d and f states as local orbitals (LOs) have been used per Fe and S atom, *i.e.* 80 additional basis functions per atom entered the FLAPW calculation via higher-energy LOs.

The convergence with the number of bands is presented in Fig. 8.1. First of all, it is surprising that about 2000-3000 bands are necessary to obtain a converged result for the transitions at the band edges from $\Gamma \to \Gamma$ (black diamonds), $X \to \Gamma$ (green squares), and $R \to \Gamma$ (red pentagons). A difference of 0.1-0.2 eV between using 800 bands and 3000 bands seems not to be very large, however, note that the energy of the transitions is quite small, and thus the relative differences are rather large with changes of almost 100% of the size in some cases. Interestingly, the convergence with the number of bands is much faster for the transitions exhibiting the same orbital character at the band edges, here for $X \to X$ (blue dots) with Fe $3d$ character, whereas it is much slower for transitions from Γ, X and R to Γ, for which the orbital character is Fe $3d$ for the valence band and S $3p$ for the conduction band. The faster convergence for $X \to X$ might be caused by an error cancellation, since bands of same orbital character experience a comparable treatment within GW, and thus systematic errors might compensate in the difference of the energies. Similar observations regarding the convergence behavior have been reported for ZnO, in which a large number of bands is needed due to a band transition of bands with different orbital character and a strong hybridization between these orbitals [101, 102].

The Fe $3s$ and $3p$ semicore states have to be included as LOs into the LAPW basis. The left panel and right panel of Fig. 8.1 show the convergence of the band transitions for the case, where they have been included into the basis (left) or they remain in the core (right). The behavior of convergence is quite similar, except that it is much smoother when the Fe $3s$ and $3p$ states are treated as LOs. However, the energy of the transitions including a change in orbital character is quite different with about 0.3 eV difference, whereas the transition from $X \to X$ exhibits again much smaller changes of only 0.05 eV. The experience shows that the inclusion of semicore states into the basis is much more important in GW (and for orbital-dependent functionals) compared to "conventional" DFT and usually it leads to improved results [136, 145–148]. Hence, the results presented in this chapter include the Fe $3s$ and $3p$ semicore states into the basis.

The required computational time of a GW calculation within the SPEX code scales quadratically with the number of $\boldsymbol{k}$-points and not linear like in "conventional" DFT calculations within FLEUR, and thus "only" a $4\times4\times4$ $\boldsymbol{k}$-mesh is used for the GW calculations. As already stated in the appendix D this $\boldsymbol{k}$-mesh is sufficient to provide converged results. A test calculation with a $6\times6\times6$ $\boldsymbol{k}$-mesh within the GW approximation yielded no significant change of the results.

The situation is different for the calculation of the optical absorption, where much more $\boldsymbol{k}$-points are needed to have a sufficiently large number of transitions. For the

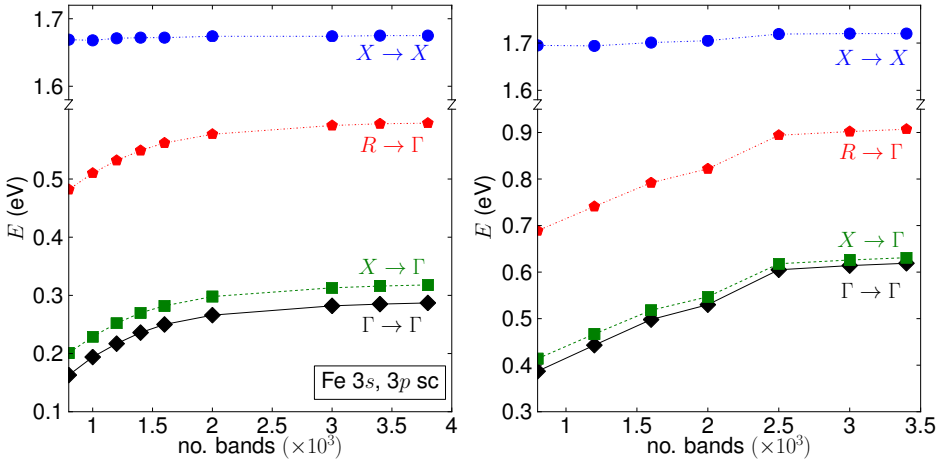

Figure 8.1.: The convergence of the transition energies of iron pyrite between the band edges for the transitions $\Gamma \to \Gamma$ (black diamonds), $X \to \Gamma$ (green squares), $R \to \Gamma$ (red pentagons), and $X \to X$ (blue circles) depending on the number of electronic bands using G_0W_0@PBE is presented. The structural parameters from experiment have been used. The left panel shows the results including the Fe $3s$ and $3p$ semicore states as LOs into the LAPW basis, whereas they have been not included in the results displayed in the right panel.

"conventional" DFT calculations at least a 10×10×10 $\boldsymbol{k}$-mesh has been used, which is computationally not feasible for GW. Hence, also there the $\boldsymbol{k}$-mesh has been restricted to 4×4×4, which might be underconverged.

8.3. Electronic Structure within G_0W_0@PBE

The electronic band structure calculated within G_0W_0@PBE using the structural parameters from experiment is presented in Fig. 8.2. The $\boldsymbol{k}$-path $R \to \Gamma \to X'$ has been used, since it contains the band edges defining the fundamental band gap in GGA-PBE as well as in GW. Most remarkable is the reduction of the size of the fundamental band gap from 0.62 eV within GGA-PBE to 0.27 eV within G_0W_0@PBE. The experience has shown that for most semiconductors and insulators the local exchange-correlation functional predicts too small fundamental band gap sizes, which then is remedied within GW by enlarging the band gap size. However, this is only a rule of thumb and not a strict rule. I will present a possible explanation of this atypical behavior in chapter 10, which is connected to the large screening in iron pyrite (and related compounds).

The shape of the bands is only slightly modified by GW with the largest change being the effective mass of the parabolic band at the CBM changing from about $0.48\ m_e$ in GGA-PBE to $0.68\ m_e$ after applying GW. Therefore, the electronic mobility is about 50%

larger within GW.[1] The valence bands of iron pyrite become slightly more flat within GW, which changes the $\boldsymbol{k}$-point at the valence band defining the fundamental band gap from a point close to X to a point nearby Γ along Γ-X. The orbital character of the electronic bands is unchanged compared to the GGA-PBE result, since only the diagonal elements of the exchange-correlation potential in representation of the Kohn-Sham wave functions have been used.[2] Thus, the fundamental band gap becomes smaller within GW, because the S $3p$ band at the conduction band edge around Γ drops down relative to the position of the Fe $3d$ states. To be more precise, the Fe $3d$ states located at the valence band edge and at the conduction band edge are both shifted upwards about 0.3-0.5 eV by the quasiparticle correction, whereas the S $3p$ band around Γ is only slightly shifted upwards by about 0.1 eV, and thus in total the fundamental band gap becomes smaller.

The transition energies for the transitions $\Gamma \rightarrow \Gamma$, $X \rightarrow \Gamma$, $R \rightarrow \Gamma$ and $X \rightarrow X$ using GGA-PBE, and G_0W_0@PBE with and without including the Fe $3s$ and $3p$ semicore states as LOs into the basis, are listed in the Table 8.1. The transition $X \rightarrow X$ between Fe $3d$ states is only slightly increased from 1.62 eV to 1.67 eV. But then, the transitions from the highest valence band to the CBM at Γ become all significantly smaller by about 0.3 eV. The quasiparticle energy corrections of the Fe $3d$ states are quite sensitive to numerical parameters like the number of bands or LOs, in contrast to the corrections for the S $3p$ band, which are insensitive to these numerical parameters. For instance there is a significant difference in the transition energies including Γ depending on the treatment of the Fe $3s$ and $3p$ semicore states, which can be as large as about 0.3 eV. The quite strong dependence of the size of the fundamental band gap on the Wyckoff parameter u is also observed in the GW results. Using the optimized structural parameters of iron pyrite ($a = 5.40$ Å and $u = 0.383$) leads to an almost metallic system with a band gap size of less than 0.1 eV when applying GW on top of GGA-PBE.

The unconventional reduction of the band gap size in iron pyrite within G_0W_0@PBE has been already briefly reported in the literature. Both Sun *et al.* and Choi *et al.* report a band gap size of about 0.4 eV after applying GW to the GGA-PBE result [29, 36]. However, no further details like the electronic band structure or a convergence analysis of the GW results are presented. As I have demonstrated in the previous section the convergence of the GW results for iron pyrite can be rather elaborate.

8.4. Optical Absorption

The optical absorption of iron pyrite calculated according to appendix B within G_0W_0@PBE is presented in Fig. 8.3. Since it is unfeasible to perform a GW calculation for iron pyrite

[1] The effective mass has been estimated in an experiment to be about $0.45\ m_e$ using the peaks in the optical absorption [149]. However, the error on this value might be quite large, since the estimation used approaches assuming a parabolic band behavior of the conduction and valence bands in iron pyrite.

[2] Using furthermore the non-diagonal matrix elements of the exchange-correlation potential $\langle\phi_i|V_{\mathrm{xc}}|\phi_j\rangle$ in representation of the Kohn-Sham wave functions ϕ_i within G_0W_0 allows a change of the wave functions. A test calculation yielded no significant changes of the electronic band structure of iron pyrite at the high-symmetry $\boldsymbol{k}$-points compared to the results presented in Fig. 8.2.

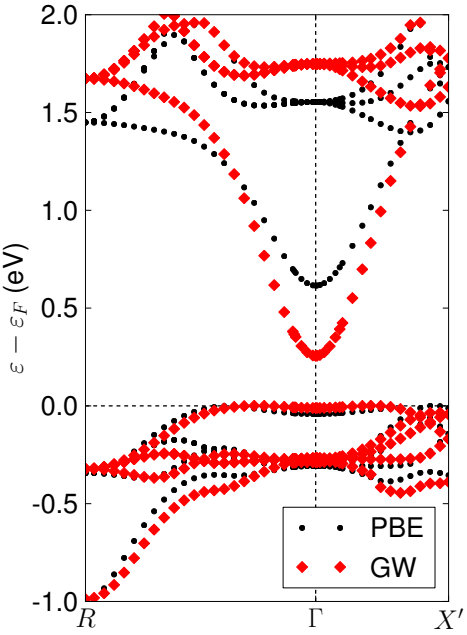

Figure 8.2.: The electronic band structure of iron pyrite calculated within single-shot GW on top of GGA-PBE using the structural parameters from experiment is indicated as red diamonds, whereas the plain GGA-PBE band structure is shown as black dots.

	$\Gamma \to \Gamma$	$X \to \Gamma$	$R \to \Gamma$	$X \to X$
GGA-PBE	0.66	0.63	0.96	1.62
G_0W_0 (w)	0.28	0.31	0.59	1.67
G_0W_0 (w/o)	0.61	0.63	0.90	1.72

Table 8.1.: The transitions energies of the transitions $\Gamma \to \Gamma$, $X \to \Gamma$, $R \to \Gamma$ and $X \to X$ for iron pyrite within GGA-PBE and single-shot GW on top of GGA-PBE (G_0W_0@PBE) are listed. The G_0W_0 calculations have been carried out with (w) and without (w/o) the inclusion of the Fe $3s$ and Fe $3p$ semicore states as local orbitals into the LAPW basis to evaluate the numerical sensitivity. Iron pyrite with the structural parameters from experiment has been used.

with a more dense $\boldsymbol{k}$-mesh than 4×4×4, the optical absorption of GW might be not fully converged. For comparison the optical absorption calculated within GGA-PBE for a 4×4×4 and 20×20×20 $\boldsymbol{k}$-mesh is displayed, showing some differences in particular for the second major peak. There are some additional peaks in the optical absorption for the coarse $\boldsymbol{k}$-mesh, which become much smaller using the dense $\boldsymbol{k}$-mesh. However, the position of the first peak is more or less already correctly predicted within the coarse 4×4×4 $\boldsymbol{k}$-mesh. Note that since the single-shot GW approach does not alter the wave functions, the only difference between the optical absorption of the GW and the DFT calculation arises from the difference in the band energies. The slightly increased energy gap between the Fe $3d$ states at the band edges is the reason of the slight shift of the first major peak by less than 0.1 eV compared to the GGA-PBE result. The considerably shifted S $3p$ band at the bottom of the conduction bands leads to a shift of about 0.5 eV of the second major peak, which then slightly overlaps with the first peak, and leaving a large dip in the absorption where the second peak has been located within GGA-PBE. However, the role of excitonic effects, which are not included in our calculations, are not clear. The tail of the optical absorption comprises of Fe $3d$-Fe $3d$ transitions and Fe $3d$-S $3p$ transitions, where the latter become more dominant for the smaller transition energies (*cf.* Fig. 7.10). Now the tail is more extended due to the shift of the S $3p$ band.

There might be still a problem to distinguish in optical experiments the low intensity contributions of the tail from defects, and thus the measured optical band gap might be overestimated. Experiments might measure the energy gap between the Fe $3d$ states instead, which is quite similar to the GGA-PBE results. Hence, regarding the optical band gap and the position of the first major peak, also the GW results of iron pyrite are in nice agreement with the experimental findings (in difference to the DFT+U results, see previous chapter), and neither GGA-PBE nor GW can be preferred for the calculation of iron pyrite.

8.5. Starting-Point Dependence of the GW Results

The single-shot GW approach suffers of a starting-point dependence, which has already been extensively discussed in the literature [58–60, 103]. The distinctiveness of the starting-point dependence is quite material-dependent, and thus I investigate the starting-point dependence of G_0W_0 for iron pyrite in this section. A systematical approach involves the DFT+U method, since it allows relatively easy and in a controllable way to realize different starting points by changing the Hubbard parameter U_{eff}. The hybrid functional HSE06 has also been used as a starting point. Finally, I briefly discuss also the results for iron pyrite using the quasiparticle selfconsistent GW (QSGW) approach, which is (almost) starting-point independent.

G_0W_0@DFT In Fig. 8.4 the energy of the transitions $\Gamma \rightarrow \Gamma$ (includes a change in orbital character), $X \rightarrow X$ (transition between two Fe $3d$ states) and the fundamental band gap are displayed using DFT+U and G_0W_0@PBE+U for U_{eff} between 0 and 4 eV. The fundamental band gap has only been calculated within DFT+U by determining the

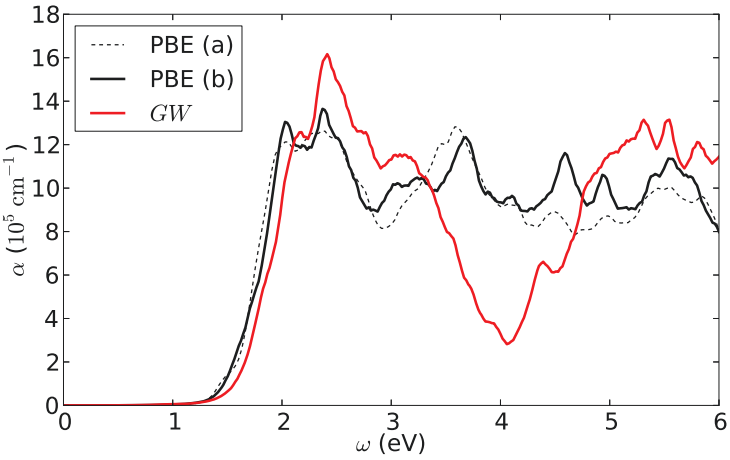

Figure 8.3.: The optical absorption of iron pyrite for the structural parameters from experiment calculated within GGA-PBE (black curves) and G_0W_0@PBE (red curve). For comparison two calculations within GGA-PBE are displayed, one using a 20×20×20 $\boldsymbol{k}$-mesh like in Fig. 7.9 denoted as (a) and another calculation using a 4×4×4 $\boldsymbol{k}$-mesh (as it is used for the GW calculation), denoted as (b). For the calculations with the 4×4×4 $\boldsymbol{k}$-meshs a tetrahedron method has been exploited.

smallest energy gap at the band edges in the electronic band structure. The orbital-resolved band structures for $U_{\text{eff}} = 0$, 2, 3 and 4 eV are presented in the appendix F. There it can be observed that the orbital character of the band structures does not significantly change when applying the Hubbard U correction. However, a more detailed analysis of the orbital contributions yields, that the upmost valence band is almost Fe 3d pure for smaller Hubbard U parameters, whereas it comprises of Fe 3d orbital character and a considerable contribution from S 3p for Hubbard U parameters larger than about 3.0 eV, due to an exchange of bands. The shape of the bands changes slightly due to these changes in the orbital hybridization, and thus a change from an indirect to a direct fundamental band gap is observed when using $U_{\text{eff}} \geq 3$ eV. That explains why the fundamental band gap and the direct transition $\Gamma \rightarrow \Gamma$ have the same values in Fig. 8.4 for $U_{\text{eff}} = 3$ and 4 eV. Note that the fully-localized limit has been used for the double counting in DFT+U, in difference to the results of the previous chapter, and thus the fundamental band gap for $U_{\text{eff}} = 2.4$ eV is slightly smaller here. However, the choice of double counting for DFT+U has no influence on the behavior of the starting-point dependence of the G_0W_0@PBE+U calculations of iron pyrite.

Overall, there is a linear dependence between the energy gaps and U_{eff} for a large interval of values for U_{eff}. Only for values U_{eff} larger than 2.5-3 eV a saturation effect is observable. As already observed for plain DFT, the application of G_0W_0 decreases the

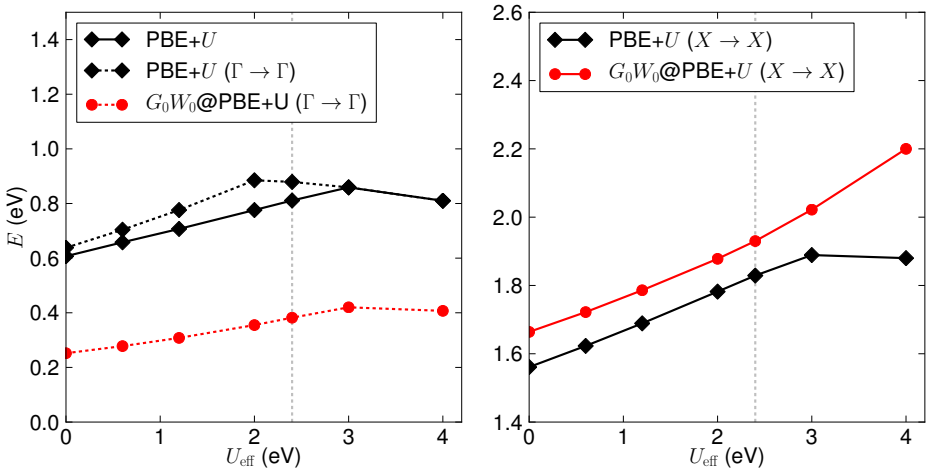

Figure 8.4.: The starting-point dependence of the G_0W_0 approach for iron pyrite using the structural parameters from experiment is represented by exploiting the results of DFT+U for different Hubbard parameters U_{eff} as starting points. In the left panel the fundamental band gap calculated within DFT+U using the GGA-PBE functional (solid black curve), the energy of the transition $\Gamma \to \Gamma$ within DFT+U (dashed black curve) and G_0W_0@PBE+U (dashed red curve) are displayed. In the right panel the energy of the transition $X \to X$ is shown for the DFT+U (solid black curve) and G_0W_0@PBE+U calculation (solid red curve). The gray dashed line indicates the results for $U_{\text{eff}} = 2.4$ eV, which is the U value calculated within constrained RPA, and which has been used in the previous chapter. All these transition energies (including the band gap) are denoted as E in the y-axis label.

energy gap of the transition $\Gamma \to \Gamma$ for all investigated values of U_{eff}. The behavior of the transition energy depending on the Hubbard U parameter remains also linear when applying G_0W_0, but it exhibits a less steep gradient. For the transition $X \to X$ the G_0W_0 approach yields slightly larger transition energies than DFT+U and the linear dependence exhibits a quite similar gradient. Overall, the G_0W_0 approach is starting-point dependent for iron pyrite, however, the dependence is smaller or at least comparable to the changes within the different DFT approaches. For the DFT+U method using different values for U the $\Gamma \to \Gamma$ transition energy ranges only from about 0.25 to 0.35 eV and the energy of the transition $X \to X$ changes from about 1.6 to 2 eV within the linear regime.

For completeness let me mention that a G_0W_0 calculation on top of the hybrid functional HSE06 has been also executed, yielding a value of about 1.7 eV for the transition at the band edges of Γ, which is smaller than the 2.2 eV calculated within HSE06.[3] However,

[3]For the HSE06 and G_0W_0@HSE06 calculation the Fe $3s$ and Fe $3p$ semicore states have been not treated as LOs in the LAPW basis.

a value of 1.7 eV is still much too large compared to experiment and the HSE06 result seems not to be a proper starting point for the G_0W_0 calculation.

Quasiparticle Selfconsistent GW The quasiparticle selfconsistent GW (QSGW) approach [61] is (almost) starting-point independent, and thus it is interesting to compare the G_0W_0 results of iron pyrite to those calculated within QSGW.[4] The QSGW approach is an iterative method, in which a mean-field potential calculated from the self energy of the GW calculation is inserted into the DFT calculation in each step.[5] In Fig. 8.5 the energy of the transitions from the states at the band edges at Γ and X is displayed for the first three iterations within QSGW. Additionally, the energy gap between the S $3pp\pi^*$ and Fe $3d$ t_{2g} states (located at about -2.0 and -1.5 eV, respectively, in Fig. 7.2) is investigated.

The zeroth iteration within QSGW corresponds to the G_0W_0@PBE calculations discussed previously, but with the difference that the non-diagonal elements of the exchange-correlation matrix in representation of the Kohn-Sham orbitals have been also considered. There is almost no difference between these G_0W_0 results and those treating only the diagonal elements, as it can be seen by comparing the results in Fig. 8.5 and Table 8.1. Interestingly, the QSGW results for iron pyrite are already converged after the first iteration, and thus the first iteration exhibits quite large changes for the energy gaps. In particular the transition energy of $\Gamma \rightarrow \Gamma$ at the band edges considerably changes from about 0.3 eV within G_0W_0 to 0.9 eV in the QSGW approach. But also the other transitions exhibit evident changes: the energy gap between the Fe $3d$ states at the band edges is increased from about 1.7 eV in G_0W_0 to 1.9 eV and the energy gap between the S $3pp\pi^*$ and Fe $3d$ t_{2g} states is decreased from 2.3 to 2.0 eV. Thus, the Fe $3d$ states are mainly pushed apart from each other, which leads to the larger fundamental band gap. Actually, these results are quite similar to the DFT+U calculation using the Hubbard U of 2.4 eV determined via constrained RPA (*cf.* Fig. 7.7), and thus the major effect of the QSGW calculation on iron pyrite seems to be the consideration of the correlation of the Fe $3d$ states. The mean-field potential entering the DFT calculation in each iteration seems to be essentially altered by the GW calculations in a manner comparable to DFT+U.

Like the DFT+U result also the fundamental band gap of QSGW is in very nice agreement to the 0.95 eV observed by experiment. However, also for QSGW the optical absorption is most probably worse than the GGA-PBE result when comparing to the experiment, since the energy gaps between the Fe $3d$ t_{2g} and Fe $3d$ e_g states at the band edges defining the first major peak in the optical absorption are considerably shifted within QSGW. These energy gaps with about 1.9 eV are even predicted to be larger than in DFT+U with 1.8 eV, which might even worsen the optical spectrum. Note that no optical absorption has been calculated for iron pyrite using QSGW, since it has been unfeasible to use a proper size for the $\boldsymbol{k}$-mesh, and thus the the discussion about the agreement of the optical absorption with experiment are pure assumptions. However, there is a report about

[4] The QSGW method is computationally quite demanding, therefore the $\boldsymbol{k}$-mesh for these calculations has been chosen to be 2×2×2.

[5] The brief basics about QSGW have been already discussed in chapter 4.

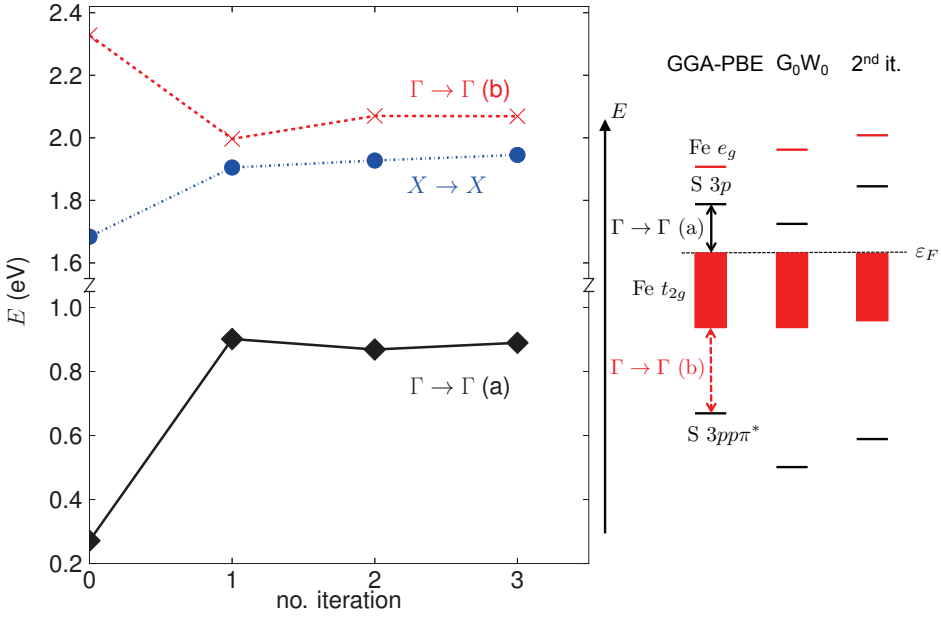

Figure 8.5.: The energies for the transitions at the band edges at Γ (solid black curve, denoted as $\Gamma \rightarrow \Gamma$ (a)) and X (dashed-dotted blue curve) as well as the energy gap between the S $3pp\pi^*$ and Fe $3d$ t_{2g} states at Γ (dashed red curve, denoted as $\Gamma \rightarrow \Gamma$ (b)) are shown for iron pyrite for the first three iterations within the selfconsistent GW approach. The zeroth iteration corresponds to the single-shot G_0W_0@PBE calculation, except that also the non-diagonal exchange-correlation matrix elements in representation of the Kohn-Sham orbitals are treated. The structural parameters from experiment have been used. In the right panel a sketch of the positions of the Fe t_{2g} and e_g band edges, the S $3p$ band defining the CBM and the highest S $3pp\pi^*$ state at Γ is displayed for the GGA-PBE, G_0W_0 (zeroth iteration) and QSGW (second iteration) results.

the electronic band structure calculated within QSGW, in which the fundamental band gap is reported to be 0.81 eV and the transition energy of the band edges at X is about 1.8-1.9 eV [63], which are both in good agreement with the QSGW results of this thesis. The band structure looks quite similar to the DFT+U band structure in Fig. 7.7, and thus the assumptions on the optical absorption within QSGW do not seem to be far-fetched.

The large difference in the results for iron pyrite using QSGW or G_0W_0@PBE are rather surprising, in particular since G_0W_0@PBE decreases the size of the fundamental band gap compared to the GGA-PBE result, whereas QSGW increases the result. Unfortunately, there has been no time any more to search for the reason in detail, and a more fundamental analysis is beyond the scope of this thesis. Hence, I can only speculate at this point. Maybe the difference is related to a significant change in orbital-character caused by the GW corrections, which does not appear yet after applying GW once, but only for an iterative approach. The similarity between the DFT+U and QSGW result indicates that the (strong) localization of the Fe $3d$ states might be treated considerably different in a selfconsistent scheme compared to the single-shot approach. Since the fundamental band gap size calculated within QSGW coincides with the experimentally measured gap, one might prefer and favor the QSGW over the single-shot results. However, apart of the arguments about the optical absorption, note that the fundamental band gaps of simple semiconductors (and many more not so simple compounds, without referring to them) are usually very well described within G_0W_0@DFT, often almost on top of the experimentally measured band gaps, whereas QSGW tends to a slight to moderate overestimation of these gaps. I present a couple of results for simple semiconductors in appendix A to back up this statement.

8.6. Conclusions

The electronic band structure and the optical properties of iron pyrite within the single-shot GW approach and the quasiparticle selfconsistent GW (QSGW) method have been discussed in this chapter.

The convergence of the GW calculations for iron pyrite is much more subtle compared to the "conventional" DFT calculations discussed in the previous chapter. Many higher-energy local orbitals (LOs), a large plane-wave cutoff, and angular momentum cutoff as well as 2000-3000 electronic bands need to be used to converge the results, and thus the calculations are computationally quite demanding. In addition, the inclusion of the Fe $3s$ and Fe $3p$ semicore states as LOs into the FLAPW basis is essential. In particular for the fundamental band gap the convergence is subtle due to the different orbital character of the VBM and CBM, whereas the convergence of the energy gap between the Fe $3d$ states profits from an error cancellation. It is quite unconventional that the G_0W_0@PBE calculation decreases the fundamental band gap of iron pyrite from about 0.6 eV to about 0.3 eV. The energy gap between the band edges at X is only slightly increased, and thus the optical absorption calculated within G_0W_0@PBE looks quite similar compared to the plain GGA-PBE result, and both are in satisfactory agreement with the experimentally measured optical absorption.

Since the optical absorption exhibits a quite long low-intensity tail comprised of the transitions between the Fe $3d$ t_{2g} and Fe $3d$ e_g states, and Fe $3d$ t_{2g} to S $3p$ transitions, where the latter transitions become more eminent for lower transition energies, it might be that experiments measure not the "real" optical band gap of iron pyrite, but the energy gap between the Fe $3d$ states, which dominate the first major peak in the absorption. The low-intensity tail might be interpreted as being caused by defects only. The fundamental band gap might be even smaller than the optical band gap, since the optical transitions between Fe $3d$ t_{2g} and S $3p$ are suppressed.

Such a small fundamental band gap like 0.3 eV as calculated within G_0W_0@PBE would have dramatic consequences for photovoltaic applications. The open-circuit voltage of maximally 0.2 V in iron pyrite [13] might be explained by a small fundamental band gap, which can hardly be detected in experiments. The large intrinsic charge carrier densities of 10^{14}-10^{18} cm^{-3} in undoped pyrite [14, 27] and an activation energy of 0.2 eV in temperature-dependent electrical resistivity measurements [37, 38] might be also caused by a small band gap. The long low-intensity absorption tail observed in the optical absorption experiments [34, 138, 139] might not only arise due to defects, but the Fe $3d$ to S $3p$ transitions might be the reason for it. If the disappointing performance of iron pyrite solar cells were based on the electronic structure of pristine pyrite, a reduction of defects and precipitates would be the wrong approach.

However, a small fundamental band gap in pristine iron pyrite would not automatically exclude iron pyrite as photovoltaic material, since there are two approaches, which might increase the gap. The aim is to shift the S $3p$ band at the CBM upwards, and as it has been discussed in the previous chapter, a smaller distance of the S atoms in the S dimer, *i.e.* a larger Wyckoff parameter u, increases the splitting between the S $pp\sigma$ states, and thus increases also the size of the gap. Hence, applying stress to FeS_2 pyrite might be a remedy, although it is not clear in which way stress influences the other bondings. The second approach, which might increase the gap size is the doping with O as substitutional defect for S. The wave functions are more localized on the O atoms leading to a reduction of the band width of the $pp\sigma^*$ states. Hu *et al.* report of a band gap opening of 0.2-0.3 eV using oxygen doping concentrations of 12.5% in iron pyrite in their DFT calculations [31]. However, the achievable oxygen doping concentrations in experiment might be quite small and it is not clear how stable the doped compounds are.

To conclude the size of the fundamental band gap in iron pyrite needs a thorough reexamination both in experiment and theory. This might be a quite difficult task, since the low-intensity contributions in the optical absorption, the untypical shape of the electronic bands far from parabolic behavior, and the small contribution of the S $3p$ state at the band edge at Γ in the density of states, display a challenge for experiments, like optical experiments, (inverse) photoemission spectroscopy or scanning tunneling microscopy. The theory still has to understand the extraordinary large deviations of the predicted band gap of iron pyrite for different exchange-correlation functionals and the large difference between the results using the G_0W_0@PBE and QSGW method. In the next two chapters I will investigate a couple of pyrite compounds and marcasite compounds, which are closely related in structure to the pyrites, and by this I speculate about the atypical behavior in DFT and GW calculations.

9. FeS_2 Marcasite: The undesired Phase?

9.1. Introduction

The FeS_2 marcasite compound is structurally closely related to iron pyrite and is observed to coexist with it under certain conditions [24]. The suitability of iron marcasite for photovoltaic applications is thus of large interest. In addition, similarities between the electronic structure of the marcasite phase and the pyrite phase are expected, and thus it might be that more systems exhibit the unconventional behavior of iron pyrite when applying hybrid functionals or the GW approximation.

The band gap of FeS_2 marcasite has been reported to be only 0.34 eV in a reference from the year 1980 using electrical resistivity measurements [32]. Since then, for a long time there have been no further investigations on iron marcasite regarding the suitability for photovoltaic applications to my knowledge, and the marcasite phase has been considered to be improper for photovoltaic applications. However, a quite recent study combining optical absorption experiments with DFT calculations indicates that FeS_2 marcasite might have a comparable absorption and an at least as large band gap as compared to iron pyrite [33], which is reported to have a 0.95 eV band gap.

Thus, in this chapter I approach the question whether FeS_2 marcasite really is an undesired phase for photovoltaic applications. Some of the results presented in this chapter are already published in the literature [25].

9.2. The Marcasite Structure

The unit cell of iron marcasite is diplayed in Fig. 9.1. It is orthorombic and it contains 2 Fe atoms and 4 S atoms. Similar to the pyrite structure the marcasite structure is characterized by S dimers and an (almost) octahedral coordination of the S atoms around the Fe atoms. In contrast to the pyrite structure, where the octahedrons share their corners, here they share their edges. Each S atom is tetrahedrally surrounded by 3 Fe atoms and one additional S atom, with which it forms a S dimer bond. The orthorombic unit cell is described via the three lattice parameters a, b and c, and the internal parameters u and v, which define the positions of the S atoms in the unit cell. The positions of the basis atoms in Bravais representation and units of (a, b, c) are as follows, with Fe^i ($i = 1, .., 2$) and S^j ($j = 1, .., 4$) denoting the Fe and S atoms in the unit cell:

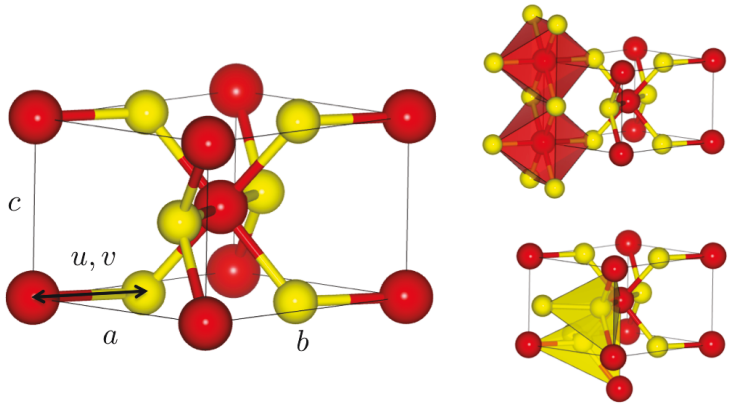

Figure 9.1.: The iron marcasite structure with the S atoms indicated as yellow spheres and the Fe atoms shown as red spheres. The lattice parameters a, b and c define the size of the orthorombic unit cell and the internal parameters u and v determine the positions of the S atoms within the cell. In the right panel the (almost) octahedral and tetrahedral surroundings of the Fe and S atoms are presented. The characteristic S dimers are clearly visible in the tetrahedrons. This figure has been created with the program VESTA [130].

$$\begin{aligned} \boldsymbol{B}_{\mathrm{Fe}^1} &= (0,0,0), & \boldsymbol{B}_{\mathrm{Fe}^2} &= (\tfrac{1}{2},\tfrac{1}{2},\tfrac{1}{2}), \\ \boldsymbol{B}_{\mathrm{S}^1} &= (u,v,0), & \boldsymbol{B}_{\mathrm{S}^2} &= (-u,-v,0), \\ \boldsymbol{B}_{\mathrm{S}^3} &= (\tfrac{1}{2}+u,\tfrac{1}{2}-v,\tfrac{1}{2}), & \boldsymbol{B}_{\mathrm{S}^4} &= (-\tfrac{1}{2}-u,v-\tfrac{1}{2},\tfrac{1}{2}). \end{aligned} \tag{9.1}$$

The distance between the S atoms in the S dimer depends on the internal parameters u and v via

$$d_{\mathrm{S-S}} = \sqrt{4u^2a^2 + (1-2v)^2b^2}. \tag{9.2}$$

The internal parameters have a strong influence on the electronic structure as it is also the case in iron pyrite.

The structural parameters from experiment with $a = 4.443$ Å , $b = 5.424$ Å and $c = 3.387$ Å for the lattice parameters and the internal parameters $u = 0.200$ and $v = 0.378$ have been used [150, 151]. A structural optimization within the GGA-PBE functional has also been conducted, yielding $a = 4.446$ Å , $b = 5.429$ Å , $c = 3.391$ Å ,$u = 0.206$ and $v = 0.375$. The optimized lattice parameters are in good agreement to the parameters from experiment, exhibiting only about 0.3% deviation for the volume of the unit cell. In difference to chapter 7 no particular section is devoted to the structural optimization of iron marcasite in this thesis. A few details about it will be presented in the next section about the computational details.

9.3. Computational Details

The DFT calculations have been performed using the GGA-PBE functional. With a plane-wave cutoff $k_{\max} = 3.9$ a.u.$^{-1}$, an angular momentum cutoff $l_{\max} = 8$ for both the Fe and S atoms, muffin tin radii of $R_{\mathrm{MT}}^{\mathrm{Fe}} = 2.12$ a.u. and $R_{\mathrm{MT}}^{\mathrm{S}} = 2.04$ a.u., and a 10×8×14 $\boldsymbol{k}$-mesh corresponding to 140 $\boldsymbol{k}$-points in the irreducible Brillouin zone, the calculations have been sufficiently converged. The inclusion of semicore states as local orbitals (LOs) or higher-energy LOs has no significant influence on the results, and thus they are not considered for the DFT calculations of FeS_2 marcasite.

The G_0W_0@PBE calculations have been performed using a plane-wave cutoff $k_{\max} = 7.0$ a.u.$^{-1}$, an angular momentum cutoff $l_{\max} = 12$ and a 4×4×4 $\boldsymbol{k}$-mesh.[1] The plane-wave cutoff is still small enough to avoid numerical problems with linear dependencies in the LAPW basis, but it allows to account for up to 2000 electronic bands in the GW calculation. The convergence of the transition energies with respect to the number of electronic bands behaves similar to iron pyrite (not shown). Again it is essential to include the Fe $3s$ and Fe $3p$ semicore states as LOs into the LAPW basis, as well as to use five full sets of s, p, d and f higher-energy LOs to avoid "ghost bands" in the unoccupied energy spectrum and to reduce the linearization error, respectively.

The determination of the optimized structural parameters using the GGA-PBE functional is more complicated for marcasite than for pyrite, since five parameters need to be optimized instead of two. First, the volume abc of the unit cell has been optimized by varying the lattice constant a, but keeping the ratio b/a and c/a as measured in experiment. Then for a couple of volumes, including the optimized value the ratio b/a, has been varied. There the lattice constant a is taken from the volume optimization, b is varied and c is changed accordingly to keep the volume fixed. In a next step, the volume of the unit cell for which the smallest total energy has been obtained in the b/a optimization is fixed and the b/a-ratio is varied for a couple of lattice constants a. In the last step the optimized set of structural parameters a, b/a, and c, which led to the smallest total energy, is used as input for a structural relaxation to obtain the optimized values for u and v. For the structural relaxation forces have been converged up to the order 10^{-4} Htr/a.u. and for the minimization of the positions a Broyden-Fletcher-Goldfarb-Shanno algorithm has been exploited.

The optical absorption of iron marcasite has been calculated using the scheme as explained in appendix B. A 16×12×20 $\boldsymbol{k}$-mesh leading to 693 $\boldsymbol{k}$-points in the irreducible wedge of the Brillouin zone guarantees convergence. For the Fe $3d$-Fe $3d$, Fe $3d$-S $3p$, S $3p$-Fe $3d$ and S $3p$-S $3p$ orbital-resolved optical absorption the factors 21, 69, 70 and 148 have been obtained by minimizing the difference to the total optical absorption. A smearing of 50 meV for the Lorentzian functions has been used for the optical absorption presented in Fig. 9.4, whereas a tetrahedron method has been employed for calculating the tail of the absorption presented in Fig. 9.5, which allows for an accurate determination of the onset of the conduction band and the size of the optical band gap.

[1] A 5×4×6 $\boldsymbol{k}$-mesh would have been more suitable, regarding the ratio of the lattice constants. However, a 4×4×4 $\boldsymbol{k}$-mesh yields sufficiently converged results for iron marcasite within GW.

The iron marcasite structure belongs to the $Pnnm$ group, and thus exhibits 8 symmetries, including the inversion-symmetry.

9.4. Electronic Structure: DFT Results

The electronic band structure of iron marcasite shows an interplay between the bonding and anti-bonding S $3s$ and $3p$ states arising from the covalent bonds in the S dimers and the crystal-field splitting into Fe $3d$ t_{2g} and Fe $3d$ e_g states caused by the octahedral symmetry of the structure. The hybridization between the S $3p$ and Fe $3d$ states is quite incisive around the Fermi energy, and thus the main features of the electronic structure are similar to iron pyrite. Since a detailed discussion about the connection of the geometry of the iron pyrite structure and its electronic structure has been presented in chapter 7, and there is nothing new in the case of iron marcasite, I will focus on the electronic structure close-by around the Fermi energy only.

In Fig. 9.2 the orbital-resolved electronic structure of iron marcasite around the Fermi energy is displayed. The band structure in the left panel is for the structural parameters from experiment, whereas the optimized structural parameters are used in the band structure of the right panel. The difference in the lattice parameters a, b and c has no significant influence on the electronic structure, but the differences in the internal parameters u and v lead to significant changes in the electronic structure, since they determine the distance of the S atoms in the S dimer via eq. (9.2) like in pyrite, although the relative differences of the parameters are only a few percent. The orbital character of the electronic bands at the band edges is mainly dominated by Fe $3d$ character. The valence bands are quite flat, whereas the conduction bands show slightly more dispersion. In the conduction bands the S $3p$ character becomes evident around the high-symmetry $\boldsymbol{k}$-points U, Y and in particular at the lowest conduction band at Γ. Hence, the orbital character resembles those of iron pyrite, with the difference, that the conduction band minimum (CBM) is not located at Γ in the marcasite.

The fundamental band gap in iron marcasite is defined between the valence band maximum (VBM) at a $\boldsymbol{k}$-point close to X and the CBM at T. It is 0.80 eV and both band edges are dominated by Fe $3d$ character, whereas the fundamental band gap in iron pyrite has been between bands of different orbital character. However, like in iron pyrite the direct transition at Γ in iron marcasite is between an Fe $3d$ rich state and a S $3p$ state, exhibiting a considerably larger transition energy with 1.76 eV than the fundamental band gap. The direct transition at Γ shows also the delicate dependence on the internal parameters. Using the optimized structural parameters decreases the direct transition at Γ to 1.55 eV, whereas the size of the fundamental band gap is almost unchanged. The decrease of the gap size is caused by the larger distance of the S atoms in the S dimer for the optimized structural setup.

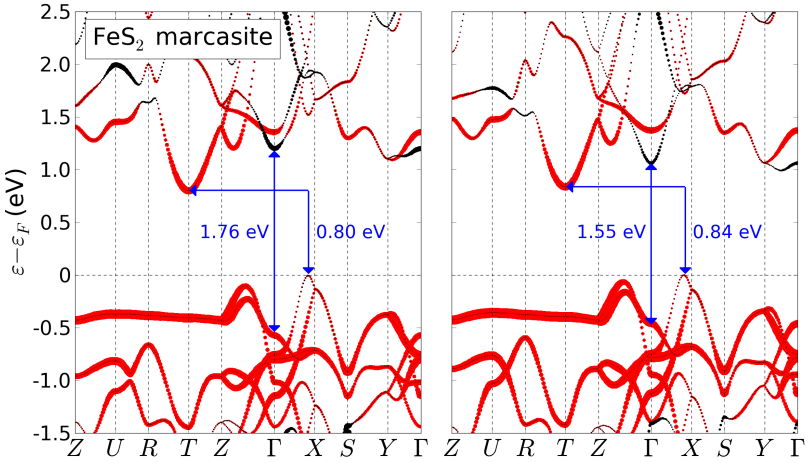

Figure 9.2.: The orbital-resolved band structure of iron marcasite is presented for the structural parameters from experiment in the left panel and for the optimized structural parameters in the right panel. The calculations have been done within the GGA-PBE functional. The red color indicates Fe $3d$ orbital contributions, whereas the S $3p$ character is displayed in black color. The size of the points correlates to the size of the corresponding orbital character. The high-symmetry $\boldsymbol{k}$-points of the $\boldsymbol{k}$-path are denoted according to the notation of Bradley and Cracknell [131]. The direct band transition at Γ and the smallest indirect transition, *i.e.* the fundamental band gap, are indicated as blue arrows.

9.5. Electronic Structure: GW Results

In Fig. 9.3 the electronic band structure of FeS_2 marcasite calculated within single-shot GW on top of the GGA-PBE result is presented. In addition, the plain GGA-PBE result is shown for comparison. The following discussion is supported by the table 9.1 listing the transition energies for the transitions $\Gamma \rightarrow \Gamma$, $X \rightarrow \Gamma$, $R \rightarrow \Gamma$ and $X \rightarrow T$.

The GW corrections of the Kohn-Sham energies are rather comparable to those of iron pyrite, and thus the Fe $3d$ states at the band edges are considerably shifted, whereas the S $3p$ state at Γ is only slightly corrected. Overall this leads to larger energy gaps between the band edges, which are dominated by Fe $3d$ orbital character, but the transition energies to Γ become smaller. Within GGA-PBE the fundamental band gap is located between a $\boldsymbol{k}$-point close to X and T. The energy of the transition between X and T is increased from 0.95 eV to 1.40 eV after applying GW. Since additionally the S $3p$ band at Γ drops down, the fundamental band gap is now between the VBM at a $\boldsymbol{k}$-point close to Z and the CBM at Γ with a size of 1.06 eV within GW (see Fig. 9.3), and thus interestingly not only the size of the fundamental band gap is altered, but also its character is changed.

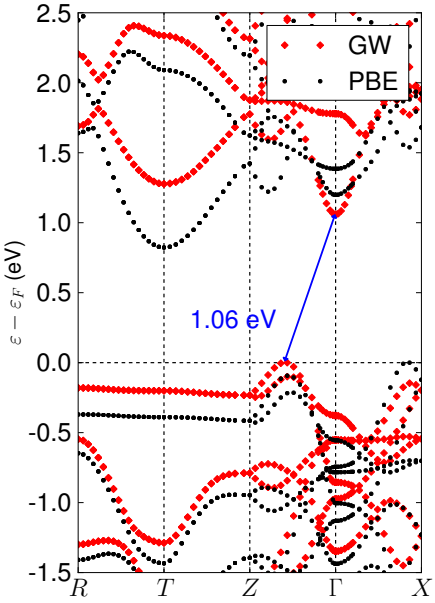

Figure 9.3.: The electronic band structure of iron marcasite using the structural parameters from experiment within GGA-PBE (black dots) and G_0W_0@PBE (red diamonds) is displayed. The blue arrow indicates the fundamental band gap predicted by the GW calculation.

If we focus only on the size of the fundamental band gap, the GW approximation behaves quite typical increasing the band gap from 0.80 eV to 1.06 eV. However, the more detailed analysis presented in the previous paragraph revealed that the GW results of iron marcasite have a lot in common with the GW results of iron pyrite presented in the last chapter. In both cases the energy gap between Fe $3d$ states at the band edges is increased, whereas the energy gap between the S $3p$ and Fe $3d$ states is reduced. In addition, the treatment of the Fe $3s$ and Fe $3p$ semicore states as local orbitals is crucial, in particular to describe the transitions between the bands of different orbital character, which exhibit changes in the transition energies of about 0.5 eV for the different treatments.

9.6. Optical Absorption

In Fig. 9.4 the optical absorption of iron marcasite calculated within the GGA-PBE functional is presented. In addition, the optical absorption is decomposed into the orbital-contributions from the Fe $3d$-Fe $3d$ (red dashed), Fe $3d$-S $3p$ (blue dotted), S $3p$-Fe $3d$ (green dashed-dotted) and S $3p$-S $3p$ (yellow striped) transitions, which are the dominant transitions up to a photon energy of 6 eV.

	$\Gamma \to \Gamma$	$X \to \Gamma$	$R \to \Gamma$	$X \to T$
GGA-PBE	1.76	1.32	1.57	0.95
G_0W_0 (w)	1.40	1.19	1.21	1.40
G_0W_0 (w/o)	1.88	1.57	1.72	1.25

Table 9.1.: The energies of the transitions $\Gamma \to \Gamma$, $X \to \Gamma$, $R \to \Gamma$ and $X \to T$ for iron marcasite within GGA-PBE and G_0W_0@PBE are listed. The G_0W_0 calculations have been carried out with (w) and without (w/o) the inclusion of the Fe $3s$ and Fe $3p$ semicore states as local orbitals into the LAPW basis to evaluate the numerical sensitivity. The structural parameters from experiment have been used.

The optical absorption is comparable in size to iron pyrite with maximal values of about $14 \cdot 10^5$ cm^{-1}. There are plenty of peaks in the optical absorption, but I will only focus on the two major peaks A and B, one located at about 1.3 eV and the other at about 2.5 eV. The main contribution to these two peaks comes from the Fe $3d$-Fe $3d$ transitions, however there is also a significant contribution from the Fe $3d$-S $3p$ transitions and S $3p$-Fe $3d$ transitions. The optical absorption for photon energies between 3.5 to 6 eV is dominated by S $3p$-Fe $3d$ transitions and to a smaller extent by S $3p$-S $3p$ transitions.

The sum of the four orbital-decomposed contributions exhibits some deviations compared to the total optical absorption. A smearing for the Lorentzian functions with a full width at half maximum of 50 meV has been used for all curves. The difference between the total absorption and $\sum \alpha_{\mu\nu}(\omega)$ seems to be caused by additional orbital contributions to the optical absorption, which are quite featureless in the energy range up to 6 eV, but lead to an overall smoother optical absorption. Interestingly, the agreement between the sum of the four orbital-decomposed optical absorptions and the total optical absorption is excellent for iron pyrite (*cf.* Fig. B.2). An explanation of these results might be the following: Since the orbital-decomposed absorption is calculated via joint density of states (see appendix B), the Fe $3d$ states are strongly filtered by this method due to the large contribution to the DOS in iron pyrite and marcasite. In iron pyrite the band edges are quite flat and are strongly dominated by Fe $3d$ states, which applies only to a lesser extent to iron marcasite. Thus, it might be that the optical absorption within the energy range up to 6 eV comprises solely of the joint density of states of the Fe $3d$ transitions to a good approximation for iron pyrite, but not for iron marcasite.

The low energy tail of the absorption is dominated by Fe $3d$-Fe $3d$ transition, which is expected, since the band edges of iron marcasite are dominated by Fe $3d$ states. In difference to iron pyrite no significant contribution from Fe $3d$-S $3p$ transitions can be observed in the tail. In Fig. 9.5 $(\alpha\omega)^n$ is plotted within the energy range from 1.0-1.3 eV, where the tail of the absorption is located. An exponent of $n = 1/2$ assumes an indirect allowed transition of the optical band gap, whereas $n = 1/3$ assumes a forbidden indirect transition. The artificial broadening of the Lorentzian functions in the calculation of the optical absorption makes it difficult to determine the absorption edge for iron marcasite (not shown), and thus a tetrahedron method has been used for the results in Fig. 9.5,

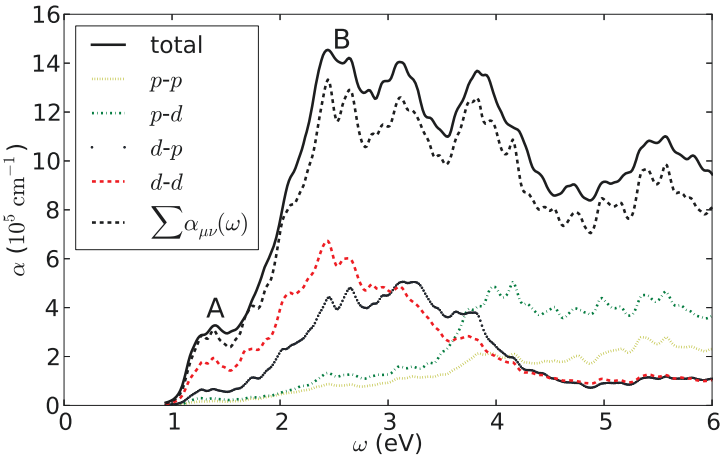

Figure 9.4.: The optical absorption of iron marcasite calculated within GGA-PBE and using the structural parameters from experiment is displayed for photon energies up to 6 eV by the black solid line. The orbital decomposition of the optical absorption into transitions between Fe $3d$-Fe $3d$ (red dashed), Fe $3d$-S $3p$ (blue dotted), S $3p$-Fe $3d$ (green dashed-dotted) and S $3p$-S $3p$ (yellow striped) is also shown. The factors for the orbital-decomposed contributions (*cf.* appendix B) have been determined to 21, 69, 70 and 148, respectively. For comparison the sum of the orbital-decomposed contributions using these factors is presented as black dashed curve (labeled $\sum \alpha_{\mu\nu}(\omega)$). The first two major peaks are denoted as A and B.

instead.[2] Note that no low-intensity contributions are present in the tail of the absorption, leading to a clearly defined absorption edge at about 1.1 eV, and thus there are no problems in determining the optical band gap by linear interpolation schemes. It is about 1.1 eV for both cases assuming an indirect allowed or forbidden transition. On the other hand, note that in iron pyrite the absorption edge could not be simply identified due to the low-intensity d-p contributions (see Fig. 7.10).[3]

[2]Note that there have been still some unsolved minor numerical problems in the tetrahedron method, just before submission of this thesis, regarding the agreement between the integral over the absorption using the tetrahedron method and the approach using Lorentzian functions. Hence, the results on the tail of the optical absorption might exhibit slight inconsistencies compared to those in Fig. 9.4. However, the peak positions and slopes are in nice qualitative agreement, and thus the determined optical band gap should be sufficiently accurate (0.1 eV accuracy).

[3]The clear absorption edge in iron marcasite is not only a result of employing the tetrahedron method, but also results from missing low-intensity contributions. In the case of iron pyrite for both, the tetrahedron method, and the approach using Lorentzian functions, the optical absorption exhibits a low-intensity tail, which makes it hard to determine an optical band gap. Since the tetrahedron method exhibits minor numerical problems (see above), I refrained from presenting results for the optical absorption using this method, wherever possible, and thus the absorption tail of iron pyrite in

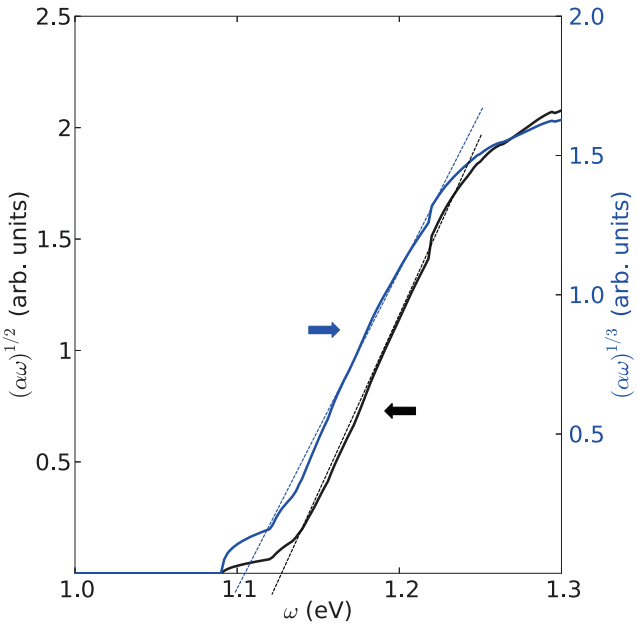

Figure 9.5.: The tail of the optical absorption of iron marcasite in the range of 1.0 to 1.3 eV has been examined in case of an allowed indirect transition ($n = 1/2$, black curve) and in case of a forbidden indirect transition ($n = 1/3$, blue curve) for the optical band gap. The left y-axis corresponds to the black curve, whereas the right y-axis is valid for the blue curve. The linear fits indicate the relevant band edges for the determination of the optical band gaps from the two curves.

A comparison with literature reveals a reasonable agreement for the major peak positions of the optical absorption of iron marcasite [33], however, the size of the optical absorption is smaller with about $5 \cdot 10^5$ cm^{-1}. Note that the samples used in this reference are not phase-pure, but only a 50% marcasite content in volume could be realized.

9.7. Conclusions

The electronic structure and the optical absorption of iron marcasite have been investigated in this chapter using DFT within the GGA-PBE functional and single-shot GW on top of the DFT result.

The octahedral symmetry and the covalent bond of the S atoms in the S dimers of the marcasite structure determine the electronic structure of iron marcasite. The band

Fig. 7.10 is calculated using the Lorentzian functions.

edges around the Fermi energy are dominated by Fe $3d$ states, but there is a significant hybridization with S $3p$ around some high-symmetry points. In particular at Γ there is a S $3p$ rich conduction band as it is also the case in iron pyrite. The fundamental band gap is 0.80 eV within GGA-PBE, it is indirect and it is located between a $\boldsymbol{k}$-point close to X (VBM) and at T (CBM). The orbital character of the VBM and CBM is in both cases Fe $3d$. When applying G_0W_0@PBE, the energy gaps between the Fe $3d$ states at the band edges are considerably increased, leading not only to a change of the size of the fundamental band gap but also its character. The fundamental band gap calculated within G_0W_0@PBE to 1.06 eV is located between the VBM at a $\boldsymbol{k}$-point close to Z exhibiting Fe $3d$ character and the CBM at Γ with S $3p$ character, and thus the band gap is between states of different orbital character like in iron pyrite.

The optical absorption of iron marcasite is dominated by Fe $3d$-Fe $3d$ transitions for the lower photon energies, and in difference to the absorption in iron pyrite, there are no significant low-intensity contributions from Fe $3d$-S $3p$ transitions for the lower energies. Thus, the tail allows a much simpler determination of the size of the optical band gap compared to the case in iron pyrite. The optical band gap is about 1.1 eV, and thus 0.3 eV larger than the fundamental band gap. Note that these results have been only calculated using the GGA-PBE functional, and a low-intensity tail in the optical absorption might be present using the G_0W_0@PBE result, since then the fundamental band gap is defined between Fe $3d$ and S $3p$ states instead.

The optical absorption of iron marcasite is comparable in amplitude to the absorption of iron pyrite. Since both, for GGA-PBE and GW, the fundamental band gap is sufficiently large, FeS_2 marcasite qualifies for photovoltaic applications from the theoretical point of view. In the quite recent literature, there are indications of a strong optical absorption and an at least as large band gap size as in iron pyrite also in experiment [33].

However, iron marcasite is reported to be thermodynamically less stable compared to iron pyrite [152], which might pose problems for photovoltaic applications.[4] Additionally, there is not much known about the role of defects for the photovoltaic performance of iron marcasite yet to my knowledge.

To conclude the iron marcasite phase seems to deserve a thorough examination of its suitability for photovoltaic applications, and hopefully there will be more experimental and theoretical investigations on this phase in the near future.

[4] The GGA-PBE functional predicts the iron marcasite phase to be more stable with 20 meV/f.u., which is a quite small energy difference, and thus this might explain the frequently observed coexistence of those two phases. However, the thermodynamic stability of marcasite and pyrite depends on the choice of exchange-correlation functional as it is reported in [29].

10. The Electronic Structure of other Pyrite and Marcasite Compounds

10.1. Introduction

The results on the band gap size of iron pyrite and iron marcasite in the chapters 7, 8 and 9 are quite remarkable. The hybrid functionals lead to a drastic overestimation of the band gap size in iron pyrite compared to the experimental value. Furthermore, even more surprising, the application of the more sophisticated G_0W_0 method yields an unconventional reduction of the energy gap between the Fe $3d$ and S $3p$ states at the band edges in iron pyrite and iron marcasite, leading even to a significant reduction of the band gap size compared to the GGA-PBE result in pyrite. According to common experience a "conventional" DFT calculation underestimates the band gap size of semiconductors, which then is usually remedied by the G_0W_0 approach and in some cases by the application of the HSE functional. However, the example of FeS_2 shows that this is not a strict rule.

In this chapter I would like to shed some light on this peculiar behavior by investigating a couple of pyrite and marcasite compounds. This is achieved by comparing the electronic structures of these compounds, and thus validate the influence of the geometrical structure, the electronic filling or the localization of bands. The isoelectronic pyrite compounds FeS_2, RuS_2, OsS_2 and NiP_2 are investigated as well as ZnS_2 in the pyrite structure with two more electrons per Zn atom. For the marcasites, the isoelectronic structures FeS_2, $FeSe_2$ and $FeTe_2$ have been used. For all these compounds "conventional" DFT, the HSE06 functional and G_0W_0@PBE are compared.

The focus in this chapter lies on the investigation of the band gaps within those methods and less on the application for photovoltaics. Though, knowing the size of the band gaps allows to choose a first selection of suitable materials for photovoltaics, detailed investigations of the optical absorption or of the occurring surfaces as it is done for iron pyrite in this thesis are necessary for a thorough discussion of the photovoltaic performance.

10.2. Computational Details

In table 10.1 the structural parameters of the investigated pyrite and marcasite compounds are listed. In the case of the simple cubic pyrite structure this are the lattice constant a and the Wyckoff parameter u (see Fig. 7.1), and for the orthorombic marcasite structures the lattice constants a, b and c, and the internal parameters u and v (see Fig. 9.1) are

		a	b	c	u	v	Ref.
Pyrites	FeS_2	5.418	5.418	5.418	0.385	-	[51]
	RuS_2	5.610	5.610	5.610	0.388	-	[153]
	OsS_2	5.620	5.620	5.620	0.387	-	[153]
	NiP_2	5.471	5.471	5.471	0.388	-	[154]
	ZnS_2	5.954	5.954	5.954	0.401	-	[45]
Marcasites	FeS_2	4.443	5.424	3.387	0.200	0.378	[150, 151]
	$FeSe_2$	4.804	5.784	3.586	0.213	0.369	[155]
	$FeTe_2$	5.266	6.268	3.874	0.224	0.362	[150]

Table 10.1.: The structural parameters for the pyrite compounds FeS_2, RuS_2, OsS_2, NiP_2, ZnS_2 and for the marcasite compounds FeS_2, $FeSe_2$ and $FeTe_2$ are listed. The pyrite and marcasite structure are displayed in Fig. 7.1 and 9.1, respectively. For the pyrite compounds the lattice parameter a (a=b=c) and the Wyckoff parameter u are needed, and for the marcasite compounds the lattice parameters a, b and c, and the internal parameters u and v are presented. The lattice parameters are all in units of Å. All the structural parameters are from experiments and the corresponding references are listed in the last column.

listed. The parameters are taken from experiments with the references listed in the table as well.

The "conventional" DFT calculations have been performed using the FLEUR code [66] within the GGA-PBE functional. The numerical parameters are quite similar to those used for the iron pyrite and iron marcasite compound (see chapter 7 and 9). The values for the plane-wave cutoffs $k_{\max}$, the muffin tin radii R_{MT} and the angular momentum cutoffs $l_{\max}$ are listed in table 10.2. Since there are small differences in the muffin tin radii depending on the compound, and as a rule of thumb $k_{\max}R_{\mathrm{MT}} \approx l_{\max}$ is used, the plane-wave cutoff ranges from about 3.9-4.2 a.u.$^{-1}$ for the pyrites, and 3.3-3.9 a.u.$^{-1}$ for the marcasite compounds. The $\boldsymbol{k}$-mesh has been chosen to 4×4×4 for all systems, which is sufficient for convergence, as already discussed in appendix D. No semicore states have been included as local orbitals into the LAPW basis for the "conventional" DFT calculations, neither have higher-energy local orbitals been included.

For the calculations using the hybrid functional HSE06 the same numerical parameters have been used as for the GGA-PBE calculations. The number of electronic bands considered in the computation has been at least 10-times the number of electrons, *i.e.* 800 bands for all pyrite compounds, except ZnS_2 with 960 bands, and 400 bands for the marcasites.

For the single-shot GW calculations on top of the GGA-PBE results computed within the SPEX code [69] the convergence is very subtle as already discussed for iron pyrite and iron marcasite in the previous chapters. Hence, the plane-wave cutoff has been increased to 6.0 a.u.$^{-1}$ for all systems[1] and $l_{\max}$ has been adjusted according to the equation $k_{\max}R_{\mathrm{MT}} \approx l_{\max}$. At least 64 additional basis functions per atom have been included via

[1] Except for ZnS_2 where $k_{\max} = 5.0$ a.u.$^{-1}$ had to be used, since larger cutoffs led to numerical problems.

	AB_2	$k_{\max}$	R^A_{MT}	R^B_{MT}	$l^A_{\max}$	$l^B_{\max}$	sc LOs
Pyrites	FeS_2	4.0	2.23	1.98	8	8	Fe $3s$, $3p$
	RuS_2	3.9	2.37	2.00	8	8	Ru $4s$, $4p$
	OsS_2	3.9	2.34	2.03	8	8	Os $5s$, $5p$
	NiP_2	4.0	2.31	1.95	8	8	Ni $3s$, $3p$
	ZnS_2	4.2	2.80	1.88	10	8	Zn $3s$, $3p$
Marcasites	FeS_2	3.9	2.12	2.04	8	8	Fe $3s$, $3p$
	$FeSe_2$	3.6	2.18	2.18	8	8	Fe $3s$, $3p$
	$FeTe_2$	3.3	2.35	2.35	8	8	Fe $3s$, $3p$

Table 10.2.: The numerical parameters for the DFT calculations within the GGA-PBE and HSE06 functional for the pyrite and marcasite compounds (AB_2). Listed are the plane-wave cutoff $k_{\max}$ (in a.u.$^{-1}$), the muffin tin radii R^A_{MT} and R^B_{MT} (in a.u.), and the angular momentum cutoffs $l^A_{\max}$ and $l^B_{\max}$. The $\boldsymbol{k}$-points and the parameters for the G_0W_0@PBE calculation are specified in the text, except of the semicore states (sc), which have been included as local orbitals (LOs) in the GW calculations, which are listed in the last column.

higher-energy local orbitals, *i.e.* at least four full s, p, d, f shells per atom have been added. Thus, we are able to obtain a sufficient number of electronic bands to converge the GW calculation. I expect the convergence of the transition energies with the number of bands to be quite similar to the case in iron pyrite as displayed in Fig. 8.1 (or at least not much worse), and thus 2000 electronic bands should guarantee convergence. Again, the inclusion of the highest lying semicore states of the cation as local orbitals into the LAPW basis is crucial to obtain the right results.

10.3. GGA-PBE Results

In this section the electronic structures of the pyrite and marcasite compounds calculated within the GGA-PBE functional are discussed.

Pyrites In Fig. 10.1 the electronic band structures of the pyrite compounds FeS_2, RuS_2, OsS_2, NiP_2 and ZnS_2 are displayed. The d character of the cations, *i.e.* Fe $3d$, Ru $4d$, Os $5d$, Ni $3d$ and Zn $3d$, and the p character of the anions, *i.e.* S $3p$ and P $3p$, are shown in red and black, respectively. The FeS_2 pyrite band structure has been already extensively discussed in chapter 7, and it is only presented for comparison. The isoelectronic pyrite compounds RuS_2 and OsS_2 exhibit quite similar features in the electronic structure as iron pyrite. The valence bands are dominated by Ru $4d$ and Os $5d$ states and also the conduction states exhibit considerable d character. However, there is a single S $3p$ state defining the conduction band minimum (CBM) at Γ as it is the case in iron pyrite. The fundamental band gap is defined between the valence band maximum (VBM) close to X and the CBM at Γ, and thus it is a transition between a d and a p state. The size of the fundamental band gap is 0.62 eV in FeS_2, 0.71 eV in RuS_2 and 0.14 eV in OsS_2. The

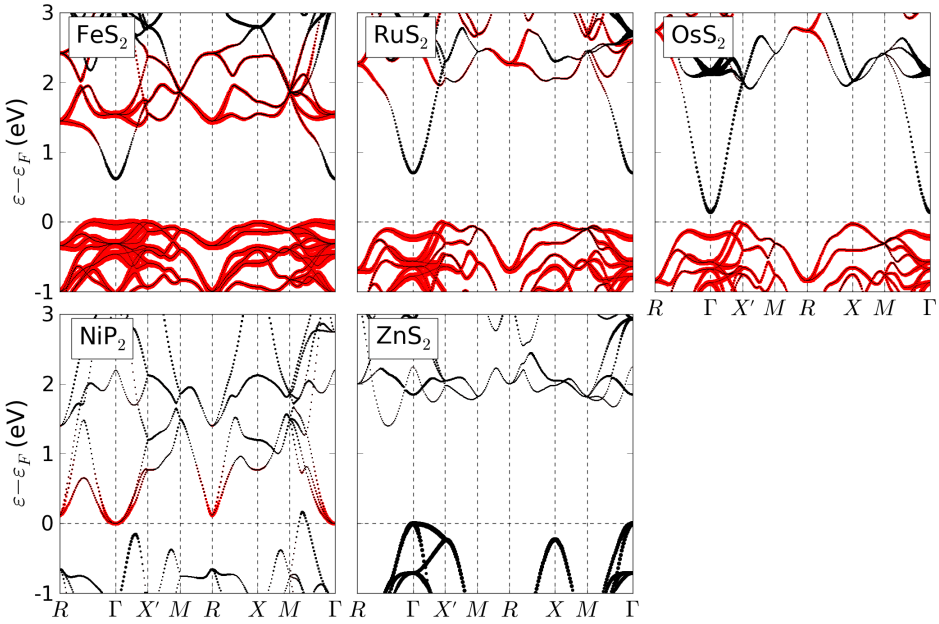

Figure 10.1.: The orbital-resolved electronic band structures of the pyrites FeS_2 (upper left), RuS_2 (upper center), OsS_2 (upper right), NiP_2 (lower left) and ZnS_2 (lower center) using the structural parameters from experiment listed in table 10.1. In red the cation d character is depicted and in black the p character of the anion is shown.

size of the fundamental band gap strongly depends on the structural parameters, in which the Wyckoff parameter u plays a crucial role. This will be discussed in detail later in the chapter.

In difference to iron pyrite the S $3p$ character in the conduction bands up to 2-3 eV is much more pronounced in RuS_2 and OsS_2. In addition, the localization and flatness of the t_{2g} states in the valence bands, which is connected to the inverse of the bandwidth of those states, decreases from FeS_2 with about 1.2 eV bandwidth (see Fig. 7.2), to RuS_2 with 1.8 eV to OsS_2 with about 2 eV bandwidth (latter two not shown). Hence, the electronic screening is expected to decrease from FeS_2 to RuS_2 to OsS_2, supported by the calculation of the static dielectric constant yielding about 20, 17 and 16, respectively (see table 10.3).

The electronic structure of NiP_2 and ZnS_2 exhibit quite some differences compared to iron, ruthenium and osmium pyrite. Although NiP_2 is isoelectronic to iron pyrite, the states directly below the Fermi energy are dominated by P $3p$ states, whereas Ni $3d$ states (with a strong admixture of P $3p$) appear just above the Fermi energy. All these bands are much more delocalized compared to those in iron pyrite. The NiP_2 pyrite compound is (semi-)metallic within the GGA-PBE functional.

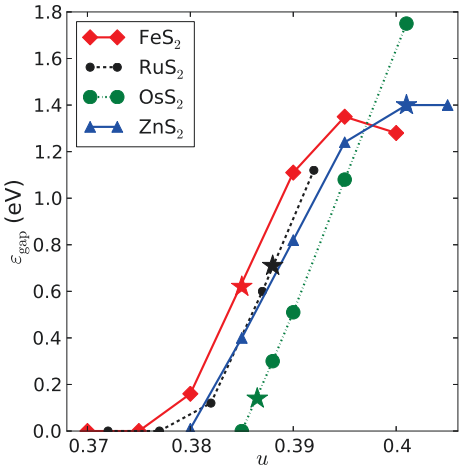

Figure 10.2.: The size of the fundamental band gap of FeS_2 (red diamonds), RuS_2 (black dots), OsS_2 (green dots) and ZnS_2 (blue triangles) in the pyrite structure is displayed depending on the Wyckoff parameter u. The star-shaped markers indicate the results for the structural parameters from experiment listed in table 10.1. The calculations for larger u values for RuS_2 did not converge.

The ZnS_2 compound exhibits two more electrons per Zn atom compared to the other investigated pyrite compounds, and thus the Zn $3d$ states are fully occupied, leading to band edges, which are mainly dominated by S $3p$ states. There is no significant contribution from Zn $3d$ states, instead Zn $4s$ states appear close to the conduction band edges (not shown). Therefore, the orbital character of the band edges in ZnS_2 is quite similar to that of simple semiconductors. In addition, the bands exhibit a parabolic behavior at the valence and conduction band edges, and thus the common approaches to determine the optical band gap in ZnS_2 by means of applying a linear regression to the tail of the optical absorption should work much better here than for FeS_2 (see chapter 7). The size of the fundamental band gap in ZnS_2 is calculated to 1.40 eV within the GGA-PBE functional.

As already adumbrated in the last paragraph and discussed for iron pyrite in chapter 7, the structural parameters have a strong influence on the electronic band structure and on the size of the fundamental band gap. This is illustrated in Fig. 10.2, where the dependence of the fundamental band gap in FeS_2, RuS_2, OsS_2 and ZnS_2 on the Wyckoff parameter u is shown. Since the band gap in FeS_2, RuS_2 and OsS_2 is defined between cation d states and S $3p$ states, it changes in the case of a relative shift between these states. Such a shift might occur when the bonding/anti-bonding splitting between the S p states changes. This, on the other hand, directly depends on the Wyckoff parameter u, since the distance between the S atoms in the S dimers of the pyrite structure is defined according to Eq. (7.2). Thus, a smaller Wyckoff parameter leads to a larger bonding distance in the S dimers (for a fixed lattice constant), which then causes a smaller bonding/anti-bonding

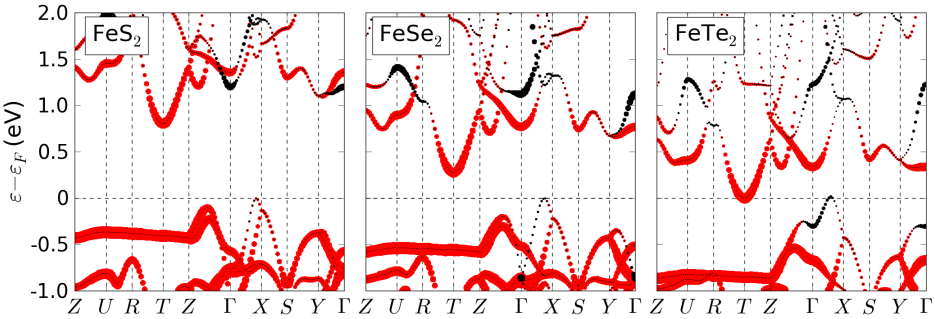

Figure 10.3.: The orbital-resolved electronic band structures of the marcasites FeS_2 (left), $FeSe_2$ (center) and $FeTe_2$ (right), where the Fe $3d$ character is shown in red and the anion p character is depicted in black. The structural parameters from experiment are used, which are listed in table 10.1.

splitting between the S p states and leads to a smaller band gap. Below a certain u the pyrite compound becomes even metallic, since the S $3p$ state at the CBM penetrates the valence bands (see also Fig. 7.6).

There is a linear dependence of the band gap size on u as long as the band gap is still defined by the cation d states at one edge and the S $3p$ states at the other edge. The gradient of the linear curve is quite similar for FeS_2, RuS_2, OsS_2 and ZnS_2, which shows that it mainly depends on the structure and not on the chemical composition. However, the size of the fundamental band gap depends on both. For instance RuS_2 and OsS_2 have similar lattice constants and Wyckoff parameters according to experiment as listed in table 10.1 (the star-shaped markers in the figure indicate the structural parameters from experiment), but the size of the band gap differs by almost 0.6 eV. For the same Wyckoff parameter the band gap size decreases in the order from FeS_2 to RuS_2 to OsS_2, which is consistent with the conventional wisdom that the band gap of semiconductors usually decreases when substituting the atoms with heavier elements from the same chemical group. Since ZnS_2 has a different electron filling, and thus exhibits significant differences in the electronic structure, it does not fit into this picture.

Note, that the linear dependence of the band gap size on u is also valid for values of u below the limit where the compound becomes metallic, when defining negative band gaps, which is not done in this thesis. For larger Wyckoff parameters there is a saturation effect observable, which is caused as soon as the band edges defining the band gap obtain the same orbital character, which are either cation d (in FeS_2, RuS_2 and OsS_2) or S $3p$ states (in ZnS_2). Then, an increase of u has no significant influence on the band gap size, since the states at the VBM and CBM experience the same energy shift.

Marcasites In Fig. 10.3 the orbital-resolved electronic band structures of the marcasite compounds FeS_2, $FeSe_2$ and $FeTe_2$ are displayed. In red color the Fe $3d$ character is shown, and black color is used for the anion p character, *i.e.* S $3p$, Se $4p$ and Te $5p$. The

electronic structure of FeS_2 marcasite has already been discussed in detail in chapter 9 and is only shown for comparison in the figure, but nevertheless let me briefly summarize the essential features. The FeS_2 marcasite band structure exhibits a couple of similarities when compared to the band structure of iron pyrite, as for instance the flat Fe $3d$ states at the valence band edge and as a dominant contribution at the conduction band edge. There is a considerable S $3p$ contribution at the conduction band edge at Γ like in iron pyrite. However, in difference to iron pyrite the fundamental band gap within GGA-PBE is defined between states of mainly Fe $3d$ character.

The $FeSe_2$ and $FeTe_2$ compounds show basically the same features in the electronic structure, but the anion p character is not located at the conduction band edge, but is now at higher energies around Γ (0.4 eV higher in $FeSe_2$ and 0.8 eV in $FeTe_2$), whereas the conduction band edge at Γ is of Fe $3d$ character. On the other hand, the character of the VBM close to X obtains increasing anion p character when going from FeS_2 to $FeSe_2$ to $FeTe_2$. Hence, in $FeSe_2$ and $FeTe_2$ there is a reversed situation compared to FeS_2 marcasite for the fundamental band gap, which is defined between a mainly p state at the VBM and a d state at the CBM located at T. The size of the fundamental band gap computed within the GGA-PBE functional is 0.80 eV for FeS_2 marcasite, 0.28 eV for $FeSe_2$ and $FeTe_2$ is predicted to be a (semi-)metal.

Note, that all the calculations have been performed in the scalar-relativistic approximation, and thus no spin-orbit coupling (SOC) has been considered. A test calculation for FeS_2, RuS_2 and $FeTe_2$ including SOC yields no significant change of the band gap and the shape of the band structure. However, in the case of OsS_2 the inclusion of SOC has a considerable influence on the size of the band gap due to the large mass of the Os atoms ($Z = 76$). The band gap is reduced by about 0.05 eV including SOC, making OsS_2 within the GGA-PBE functional almost metallic with a band gap of 0.09 eV.

10.4. GW Results

The G_0W_0@PBE results for the pyrites and marcasites are discussed in this section.

Pyrites In Fig. 10.4 the electronic band structures of the pyrite compounds FeS_2, RuS_2, OsS_2, NiP_2 and ZnS_2 are shown using the GW approximation. For comparison the GGA-PBE results are also displayed. Note, that the orbital character of the bands does not change when applying G_0W_0, and thus I refer to Fig. 10.1 displaying the orbital-resolved band structure within GGA-PBE.

The GW results of iron pyrite have been discussed in detail in chapter 8. Hence, I will only present a brief summary. The application of GW on top of the GGA-PBE results slightly increases the energy gap between the Fe $3d\,t_{2g}$ valence states and the Fe $3d\,e_g$ conduction states, but the S $3p$ conduction state around Γ drops down,[2] which reduces

[2]Note that the Fe $3d$ states are considerably corrected when applying GW, yielding a positive energy shift for both the Fe $3d$ valence as well as the conduction states. On the contrary the S $3p$ states experience only slight GW corrections, and thus, by adjusting the Fermi energy to the top of the valence band, it seems as the S $3p$ state are influenced most by GW, which is actually not the case.

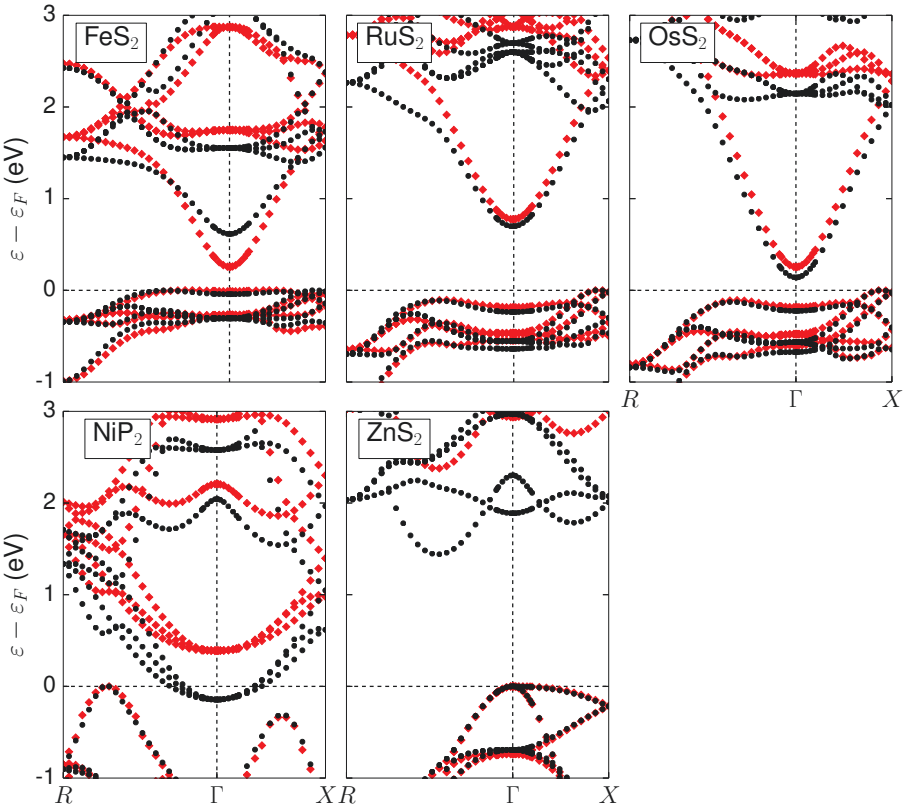

Figure 10.4.: The electronic band structures of FeS_2 (upper left), RuS_2 (upper center), OsS_2 (upper right), NiP_2 (lower left) and ZnS_2(lower center) pyrite calculated within G_0W_0@PBE (red diamonds). For comparison the "plain" GGA-PBE results are also shown as black dots. The pyrites have been calculated using the structural parameters from experiment as listed in table 10.1. The sizes of the fundamental band gaps within GGA-PBE and GW are listed in table 10.3.

the size of the fundamental band gap from 0.62 eV to 0.27 eV. Iron pyrite is the only investigated pyrite compound, where this unconventional reduction of the band gap size occurs to such an extent. However, RuS_2 and OsS_2 behave quite similar when applying GW. The energy gap between the Ru $4d$ and Os $5d$ states at the band edges is slightly increased, whereas the S $3p$ conduction state around Γ remains almost at the former energy position. Overall this leads to a small correction of the fundamental band gap within GW, *i.e.* from 0.71 eV to 0.77 eV in RuS_2 and from 0.14 eV to 0.25 eV in OsS_2. The combination of a strong electronic screening and the p-d character of the band edges is presumably the reason for this peculiar behavior in FeS_2, RuS_2 and OsS_2, which will be discussed in detail in the next section.

The GW results of NiP_2 and ZnS_2 pyrite are quite different compared to FeS_2, RuS_2 and OsS_2 due to the different orbital character at the band edges. In NiP_2 and ZnS_2 both band edges comprise of mainly P $3p$ and S $3p$ states, respectively, and the fundamental band gap is between states of similar orbital character (see Fig. 10.1), and thus the GW correction behaves like for simple semiconductors. The energy gap between the $3p$ valence and conduction states is significantly increased, leading to an opening of the fundamental band gap from 1.40 eV to 2.38 eV in ZnS_2 and making the metallic NiP_2 within GGA-PBE to a semiconductor with a 0.39 eV band gap. The main effect when applying GW is an almost rigid shift of the bands in NiP_2 and ZnS_2, indicating that a DFT+U approach might lead to similar results.

The shape of the band structures of all investigated pyrites is not significantly altered by GW. Note that all calculations have been carried out without SOC, since no significant changes are expected for the band structures (see last section), except for OsS_2. In OsS_2 a similar reduction of the fundamental band gap of about 0.05 eV as it is the case using the GGA-PBE functional is expected within GW.

Marcasites In Fig. 10.5 the band structures of FeS_2, $FeSe_2$ and $FeTe_2$ marcasite are displayed using G_0W_0@PBE and, for comparison, using a "plain" GGA-PBE calculation. For the orbital character of the bands I refer to Fig. 10.3 showing the results within GGA-PBE, since it does not change upon applying single-shot GW.

The essential features of the band structure of FeS_2 marcasite are only briefly discussed in the following, and I refer the reader to chapter 9 for more details. In difference to iron pyrite, the fundamental band gap of FeS_2 marcasite within GGA-PBE is defined between states of mainly Fe $3d$ character, whereas the S $3p$ band at Γ is located at higher energies. However, the GW corrections of the bands behave similar to those in iron pyrite, *i.e.* the energy gap between the valence and conduction Fe $3d$ states is increased, and the S $3p$ conduction state at Γ drops down. As a consequence the band gap does not only change the size upon applying GW, but also the character is altered. Within GGA-PBE the band gap is defined between Fe $3d$ states close to X and T, whereas in GW the VBM is an Fe $3d$ state close to Z and the CBM the S $3p$ state at Γ.

For $FeSe_2$ and $FeTe_2$ marcasite the main features of the band structure are the same, however, the Se $4p$ and Te $5p$ state at Γ are located at higher energies, and thus they are

The same is valid for the other pyrite compounds.

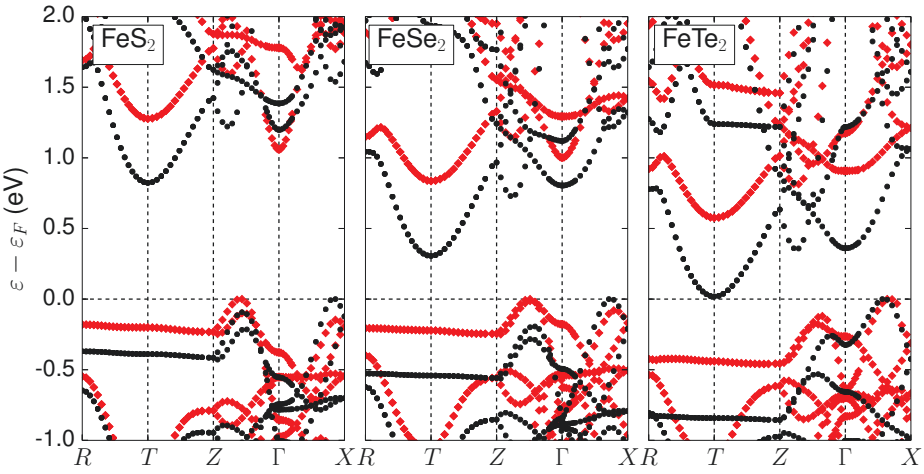

Figure 10.5.: The electronic band structure of FeS_2 (left), $FeSe_2$ (center) and $FeTe_2$ marcasite (right) using the structural parameters from table 10.1 within the G_0W_0@PBE (red diamonds) and "plain" GGA-PBE calculation (black dots). The sizes of the fundamental band gaps within GGA-PBE and GW are listed in table 10.3.

not lying at the band edge within GGA-PBE. When applying GW the p state approaches the conduction band edge in both case. In the case of $FeSe_2$, where the p band has been already close to the band edge within GGA-PBE, it even becomes a state at the band edge. For both marcasites the CBM is still an Fe $3d$ state at T, whereas the VBM in $FeSe_2$ changes from a Se $4p$ state close to X to an Fe $3d$ state between Z and Γ using GW, since the Se $4p$ state at the valence band edge drops down. In $FeTe_2$ the VBM is still a Te $5p$ state close to X. Overall this leads to an opening of the band gap in $FeSe_2$ from 0.28 eV within GGA-PBE to 0.84 eV within GW, and $FeTe_2$ predicted to be metallic within GGA-PBE obtains a band gap of 0.58 eV.

To conclude the application of GW on the investigated pyrites and marcasites behaves quite similar in all cases, with the difference that, depending on the band character of the band edges, the unconventional behavior of the GW correction is more (FeS_2, RuS_2 and OsS_2 pyrite) or less obvious (marcasites, NiP_2 and ZnS_2 pyrite).

10.5. HSE06 Results and Comparison with Experiment

After having discussed in detail about the orbital decomposition of the pyrite and marcasite compounds, and its influence on the GW results, I will compare the band gaps calculated within GGA-PBE and GW to experiment. In addition, the HSE06 results are presented

	PBE	HSE06	GW	PBE	G_0W_0	exp.	$\epsilon(\omega = 0)$
Pyrites	$X \to \Gamma$			$\varepsilon_{\mathrm{gap}}$			
FeS_2	0.64	2.34	0.31	0.62	0.25	0.95 [13]	20
RuS_2	0.72	1.78	0.79	0.71	0.77	1.3 [156]	17
OsS_2	0.17	0.99	0.28	0.14	0.25	2.0 [156]	16
NiP_2	1.00	1.43	1.58	0	0.39	-	-
ZnS_2	2.11	3.21	3.15	1.40	2.38	2.5 [45]	8
Marcasites	$X \to T$			$\varepsilon_{\mathrm{gap}}$			
FeS_2	0.95	2.82	1.47	0.80	1.06	0.34 [32]	19
$FeSe_2$	0.52	2.15	1.00	0.28	0.84	0.5-1.0 [157]	24
$FeTe_2$	0.44	1.68	0.89	0	0.58	0.2-0.5 [157]	-

Table 10.3.: The transition energy (in eV) between the states at the valence and conduction band edge for $X \to \Gamma$ for the pyrite compounds FeS_2, RuS_2, OsS_2, ZnS_2 and NiP_2 and for the transition $X \to T$ for the marcasite compounds FeS_2, $FeSe_2$ and $FeTe_2$. The calculations have been performed within the GGA-PBE and HSE06 functional, and the G_0W_0@PBE method. The structural parameters from experiment as listed in table 10.1 are used for the calculations. In addition the size of the fundamental band gap $\varepsilon_{\mathrm{gap}}$ is listed for the same compounds using GGA-PBE and G_0W_0@PBE. For comparison the experimentally determined band gaps and the corresponding references are presented, if available. Note that the structural parameters given in those references and the references of table 10.1 might be different. The last column lists the electronic contribution to the static dielectric constant $\epsilon(\omega = 0)$ calculated within the GGA-PBE functional. For NiP_2 and $FeTe_2$ the static dielectric constant is not listed, since the systems are predicted to be (semi-)metallic within the GGA-PBE functional.

and also included into this comparison.

In table 10.3 the fundamental band gaps calculated within GGA-PBE and G_0W_0@PBE for the pyrites FeS_2, RuS_2, OsS_2, NiP_2 and ZnS_2, and the marcasites FeS_2, $FeSe_2$ and $FeTe_2$ are listed. The experimentally measured band gaps are also presented with the corresponding references. However, note that except for FeS_2 pyrite there is not much "high-quality" literature about the band gaps of these compounds. For instance for ZnS_2 the band gap is only estimated to be at least 2.5 eV due to the bright yellow appearance of the crystals, and for $FeSe_2$ and $FeTe_2$ the band gaps are estimated to be in the listed range by using temperature-dependent electrical resistivity measurements, which are very sensitive to defects. To allow a better comparison of the results, the fundamental band gap sizes are also displayed in Fig. 10.6 in a bar plot.

Since the calculation of electronic band structures within hybrid functionals are not straight-forward, I have only calculated the transition energy of some specific transitions between high-symmetry $\boldsymbol{k}$-points in this case. In order to compare the HSE06 results to those calculated within the GGA-PBE functional and G_0W_0@PBE, the transition energies

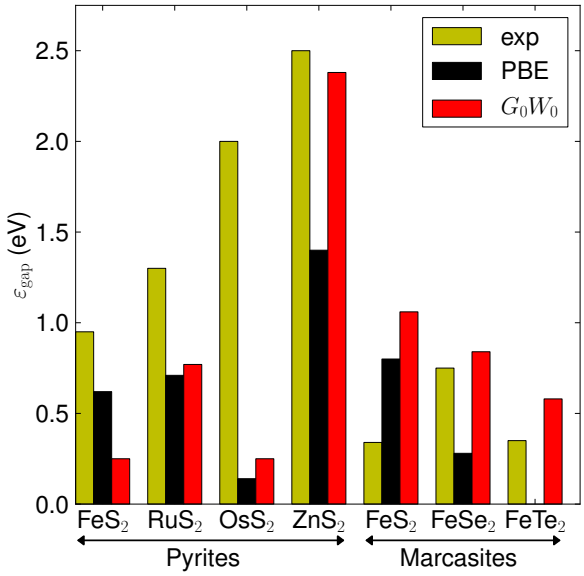

Figure 10.6.: The calculated fundamental band gaps within the GGA-PBE functional (black) and G_0W_0@PBE (red) are compared to the band gaps measured in experiment (yellow) for the pyrite compounds FeS_2, RuS_2, OsS_2 and ZnS_2, and the marcasites FeS_2, $FeSe_2$ and $FeTe_2$. The values as listed in table 10.3 are used.

for $X \to \Gamma$ for the pyrites and $X \to T$ for the marcasites are listed in table 10.3. In this case a comparison with experiment is not straight-forward, and only estimations about the agreement between the HSE06 results and experiment can be drawn.

In the case of NiP_2 and ZnS_2, where the orbital character of the band edges is quite different as compared to the other compounds (see previous sections), there is a good agreement between the transition energy of $X \to \Gamma$ calculated within HSE06 and G_0W_0@PBE. Since the fundamental band gap of ZnS_2 calculated within G_0W_0@PBE is in nice agreement with the (estimated) size of the band gap from experiment, it should be not too far-fetched to conclude that also the HSE06 calculation might be in good agreement with the experimentally determined band gap. Thus, the band gaps of ZnS_2 and NiP_2 behave quite as expected, *i.e.* like simple semiconductors (see appendix A), when applying GW or hybrid functionals. This means there is a significant opening of the band gap compared to the gap within "plain" GGA-PBE improving the agreement with experiment.

For all other compounds the application of hybrid functionals or GW leads to less expected results. The transition energies calculated within HSE06 are much larger compared to the GGA-PBE and the GW results. In particular for FeS_2 pyrite and the marcasites FeS_2, $FeSe_2$ and $FeTe_2$ the band gaps increase by almost 200-300%. The band gaps

within HSE06 are also much larger than those from experiment, indicating that the HSE06 functional is not suited to describe these compounds.

It is known that the HSE06 functional fails to describe systems with a large screening (in the extreme case metals), and thus I calculated the static dielectric constants of the compounds, which are listed in table 10.3.[3] The ZnS_2 compound with small dielectric constant is well described within HSE06, whereas the other compounds exhibiting dielectric constants around 20 are not. These large values for the static dielectric constants are caused by the localized d states at the band edges. It might be that a modified HSE06 approach using $\epsilon^{-1}(\omega = 0)$ instead of 0.25 as Hartree-Fock mixing parameter leads to improved results for the band gaps (*c.f.* [90, 91]). In this case the exchange contribution is mainly dominated by the GGA-PBE exchange.

Let me focus on the pyrites FeS_2, RuS_2 and OsS_2 now. The GW correction on top of the GGA-PBE band gaps is quite small in all three cases, exhibiting even a reduction of the size of the band gap in FeS_2. What might be the reason for this small correction or even reduction of the band gap size? - In a simplified picture the GW correction comprises of two major corrections of the self energy, one for the exchange denoted as Σ_{ex} in the following and another in the screening (correlation) denoted as Σ_{cor}. The correction Σ_{ex} opens the band gap, whereas Σ_{cor} tends to reduce the band gap size. In a typical simple semiconductor like Si Σ_{ex} is considerably larger than Σ_{cor} leading in total to an opening of the band gap. Since the screening is connected to the size of the static dielectric constant, it is quite large in FeS_2, RuS_2 and OsS_2, which might lead to a situation, where Σ_{cor} is as large as Σ_{ex} or even larger. Then, as a consequence the size of the band gap decreases compared to the GGA-PBE result. Up to now these are only "hand-waving" arguments, but I plan to investigate this peculiar behavior in more detail in the future.

The reported experimentally measured band gaps of about 1, 1.3 and 2 eV for FeS_2, RuS_2 and OsS_2 do not agree with the calculated results, both in size as well as the sequence of the gap sizes, since RuS_2 has the largest band gap in the calculations. However, the band gaps of FeS_2, RuS_2 and OsS_2 from experiment are measured using optical experiments, and, as already discussed for FeS_2 pyrite in chapter 7, the optical band gap is difficult to measure due to the low-intensity states from the S $3p$ band around Γ. Thus, the optically measured band gap might be significantly larger than the "real" optical band gap, and furthermore the fundamental band gap might be even smaller than the "real" optical band gap. Therefore, the experiments might actually measure the energy gap between the d states at the band edges instead. This might explain why the energy gaps between the t_{2g} valence states and e_g conduction states, which increase in size from FeS_2 with about 1.5 eV to RuS_2 with 2.2 eV to OsS_2 with 2.7 eV (see Fig. 10.1), are in better agreement with the reported band gaps than the fundamental band gaps.

[3] Note, that the calculation of the dielectric constants has shown some minor numerical problems for RuS_2, OsS_2, and ZnS_2, and thus the values should be regarded with caution. The static dielectric constant for $\omega = 0$ could not be calculated for these systems, but only for a small finite $\omega = 0.2$ eV. However, the values of the dielectric constant for $\omega = 0.2$ eV are quite close to the value of the static dielectric constant in the case of the FeS_2 and $FeSe_2$ compound, and thus the ϵ for RuS_2, OsS_2, and ZnS_2 should be not too far off from the static value. Note, that the values for the static dielectric constants comprise only of the electronic contributions.

The fundamental band gaps of RuS_2 and OsS_2 are in reasonable agreement with the results of Sun *et al.* [158], although the band gaps are smaller there. Most probably the differences can be attributed to the structural relaxation leading to different Wyckoff parameters compared to the structural parameters used in this thesis.

Finally, let me compare the results of FeS_2, $FeSe_2$ and $FeTe_2$ marcasite. Since the orbital character of the band edges defining the fundamental band gap is of Fe $3d$ character within the GGA-PBE functional (see Fig. 10.3), the band gap opens for all three compounds when applying GW. The calculated band gap sizes within GW are not far off from the experimentally measured gaps for $FeSe_2$ and $FeTe_2$. For FeS_2 marcasite the GGA-PBE and GW band gap is much larger than the experimentally measured gap. In addition, the calculated band gap sizes within GGA-PBE, HSE06 and GW decrease when going from FeS_2 to $FeSe_2$ to $FeTe_2$, whereas this is not the case in experiment due to the small band gap of 0.34 eV reported for FeS_2 marcasite. In a recent publication there are indications that FeS_2 marcasite has an at least as large band gap as iron pyrite [33], and thus a thorough reexamination of the band gap in FeS_2 marcasite would be desirable.

10.6. Conclusions

The electronic structure of the pyrite compounds FeS_2, RuS_2, OsS_2, NiP_2 and ZnS_2, and of the marcasite compounds FeS_2, $FeSe_2$ and $FeTe_2$ has been investigated using the GGA-PBE and HSE06 functional, and the G_0W_0@PBE approach. The results have been compared to each other and a comparison between the calculated and experimentally measured band gaps has been presented.

Overall, the investigated pyrite and marcasite compounds behave quite similar under the application of GW, when focusing on the correction of states depending on the orbital character. The energy gaps between states exhibiting either mainly d or p character on both the valence band as well as conduction band edge are significantly increased, whereas the energy gaps between states of different orbital character, *i.e.* p-d or d-p, experience only a small change or even decrease around ε_F in the case of iron pyrite and iron marcasite upon applying GW. The major difference between the GW results of the compounds arises due to the different orbital character of the band edges and the states defining the fundamental band gap. In the following a brief summary of the results for each of the compounds is presented.

The band gap in FeS_2, RuS_2 and OsS_2 is defined by localized d states at the valence band edge and the S $3p$ conduction state around Γ, which position is quite sensitive to the structural parameters. The localized d states give rise to a strong screening in the materials, *i.e.* large static dielectric constants, which might explain the significantly overestimated band gaps within the HSE06 functional. The unconventionally small GW correction of the band gap in RuS_2 and OsS_2, or even the reduction of the band gap size in FeS_2 when applying GW might be also attributed to the screening. The calculated band gaps within GGA-PBE, HSE06 and GW do not agree with the experimentally measured ones. However, the experiments are based on optical measurements, and thus instead of using the low-intensity d-p transitions (see chapter 7) for the determination of the

optical band gap, the energy gap between the t_{2g} and e_g states of the band edges might be measured instead. The calculated energy gaps between the t_{2g} and e_g states are in more reasonable agreement with the experimentally determined band gaps.

The band edges of NiP_2 and ZnS_2 pyrite comprise of mainly P $3p$ and S $3p$ states, respectively. Employing GW or HSE06 opens the band gap in both systems, and the GW and HSE06 results agree quite well. The HSE06 functional seems to work for these compounds, since the screening is not too large. For ZnS_2 the band gap calculated within GW and HSE06 is even in nice agreement with the estimated band gap from experiment.

For the marcasite compounds FeS_2, $FeSe_2$ and $FeTe_2$ the fundamental band gap is defined mainly between Fe $3d$ states within GGA-PBE, and thus it opens in for all three systems when applying GW or HSE06. The HSE06 functional predicts again too large band gaps, due to the large screening of the systems. The GW band gaps of $FeSe_2$ and $FeTe_2$, however, agree well with the experimentally reported values. The FeS_2 marcasite band gap from experiment is much smaller than the calculated band gaps. However, in the recent literature a band gap of iron marcasite, which is at least as large as in iron pyrite, is reported [33]. Since most of the experimentally reported band gaps are only estimated, new thoroughly conducted experiments for the pyrite and marcasite compounds are desirable.

11. Thermodynamics of Iron Pyrite Films

11.1. Introduction

In the chapters 7 and 8 the electronic and optical properties of the iron pyrite bulk phase have been discussed in detail. It has been pointed out that the size of the fundamental band gap might be still not settled, and thus further thorough experimental and theoretical investigations on that in the near future would be desirable. Nevertheless, starting from this chapter, I would like to extend the investigation to iron pyrite films and surfaces, since realistic solar cell devices possess interface regions, which might have a crucial influence on the electronic structure and the photovoltaic performance. However, to model realistic interfaces very large supercells are necessary, making the DFT calculations unfeasible.[1] Therefore, the investigation is restricted to free standing iron pyrite films in this thesis, which can be interpreted as a simple model for an interface in a device. The electronic surface states of the pyrite films might lead to a reduction of the photovoltaic performance by reducing the size of the band gap or acting as charge recombination centers when located within the band gap. Thus, already a lot can be learned by studying the free standing surfaces only.

In this chapter the thermodynamic stability of several iron pyrite films is examined. Since the common facets of natural and synthetic FeS_2 pyrite crystals are reported to be along the (001), (111) and (210) direction [159], the discussion is restricted to the in total 14 different iron pyrite films of different terminations and those crystallographic orientations in the following. Rarely, the (110) facet is also observed in iron pyrite, and there are indications that it has the highest energy of the low index surfaces in iron pyrite, and thus it is not included in the study of this thesis. The influence of structural relaxation and magnetism on the thermodynamic stability is also discussed.

11.2. Geometry of the Films

In the FLEUR code [66] films need to be defined with a finite thickness, and thus they have a surface on the top and on the bottom of the film. The thickness of a film needs to be sufficiently large to prevent spurious interactions between the two surfaces (more

[1] Realistically speaking, the FLEUR code [66] is currently capable to treat systems up to a few hundreds of atoms within conventional "DFT" on state-of-the-art computers. For more sophisticated schemes the number of atoms has to be much smaller.

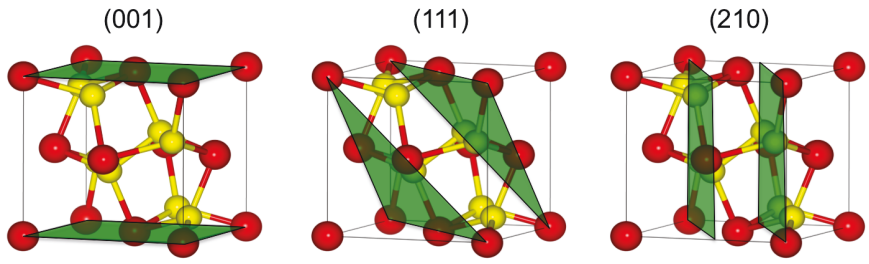

Figure 11.1.: The lattice planes of the crystallographic orientations (001), (111) and (210) in the bulk unit cell of iron pyrite.

details are discussed in the next section). The iron pyrite films investigated in this thesis have been chosen symmetric, otherwise, it is difficult to separate energetics and electronics structure of the two different surfaces, and so the termination of the two surfaces is the same.

All possible terminations of the films with crystallographic orientations along the (001), (111) and (210) direction have been examined. In Fig. 11.1 the corresponding lattice planes are depicted in the bulk unit cell of iron pyrite. For the (001) orientation there are three different surface terminations denoted as (001)-S, (001)-2S and (001)-Fe (see Fig. 11.2). For this orientation a S-Fe-S layer is repeated along the z direction in ABAB stacking, where the layers A and B exhibit different positions for the S and Fe atoms, but they are related via symmetry. Depending on whether the order of the top-most atomic layers is S-Fe-S-... , S-S-Fe-... or Fe-S-S-... the film is S, 2S or Fe terminated, explaining the notation.

For the (111) orientation there are five different terminations, namely (111)-Fe, (111)-S, (111)-2S, (111)-3S and (111)-4S. In the case of the (210) orientation there exist even six different terminations, (210)-Fe, (210)-S, 210-2S, (210)-Fe', (210)-S' and (210)-2S'. The primed and unprimed notation distinguishes between terminations with the same order of S and Fe atomic layers, but due to a different in-plane position of these atoms the primed and unprimed termination are not equivalent. The notation corresponds to this used by D. Alfonso [160], except that the primed and unprimed terminations of the (210) films are exchanged.

In total these are 14 different iron pyrite films. For all films a side and top view of the structure is presented in the appendix G. There it becomes also more clear why there are five and six different terminations for the (111) and (210) orientation.

For the lattice parameter a and the Wyckoff parameter u the optimized structural parameters of the iron pyrite bulk structure using GGA-PBE ($a = 5.40$ Å and $u = 0.3826$) including or excluding further structural relaxations of the films have been exploited. More details about the structural relaxation of the films will be discussed in the next section.

The two-dimensional in-plane unit cell is quadratic with the lattice constant a for the (001) films, triangular for the (111) films with lattice constant $\sqrt{2}a$ and rectangular with the lattice constants $\sqrt{5}a$ and a for the (210) films. The primitive lattice vectors of the

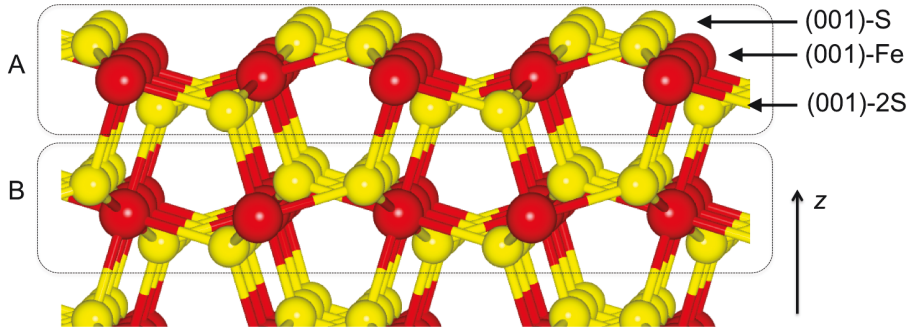

Figure 11.2.: The top-most 6 atomic layers of a (001)-S iron pyrite film from side view. The Fe atoms are indicated in red and the S atoms in yellow. The arrows indicate the three possible terminations for the (001) iron pyrite films, *e.g.* the (001)-Fe film has the Fe atomic layer as top-most layer and the (001)-2S film exhibits the two atomic layers of S on top. There are only three different terminations for the (001) orientation and not 6, because the S-Fe-S layers A and B are equivalent via symmetry.

unit cell are depicted in the top views of appendix G.

11.3. Computational Details

The calculations have been conducted using the FLEUR code. Since there is not yet a consensus on which exchange-correlation functional or computational method predicts a realistic band gap of iron pyrite bulk (*cf.* chapters 7 and 8), the GGA-PBE functional is used for all the computations of the iron pyrite films. The GGA-PBE functional represents a good compromise between being a fast computational method and predicting a reasonable band gap size and optical absorption for iron pyrite when compared to experiment.

All the films have been structurally relaxed by using the optimized structural parameters including the relaxed value for the Wyckoff parameter u from the bulk phase as starting structure, and allowing relaxation only for the top-most 6 atomic layers on both surface sides. The relaxed structure of the bulk phase is a good approximation for the bulk-like middle of the film. The forces have been converged up to 10^{-4} Htr/a.u. and the Broyden-Fletcher-Goldfarb-Shanno mixing has been exploited for structural optimization.

The computational parameters (*cf.* chapter 5) for the structural relaxation are all slightly different for the different films. For instance, the plane-wave cutoff varies from 3.6 to 4.0 a.u.$^{-1}$ depending on the structure and also the muffin tin radii vary due to a different course of the structural relaxation. For each film the used computational parameters are presented in a table in appendix G. No local orbitals have been included in the calculations.

For the calculation of the surface energies an approach as described in appendix C has been used. To compare the total energies the computational parameters of the 14

films (relaxed and unrelaxed), iron pyrite bulk, S_8 bulk and bcc-Fe (magnetic) need to be chosen as similar as possible. That is the reason why additionally to the discussed numerical parameters of chapter 5, more numerical parameters are listed in the appendix G like the difference in the vacuum constants D and $\tilde{D}$ (see Fig. 5.2), the number of radial mesh points and the logarithmic increment for the description of the wave functions within the muffin tins of the Fe and S atoms, and the two cutoff parameters $G_{\max}$.[2] With the following set of parameters the total energies have been calculated and the surface energies are converged at least up to 1 meV/Å^2: $\Delta_{\text{vac}} = \tilde{D} - D = 3.34$ a.u., $R_{\text{MT}}^{\text{Fe}} = 2.0$ a.u. using 705 grid points and a logarithmic increment of 0.016, $R_{\text{MT}}^{\text{S}} = 1.6$ a.u. using 641 grid points and a logarithmic increment of 0.017, $k_{\max} = 4.0$ a.u.$^{-1}$, the density and exchange-correlation potential cutoff $G_{\max}$ values of 12.3 a.u.$^{-1}$ and 10.3 a.u.$^{-1}$, and a $\boldsymbol{k}$-mesh density of about 100 $\boldsymbol{k}$-points in the full Brillouin zone of the square lattice of the (001) surfaces.

For the investigation of the influence of magnetism on the surface energy, spin-polarized DFT calculations with the FLEUR code have been performed. All the numerical parameters have been chosen as aforementioned, and thus it might be that the magnetic moments are a bit underconverged, since depending on the system a lot of $\boldsymbol{k}$-points might be needed to carefully converge magnetic moments. The difference between the total energy of the spin-polarized and non-magnetic DFT calculation has been determined to examine the effect of magnetism on the surface energy.

Since the structure of films in the FLEUR code exhibit a periodicity solely in the in-plane directions, there is no need to converge the thickness of the vacuum to prevent a spurious interaction between periodically repeated films along the z direction (*cf.* chapter 5). However, the thickness of the films needs to be converged to prevent a spurious interaction between the two surfaces located at the top and the bottom of the symmetric films. In table 11.1 the surface energies of unrelaxed (001)-S films of different thicknesses are listed, showing that the surface energy converges quite fast with the thickness. For all films thicknesses about 2 nm (20 Å) are chosen to be on the safe side, since the convergence of the surface energy for the (111) and (210) films might be more problematic than that for the (001) films. The exact values of the thicknesses are listed in the appendix G.

11.4. Surface Energies of the Films

In this section some general behavior of the structurally relaxed iron pyrite films are discussed and compared to literature. Following the method described in appendix C the surface energies of the films depending on the chemical potential of S are calculated and the influence of structural relaxations and magnetism is investigated.

[2] These parameters are not explained in chapter 5, since they usually are not essential to obtain good convergence. However, for comparing the surface energies, all possible parameters should be chosen similar, if possible. For the interested reader I recommend to take a look to the reference [66] to find more information on those parameters.

d (Å)	8.1	18.9	29.7	40.5	51.3
N_{bulk}	1.5	3.5	5.5	7.5	9.5
N_{atoms}	18	42	66	90	114
E_{sur} (meV/Å^2)	73.18	72.92	73.02	73.10	73.11

Table 11.1.: The surface energy E_{sur} of unrelaxed (001)-S films as function of the thickness d of the films. Additionally, the number of atoms N_{atoms} of the films and the number of iron pyrite bulk unit cells N_{bulk} corresponding to the thickness is listed.

	δ_x	δ_y	δ_z
S_{1a}, S_{1b}	±0.04	-0.06	-0.01
Fe_{1a}, Fe_{1b}	±0.05	0.04	-0.08
S_{2a}, S_{2b}	±0.01	0.04	0.09
S_{3a}, S_{3b}	±0.01	0.00	0.02

Table 11.2.: The displacements (in Å) along x, y and z of the atoms of the first four atomic layers in the (001)-S film within structural relaxation. The directions of x, y and z are chosen as in Fig. 11.3 and as discussed in appendix G. The atoms S_{1a} and S_{1b} are located in the top-most S layer, Fe_{1a} and Fe_{1b} are in the top-most Fe layer and S_{2a}, S_{2b} and S_{3a}, S_{3b} are the atoms in the second and third S layer, respectively. Due to symmetry the displacements along x of the a and b atoms in the same atomic layer have the same value but a different sign.

Structural Relaxation As expected the relaxations are largest for the atoms located at or nearby the surfaces, whereas only minor displacements occur in the bulk-like middle of the films. The Fe terminated films exhibit larger relaxations than the S terminated films which, on the other hand, show smaller relaxations the more S atoms are located on the surface.

A general feature in almost all films is the relaxation of the top-most Fe atoms towards the bulk-like middle and at the same time the displacement of the below located S layer towards this Fe atoms, leading to a significant decrease of the interlayer distance between the top-most Fe and the S layer located below, in some cases up to 0.4 Å. It seems this process is driven by electrostatics in order to screen the Fe atoms, which are "too" unscreened when located at the unrelaxed surface. In table 11.2 the displacements in the (001)-S film along the x, y and z direction are listed for the atoms of the first four atomic layers. The significant reduction of the interlayer distance between the top-most Fe layer and the S layer located below is clearly observable. The in-plane relaxations are also not small for the first three atomic layers. The displacements are indicated in Fig. 11.3 to illustrate the choice of unit cell and x, y and z direction for the values.

For specific details on the relaxation of each of the 14 films, I refer to the appendix G. The (210)-Fe and (210)-2S' film could not be structurally relaxed due to convergence problems, indicating that those films exhibit some structural instabilities.

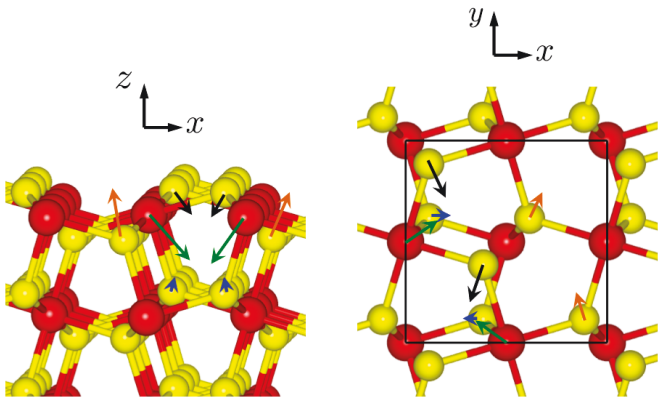

Figure 11.3.: The displacements of the atoms in the first four atomic layers of (001)-S within the structural relaxation are indicated in arrows using a side (left panel) and top view (right panel) of the structure. The arrows are not true to scale, but the relative size among them is approximately reproduced. The displacements are color coded depending on the atoms: S_{1a} and S_{1b} (black), Fe_{1a} and Fe_{1b} (green), S_{2a} and S_{2b} (orange) and S_{3a} and S_{3b} (blue). The quadratic 2-dimensional unit cell of the (001) film is depicted as black frame in the top view.

Comparing the results to those in literature reveals that the decrease of the interlayer distance between the top-most Fe and subsurface S layer is pointed out in several other references [160–162]. The in-plane relaxations of the top-most atoms in the (001)-S film are also in reasonable agreement with [161, 162].[3] The change in the interlayer distances due to relaxation for the (111)-2S and (210)-S surface (not shown) is in reasonable agreement with those of Hung *et al.* [163].

Thermodynamic Stability In Fig. 11.4 the surface energies calculated within the approach discussed in appendix C are displayed depending on the chemical potential of S. The chemical potential of S ranges between the two extreme cases of a S lean or S rich condition, *i.e.* the experimental situation in which bcc-Fe or S_8 is formed in the film during synthesis.

The surface energy of the stoichiometric films[4] (001)-S, (210)-S, (210)-S' and (111)-2S is independent of the chemical potential μ_S, whereas the surface energy of the S-poor films (210)-Fe, (210)-Fe', (111)-1S, (001)-Fe and (111)-Fe increases towards the S rich

[3] The signs of the displacements are not simple to compare, since it depends on the definition of the unit cells and the choice of the representative atom in the atomic layer, which does not become always clear in the references.

[4] If the number of atoms of the chemical constituents in the symmetric film equals the ratio of the bulk phase, the film is called stoichiometric.

limit. The surface energy of the S rich films (111)-3S, (210)-2S, (111)-4S, (001)-2S and (210)-2S' decreases with larger μ_S. The S poor films show higher surface energies ranging from about 120 to 250 meV/Å^2, whereas the S rich films exhibit significantly smaller surface energies between 40 and 120 meV/Å^2, except for (210)-2S', which is located at higher energies. However, the (210)-2S' film could not be structurally relaxed due to convergence problems, partially explaining the relatively large energy compared to the other S rich films. Thus, the S poor films are less stable, which explains also the larger structural relaxations as compared to the S rich films (*cf.* appendix G).

The most stable films are the (001)-S, (210)-2S and (111)-3S film. The (001)-S film has a surface energy of 61 meV/Å^2 and is clearly the most stable surface in the S lean limit. The (111)-3S film has a surface energy between about 40-80 meV/Å^2 depending on μ_S and is the most stable surface in the S rich limit. The surface energy of the (210)-2S film ranges from about 50-70 meV/Å^2 and there is no region for μ_S, where it represents the most stable surface. However, there is an interval of μ_S leading to almost the same surface energies with about 60-62 meV/Å^2 for these three films, and thus a coexistence might be possible under these conditions. In addition, note that the numerical accuracy of the results is limited to about 1 meV/Å^2.

The literature reports the surface energy of the relaxed (001)-S surface to be about 1.06 J/m^2 corresponding to about 66 meV/Å^2 [161, 162], which is in nice agreement to the result of 61 meV/Å^2 reported in this thesis. Qiu *et al.* [164] report a larger surface energy for the relaxed film of 1.23 J/m^2 (77 meV/Å^2), which corresponds to the value reported by Alfonso [160]. The surface energies of the (111)-2S and (210)-S film are reported to be about 87 and 94 meV/Å^2, respectively [163], which fits to the results of 93 and 92 meV/Å^2 in this thesis.

In [160] the surface energies of all the 14 films investigated in this thesis are also presented depending on the chemical potential, showing an overall nice agreement. The relative position of the surface energies to each other is quite similar in both cases, however, there is a small interval of μ_S, where the (210)-2S film[5] is most stable, leading to a smaller interval with (001)-S as most stable film.

Influence of Relaxation and Magnetism It is enlightening to discuss the effect of structural relaxation and magnetism on the surface energies of the iron pyrite films. In Fig. 11.5 this effect is depicted by a histogram, which is adequate to evaluate the differences between the surface energies when including structural relaxation or magnetism. The surface energies have been evaluated at a chemical potential of S located exactly between the two extreme cases of the S lean and S rich limit, and thus where the three most stable surfaces (001)-S, (210)-2S and (111)-3S exhibit quite small differences in the surface energies. Hence, the surface energies of the relaxed films correspond to those in Fig. 11.4 at the corresponding chemical potential.

The effect of structural relaxation can be discussed by comparing the surface energies of the relaxed to the energy of the unrelaxed films, *i.e.* the films using the optimized bulk

[5] Please note that the unprimed (210) films are the primed and vice versa when comparing the results of this thesis to the reference.

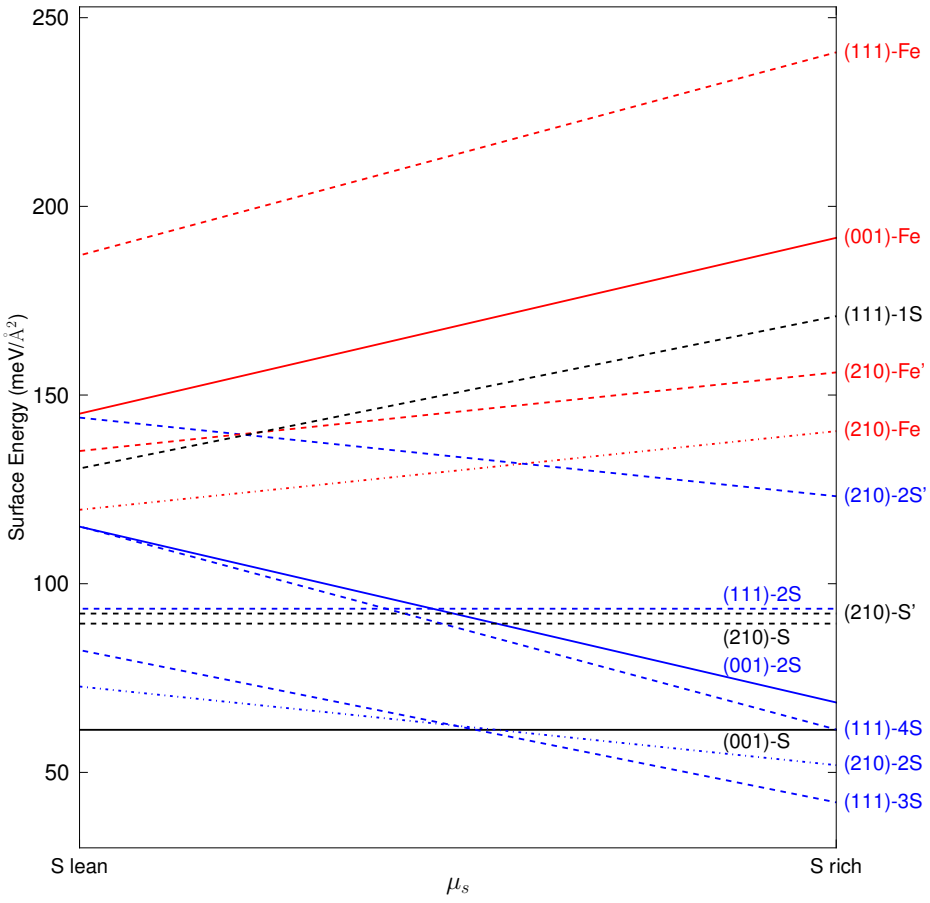

Figure 11.4.: The surface energies of the 14 investigated iron pyrite films of different terminations and orientations depending on the chemical potential of S, denoted as μ_S. The color code is as follows: the Fe terminated films are red, the single S terminated films are black and the multiple S terminated films are blue. The surface energies of the films of (001) orientation are drawn in solid lines, whereas the (111) films and primed (210) films are indicated as dashed and the unprimed (210) films as dashed-dotted lines. The minimum and maximum of μ_S, denoted as S lean and S rich limit, corresponds to the experimental situation where the conditions cause a formation of bcc-Fe or S_8 on the surface in a synthesis. The difference between the S lean and S rich limit is about 0.7 eV.

structure parameters without a relaxation of the film structure. The structural relaxation of the (210)-Fe and (210)-2S' film did not converge, and thus no results could be displayed for them. The structural relaxation leads to a significant decrease of the surface energies of about 10-20%. The films with larger surface energies experience larger displacements of the atoms at the surface leading to a larger difference between the surface energy of the unrelaxed and relaxed film regarding the absolute values.

The effect of magnetism on the surface energies has been investigated by applying spin-polarized DFT to the unrelaxed films. For that matter only collinear ferromagnetic calculations have been carried out, and thus it might be that some of the films have antiferromagnetic or non-collinear magnetic configurations even lowering the surface energy. Again some results are missing, since for (001)-Fe, (210)-Fe, (210)-S, (210)-Fe' and (210)-2S' the magnetic calculations did not converge. The surface energies are reduced by a few percent due to the inclusion of magnetism, and thus they have less of an effect compared to the structural relaxation. Note, that if we had carried out magnetic calculations for the relaxed structures, an even lower reduction of the surface energies or a loss of magnetic moments might occur.

Although the influence of magnetism on the surface energies is quite small, it might have an effect on the stabilization of the most stable iron pyrite films (001)-S, (210)-2S and (111)-3S in the region, where they exhibit almost the same surface energies. Since the (001)-S film is non-magnetic, but the (210)-2S film and the (111)-3S film exhibit magnetism, the stability region regarding μ_S might be expanded for (210)-2S and (111)-3S, whereas the (001)-S becomes less stable. However, note that with a 5 and 4 meV/Å^2 smaller surface energy of the (210)-2S and (111)-3S film due to magnetism, the surface energies of these three films are still quite close to each other.

All investigated iron pyrite films, except the (001)-S film, show a stable magnetic configuration. In the case of the (111) films, the magnetic moments of the top-most Fe atoms and the neighboring S atoms becomes smaller, and thus also the difference in the surface energy between magnetic and non-magnetic film becomes smaller, in the order (111)-Fe, (111)-S, (111)-2S, (111)-3S and (111)-4S. That behavior is quite expected, since bulk iron pyrite is non-magnetic and only the Fe atoms on the surfaces might tend to become magnetic due to changes of the local atomic surrounding. The energy difference between the spin-polarized film and the non-magnetic one as well as the magnetic moments of the top-most atoms is listed in appendix G for all investigated films.

In the literature the (001)-S film is also reported to be non-magnetic [160, 162], however, there is a report that the (001)-S film becomes magnetic within DFT+U [19]. Alfonso shows that the (111)-3S film is magnetic with magnetic moments in reasonable agreement to those listed in this thesis, but he finds that the (210)-2S film is non-magnetic in contradiction to my results [160], which might be an effect of the structural relaxation.

11.5. Conclusions

The thermodynamic stability of 14 iron pyrite films of different terminations and orientations has been investigated in this chapter. The influence of structural relaxation and magnetism

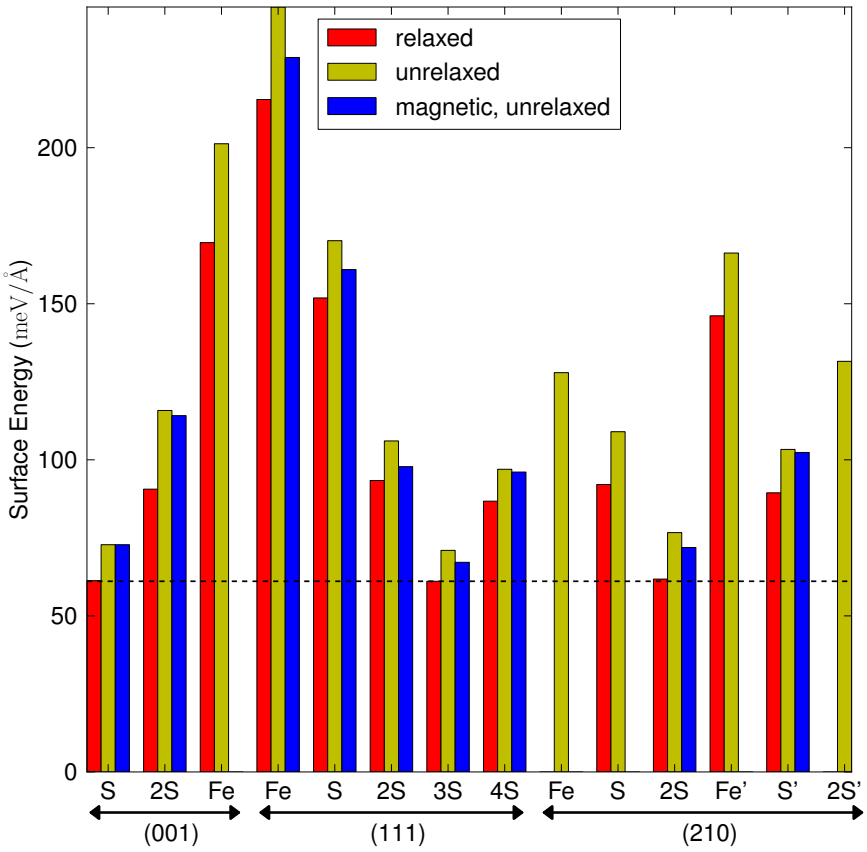

Figure 11.5.: The influence of structural relaxation and magnetism on the surface energies of the 14 iron pyrite films with (001), (111) and (210) orientation is depicted in this histogram. A chemical potential which is exactly between the S lean and S rich limit has been used for the evaluation. The surface energies of the relaxed films are indicated as red bars and they correspond to the values in Fig. 11.4 for corresponding μ_S. The yellow bars show the surface energies of the unrelaxed films, *i.e.* the films within the optimized bulk lattice parameters within GGA-PBE but without a relaxation of the film. The blue bars depict the surface energies of the unrelaxed films including magnetism, *i.e.* using a spin-polarized DFT calculation. For some films the structural relaxation or the magnetic calculation did not converge leading to missing bars. The dashed line indicates the surface energy of the most stable film for this particular chemical potential μ_S, *i.e.* (111)-3S.

has been also discussed.

The S rich films exhibit a smaller surface energy than the S poor films. The most stable iron pyrite films are the (001)-S film in the S poor regime and the (111)-3S film in the S rich limit. However, the (210)-2S film is quite close in energy, and thus there are chemical conditions for S, in which all three surface configurations might coexist.

The effect of structural relaxation on the surface energies is quite large for the iron pyrite films with a reduction of about 10-20%. On the other hand, magnetism has a smaller influence on the surface energies, changing them only by a few percent. However, since the (001)-S film is the only investigated iron pyrite film showing no magnetism, the stability regime of the most stable films, namely (001)-S, (210)-2S and (111)-3S, might shift slightly due to magnetism.

In the next chapter a detailed discussion about the electronic structure of these three most stable films is presented.

12. The Electronic Structure of the most stable FeS_2 (001), (111) and (210) surfaces

12.1. Introduction

Interfaces and surfaces play an important role in photovoltaics, and thus the investigation of iron pyrite should not be restricted to the bulk phase only. As stated earlier, the free standing surface can be seen as a simple model of an interface in a device, and the position of electronic surface states in the band structure might reveal bottlenecks for the photovoltaic performance.

In the last chapter the thermodynamically most stable iron pyrite surfaces have been determined to be (001)-S in the S poor limit, (111)-3S in the S rich limit and (210)-2S exhibiting surface energies close-by. The electronic structure of these films will be discussed in this chapter with the main focus lying on the (001)-S film, since it is the most simple of them, whereas the (210)-2S film is only briefly discussed. Note, that the (210)-2S film is also the least stable of these films corresponding to Fig. 11.4. The position of the electronic surface states will be analyzed and, in the case of the (001)-S film, the optical absorption and first attempts for passivation of these surface states using adatoms on top of the surface are presented.

12.2. Computational Details

The electronic band structures have been calculated using DFT within the GGA-PBE functional as implemented in the FLEUR code [66]. The structurally relaxed films have been used (see last chapter and appendix G for results) and no magnetism has been considered.

The computational parameters for the FLEUR code have been chosen as listed in appendix G for the (001)-S, (111)-3S and (210)-2S film.

For the bulk-projected band structures the electronic band structure of iron pyrite bulk has been calculated for the same high-symmetry $\boldsymbol{k}$-path as for the band structure of the film, except that a variable z component has been included, which goes from the Brillouin zone center to the boundary. In the case of the (001)-S film the bulk-projected band structure has been calculated for the iron pyrite bulk structure as shown in Fig. 7.1, whereas for the (111)-3S film a hexagonal unit cell containing 36 atoms has been used, *i.e.* the volume of the unit cell is 3-times as large the simple cubic one of Fig. 7.1. The

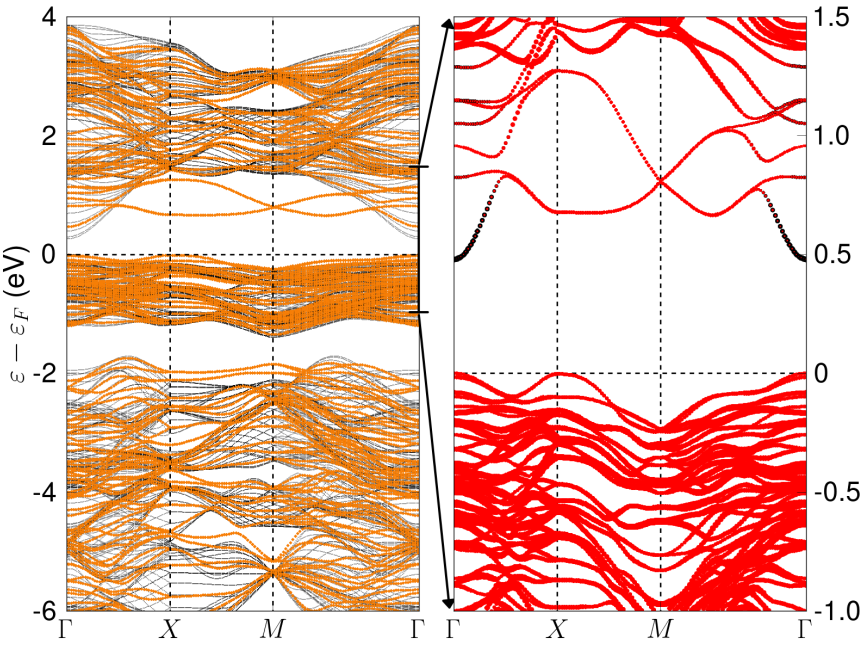

Figure 12.1.: The electronic band structure of the relaxed (001)-S iron pyrite film is displayed once together with the bulk-projected band structure of iron pyrite (left panel: film bands in orange and bulk-projected bands in black), and then for a zoomed section of the energy range indicated by the arrows the orbital-resolved band structure of the film (right panel: S $3p$ in black and Fe $3d$ in red) is shown.

choice of the hexagonal unit cell allows to compare the bulk-projected band structure directly to the band structure of the film without dealing with band folding effects, since the two-dimensional base area of the hexagonal unit cell corresponds to the unit cell of the film.

For the optical absorption of the (001)-S film a $\boldsymbol{k}$-mesh of $10\times10\times1$ has been used. More $\boldsymbol{k}$-points made the calculations in SPEX [69] computationally too demanding.

12.3. Electronic Structure of the (001)-S, (111)-3S and (210)-2S Iron Pyrite Films

The electronic band structure of the (001)-S, (111)-3S and (210)-2S film are investigated in this section. The position of the surface bands and the orbital character are discussed. In the case of the (001)-S film additionally the optical absorption is presented.

(001)-S In Fig. 12.1 the electronic band structure of the (001)-S film is presented. In the left panel the presentation together with the bulk-projected band structure allows to locate the surface bands of the film. The bands of the film have been adjusted to the bulk-projected bands such that some features like the local gaps in the band structure are aligned, *e.g.* around M between -4 to -3.5 eV or from 2.5 to 3 eV.

Of particular interest are the surface bands close to or in the band gap region, since they might have an influence on the photovoltaic performance by reducing the band gap size or acting as charge recombination centers. There are surface bands at the bottom of the conduction bands at around 0.7 eV and also at the top of the valence band defining the valence band edge. A "plain" orbital-resolved density of states plot as it is done in [29] is not accurate enough to find the surface states at the valence band edge, and thus they report only of the surface states in the conduction band, which are in reasonable agreement to the results in this thesis. Zhang *et al.* find two surface states in agreement with my findings, although the surface state at the conduction band is located at higher energies since they applied the DFT+U method [19]. The surface states at the top of the valence bands have been also reported in [20].

The right panel in Fig. 12.1 displays the orbital-resolved band structure of the film, revealing that both surface states are of strong Fe $3d$ character. Hence, the surface states arise due to dangling bonds from the top-most Fe atoms, and thus an incorporation of adatoms on top of the surface might bind to these dangling bonds leading to a passivation of these surface states. In the next section I will discuss about the passivation of the (001)-S surface states in detail.

The fundamental band gap of the (001)-S film is defined by the Fe $3d$ surface states at the top of the valence bands and still (as in bulk) by the S $3p$ conduction band at Γ. The band gap with 0.48 eV is larger than the fundamental band gap of the iron pyrite bulk structure using the optimized structural parameters within GGA-PBE, which is 0.39 eV (see chapter 7). Note that this is a numerical artifact, since an accurate determination of the band edges of the electronic band structure needs also the $\boldsymbol{k}$-path along $\Gamma \rightarrow Z$, which is not possible for the film calculation with finite film thickness. Therefore, band gaps defined by bands showing a large dispersion along $\Gamma \rightarrow Z$, for instance the S $3p$ band in iron pyrite, might be too large.

Since the band gap of iron pyrite in the bulk phase exhibits a strong dependence on the structural parameters (see chapter 7), it is interesting to investigate whether the surface states are also sensitive to the structural parameters. For this in Fig. 12.2 the orbital-resolved band structure of the (001)-S film is displayed for three different structural setups. In the left panel and the central panel the optimized structural parameters a and u within GGA-PBE have been used ($a = 5.40$ Å and $u = 0.3826$), where in the first case the film has been additionally structurally relaxed and for the latter not. The right panel shows the band structure using the structural parameters a and u taken from experiment, *i.e.* $a = 5.418$ Å and $u = 0.385$, with no further structural relaxation of the film.

First of all a difference in the u parameter leads to a different position of the S $3p$ band at Γ with respect to the Fe $3d$ states, as it has been already discussed for iron pyrite bulk, which can be clearly seen by comparing the results for the (bulk-)optimized structural parameters with those using the parameters from experiment, both without

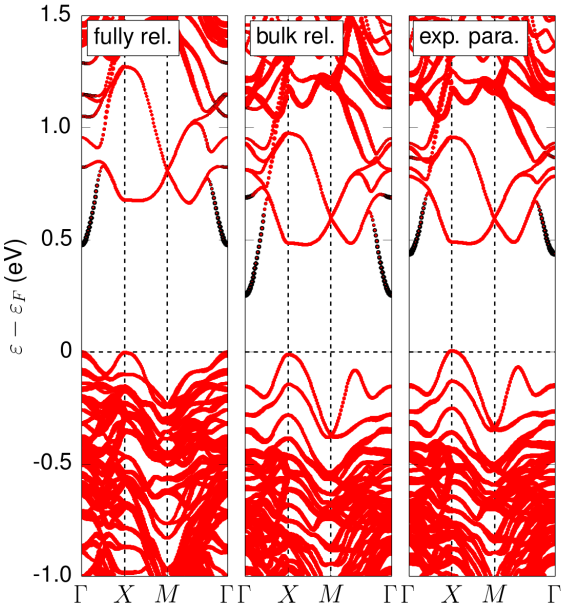

Figure 12.2.: The orbital-resolved band structure of the (001)-S film using the fully relaxed structure (left panel, denoted as "fully rel.") as it is already presented in Fig. 12.1, using the optimized structural parameters of iron pyrite bulk (central panel, denoted as "bulk rel.") and using the structural parameters of iron pyrite bulk from experiment (right panel, denoted as "exp. para."). In the last two cases no further relaxation of the film has been carried out. The S $3p$ character of the bands is indicated in black and the Fe $3d$ character in red like in Fig. 12.1 (right panel). The larger the size of the points is, the stronger is the corresponding orbital character.

further structural relaxation. The Fe $3d$ states in the electronic structure are only slightly affected, including the position and the shape of the Fe $3d$ surface states, and thus the structural parameters have a much smaller influence on the surface bands than on the fundamental band gap.

On the other hand, the structural relaxation of the film significantly changes the position of the surface states. The surface states at the bottom of the conduction band appear slightly shifted upwards, whereas the surface states at the valence band edge are considerably shifted into the bulk bands. The valence band edge is still defined by the Fe $3d$ surface states as it can bee seen in the bulk-projected band structure of Fig. 12.1, but due to the considerable shift at the valence band edge the band gap opens from about 0.25 eV to 0.48 eV. In addition the shape of the top-most valence band is changed. The VBM is located at X before relaxation, but after relaxation the energy of the top-most

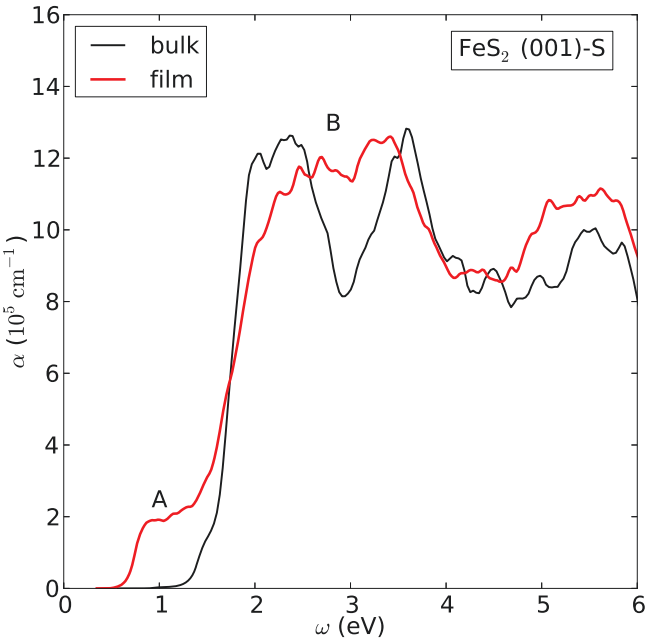

Figure 12.3.: The optical absorption of the relaxed iron pyrite (001)-S film is displayed as red curve, and for comparison the optical absorption of iron pyrite bulk is drawn in black. The first two major peaks of the absorption of the film are denoted as A and B.

valence states at Γ and X are almost the same.

The optical transition elements of iron pyrite in bulk phase between the Fe $3d$ states and the S $3p$ band at the band edges are strongly suppressed, leading to the low-intensity tail in the optical absorption, whereas the transitions between the Fe $3d$ states dominate the first major peak (see chapter 7). Therefore, a considerable influence on the optical absorption from the surface states is expected. In Fig. 12.3 the optical absorption of the (001)-S film is shown compared to the absorption curve of iron pyrite in the bulk phase. The magnitude of the optical absorption is comparable to that of the bulk phase with about $10\text{-}12 \cdot 10^5 \text{cm}^{-1}$. However, the Fe $3d$ surface states lead to considerable changes of the peaks. The two major peaks at $\omega = 2$ and 3.5 eV from the absorption of the bulk phase overlap in the absorption of the film (denoted as peak B), since the first peak is shifted to larger transition energies and becomes broader, whereas the second peak is shifted to smaller energies instead. Most noticeable, there is an additional major peak (denoted as A) at transition energies of about $\omega = 1$ eV, which is caused by the Fe $3d$ transitions between the surface states.

Since the bulk to surface ratio in experiments is much smaller than this in the calculation

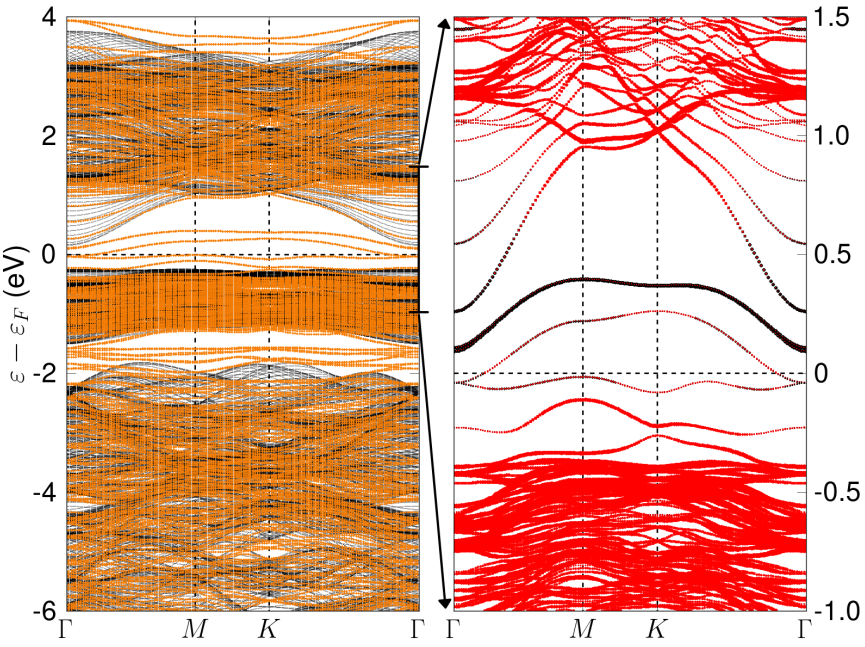

Figure 12.4.: The electronic band structure of the relaxed (111)-3S film is displayed in the left panel (orange curves) together with the bulk-projected band structure (black curves) and in the right panel orbital-resolved into Fe $3d$ (red) and S $3p$ character (black) for a zoomed energy region around the Fermi energy.

of the 1.7 nm thick film, the peak A is expected to be less pronounced in experiments.[1] However, it still might have an influence on the optical band gap size. In [26, 165] the experimental data on the optical absorption of iron pyrite thin films is discussed, showing that the thin films exhibit a smaller optical band gap, although a peak structure like peak A in Fig. 12.3 is not visible.

(111)-3S In Fig. 12.4 the band structure of the relaxed (111)-3S film is presented, aligned to the bulk-projected band structure in the left panel. There are surface bands in the whole energy range of the former band gap region of iron pyrite bulk, making the (111)-3S film metallic. The orbital-resolved band structure in the right panel shows that the surface bands at the top of the former valence band consist mainly of Fe $3d$ character, whereas the S $3p$ character of the surface bands increases when approaching the former conduction band edge.

[1] At least this is expected for experiments measuring the optical transmission. For experiments using the reflection instead, the bulk to surface ratio in the absorption spectrum depends on the penetration depths of the incident light.

Comparing the band structures of the (111)-Fe, (111)-S, (111)-2S, (111)-3S and (111)-4S films in appendix G, reveals that the surface band character is more and more dominated by S $3p$. Since all of these films exhibit (almost) metallic behavior, the strategy to put S in a (111)-like fashion on top of the surface seems not to be a successful strategy to passivate surface states. All these surfaces, including the quite stable (111)-3S surface, are fatal for the photovoltaic performance, and thus they should be avoided when synthesizing iron pyrite. Using S poor conditions in the synthesis should favor the growth of the more promising (001)-S surface.

(210)-2S and other iron pyrite films The electronic structure of the (210)-film will be only briefly discussed, and I refer the reader to the appendix G for the orbital-resolved electronic band structure of the film. There are surface states at the valence band edge and at about 0.3 eV, which exhibit mainly Fe $3d$ character with a small admixture of S $3p$. The latter surface bands are located in the former band gap region of iron pyrite bulk, leading to a significantly reduced band gap of about 0.2 eV compared to the gap in the bulk phase.

Except of the (001)-2S, (111)-3S and (111)-4S films all other films exhibit surface states of Fe $3d$ character around the band edges, which arise due to dangling bonds from the top-most Fe atoms. Thus, the passivation of the Fe $3d$ surface bands by finding suitable adatoms to bind to the dangling bonds of Fe is most important to improve the photovoltaic performance of the iron pyrite films. Without passivation most of the investigated iron pyrite surfaces are metallic or exhibit a very small band gap. The (210)-S and (210)-S' films have a band gap of about 0.5 eV, but are thermodynamically quite unstable. Most promising seems to be the (001)-S film, which is the reason why the next section deals with first attempts to passivate the surface states in this film.

Note that all the films (except the (001)-S film) exhibit a more stable magnetic configuration, and thus the position of the surface bands in the electronic band structure might change when accounting for magnetism in the DFT calculations, which has not been done in this section. However, also note that the magnetic properties of the films are expected to disappear with passivation of the surface states.

12.4. Adatoms on top of the Iron Pyrite (001)-S Surface

Since there are Fe $3d$ surface bands in the (001)-S film, which are located in the former band gap region of iron pyrite bulk, more precisely at the top of the valence bands, it is necessary to find a suitable approach to shift these surface states out of the band gap. The Fe $3d$ surface states arise due to dangling bonds from the top-most Fe atoms, and thus one successful approach might be to bind suitable adatoms to the dangling bonds.

A first obvious choice is the deposition of S atoms on top of the surface. However, putting S atoms in a (001)-like fashion with two S atoms per two-dimensional unit cell on top of the surface, *i.e.* growing the (001)-2S surface, worsens the situation, since new

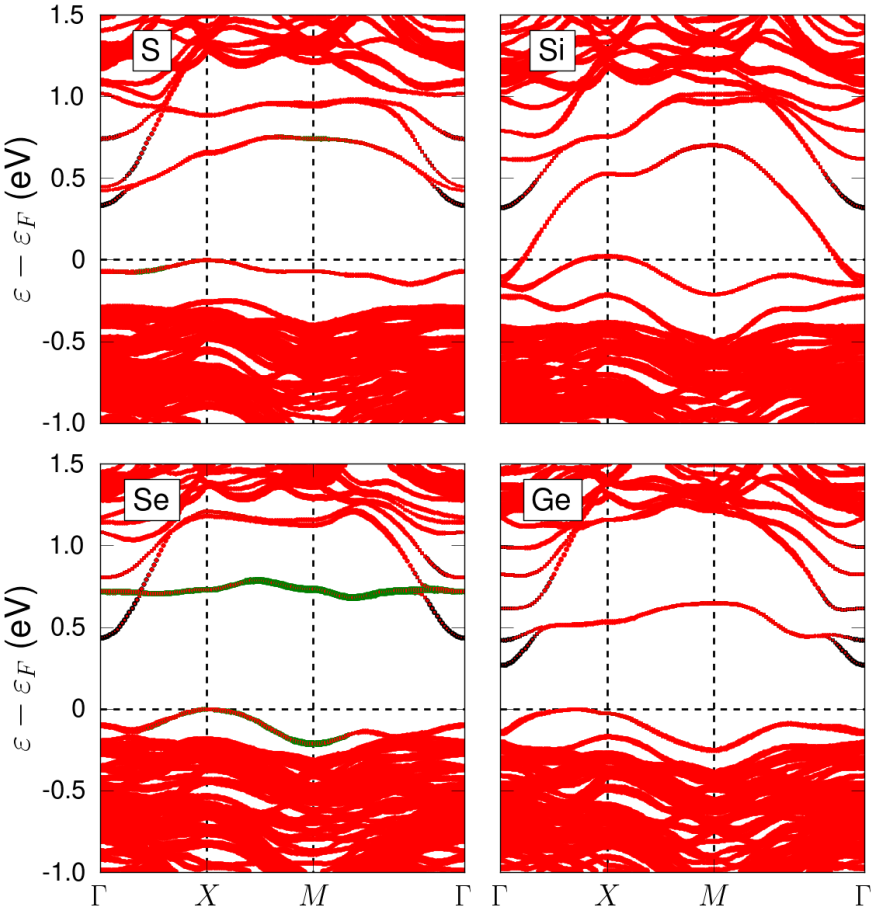

Figure 12.5.: The orbital-resolved electronic band structures of the (001)-S film with S (upper left), Se (lower left), Si (upper right) and Ge (lower right) adatoms deposited on top of the surface. In red the Fe $3d$ character is depicted, and the S $3p$ character and the p character of the adatom is drawn in black and green, respectively. The size of the markers correlates to the contribution of the corresponding orbitals.

dangling bonds from the top-most S atoms appear (see appendix G). Then, surface states of mainly S $3p$ character are located in the band gap region, which even lead to metallic behavior. Hence, it seems there are too many S atoms on the surface in the (001)-2S surface to successfully passivate the Fe $3d$ surface states, and thus a reasonable choice might be to deposit only one S adatom per 2-dimensional unit cell on top of the surface.

To obtain a reasonable starting point for the structural relaxation, the S adatom is put in the center of the connection line between the two positions, where the two top-most S atoms are located in the (001)-2S film. Then, the distances between the adatom and the two top-most Fe atoms are only slightly different with both about 3 Å.[2] Not only the electronic structure of the relaxed (001)-S film with a S adatom on top has been calculated, but also isoelectronic Se has been used as adatom, and furthermore Si and Ge have been used, which exhibit two less electrons per atom than S. I also tried to use O and C as adatoms, but the structural relaxation did not converge for this very light atoms. The orbital-resolved band structures for S, Se, Si and Ge as adatoms are presented in Fig. 12.5.

In all cases the situation has not improved compared to the "plain" (001)-S film. However, interesting conclusions can be drawn by comparing the electronic structures. First of all, except for Si, the surfaces with the adatoms have an improved band structure compared to the (001)-2S film. In the case of Si adsorption the film becomes metallic due to Fe $3d$ surface states. For the S adatom an Fe $3d$ surface band is split off from the bulk valence bands significantly reducing the band gap size. The same happens for the Ge adatom, except that the Fe $3d$ surface states split off from the bulk conduction bands, and pull down the S $3p$ bulk band around Γ together. The best results can be obtained using Se adatoms, which seems to be the only case, where the adatom binds to the dangling bonds of the top-most Fe atoms, since the surface states exhibit considerable Se $4p$ character. In addition, there is only one of the former two surface states left in the conduction band, which can be seen as an improvement. Except of these two points, the electronic structure of the Se-passivated (001)-S film looks quite similar to the "plain" (001)-S film with a slightly smaller band gap size. Therefore, the usage of Se or other heavy adatoms seems more promising than that of light adatoms regarding the passivation of the surface states in the (001)-S film.

12.5. Conclusions

In this chapter the electronic structure of the most stable iron pyrite surfaces (001)-S, (111)-3S and (210)-2S have been discussed.

The (001)-S film exhibits a band gap of 0.48 eV limited by Fe $3d$ surface states located at the valence band edge. There are also Fe $3d$ surface states in the lower conduction bands, but they have no influence on the band gap. The optical absorption is significantly affected by those Fe $3d$ surface states, leading to a peak at smaller energies than the major absorption features caused by transitions between bulk-like states. This peak might appear much smaller in experiment, since the surface to bulk ratio is much smaller in

[2] Preferably, the distances between the S adatom and the two Fe atoms should be the same, but fulfilling this condition leads to unphysically small distances between some other S atoms.

experiment than in the calculations. First attempts to passivate the Fe $3d$ surface states reveal that heavy elements like Se might be better suited to bind to the dangling bonds of the top-most Fe atoms. The (001)-S surface is the most promising of all investigated iron pyrite surfaces from photovoltaic perspective.

The (111)-3S film is metallic due to surface states with Fe $3d$ and S $3p$ character, where the latter becomes dominant the closer the surface states are to the conduction band edge. The metallicity is fatal for photovoltaic performance, which is why the (111)-3S surface poses a problem without further post-treatment.

The (210)-2S films and all other observed iron pyrite films have either a too small band gap, some of them are even metallic, or they are thermodynamically unstable.

13. Conclusions

In this thesis first-principles calculations for pyrite and marcasite compounds have been discussed. The focus has been on the analysis of their fundamental and optical band gap, and their optical absorption, which are essential quantities for photovoltaic applications. The calculations have been performed within density-functional theory (DFT) [39, 40] using various exchange-correlation functionals like the local density approximation (LDA) functional [41, 42], the generalized gradient approximation (GGA) proposed by Perdew, Burke, and Ernzerhof (PBE) [43], as well as hybrid functionals with a focus on the HSE06 functional [56, 57]. To obtain an improved description of electronic excitations the GW approximation [54] has been considered as well. For the DFT calculations the FLEUR code [66] has been used, and the SPEX code [69] has been employed for the GW calculations.

The main part of the thesis is concerned with the electronic structure and the optical properties of iron pyrite, which is reported to be a promising material for photovoltaic applications due to its large optical absorption of 6×10^5 cm^{-1}, a band gap size of 0.95 eV and a photocurrent of 40 mA/cm^2 [13]. In addition, iron pyrite consists of abundant materials, and thus might be suitable for large-scale and long-term applications. However, a reported open-circuit voltage of merely 200 mV, leading to a conversion efficiency of only 3% in iron pyrite solar cells [13], currently still disqualifies iron pyrite for photovoltaic applications. In this thesis a possible cause for this low open-circuit voltage based on the fundamental band gap of iron pyrite in the bulk phase has been presented, which is fundamentally different compared to other explanations reported in literature, which are based on defects, surfaces or precipitations. In addition, the thermodynamic stability and electronic structure of iron pyrite surfaces have been investigated in this thesis, in order to locate electronic surface states, which might act as charge recombination centers, and thus limit the photovoltaic performance.

The analysis of the electronic structure and optical properties of FeS_2 in the marcasite phase has also covered a part of the thesis. The marcasite phase of FeS_2 is reported to coexist with iron pyrite, and a reported band gap size of 0.34 eV made it to an undesired phase impurity [32]. However, the results in this thesis indicate that the FeS_2 marcasite phase might be better suited for photovoltaic applications than iron pyrite.

Since the first-principles results on iron pyrite and iron marcasite within the GW approximation and the more sophisticated hybrid functionals are rather unconventional in comparison to the usually studied main-group semiconductors, the investigation has been extended to a couple of other pyrite and marcasite compounds, revealing that the transitions between p and d states, as well as the large screening of the d states plays a key role for these results.

After having presented a very short summary of the thesis, let me summarize and

conclude this thesis in more detail. For this, the conclusions are partitioned into paragraphs with a different focus.

Iron Pyrite The electronic structure of iron pyrite originates from a complex interplay between the bonding and anti-bonding S $3p$ states of the covalent bond in the S dimers on the one hand, and the crystal field splitting into Fe $3d$ t_{2g} and e_g states due to the octahedral symmetry of the structure on the other hand. This interplay leads to a complex hybridization between the Fe $3d$ and S $3p$ states around the Fermi energy, with quite localized valence band states comprised of mainly Fe $3d$ with an admixture of S $3p$ character, and a single S 3p rich band at Γ defining the conduction band minimum. Thus, the fundamental band gap of iron pyrite is defined between an Fe $3d$ valence state and a S $3p$ conduction state, which has an eminent impact on the sensitivity of the band gap and the optical absorption of iron pyrite.

The Wyckoff parameter u has a considerable influence on the bond length of the S atoms in the S dimers, and thus also on the position of the S $3p$ states with respect to the Fe $3d$ states. Hence, a smaller Wyckoff parameter leads to a smaller fundamental band gap in iron pyrite. For instance, the calculations within the GGA-PBE functional yield a band gap of 0.62 eV using the structural parameters from experiment [51] ($a = 5.42$ Å, $u = 0.385$), whereas the gap is significantly smaller with 0.39 eV using the optimized structural parameters ($a = 5.40$ Å, $u = 0.383$), although the relative difference of the Wyckoff parameters is less than 1%. The fundamental band gap is sensitive to the computational methods like the choice of the exchange-correlation functional as well. Within the hybrid functional HSE06 the band gap is largely overestimated with 2.24 eV, whereas the single-shot GW approach based on PBE results yields an unconventional reduction of the d-p splitting, resulting in a gap of 0.27 eV. In particular the convergence of the GW results is far from trivial, since about 2000 electronic bands need to be considered and the inclusion of local orbitals into the linear augmented plane-wave basis is essential. The DFT+U model [166] using an effective Hubbard-U parameter of 2.4 eV calculated within the constrained random-phase approximation [85] yields apparently the best agreement with a band gap of 0.90 eV compared to the experimentally measured 0.95 eV.

However, one should be careful in only comparing the plain numbers of the band gaps, since the calculated optical absorption within DFT+U is in worse agreement with experiment [33, 34, 138, 139] than the "plain" GGA-PBE or GW result, and thus it is questionable whether the DFT+U model is a suitable approach for iron pyrite. The first major peak in the absorption spectrum comprises mainly of transitions between Fe $3d$ states and it is located at about 2.0-2.2 eV in the experiments and calculations using GGA-PBE and GW, whereas the peak is shifted by about 0.4 eV to larger energies within DFT+U. For all the applied calculation methods in this thesis, the optical absorption exhibits low-intensity contributions from Fe $3d$ to S $3p$ transitions for smaller transition energies, which are situated in the tail of the optical absorption. They are small since on the one hand the contribution of the S $3p$ states to the total density of states is small, and on the other hand the matrix elements of the electric dipole operator are small due to the

localization of the corresponding wave functions on different atoms. These low-intensity contributions paired with the non-parabolic shape of the valence bands make it difficult to use conventional methods to extract the optical band gap from the tail of the optical absorption.

The sensitivity of the band gap and the unconventional optical absorption tail might explain the wide spread of results for the band gap of iron pyrite in literature for both computational results [29, 45–50] as well as experimental measurements [13, 33, 34, 138, 139]. Since the most accepted experimentally measured value for the band gap of 0.95 eV is based on optical absorption measurements, the experiments might not obtain the limiting, fundamental band gap of iron pyrite. First, the fundamental band gap might be smaller than the optical gap due to electric dipole transition elements between Fe $3d$ and S $3p$ states along the high-symmetry $\boldsymbol{k}$-path $\Gamma \rightarrow X$ which are zero due to symmetry and, second, the low-intensity tail of the optical absorption might be wrongly interpreted to be caused by defects, and thus the measured optical band gap is actually too large. The same arguments have been discussed in a quite recent reference for iron pyrite [26].

Assuming that iron pyrite exhibits a quite small fundamental band gap like the 0.3 eV calculated within G_0W_0@PBE, there would be significant consequences for the photovoltaic performance of iron pyrite solar cells. The reported small open-circuit voltage of 0.2 V could be simply explained by a small fundamental band gap, as well as the large free charge carrier densities of 10^{14}-10^{18} cm^{-3} in undoped pyrite using electrical resistivity measurements [14, 27], whereas pristine pyrite should exhibit free charge carrier densities of about 10^{10} cm^{-3} at room temperature. An activation energy of 0.2 eV as measured in temperature-dependent electrical resistivity experiments [37, 38] might be also explained by a small fundamental band gap. A reduction of defects and precipitates to obtain as clean as possible iron pyrite is not going to remedy the cause of the low performance, if the fundamental band of the bulk phase of iron pyrite is already too small, since the photovoltaic performance of the pristine bulk material is one of the most essential limits of a solar cell device.

Although it seems tempting to make the pristine bulk phase of iron pyrite responsible for the low performance, note that the experimental measurements are also quite sensitive to defects or surface-related effects. In addition, it is still not quite clear, whether the GW calculations for iron pyrite need to be performed selfconsistently. The quasiparticle selfconsistent GW (QSGW) [61] results of iron pyrite in this thesis exhibit a quite different size of the band gap with about 0.8 eV compared to the 0.27 eV within single-shot GW. However, note also that although the QSGW method does not suffer of a starting-point dependence and it is a more sophisticated approach than single-shot GW, it tends to overestimate band gaps, as demonstrated in appendix A of this thesis. Additionally, the calculated transition energies within QSGW indicate that the optical absorption might resemble the DFT+U result, and thus are in worse agreement with experiment than the single-shot GW results. For a further analysis, new thoroughly conducted experiments are desirable.

However, even if iron pyrite exhibits a smaller fundamental band gap than expected, it is not automatically inappropriate for photovoltaic applications, since there are ways to increase the band gap size. The application of stress might decrease the bond length of

the S dimers, and thus lead to a larger band gap.

Since interfaces and surfaces play an important role in realistic solar cells, free standing iron pyrite surfaces have been used as a simplified and computationally feasible model of those. The electronic structure of the stoichiometric and non-stoichiometric iron pyrite films with (001), (111) and (210) orientation have been investigated using the GGA-PBE functional. The S rich films are thermodynamically more stable than the S poor films. The most stable films are the (001)-S film for S poor chemical conditions, whereas the (111)-3S film becomes most stable for S rich conditions. The (210)-2S film is close in energy, and there are chemical conditions for which all three surface configurations might coexist.

The electronic structure reveals surface states for all three most stable iron pyrite films, reducing the band gap compared to pristine iron pyrite, which even lead to a metallic surface layer for the (111)-3S film. The surface states comprise mainly of Fe $3d$ character, indicating that they are caused by Fe dangling bonds from the top-most Fe atoms. The (001)-S film exhibits these surface states at the top of the valence band edge. There are surface states at the conduction band too, which do not reduce the size of the fundamental band gap, but they are responsible for a peak in the optical absorption, which is located at lower transition energies than the major peak in the absorption of iron pyrite in the bulk phase.

First attempts to passivate the Fe $3d$ surface states in the (001)-S film have been carried out by placing adatoms on top of the surface, revealing that heavy elements like Se or Ge might be better suited than lighter atoms like S or Si. The (001)-S iron pyrite film is the most promising surface configuration for photovoltaic applications of all those configurations which have been investigated.

Iron Marcasite and other Pyrite and Marcasite Compounds The unconventional results for the band gap size of iron pyrite when applying the HSE06 functional or the GW approximation are not an isolated case, but they occur in a couple of other pyrite and marcasite compounds. The marcasite structure is structurally related to the pyrite structure, also having as characteristics an octahedral coordination of the transition metal atoms and covalent bonds in the dimers, and thus the electronic structure exhibits similar key features to iron pyrite. The pyrite compounds FeS_2, RuS_2, OsS_2, NiP_2 and ZnS_2, and the marcasite compounds FeS_2, $FeSe_2$ and $FeTe_2$ have been investigated and compared. It is found for these compounds that the single-shot GW approach corrects the Kohn-Sham energies of the DFT calculation differently depending on their orbital character, *i.e.* the energy gaps between states of both either mostly d or p character are significantly increased, whereas the energy gaps between a state of p and a state of d character are only slightly increased or even decreased like in the case of iron pyrite and iron marcasite. A large electronic screening caused by the d states seems to be responsible for the rather small increase or even decrease of the p-d gap. In addition, a large screening might be also the reason for the largely overestimated band gaps obtained within the HSE06 functional.

The application of GW and the HSE06 functional on the pyrite and marcasite compounds exhibits this rather universal behavior, and the individual results for the fundamental band

gap and other transition energies depend on their orbital character and the strength of the screening of the corresponding compound. For instance the small screening and the mostly uniform orbital character of the band edges in NiP_2 and ZnS_2 lead to a nice agreement between the HSE06 and GW results, as well as to the experimentally reported band gap for ZnS_2, which is consistent with the conventional wisdom that the HSE06 functional and the GW approach both improve the agreement to experiment compared to the "plain" DFT results. On the other hand, an interesting interplay between a large screening and the complex hybridization between the p and d states in all other investigated pyrite and marcasite compounds is responsible for large deviations between the GGA-PBE, HSE06 and GW results. Since most of the reported, experimentally measured band gaps in literature for these compounds are only estimations (*i.e.* they might be affected by defects, surface states, unusual band shapes and transition matrix elements), new thoroughly conducted measurements are desirable to benchmark the GW and HSE06 results for this intriguing compounds.

Regarding the size of the fundamental band gap calculated within G_0W_0@PBE, RuS_2 pyrite with 0.77 eV, $FeSe_2$ marcasite with 0.84 eV and FeS_2 marcasite with 1.06 eV are most interesting for photovoltaic applications. In particular the latter has been investigated in detail in this thesis, since it consists of abundant elements and it has been reported to coexist in iron pyrite crystals [32]. Iron marcasite has been tagged as undesired phase impurity for a long time, since it is reported to have a rather small band gap of 0.34 eV [32], however, the calculations in this thesis show not only a larger band gap in iron marcasite than in iron pyrite, but the optical absorption is also significantly larger, which makes it highly suitable for photovoltaic applications from the theoretical point of view. In difference to iron pyrite there are no low-intensity transitions in the tail of the absorption and the valence and conduction band edge are more parabolic, which allows to determine the absorption edge, and thus the optical band gap, much more accurate compared to the case in iron pyrite. Hence, iron marcasite deserves to be reinvestigated.

A. Quasiparticle Selfconsistent GW Results for Simple Semiconductors and Insulators

Introduction The GW approximation has earned its merits in the prediction of band gaps of semiconductors and insulators, and is (almost) a standard tool in the computation of these systems nowadays. Mostly, single-shot GW approaches are still used due to the computational demand of the GW calculations and the conceptional difficulties of a selfconsistent GW implementation. However, single-shot GW approaches suffer of a starting-point dependence, which also means that in cases where the starting point is "pretty bad", they might lead to wrong results. For instance, a system predicted to be metallic within the GGA-PBE functional might remain metallic after applying GW, although the experiment clearly finds a semiconductor.

A remedy of the starting-point dependence are selfconsistent GW approaches. In this thesis I employ the recently developed and already well-accepted quasiparticle selfconsistent GW (QSGW) method [61]. Some details about the theory are presented in chapter 4 and the references within.

To evaluate the performance of the QSGW method I have calculated the transition energies of a couple of simple semiconductors and compared them to the single-shot GW results and to calculations using the hybrid functional HSE06 (see chapter 3), both well-accepted methods for calculating band gaps in these materials.

Computational Details For the DFT calculations within the GGA-PBE functional and the HSE06 functional the FLEUR code [66] has been employed.[1] For the GW calculations (single-shot and QSGW) the SPEX code [69] has been used.

The DFT and the GW results have been carefully converged with respect to the plane-wave cutoff $k_{\max}$, the number of $\boldsymbol{k}$-points, the angular momentum cutoff $l_{\max}$, and the number of electronic bands N_{bands}. The inclusion of higher-energy local orbitals or semicore states as local orbitals into the LAPW basis has been tested, too. A detailed explanation of these computational parameters is presented in chapter 5.

In table A.1 the computational parameters for the GW calculations of the simple semiconductors are listed, including the lattice parameter of the conventional cubic unit cell.[2] The investigated semiconductors and insulators are Si, C, Ar, MgO, NaCl and GaAs,

[1] The calculations within the HSE06 functional have been carried out by Dr. Martin Schlipf. A future publication containing also these results is in preparation.

[2] The computational parameters of the DFT calculations are not listed in the table, since the focus of

	$k_{\max}$	$l_{\max}$	$\boldsymbol{k}$-mesh	N_{band}	LOs	a	Ref.
Si	3.8	10	4×4×4	150	4s; 4p; 4d; 5f	5.431	[167]
C	4.9	8	4×4×4	150	3s; 3p; 4d; 5f	3.567	[168]
Ar	4.3	10	6×6×6	150	4,5s; 4,5p; 4,5d; 5,6f	5.311	[167]
MgO	5.0	10, 6	4×4×4	200	Mg: 4s; 4p; 4d; 5f; 2p O: 3,4s; 3,4p; 4,5d; 5,6f	4.212	[169]
NaCl	4.4	10, 8	4×4×4	250	Na: 4s; 4p; 4d; 5f; 2p Cl: 4s; 4p; 4d; 5f	5.620	[170]
GaAs	3.9	10, 10	4×4×4	300	Ga: 5s; 5p; 4d; 5f As: 5s; 5p; 4d; 5f	5.653	[171]

Table A.1.: The computational parameters for the GW calculation of Si, C, Ar, MgO, NaCl and GaAs. The plane-wave cutoff $k_{\max}$ (in a.u.$^{-1}$), the angular momentum cutoff $l_{\max}$ (for both atom types in MgO, NaCl and GaAs), the $\boldsymbol{k}$-mesh, the number of electronic bands N_{band}, and the considered local orbitals are listed. In addition the lattice parameters a (in Å) from experiment with the corresponding references are also given.

and thus a large range of fundamental band gap sizes is covered.

The GW results are sufficiently converged using a 4×4×4 $\boldsymbol{k}$-mesh (except of Ar, where a 6×6×6 $\boldsymbol{k}$-mesh has been used), and about 150-300 electronic bands depending on the compound have been used. In all cases at least one full set of s, p, d and f orbitals has been included as higher-energy local orbitals. For the ionic compounds MgO and NaCl the inclusion of the Mg 2p and Na 2p semicore state as local orbital into the LAPW basis is important for convergence. Plane-wave cutoffs of about 3.8-5.0 a.u.$^{-1}$ and angular momentum cutoffs of about 8-10 are sufficient. The muffin tin radii are between 1.4 and 2.8 a.u. depending on the system (not listed in table A.1). They are chosen such that they almost touch each other in the corresponding structure, and they approximately fulfill the condition $k_{\max}R_{\text{MT}} = l_{\max}$.

Results In Fig. A.1 the transition energies of Si, C, Ar, MgO, NaCl and GaAs calculated within the GGA-PBE and HSE06 functional, and G_0W_0@PBE and QSGW are displayed and compared to the energy measured in the experiment. Therefore, the gray linear curve indicates a perfect agreement between the calculated transition energies and the experimentally measured ones ($\varepsilon_{\text{gap}}^{\text{exp}} = \varepsilon_{\text{gap}}^{\text{theo}}$). In the figure only those transition energies of the investigated systems are drawn, for which an experimentally measured value is reported. The $\Gamma \to \Gamma$ transition for all the semiconductors and the $\Gamma \to X$ and $\Gamma \to L$ transition for Si and GaAs are used. The calculated and, if available, experimentally measured transition energies of $\Gamma \to \Gamma$, $\Gamma \to X$ and $\Gamma \to L$ for all the investigated semiconductors are listed

this chapter lies on the GW results.

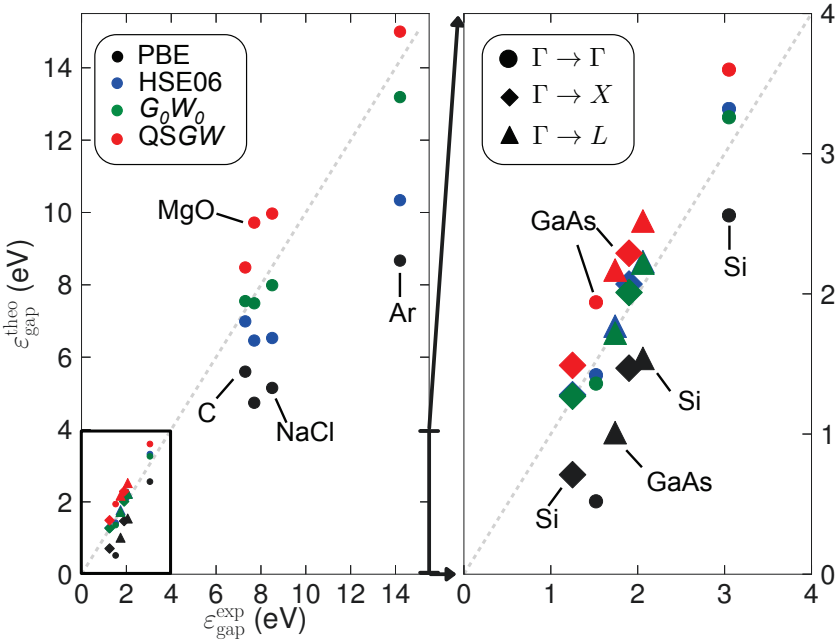

Figure A.1.: The transition energies of $\Gamma \to \Gamma$ (circles) for Si, C, Ar, MgO, NaCl and GaAs, and additionally the transition energies of $\Gamma \to X$ (diamonds) and $\Gamma \to L$ (triangles) for Si and GaAs are displayed. The transition energies are calculated within GGA-PBE (black), HSE06 (blue), G_0W_0@PBE (green) and QSGW (red), and they are plotted against the values measured in experiment. Hence, a value on the gray dashed linear curve means a perfect agreement between theory and experiment. Since the results within the energy scale between 0 and 4 eV are difficult to display in the left panel, a zoom into the corresponding energy range is shown in the right panel. The transition energies are also listed in table A.2.

in table A.2.

The investigated semiconductors and insulators cover a wide range of energy gaps with Si and GaAs exhibiting small to moderate energy gaps from about 1 to 4 eV, then diamond and the ionic compounds MgO and NaCl with energy gaps between 6 to 10 eV and finally a very large band gap insulator with Ar with up to 14 eV transition energies. Since the transition energies between 0 and 4 eV are hard to analyze on the energy scale of the left panel of Fig. A.1, a zoom into this energy range is presented in the right panel of the figure.

The calculated energy gaps within the GGA-PBE functional are in all cases smaller than the gaps measured in experiment, which is consistent with the conventional wisdom that the energy gaps within (semi-)local exchange-correlation functionals like the LDA or the GGA functionals are underestimated.[3] In some cases like MgO or Ar the underestimation is quite strong, exhibiting an almost 50% smaller energy gap.

The hybrid functional HSE06 yields a nice agreement of the energy gaps with experiment for the small to moderate band gap semiconductors Si and GaAs. However, the energy gaps in the large band gap systems seem to be systematically underestimated by HSE06. The calculated transition energies of the simple semiconductors within the GGA-PBE and HSE06 functional in this thesis are in excellent agreement with those of reference [93].

The G_0W_0@PBE calculations yield overall the best agreement with experiment. The maximal relative differences between the experimentally measured and calculated transition energies are about 10% in the $\Gamma \rightarrow \Gamma$ transition of GaAs, but the average relative difference is only about 5-6%. There is no clear under- or overestimation of the results compared to experiment. The HSE06 and G_0W_0@PBE results for Si and GaAs are in a quite nice agreement.

The energy gaps within QSGW exhibit in all cases a slight to moderate overestimation compared to experiment, *e.g.* in the case of MgO the energy gap is about 30% larger. The average overestimation is about 20%.

At first sight it is quite surprising, that G_0W_0@PBE performs better for the simple semiconductors than QSGW, since the QSGW method is more sophisticated and does not suffer of a starting-point dependence. However, a possible explanation might be that in both methods no excitonic and thermal effects are included, which both would reduce the size of the energy gaps. Accounting for these effects might significantly improve the QSGW results, as it is reported in [61]. On the other hand, the screening in the single-shot GW approach might be overestimated, leading to energy gaps, which would be systematically too small if thermal and excitonic effects were considered. Thus, single-shot GW might profit from a fortuitous error cancellation.

[3] At least this is the case for most simple semiconductors and insulators. As I discuss in this thesis, there are compounds like the pyrites and marcasites, which might not follow this rule-of-thumb.

		GGA-PBE	HSE06	G_0W_0	QSGW	exp.	Ref.
Si	$\Gamma \to \Gamma$	2.56	3.32	3.26	3.60	3.05	[172]
	$\Gamma \to X$	0.71	1.28	1.27	1.49	1.25	[172]
	$\Gamma \to L$	1.54	2.23	2.22	2.52	2.06	[173]
C	$\Gamma \to \Gamma$	5.60	6.99	7.55	8.48	7.3	[174]
	$\Gamma \to X$	4.77	5.92	6.26	7.09	-	-
	$\Gamma \to L$	8.48	10.03	10.49	11.57	-	-
Ar	$\Gamma \to \Gamma$	8.67	10.34	13.19	15.00	14.2	[175]
	$\Gamma \to X$	11.33	13.02	16.10	17.79	-	-
	$\Gamma \to L$	11.50	13.24	16.39	18.16	-	-
MgO	$\Gamma \to \Gamma$	4.74	6.46	7.49	9.72	7.7	[176]
	$\Gamma \to X$	9.14	10.84	11.70	13.95	-	-
	$\Gamma \to L$	7.91	9.67	10.69	12.95	-	-
NaCl	$\Gamma \to \Gamma$	5.15	6.53	7.99	9.97	8.5	[177]
	$\Gamma \to X$	7.55	9.03	10.73	12.73	-	-
	$\Gamma \to L$	7.28	8.64	10.22	12.17	-	-
GaAs	$\Gamma \to \Gamma$	0.52	1.42	1.36	1.94	1.52	[174]
	$\Gamma \to X$	1.47	2.07	2.01	2.29	1.90	[174]
	$\Gamma \to L$	1.01	1.77	1.72	2.17	1.74	[174]

Table A.2.: The transition energies of $\Gamma \to \Gamma$, $\Gamma \to X$ and $\Gamma \to L$ for Si, C, Ar, MgO, NaCl and GaAs within the GGA-PBE and HSE06 functional, and the G_0W_0@PBE and QSGW approach. The experimental values (if available) with the corresponding references are listed in the last two columns.

B. Calculating the Optical Absorption

Introduction The optical absorption of a material is an important quantity for photovoltaic applications. A large optical absorption within a wide range of the (visible) light spectrum is desirable, since then already thin absorption layers can absorb most of the light, and thus the amount of material for the solar cell can be significantly reduced.

For an exact calculation of the optical absorption, a two-particle Green's function is necessary, since an optical excitation does not change the number of particles, as it is the case for photoemission (*cf.* chapter 4), but a coupled electron-hole pair is created. Therefore, an accurate description of excitonic effects might be important for the optical absorption. The simplest methods capable of calculating excitonic effects are time-dependent density-functional theory methods with specific kernels or the Bethe-Salpeter equations [105]. Both methods are computationally quite demanding, and thus limited to smaller systems. However, for many systems the specific excitonic effects are rather small, and thus the optical absorption calculated from "conventional" DFT can be seen as a good approximation. In this appendix I will discuss the approach how the optical absorption is calculated in this thesis and the numerical difficulties. In this appendix the SI unit system is used instead of atomic units.

The Total Transition Rate The electrons couple to the light via the vector potential

$$\boldsymbol{A}(\boldsymbol{r},t) = A_0\hat{\boldsymbol{e}}\mathrm{e}^{\mathrm{i}(\boldsymbol{q}\boldsymbol{r}-\omega t)}, \tag{B.1}$$

where $\hat{\boldsymbol{e}}$ is a unit vector pointing along the direction of $\boldsymbol{A}$ and A_0 is the amplitude of the vector potential. The frequency is related to the wave vector via

$$\omega = cq/n, \tag{B.2}$$

where n is the refraction index of the medium in which the light wave travels. Then, the linear momentum of an electron is transformed to a "generalized" linear momentum $\boldsymbol{p} - e\boldsymbol{A}$, and thus the kinetic energy term transforms to

$$\hat{T}_{\mathrm{gen}} = \frac{(\boldsymbol{p}-e\boldsymbol{A})^2}{2m_e} = \hat{T} + \hat{H}_{e-l} + \mathcal{O}(\boldsymbol{A}^2), \tag{B.3}$$

with

$$\hat{T} = \frac{\boldsymbol{p}^2}{2m_e} \tag{B.4}$$

$$\hat{H}_{e-l} = -\frac{e}{m_e}\boldsymbol{A}\boldsymbol{p}. \tag{B.5}$$

The former expression is the kinetic energy of an electron, whereas the latter term is the linear coupling between an electron and the light. The term proportional to $\boldsymbol{pA}$ is chosen to zero using the Coulomb gauge. In the following non-linear terms in the vector potential $\boldsymbol{A}$ are neglected, since they are small for not too large light intensities.

Defining $\hat{H}_{e-l}$ as the perturbation acting on an electron in a solid and exploiting Fermi's Golden Rule we obtain

$$W_{i\to f} = \frac{2\pi}{\hbar}|\langle f|\hat{H}_{e-l}|i\rangle|^2\delta(\hbar\omega - \varepsilon_f + \varepsilon_i), \tag{B.6}$$

where i and f are the initial and final state of the electron with the corresponding band energies ε_f and ε_i, respectively, δ is the Kronecker-delta function and $W_{i\to f}$ is the transition rate for the transition between the states i and f. The delta function in the energies represents the energy conservation of the process, since the energy of the absorbed photon has to correspond to the energy of the transition $\varepsilon_f - \varepsilon_i$.

For slowly varying light waves in space, the electric dipole approximation is quite reasonable, *i.e.* $\mathrm{e}^{\mathrm{i}\boldsymbol{kr}} \approx 1$. Then, the matrix elements of the perturbation become

$$\langle f|\hat{H}_{e-l}|i\rangle = -\frac{eA_0}{m_e}\langle f|\hat{\boldsymbol{e}}\boldsymbol{p}|i\rangle. \tag{B.7}$$

The connection to the electric dipole operator $\hat{\boldsymbol{d}} = -\mathrm{e}\hat{\boldsymbol{r}}$ can be seen by considering the Heisenberg equation of motion for the spatial operator $\hat{\boldsymbol{r}}$:

$$\begin{aligned}\langle f|\hat{p}|i\rangle &= \mathrm{i}\frac{m_e}{\hbar}\langle f|[\hat{H},\hat{r}]|i\rangle = \mathrm{i}\frac{m_e}{\hbar}(\varepsilon_f - \varepsilon_i)\langle f|\hat{r}|i\rangle \\ &= \mathrm{i}\omega m_e\langle f|\hat{r}|i\rangle.\end{aligned} \tag{B.8}$$

For the matrix elements $\langle f|\hat{\boldsymbol{e}}\boldsymbol{p}|i\rangle$ the selection rules of the electric dipole apply, *i.e.* $\Delta l = \pm 1$ and $\Delta m = 0, \pm 1$ for transitions exhibiting no spin-flip ($\Delta s = 0$).

To obtain the total transition rate of all possible transitions per unit volume from eq. (B.6), we have to sum over all $\boldsymbol{k}$-points and all initial and final states and divide by the volume of the unit cell V.[1] Additionally, usually the spherical average over all directions $\hat{\boldsymbol{e}}$ is taken, indicated by $\overline{\hat{\boldsymbol{e}}\boldsymbol{p}}$, which leads to an additional factor $1/3$. This can be seen by taking the integral of the vector product of the unit vectors with an angular-independent matrix $\underline{\mathbf{M}}$ over the complete sphere, which is of similar form to $|\langle f|\hat{\boldsymbol{e}}\boldsymbol{p}|i\rangle|^2$:

$$\frac{1}{4\pi}\int d\Omega \sum_{i,j}\hat{\boldsymbol{e}}_i^T(\Omega)M_{ij}\hat{\boldsymbol{e}}_j(\Omega) = \frac{1}{4\pi}\frac{4\pi}{3}\overline{\hat{\boldsymbol{e}}^T\underline{\mathbf{M}}\hat{\boldsymbol{e}}}. \tag{B.9}$$

Note that the terms with $i \neq j$ vanish for angular-independent $\underline{\mathbf{M}}$, and the factor $1/3$ enters due to the three diagonal terms.

With this the total transition rate looks as follows:

$$W(\omega) = \frac{2\pi}{3V\hbar}\left(\frac{eA_0}{m_e}\right)^2\sum_{\boldsymbol{k},i,f}|\langle f|\overline{\hat{\boldsymbol{e}}\boldsymbol{p}}|i\rangle|^2\delta(\hbar\omega - \varepsilon_f + \varepsilon_i). \tag{B.10}$$

[1] The sum over the $\boldsymbol{k}$-points needs to be normalized by dividing by the number of $\boldsymbol{k}$-points, which is not explicitly shown in the following equations.

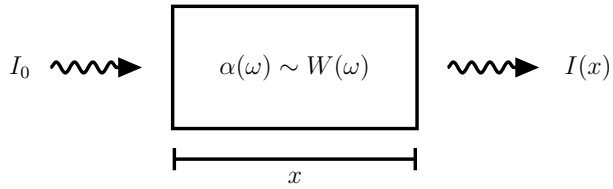

Figure B.1.: The intensity of an incident light wave I_0 decreases in the material due to optical absorption to a value $I(x)$ after the light traveled a distance x. That is the so-called Beer-Lambert law. The material-dependent optical absorption coefficient $\alpha(\omega)$ describes this process and is related to the total transition rate $W(\omega)$ of the system as explained in the text.

The Connection to the Optical Absorption To connect the total transition rate to the optical absorption $\alpha(\omega)$, let me first define the optical absorption. The optical absorption coefficient of a material is the exponent describing the exponential decrease of the intensity of a traveling light wave in this material. This exponential decrease is also known as Beer-Lambert law. In Fig. B.1 the process of absorption is depicted.

The exponential decay of the intensity

$$I(x) = I_0 \mathrm{e}^{-\alpha x} \tag{B.11}$$

follows from the attenuation for small x:

$$I(x) - I_0 = \Delta I = -\alpha I_0 x. \tag{B.12}$$

Due to energy conservation the change in the intensity, which is the transferred energy per unit area and time, has to correspond to the energy transitions in the material, and thus

$$\alpha I_0 x = \hbar\omega W(\omega) x, \tag{B.13}$$

and thus

$$\alpha = \hbar\omega \frac{W(\omega)}{I_0}. \tag{B.14}$$

Now, we need the connection between the intensity I_0 and the vector potential amplitude A_0 to find a suitable expression for α. The energy flow per area and per time in the light wave can be calculated via the Poynting vector

$$\boldsymbol{S} = \boldsymbol{E} \times \boldsymbol{H}, \tag{B.15}$$

where $\boldsymbol{E}$ is the electric field and $\boldsymbol{H}$ the magnetic field of the light wave. Since it holds[2]

$$\boldsymbol{E} = -\frac{\partial \mathrm{Re}(\boldsymbol{A})}{\partial t} \tag{B.16}$$

$$\boldsymbol{H} = \frac{1}{\mu_0} \mathrm{rot}\left(\mathrm{Re}(\boldsymbol{A})\right), \tag{B.17}$$

[2]We have introduced a complex vector potential to simplify calculations, but the electric field and the magnetic field as well as the Poynting vector needs to be a real quantity, and thus a cosine vector potential is used here via the real part.

with μ_0 the vacuum permeability, the Poynting vector can be expressed as

$$\boldsymbol{S} = \frac{\omega}{\mu_0}|\boldsymbol{A_0}|^2 \sin^2(\boldsymbol{qr} - \omega t)\boldsymbol{q}. \tag{B.18}$$

The magnitude of the time-averaged Poynting vector is the intensity of the light wave and thus

$$I_0 = \frac{\omega^2 n}{2\mu_0 c} A_0^2 = \frac{1}{2}\omega^2 n c \epsilon_0 A_0^2, \tag{B.19}$$

where we have used $k = \frac{\omega n}{c}$ with n the refraction index of the material and $\epsilon_0 = \frac{1}{\mu_0 c^2}$. With all that solving eq. (B.13) for α holds:

$$\alpha(\omega) = \frac{4\pi e^2}{3Vm_e^2\epsilon_0 cn}\frac{1}{\omega}\sum_{\boldsymbol{k},i,f}|\langle f|\overline{\hat{\boldsymbol{e}}\boldsymbol{p}}|i\rangle|^2\delta(\hbar\omega - \varepsilon_f + \varepsilon_i) \tag{B.20}$$

$$= \frac{4\pi}{3V\epsilon_0 cn}\omega\sum_{\boldsymbol{k},i,f}|\langle f|\overline{\hat{\boldsymbol{e}}\boldsymbol{d}}|i\rangle|^2\delta(\hbar\omega - \varepsilon_f + \varepsilon_i). \tag{B.21}$$

The first expression uses the matrix elements of the linear momentum operator, whereas in the second expression the matrix elements of the electric dipole operator enter. The SPEX code [69] allows to calculate the matrix elements of the dipole operator. In this thesis broadened Lorentzian functions have been used for the delta-functions.

For more details on the theory behind the optical absorption, I recommend to read the following references [178, 179], which I have also used as a guideline for this appendix.

Orbital-resolved Transition Rates From the total optical absorption and the total transition rates no information about the contributing orbitals can be drawn. For that an orbital-resolved analysis is necessary, which is done in the following way:

$$W_{\mu\to\nu}(\omega) = \frac{2\pi}{3V\hbar}\left(\frac{eA_0}{m_e}\right)^2\sum_{\boldsymbol{k},i,f}|\langle f|\overline{\hat{\boldsymbol{e}}\boldsymbol{p}}|i\rangle|^2 D_{i\mu}D_{f\nu}\delta(\hbar\omega - \varepsilon_f + \varepsilon_i), \tag{B.22}$$

where $D_{i\mu}$ and $D_{f\nu}$ are the $\boldsymbol{k}$-resolved and into the orbitals μ and ν resolved orbital contributions of the initial and final state i and f. That definition of the orbital resolved transition rate is in the spirit of a joint density of states. However, with this definition we encounter the problem that the sum over all orbital contributions μ and ν do not add up to the total transition rate.

In this work I have avoided this problem in the following way. First I analyzed the most important orbital contributions to the optical transitions within the observed energy range for the system. Then the appropriate multiplication factors for the corresponding transition rates $W_{\mu\to\nu}(\omega)$ are calculated such that their sum yields approximately the total transition rate in the observed energy range. The multiplication factors are calculated from a system of linear equations, which I get by equalizing a certain number of characteristic values of the total transition rate to the sum of the orbital-resolved transition rates. The

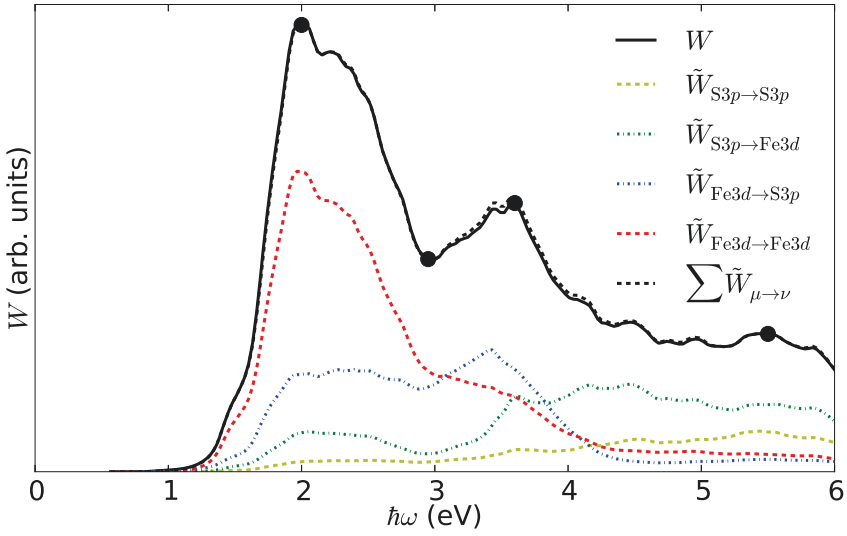

Figure B.2.: The total transition rate W of iron pyrite is presented as a black solid curve. The orbital-resolved transition rates $W_{\mu\to\nu}$ do not add up to the total transition rate, and thus a system of linear equations is solved to find factors such that the multiplied transition rates $\tilde{W}_{\mu\to\nu}$ approximately sum up to the total transition rate. The most important orbital-resolved transition rates are those of the Fe $3d$-Fe $3d$ (red dashed curve), the Fe $3d$-S $3p$ (blue dashed-dotted curve), the S $3p$-Fe $3d$ (green dashed-dotted curve) and the S $3p$-S $3p$ transitions (yellow dashed curve) within the energy range of 6 eV. The sum of these four transition rates is indicated as black dashed curve. The four large black markers show the chosen values for the total transition used in the system of linear equations to obtain reasonable multiplication factors for the orbital-resolved transition rates.

characteristic values in the total transition rate have been peak positions or dips in the most cases.

As an example let me demonstrate this procedure for the case of the total transition rate of FeS_2 pyrite, which is displayed in Fig. B.2. The large black filled circles in the figure indicate the chosen characteristic values of the total transition rate used for the system of linear equations. The main peak at 2 eV, the dip at about 3 eV, the second main peak at about 3.6 eV and a value in the tail of the transition rate at 5.5 eV have been selected. Within the energy range of 6 eV, the main contributions to the total transition rate are from the Fe $3d$-Fe $3d$ (red dashed curve), the Fe $3d$-S $3p$ (blue dashed-dotted curve), the S $3p$-Fe $3d$ (green dashed-dotted curve) and the S $3p$-S $3p$ transitions (yellow

dashed curve).[3] The multiplication factors have been determined to 22, 57, 74 and 150, respectively. The sum of those four orbital-resolved transition rates, each multiplied with the corresponding multiplication factor, yields approximately the total transition rate in the observed energy range. For larger energies (not shown in the figure) the deviations are considerably larger, since other orbital-contributions become eminent.

[3] The term Fe $3d$-Fe $3d$ or S $3p$-S $3p$ transitions with respect to optical transitions might be confusing. The dipole selection rule forbids $\Delta l = 0$, and thus with this term I mean a transition from Fe $3d$ rich bands to Fe $3d$ rich bands, in which a hybridization with other orbital character is essential to obtain non-vanishing dipole matrix elements for these transitions. Formally, it corresponds to equation (B.22).

C. Thermodynamics of Surfaces

Introduction In order to determine the most stable surface configurations of FeS_2 pyrite surfaces, the surface energies have to be compared. The different surface configurations comprise different crystallographic orientations and different surface terminations. Since I consider also non-stoichiometric, symmetric films,[1] the total energies of the density-functional theory calculation can not be compared directly. The number of Fe and S atoms are different for different surface configurations, which has to be accounted for when comparing the energies. Additionally, the non-stoichiometric surfaces exhibit a dependence on the chemical potential of the S and Fe atoms. Thus, the quantity to compare here is the free energy F. I followed the approach of the references [180, 181] to calculate the free energy of the surface systems, which is presented in the next paragraph.

Calculating Surface Energies Let us consider an iron pyrite film consisting of N_{Fe} Fe atoms and N_{S} S atoms with the corresponding chemical potentials μ_{Fe} and μ_{S}. The following equations can be also used for every other film of a binary compound, when replacing Fe with atom type A and S with atom type B. For the free energy of the iron pyrite film the following equation holds:

$$F_{\mathrm{film}} = E_{\mathrm{film}} - N_{\mathrm{Fe}}\mu_{\mathrm{Fe}} - N_{\mathrm{S}}\mu_{\mathrm{S}}, \tag{C.1}$$

where E_{film} is the total energy of the film system obtained in the DFT calculation. This equation depends on two chemical potentials making it quite difficult to analyze, and thus let us try to eliminate one chemical potential from the equation. For this we can exploit that

$$\mu_{\mathrm{Fe}} + 2\mu_{\mathrm{S}} = \mu_{\mathrm{FeS_2}}^{\mathrm{bulk}} \tag{C.2}$$

has to be fulfilled in thermodynamic equilibrium. Here, we have defined an effective chemical potential $\mu_{\mathrm{FeS_2}}^{\mathrm{bulk}}$ for iron pyrite bulk. Solving this equation for μ_{Fe} and inserting it into eq. (C.1) leads to

$$F_{\mathrm{film}} = \left(E_{\mathrm{film}} - N_{\mathrm{Fe}}\mu_{\mathrm{FeS_2}}^{\mathrm{bulk}}\right) - \left(N_{\mathrm{S}} - 2N_{\mathrm{Fe}}\right)\mu_{\mathrm{S}}. \tag{C.3}$$

For stoichiometric surfaces it holds $N_{\mathrm{S}} = 2N_{\mathrm{Fe}}$, and thus the free energy is independent of the chemical potential of the S atoms. The chemical potential of S can be limited to a certain range, for instance representing the experimental conditions during the growth of the surfaces. For $\mu_{\mathrm{S}} \geq \mu_{\mathrm{S}}^{\mathrm{bulk}}$ bulk-phases of S will be formed in the film during the

[1] If the number of atoms of the chemical constituents in the symmetric film does not yield the ratio of the bulk phase, the film is called non-stoichiometric.

synthesis. In the other limit for too small μ_{S}, Fe bulk will be created, and thus we can limit the chemical potential of S to

$$\frac{1}{2}(\mu_{\mathrm{FeS_2}}^{\mathrm{bulk}} - \mu_{\mathrm{Fe}}^{\mathrm{bulk}}) \leq \mu_{\mathrm{S}} \leq \mu_{\mathrm{S}}^{\mathrm{bulk}}, \tag{C.4}$$

where $\mu_{\mathrm{S}}^{\mathrm{bulk}}$ is the effective chemical potential of the most stable S bulk structure, *i.e.* S_8, and $\mu_{\mathrm{Fe}}^{\mathrm{bulk}}$ is the effective chemical potential of the magnetic bcc Fe bulk phase. All these effective chemical potentials are not directly accessible, and thus they are approximated by the total energies of the corresponding bulk phases per formula unit (see [180, 181]).

It is almost unavoidable to have slight inconsistencies between the computational parameters of the film calculations and the bulk calculation of iron pyrite and between the films of different crystallographic orientation due to different two-dimensional unit cells. In the worst case this can falsify the comparison between the surface energies. Therefore, instead of calculating the total energy of iron pyrite bulk from the setup of the bulk structure it is more consistent to calculate it directly from the film calculations. For this the total energies of films with different thicknesses need to be calculated and the following expression yields the total energy of iron pyrite bulk:

$$E_{\mathrm{FeS_2}}^{\mathrm{bulk}} = \frac{E_{\mathrm{film}}^{N'} - E_{\mathrm{film}}^{N}}{N' - N}, \tag{C.5}$$

where N and N' indicate the thickness of the film structures in iron pyrite bulk unit cells and $E_{\mathrm{film}}^{N'}$ and E_{film}^{N} are the corresponding total energies of those films. In this thesis I have calculated the total energy of iron pyrite bulk in this vein for each crystallographic orientation (001), (111) and (210).

Finally, one could ask why can we interpret the free energy of the films as surface energies? - The different surface configurations only differ in a few layers at the top and the bottom of the film, whereas the bulk-like middle is almost the same. Hence, the differences in the free energy of different surface configurations has to be caused by the different surfaces. It is quite common to divide the energy F_{film} by the area of the two-dimensional unit cell to obtain the surface energy in units of J/m^2 or meV/Å^2. Since the films in this thesis exhibit two surfaces, the free energy is furthermore divided by 2. In this thesis I call the free energy of the film also surface energy occasionally.

Important for the comparison of the different surface energies is the (best-possible) consistency of the computational parameters, *i.e.* k_{max}, R_{MT}, l_{max}, the density of the $\boldsymbol{k}$-mesh etc. should be equal. That has been done in this work and the specific parameter setup is discussed in the main text of chapter 11. Before the surface energies are compared, the films have been relaxed, and there the parameters can hardly be chosen equal for all systems. The results for the relaxations and the used computation parameters are displayed in the appendix G.

D. Numerical Parameters for the DFT Calculations of Iron Pyrite

The convergence of the total energy and the fundamental band gap of iron pyrite for the numerical parameters of the FLAPW code FLEUR [66] (see chapter 5) are discussed in this appendix.

In Fig. D.1 the dependence of the total energy and the band gap at Γ for iron pyrite on the plane-wave cutoff $k_{\max}$ is displayed. Note, that the differences between the total energies calculated with different plane-wave cutoffs is much larger than the energy differences for the band gap. The convergence behavior looks quite similar for the total energy and the band gap. Comparing the values for $k_{\max} = 4.0$ a.u.$^{-1}$ with those for $k_{\max} = 4.6$ a.u.$^{-1}$, we see that the total energy changes less than 0.2 eV and the size of the band gap changes less than 10 meV. Since a plane wave cutoff of $k_{\max} = 4.6$ a.u.$^{-1}$ can be regarded as extraordinary large for "conventional" DFT calculations, the choice of $k_{\max} = 4.0$ a.u.$^{-1}$ yields sufficiently accurate results. With $k_{\max} = 4.0$ a.u.$^{-1}$ the LAPW basis contains already about 100 basis functions per atom for iron pyrite, whereas more than 140 basis functions per atom are used for $k_{\max} = 4.6$ a.u.$^{-1}$. For much larger plane wave cutoffs ($k_{\max} > 7.0$ a.u.$^{-1}$) the total energy follows the trend of convergence first, but then the total energy starts to strongly decrease (not shown in figure). This numerical artifact is caused by linear dependencies in the LAPW basis.

With the sufficiently high plane wave cutoff $k_{\max} = 4.0$ a.u.$^{-1}$ I have calculated the band gap depending on the angular momentum cutoff $l_{\max}$, which is presented in the table on the right side of Fig. D.1. By varying $l_{\max}$ from 6 to 12 the band gap changes about 2 meV, which means the "standard" value of $l_{\max} = 8$ is good enough for our purposes. The same is true for a $\boldsymbol{k}$-mesh of 10×10×10 $\boldsymbol{k}$-points. The band gap at Γ varies in the region of μeV for the different $\boldsymbol{k}$-meshs (the accuracy in the table beside Fig. D.1 only covers meV), and thus iron pyrite is accurately described already with a much less dense $\boldsymbol{k}$-mesh like 4×4×4. However, since we are not only interested in the band gap, but also orbital contributions and in the case of the surfaces also magnetic properties, it is safer to use a dense $\boldsymbol{k}$-mesh from the beginning, in particular since these $\boldsymbol{k}$-mesh sizes present not the bottleneck for "conventional" DFT calculations. Due to the 24 symmetries of the iron pyrite system the 6×6×6 $\boldsymbol{k}$-mesh contains 11 irreducible $\boldsymbol{k}$-points, whereas the 10×10×10 $\boldsymbol{k}$-mesh has 45 irreducible points.

Since the FLAPW calculations do almost not depend on the radii of the muffin tins,[1]

[1] This is the case as long as the muffin tin radii are not chosen too small, since then core states and valence states can not be separated any more. In addition, note that as a rule-of-thumb the relation $R_{\mathrm{MT}} k_{\max} \approx l_{\max}$ should be fulfilled.

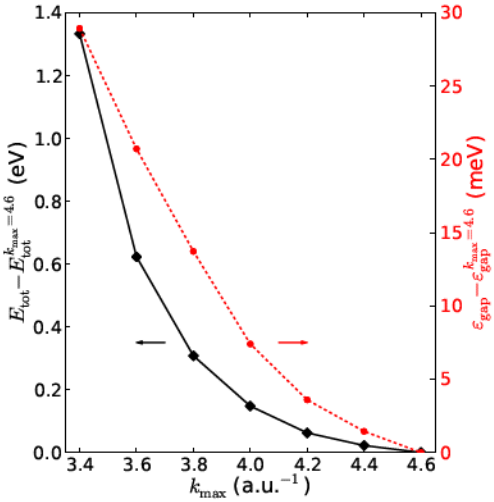

$l_{\max}$	6	8	10	12
ε_{gap}	0.622	0.621	0.620	0.620
$n_{\boldsymbol{k}}$	6	8	10	12
ε_{gap}	0.621	0.621	0.621	0.621

Figure D.1.: The convergence of the total energy (left axis) and the band gap at Γ (right axis) of iron pyrite with respect to the plane-wave cutoff $k_{\max}$ is displayed for a "conventional" DFT calculation using the GGA-PBE functional. For both the total energy and the band gap the value at $k_{\max} = 4.6$ has been subtracted. For these calculations an angular momentum cutoff $l_{\max} = 8$ and $10{\times}10{\times}10$ $\boldsymbol{k}$-points have been used. The two tables beside the figure display the convergence of the band gap (in eV) of iron pyrite with respect to $l_{\max}$ and the $\boldsymbol{k}$-mesh, which has been chosen to $n_{\boldsymbol{k}} \times n_{\boldsymbol{k}} \times n_{\boldsymbol{k}}$. There the converged value of $k_{\max} = 4.0$ has been used.

they are no convergence parameters. The muffin tin radii for the iron pyrite structure with a lattice parameters of $a = 5.418$ Å and a Wyckoff parameter of $u = 0.385$ are chosen to $R_{\text{MT}}^{\text{Fe}} = 2.23$ a.u. and $R_{\text{MT}}^{\text{S}} = 1.98$ a.u., and thus they almost touch each other. However, the iron pyrite structure is a quite open structure, *i.e.* the interstitial region covers a relatively large part of the space.

E. Charge Density Slices of Iron Pyrite

In the following figures the projected charge density of FeS_2 pyrite onto the plane spanned by the directions (111) and $(1\bar{1}0)$ is presented for different energy regions (see also Fig. 7.4). The band structure can be divided into distinct regions of quite different orbital character, which is explained in detail in the chapter 7 and Fig. 7.2. Each charge density plot has been plotted on a logarithmic scale with a RGB (Red-Green-Blue) color code (*i.e.* red/blue minimal/maximal charge density contribution). The black box indicates the two S atoms forming the S dimer orientated along the (111) direction and the red box indicates the position of the Fe atoms along the same direction.

- ad (a): This charge density slice has been calculated in the energy interval of -18 to -10 eV, where the s states of S are dominating. The s-s hybridization can be clearly seen between the S-dimers. The complicated inner structure of the isolines originates from the roots of the $3s$ function. A little bit of hybridization between the Fe $3d$ and S $3s$ states is also visible.

- ad (b): For this charge density slice an energy interval of -8 to -2 eV has been considered, where mainly the $3p$ states of S are contributing. Note the increased content of Fe $3d$ character. However, the S $3p$ character dominates, forming typical $pp\sigma$ bonds.

- ad (c): The energy interval for this charge density slice is chosen to -1.5 to 0.5 eV, and thus includes the VBM. The S $3p$ character is almost not visible any more, instead the Fe $3d$ character dominates the charge density. An sp^3d^2 hybridization can not be located, which indicates a more ionic bonding between Fe and S.

- ad (d): For this charge density slice an energy interval between 0.5 to 5 eV has been used. There is still a dominating Fe $3d$ character. However, S $3p$ character coming from $pp\pi^*$ bonds is also observable.

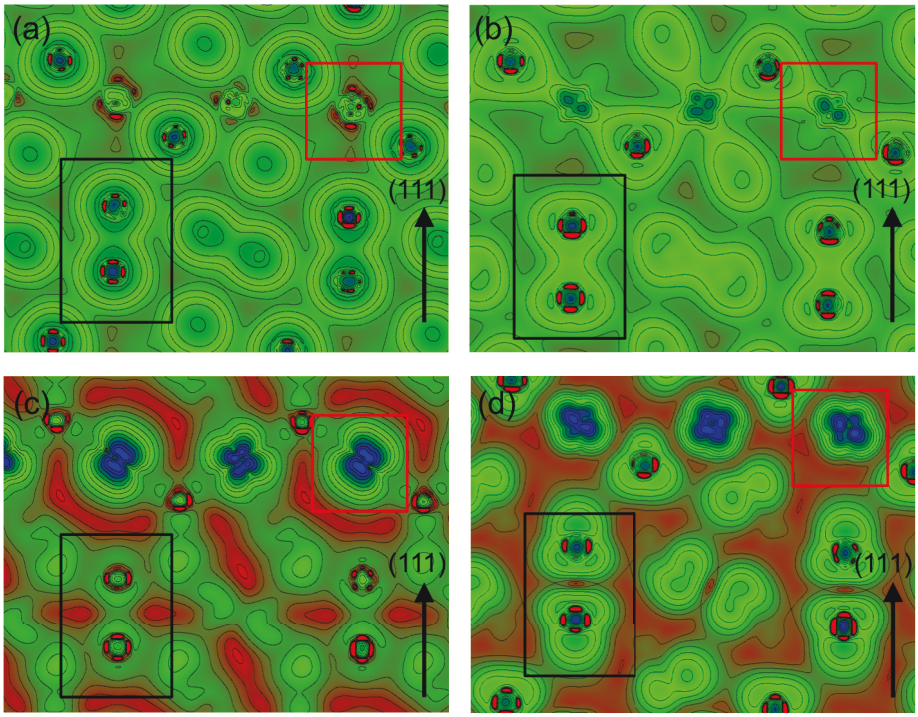

Figure E.1.: The figures are described in detail in the text. See the corresponding statements to “ad (a)”, “ad (b)”, “ad (c)” and “ad (d)”.

F. Electronic Band Structures of Iron Pyrite within DFT+U

In these figures the orbital-resolved band structure of iron pyrite using the PBE+U functional is shown for different values of U_{eff}. Following U-values have been used: $U_{\text{eff}} = 0$ eV (upper left), $U_{\text{eff}} = 2$ eV (upper right), $U_{\text{eff}} = 3$ eV (lower left) and $U_{\text{eff}} = 4$ eV (lower right). The red markers in the band structures indicate the Fe $3d$-character, whereas the black markers show the S $3p$-character. The size of the points correlates to the size of the orbital contribution. The high-symmetry $\boldsymbol{k}$-points of the $\boldsymbol{k}$-path are denoted according to Bradley and Cracknell [131], with X' being equal to X.

The orbital character of the electronic band structure experiences only minor changes when changing U_{eff} from 0 to 4 eV. The most obvious change concerns the relative energy position of the S $3p$ states to the Fe $3d$ states. For a larger U_{eff} the energy gap between the Fe $3d\,t_{2g}$ and Fe $3d\,e_g$ states between 1.5 and 2.5 eV above the Fermi energy ε_F is increased, and thus the S $3p$ band at the lowest conduction band around Γ is also shifted upwards, which leads to a larger fundamental band gap. The energy gap between the Fe $3d\,t_{2g}$ states lying between -1.5 eV and the Fermi energy and the S $3pp\pi^*$ states starting from about -2 eV becomes smaller with increasing U_{eff}. In particular the shape of the Fe $3d$ valence bands changes slightly with different U_{eff} due to small changes in the orbital hybridization. Hence, the fundamental band gap is indirect for the Hubbard U values of 0 and 2 eV, but it becomes direct for larger values.

For the DFT+U calculations the fully-localized limit has been chosen, in difference to the results presented in chapter 7. However, except of slight changes in the size of the band gap the main messages stay the same also for the around mean-field limit.

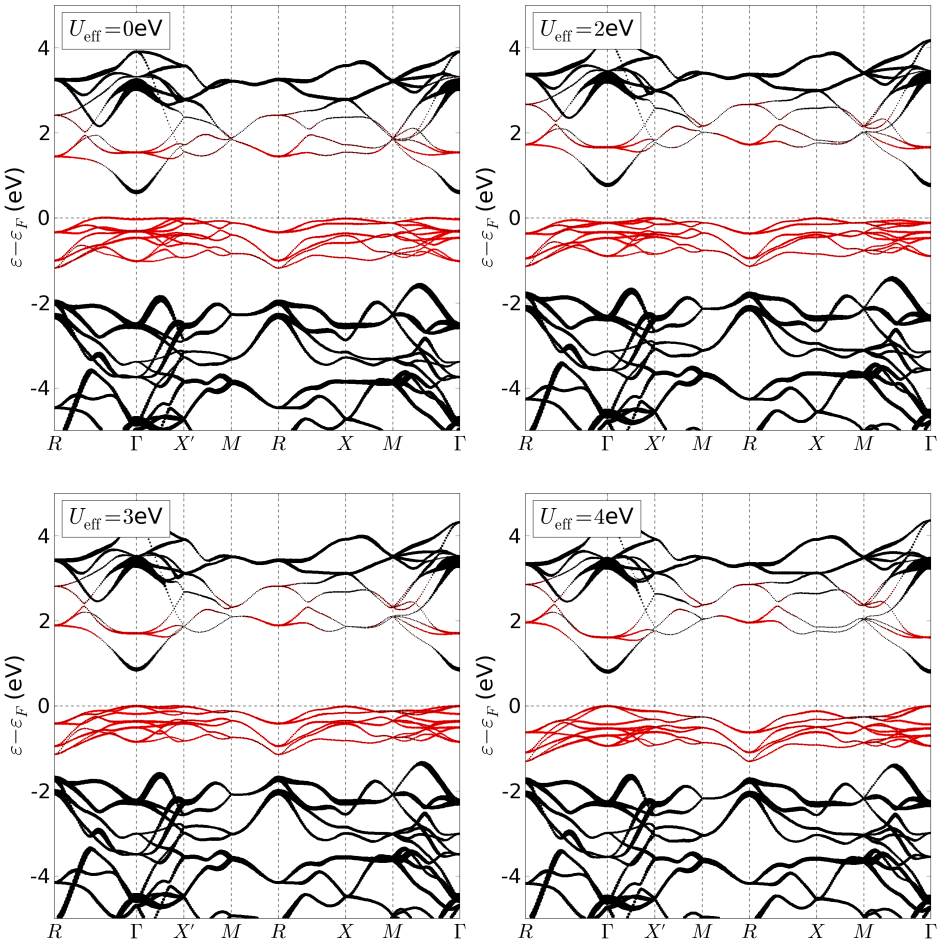
U_{eff}=0eV
U_{eff}=2eV
U_{eff}=3eV
U_{eff}=4eV
$\varepsilon-\varepsilon_F$ (eV)
4
2
0
-2
-4
R
Γ
X′
M
R
X
M
Γ

G. Results on Iron Pyrite Films

This appendix lists the results for all 14 iron pyrite (001), (111) and (210) films, which have been to detailed to show them in the chapters 11 and 12. The 14 iron pyrite films are the three terminations (001)-S, (001)-2S and (001)-Fe of the (001) orientation, the five terminations of (111), namely (111)-Fe, (111)-S, (111)-2S, (111)-3S and (111)-4S and finally the six terminations (210)-Fe, (210)-S, (210)-2S, (210)-Fe', (210)-S' and (210)-2S' of the (210) films.

In each case a data sheet of one page displays a side and top view of the film,[1] some brief remarks about the results of the structural relaxation including a table of computational parameters used for the calculation of the relaxations, and the orbital-resolved electronic band structure around the Fermi energy for the relaxed, non-magnetic films.[2] Additionally, the surface energy of the unrelaxed (in brackets) and relaxed film for the same chemical potential μ_S as in Fig. 11.4 (without magnetism), the size of the band gap, the orbital character of the surface bands within the band gap region and the magnetic moments (if any) of the top-most Fe and S atoms including the energy difference between the surface energy calculated within a spin-polarized and non-magnetic calculation are listed.[3] The magnetic calculations have been performed for the unrelaxed films.

Finally, let me give some brief remarks about the computational parameters listed in the tables. Most of them are already explained in chapter 5 and for those which are not explained there I refer to reference [66] for more details. These parameters have been only used for conducting the structural relaxation and calculating the electronic band structure. To determine the surface energies and allow for a reasonable comparison between them, the computational parameters have been chosen to be equal for all films. Details about the chosen parameters can be found in the section about computational details in chapter 11. Here is a list defining the computational parameters listed in the tables:

- Δ_{vac}: difference between the two vacuum constants D and $\tilde{D}$ in a.u.

[1] The direction of the first primitive lattice vector of the two-dimensional unit cell is denoted as a axis and the second one as b axis in the following. The unit cells are depicted as black frames in the top views of the films. For (001) and (210) both the top view and side view are chosen such, that the a axis of the two-dimensional unit cell is along x, whereas in the (111) films the a and b axis, spanning an angle of $120°$, have both an angle of $30°$ with respect to the x axis for the top and side view. The x axis is always from left to right on the paper (*c.f.* 11.3). The figures have been made with the program VESTA [130].

[2] Except for the (210)-Fe and (210)-2S' film, where the bands of the unrelaxed structure are presented, because the relaxation did not converge. The red circles in the band structure indicate Fe $3d$ character, whereas the black circles represent the S $3p$ character. The larger the circles, the more pronounced the orbital-character.

[3] In some cases the top-most Fe or S atoms split up each into two different atom types due to symmetry. In these cases two magnetic moments are presented for the top-most layer.

- $R_{\mathrm{MT}}^{\mathrm{Fe}}$: muffin-tin (MT) radius of the Fe atoms in a.u.
- n_r^{Fe}: number of radial mesh points for the description of the wave functions in MT of Fe atoms
- $\log_r^{\mathrm{Fe}}$: logarithmic increment of the description of the wave functions in MT of Fe atoms
- $R_{\mathrm{MT}}^{\mathrm{S}}$, n_r^{S}, $\log_r^{\mathrm{S}}$: same for S atoms
- $G_{\max}$: $G_{\max}$ cutoffs in a.u.$^{-1}$ for density and exchange-correlation potential
- $k_{\max}$: plane wave cutoff in a.u.$^{-1}$
- N_k: number of $\boldsymbol{k}$-points in the irreducible Brillouin zone; note that there are two symmetries in the (001) films, six symmetries in the (111) films and only the identity for the (210) films
- d: thickness of the film in nm (from top-most to bottom-most atom)

G.1. (001)-S

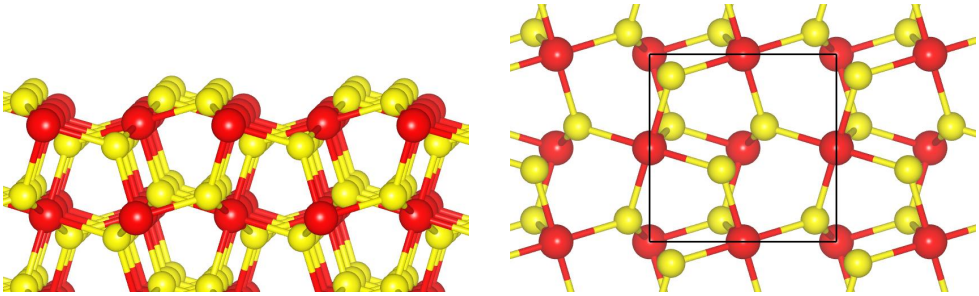

Relaxations: The top-most Fe layer relaxes about 0.2 a.u. into the bulk. All other atoms exhibit only minor relaxations. See Fig. 11.3 for more details.

Δ_{vac}	$R_{\text{MT}}^{\text{Fe}}$	n_r^{Fe}	$\log_r^{\text{Fe}}$	R_{MT}^{S}	n_r^{S}	$\log_r^{\text{S}}$	G_{max}	k_{max}	N_k	d
3.27	2.10	719	0.016	1.90	649	0.017	12.2 10.1	4.0	50	1.7

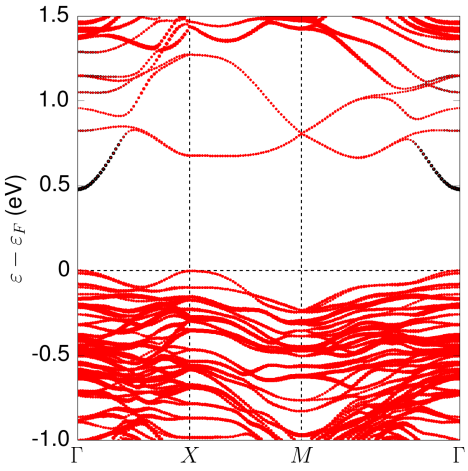

- surface energy: 61 (73) meV/Å^2
- band gap: 0.48 eV
- surface band character: mainly Fe $3d$ character
- magnetism: non-magnetic, however reported to be magnetic within a DFT+U approach [19]

G.2. (001)-2S

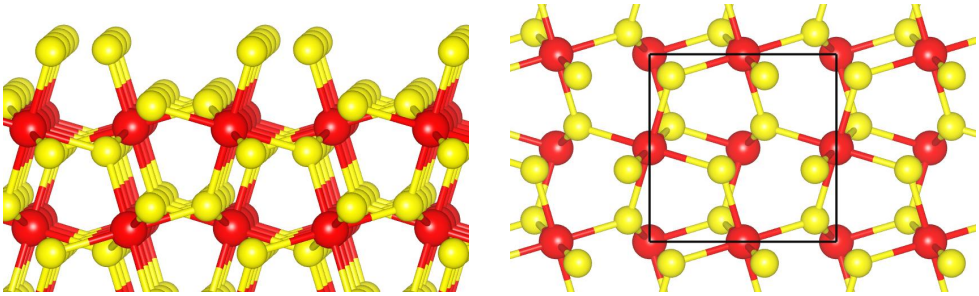

Relaxations: There are no major relaxations in the system, except of a slight shift of the top-most Fe atoms into the bulk. Surprisingly when using the thinner film with about 1 nm thickness there are quite large relaxations of the top-most S atoms.

Δ_{vac}	$R_{\mathrm{MT}}^{\mathrm{Fe}}$	n_r^{Fe}	$\log_r^{\mathrm{Fe}}$	$R_{\mathrm{MT}}^{\mathrm{S}}$	n_r^{S}	$\log_r^{\mathrm{S}}$	G_{max}	k_{max}	N_k	d
3.27	2.00	705	0.016	1.80	551	0.017	12.2 10.2	4.0	50	2.0

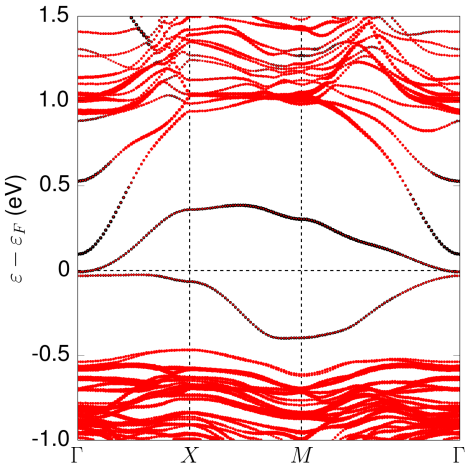

- surface energy: 91 (116) meV/Å^2
- band gap: (semi-)metal
- surface band character: mainly S $3p$
- magnetism: magnetic with an about 2 meV/Å^2 smaller surface energy; top-most Fe atoms have a magnetic moment of 0.5 μ_B, whereas the top-most S atoms exhibit a moment of about 0.1 μ_B.

G.3. (001)-Fe

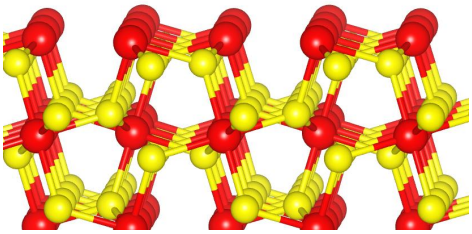

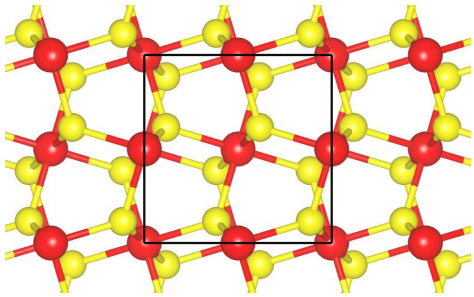

Relaxations: The top-most Fe atoms relax about 0.15 a.u. into the bulk and exhibit large in-plane displacements of about 0.4 a.u. The top-most S layer shifts 0.2 a.u. towards the top-most Fe layer.

Δ_{vac}	$R_{\text{MT}}^{\text{Fe}}$	n_r^{Fe}	$\log_r^{\text{Fe}}$	R_{MT}^{S}	n_r^{S}	$\log_r^{\text{S}}$	G_{max}	k_{max}	N_k	d
3.26	2.10	719	0.016	1.60	649	0.017	12.2 10.1	4.0	50	1.6

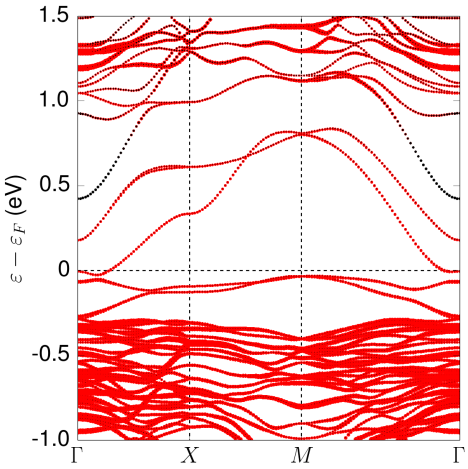

- surface energy: 170 (201) meV/Å^2
- band gap: metal
- surface band character: Fe $3d$
- magnetism: magnetic calculation did not converge

G.4. (111)-Fe

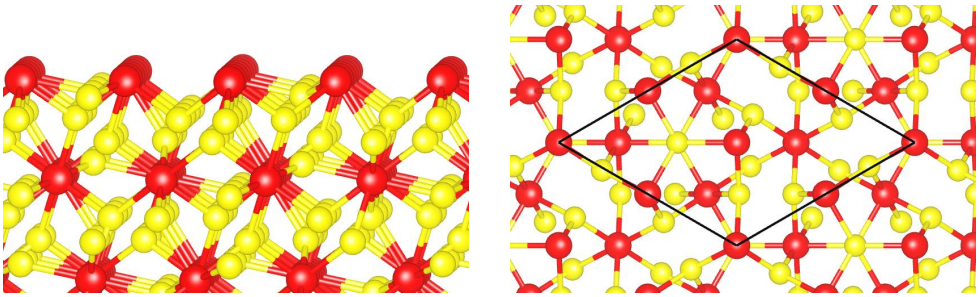

Relaxations: The largest displacements are about 0.5 a.u. and lead to a significantly smaller interlayer distance of the top-most Fe layer and the below located S layer. From before 0.9 a.u. the interlayer distance of the two top-most layers decreases to about 0.3 a.u. The relaxations in all other layers are negligible.

Δ_{vac}	$R_{\text{MT}}^{\text{Fe}}$	n_r^{Fe}	$\log_r^{\text{Fe}}$	R_{MT}^{S}	n_r^{S}	$\log_r^{\text{S}}$	G_{max}	k_{max}	N_k	d
3.33	2.10	735	0.016	1.70	641	0.017	12.3 10.3	3.6	49	1.9

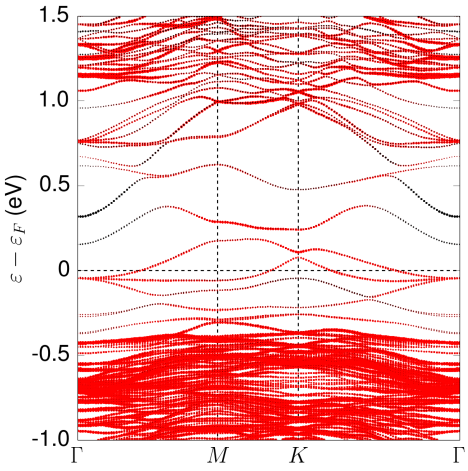

- surface energy: 215 (245) meV/Å^2
- band gap: metal
- surface band character: Fe $3d$
- magnetism: magnetic with an about 16 meV/Å^2 smaller surface energy; top-most Fe atoms have a magnetic moment of 2.52 and 1.74 μ_B.

G.5. (111)-S

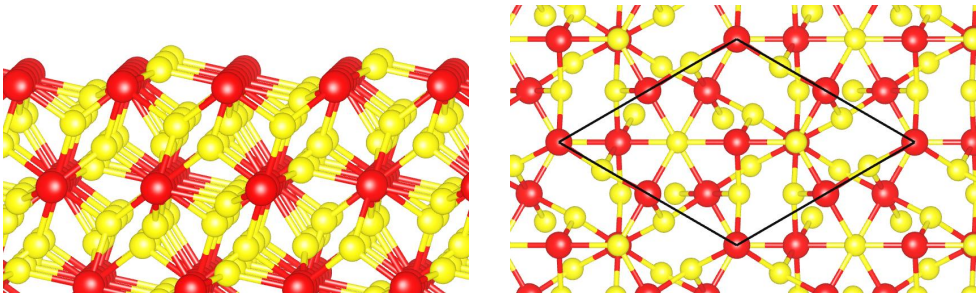

Relaxations: The top-most S layer does not exhibit any significant relaxations. The largest relaxation with displacements of about 0.3 a.u. take place in the second and third top-most Fe and S layer. The interlayer distance between these layers is reduced from about 0.9 to 0.3 a.u. All other atoms do not exhibit major relaxations.

Δ_{vac}	$R_{\text{MT}}^{\text{Fe}}$	n_r^{Fe}	$\log_r^{\text{Fe}}$	R_{MT}^{S}	n_r^{S}	$\log_r^{\text{S}}$	G_{max}	k_{max}	N_k	d
3.33	2.10	735	0.016	1.80	641	0.017	12.3 10.3	3.6	49	2.0

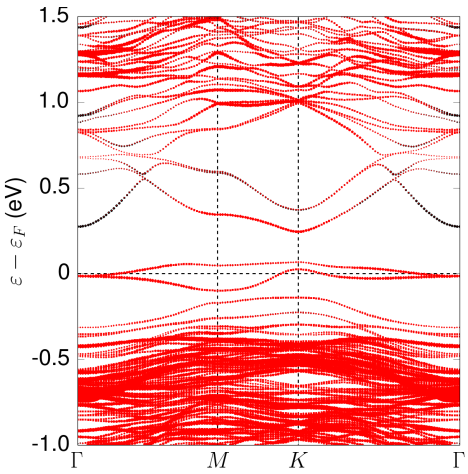

- surface energy: 152 (170) meV/Å^2
- band gap: metal
- surface band character: mainly Fe $3d$
- magnetism: magnetic with an about 9 meV/Å^2 smaller surface energy; top-most Fe atoms have a magnetic moment of 2.51 and -0.48 μ_B, and thus are anti-ferromagnetically coupled.

G.6. (111)-2S

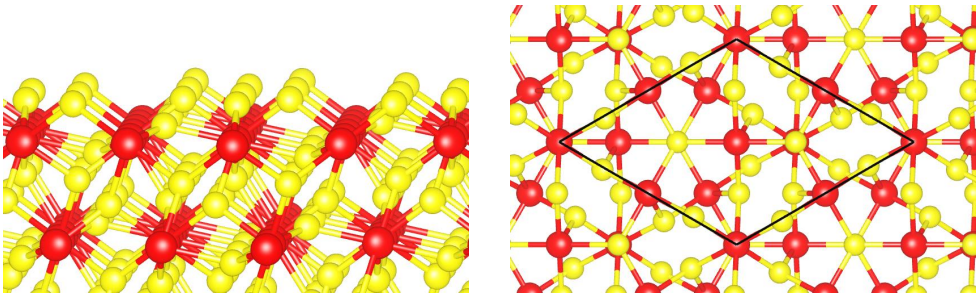

Relaxations: Smaller relaxations than the 111-S film. The two top-most S layers exhibit negligible relaxations. However, the Fe layer located below and next S layer show displacements of about 0.2 a.u., leading to smaller interlayer distances. All other atoms do not exhibit major relaxations.

Δ_{vac}	$R_{\text{MT}}^{\text{Fe}}$	n_r^{Fe}	$\log_r^{\text{Fe}}$	R_{MT}^{S}	n_r^{S}	$\log_r^{\text{S}}$	G_{max}	k_{max}	N_k	d
3.33	2.10	735	0.016	1.80	641	0.017	12.3 10.3	3.6	49	2.1

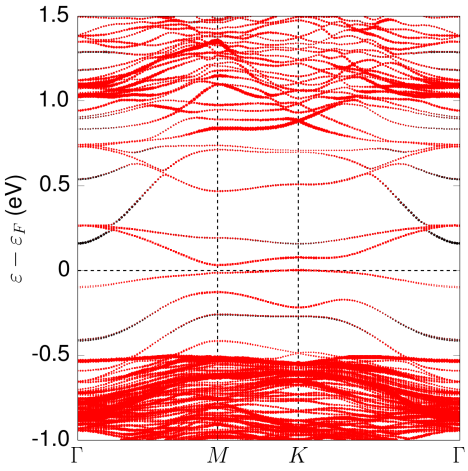

- surface energy: 93 (106) meV/Å^2
- band gap: 0.03 eV
- surface band character: mainly Fe $3d$
- magnetism: magnetic with an about 8 meV/Å^2 smaller surface energy; top-most Fe atoms have a magnetic moment of 1.16 and 0.63 μ_B, and the top S atom exhibits a moment of 0.21 μ_B.

G.7. (111)-3S

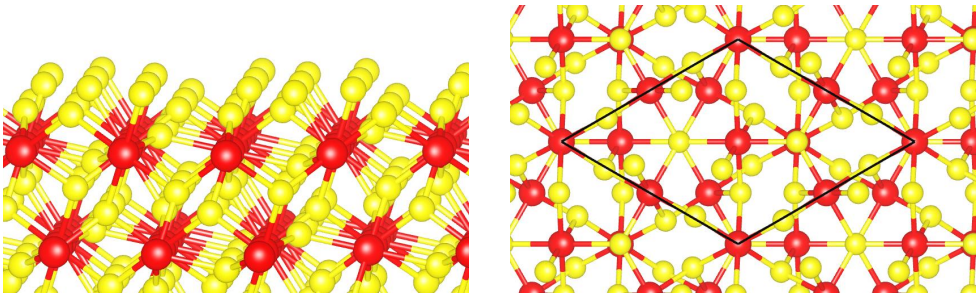

Relaxations: Except of the third top-most S layer experiencing a displacement of 0.2 a.u. in direction to the below Fe layer, there are only minor relaxations of the film.

Δ_{vac}	$R_{\text{MT}}^{\text{Fe}}$	n_r^{Fe}	$\log_r^{\text{Fe}}$	R_{MT}^{S}	n_r^{S}	$\log_r^{\text{S}}$	G_{max}	k_{max}	N_k	d
3.33	2.10	735	0.016	1.80	641	0.017	12.3 10.3	3.6	49	2.2

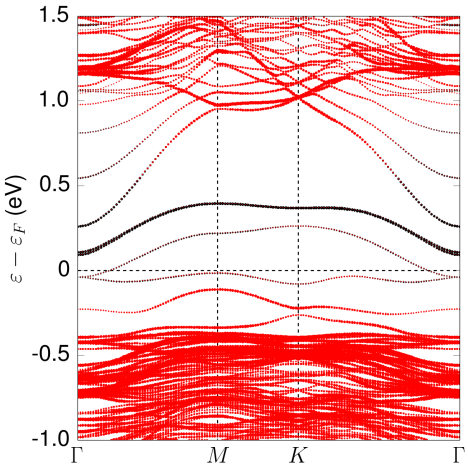

- surface energy: 61 (71) meV/Å^2
- band gap: metal
- surface band character: Fe $3d$ with a considerable amount of S $3p$
- magnetism: magnetic with an about 4 meV/Å^2 smaller surface energy; top-most Fe atoms have a magnetic moment of 0.75 and 0.37 μ_B, whereas the top three layers of S atoms exhibit moments in the order of 0.1 μ_B.

G.8. (111)-4S

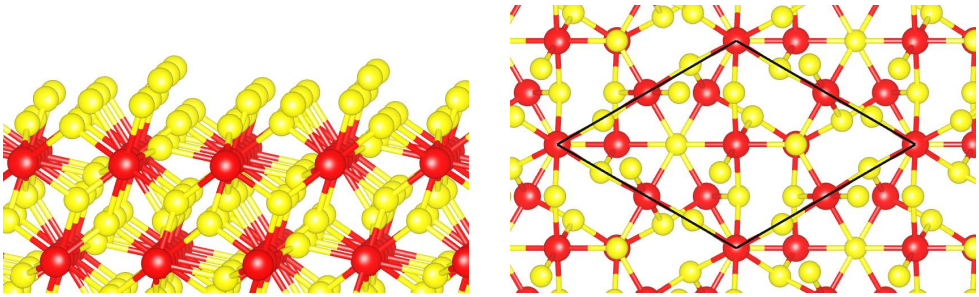

Relaxations: Minor relaxations, except of the 4th S layer, which relaxes in direction of the S-S dimer direction. The corresponding displacement is about 0.3 a.u.

Δ_{vac}	$R_{\text{MT}}^{\text{Fe}}$	n_r^{Fe}	$\log_r^{\text{Fe}}$	R_{MT}^{S}	n_r^{S}	$\log_r^{\text{S}}$	G_{max}	k_{max}	N_k	d
3.33	2.10	735	0.016	1.80	641	0.017	12.3 10.3	3.6	49	2.4

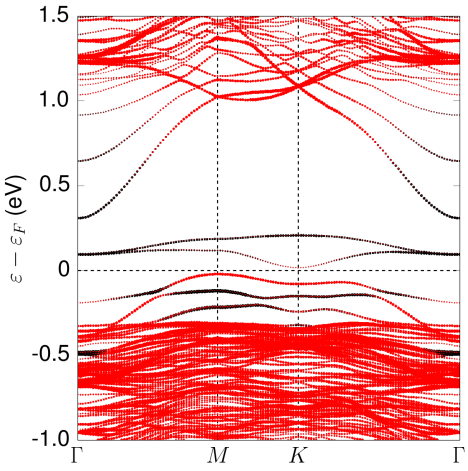

- surface energy: 87 (97) meV/Å^2
- band gap: 0.04 eV
- surface band character: mainly S $3p$
- magnetism: magnetic with an about 1 meV/Å^2 smaller surface energy; topmost Fe atoms have a magnetic moment of 0.42 and 0.55 μ_B, and the top three layers of S atoms exhibit moments in the order of 0.2 μ_B

G.9. (210)-Fe

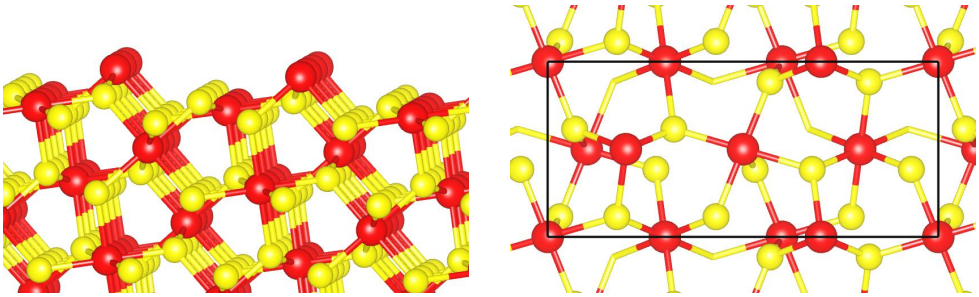

Relaxations: Problems with convergence, therefore no results for the relaxed film.

Δ_{vac}	$R_{\text{MT}}^{\text{Fe}}$	n_r^{Fe}	$\log_r^{\text{Fe}}$	R_{MT}^{S}	n_r^{S}	$\log_r^{\text{S}}$	$G_{\max}$	$k_{\max}$	N_k	d
3.33	2.10	735	0.016	1.80	641	0.017	12.3 10.3	3.6	18	1.7

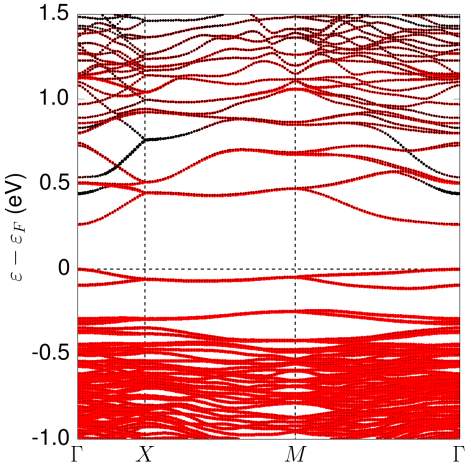

- surface energy: n.a. (128) meV/Å^2
- band gap: 0.26 eV
- surface band character: Fe $3d$
- magnetism: magnetic calculation did not converge

G.10. (210)-S

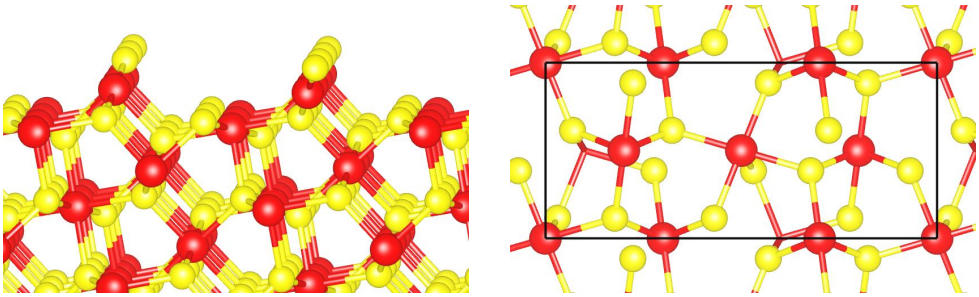

Relaxations: There are considerable in-plane relaxations for the top-most S atoms, which exhibit displacements of about 0.8 a.u. Additionally, the top-most Fe atoms tend to relax into the bulk-like middle again.

Δ_{vac}	$R_{\text{MT}}^{\text{Fe}}$	n_r^{Fe}	$\log_r^{\text{Fe}}$	R_{MT}^{S}	n_r^{S}	$\log_r^{\text{S}}$	G_{max}	k_{max}	N_k	d
3.34	2.10	735	0.016	1.80	641	0.017	12.3 10.3	3.6	18	1.9

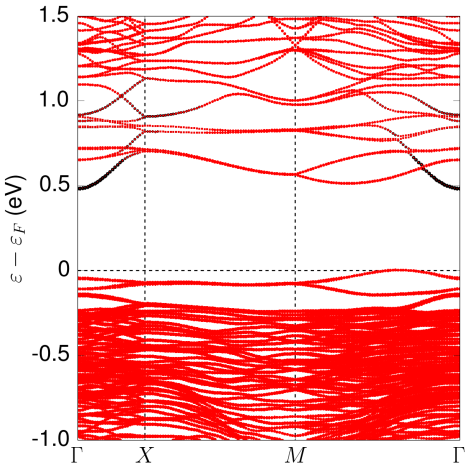

- surface energy: 92 (109) meV/Å^2
- band gap: 0.48 eV
- surface band character: mainly Fe $3d$
- magnetism: magnetic with an about 1 meV/Å^2 smaller surface energy; the top-most Fe atoms have a magnetic moment of 1.93 μ_B and all other atoms exhibit magnetic moments in the order of 0.01-0.1 μ_B.

G.11. (210)-2S

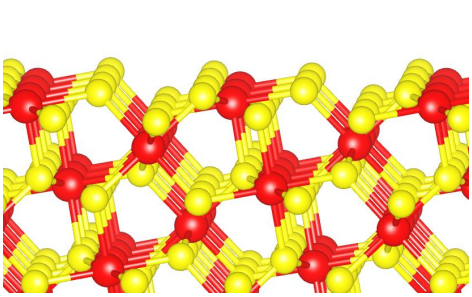

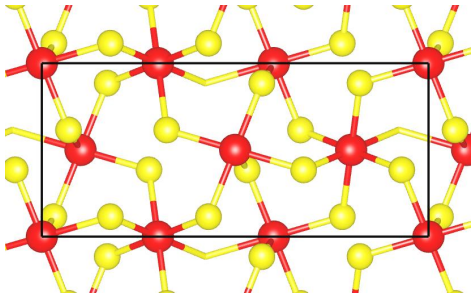

Relaxations: The top-most S layer exhibits quite large in-plane relaxations of about 0.5 a.u. The top-most Fe layer shifts 0.4 a.u. into the bulk.

Δ_{vac}	$R_{\text{MT}}^{\text{Fe}}$	n_r^{Fe}	$\log_r^{\text{Fe}}$	R_{MT}^{S}	n_r^{S}	$\log_r^{\text{S}}$	$G_{\max}$	$k_{\max}$	N_k	d
3.34	2.05	735	0.016	1.70	641	0.017	12.3 10.3	3.8	18	1.5

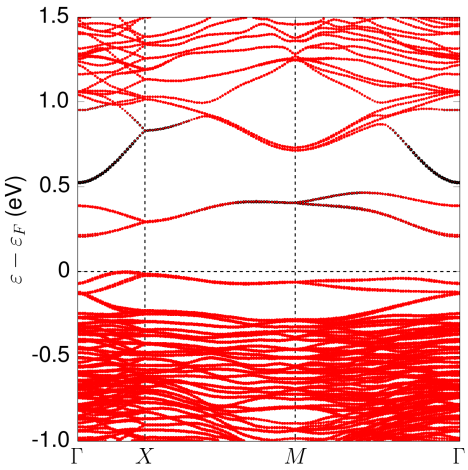

- surface energy: 62 (77) meV/Å^2
- band gap: 0.22 eV
- surface band character: mainly Fe $3d$ with small admixture of S $3p$
- magnetism: magnetic with an about 5 meV/Å^2 smaller surface energy; top-most Fe atoms have a magnetic moment of 1.13 μ_B and second top-most Fe atoms exhibit a moment of 0.38 μ_B. The top-most S atoms have a small moment of 0.15 μ_B, whereas all other atoms have moments much smaller than 0.1 μ_B.

G.12. (210)-Fe'

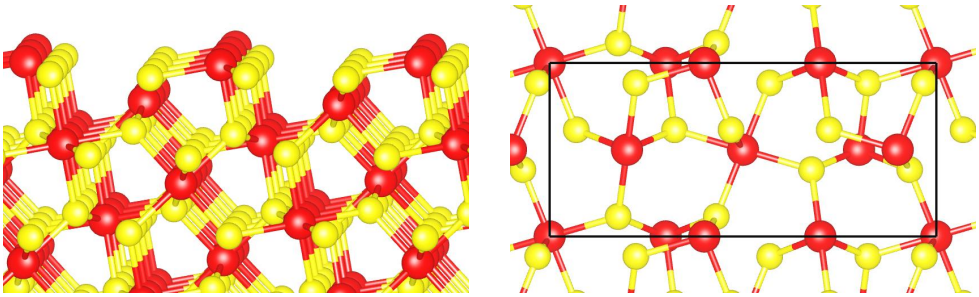

Relaxations: The top-most and next Fe layer relaxes into the bulk with the first layer exhibiting displacements of about 0.2 a.u. and the second Fe layer showing twice larger displacements. The first two top-most S layers show considerable in-plane relaxation of about 0.2 a.u.

Δ_{vac}	$R_{\text{MT}}^{\text{Fe}}$	n_r^{Fe}	$\log_r^{\text{Fe}}$	R_{MT}^{S}	n_r^{S}	$\log_r^{\text{S}}$	G_{max}	k_{max}	N_k	d
3.34	2.10	735	0.016	1.60	641	0.017	12.3 10.3	3.6	18	1.9

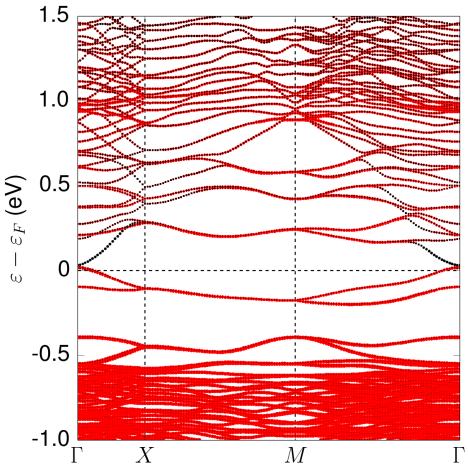

- surface energy: 146 (166) meV/Å^2
- band gap: (semi-)metal
- surface band character: Fe $3d$
- magnetism: magnetic calculations did not converge

G.13. (210)-S'

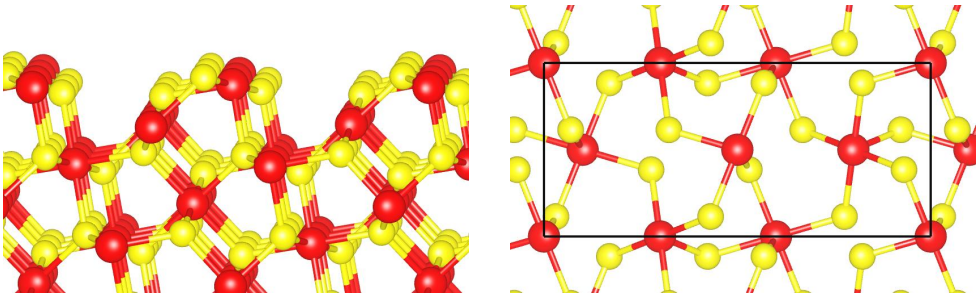

Relaxations: The top-most S layer does not exhibit significant relaxations. The top-most Fe atoms relax about 0.2 a.u. into the bulk, and the below lying S layer shows in-plane relaxations of the same order.

Δ_{vac}	$R_{\text{MT}}^{\text{Fe}}$	n_r^{Fe}	$\log_r^{\text{Fe}}$	R_{MT}^{S}	n_r^{S}	$\log_r^{\text{S}}$	G_{max}	k_{max}	N_k	d
3.28	2.00	705	0.016	1.80	551	0.017	12.2 10.2	4.0	39	1.5

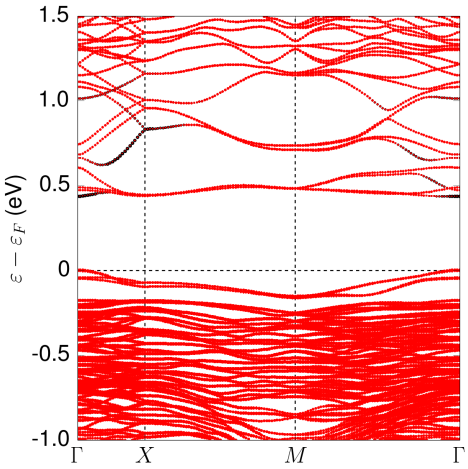

- surface energy: 89 (103) meV/Å^2
- band gap: 0.43 eV
- surface band character: mainly Fe $3d$
- magnetism: magnetic with an about 1 meV/Å^2 smaller surface energy; top-most Fe atoms have a magnetic moment of 2.02 μ_B, whereas all other atoms show magnetic moments in the order of 0.01 μ_B.

G.14. (210)-2S'

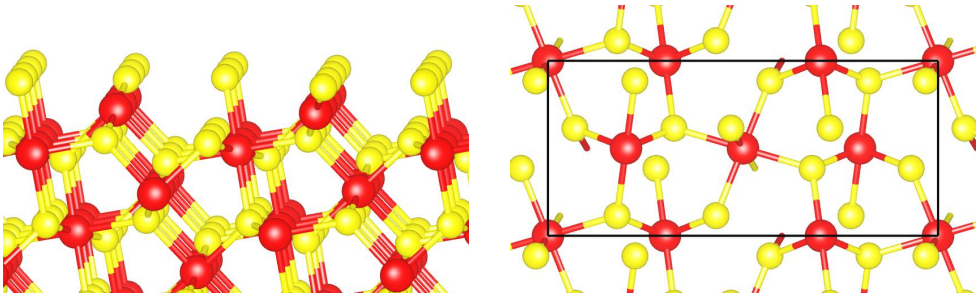

Relaxations: Problems with convergence, therefore no results for the relaxed film.

Δ_{vac}	$R_{\mathrm{MT}}^{\mathrm{Fe}}$	n_r^{Fe}	$\log_r^{\mathrm{Fe}}$	$R_{\mathrm{MT}}^{\mathrm{S}}$	n_r^{S}	$\log_r^{\mathrm{S}}$	G_{max}	k_{max}	N_k	d
3.33	2.10	735	0.016	1.80	641	0.017	12.3 10.3	3.6	18	1.7

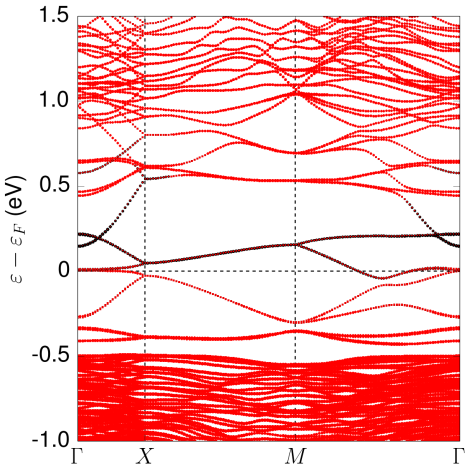

- surface energy: n.a. (132) meV/Å^2
- band gap: metal
- surface band character: Fe $3d$ with admixture of S $3p$
- magnetism: magnetic calculations did not converge

Bibliography

[1] N. Armaroli and V. Balzani, "The Future of Energy Supply: Challenges and Opportunities", Angewandte Chemie International Edition **46**, 52–66 (2007).

[2] Statistisches Bundesamt, *Bruttostromerzeugung in Deutschland für 2011 bis 2013*, 2013.

[3] C. Kost, J. N. Mayer, J. Thomsen, N. Hartmann, C. Senkpiel, S. Philipps, S. Nold, S. Lude, and T. Schlegl, *Stromgestehungskosten Erneuerbare Energien*, Fraunhofer-Institut für Solare Energiesysteme (2013).

[4] V. Smil, *General Energetics: Energy in the Biosphere and Civilization* (Wiley-Interscience, 1991).

[5] U.S. Energy Information Administration, *International Energy Statistics*, 2013.

[6] J. Evers, P. Klüfers, R. Staudigl, and P. Stallhofer, "Czochralskis schöpferischer Fehlgriff: ein Meilenstein auf dem Weg in die Gigabit-Ära", Angewandte Chemie **115**, 5862–5877 (2003).

[7] W. Shockley and H. J. Queisser, "Detailed Balance Limit of Efficiency of p-n Junction Solar Cells", Journal of Applied Physics **32**, 510–519 (1961).

[8] M. A. Green, "Estimates of Te and In Prices from Direct Mining of Known Ores", Prog. Photovolt. Res. Appl. **17** (2009).

[9] T. E. Graedel, "On the Future Availability of the Energy Materials ", Annu. Rev. Mater. Res. **41** (2011).

[10] W. C. Dash and R. Newman, "Intrinsic Optical Absorption in Single-Crystal Germanium and Silicon at 77K and 300K", Phys. Rev. **99**, 1151–1155 (1955).

[11] T. Unold and H. W. Schock, "Nonconventional (Non-Silicon-Based) Photovoltaic Materials", Annu. Rev. Mater. Res. **41** (2011).

[12] C. Wadia, A. P. Alivisatos, and D. M. Kammen, "Materials Availability Expands the Opportunity for Large-Scale Photovoltaics Deployment", Environmental Science & Technology **43**, 2072–2077 (2009).

[13] A. Ennaoui, S. Fiechter, C. Pettenkofer, N. Alonso-Vante, K. Büker, M. Bronold, C. Höpfner, and H. Tributsch, "Iron disulfide for solar energy conversion", Solar Energy Materials and Solar Cells **29**, 289 –370 (1993).

[14] S. Lehner, K. Savage, and J. Ayers, "Vapor growth and characterization of pyrite (FeS2) doped with Co, Ni, and As: Variations in semiconducting properties", Journal of Crystal Growth **286**, 306 –317 (2006).

[15] C. Steinhagen, T. B. Harvey, C. J. Stolle, J. Harris, and B. A. Korgel, "Pyrite Nanocrystal Solar Cells: Promising, or Fool's Gold?", The Journal of Physical Chemistry Letters **3**, 2352–2356 (2012).

[16] M. Birkholz, S. Fiechter, A. Hartmann, and H. Tributsch, "Sulfur deficiency in iron pyrite (FeS_{2-x}) and its consequences for band-structure models", Phys. Rev. B **43**, 11926–11936 (1991).

[17] R. Sun, M. K. Y. Chan, S. Kang, and G. Ceder, "Intrinsic stoichiometry and oxygen-induced p-type conductivity of pyrite FeS_2", Phys. Rev. B **84**, 035212 (2011).

[18] M. Bronold, Y. Tomm, and W. Jaegermann, "Surface states on cubic d-band semiconductor pyrite (FeS2)", Surface Science **314**, L931 –L936 (1994).

[19] Y. N. Zhang, J. Hu, M. Law, and R. Q. Wu, "Effect of surface stoichiometry on the band gap of the pyrite FeS_2 (100) surface", Phys. Rev. B **85**, 085314 (2012).

[20] F. W. Herbert, A. Krishnamoorthy, K. J. Van Vliet, and B. Yildiz, "Quantification of electronic band gap and surface states on FeS_2(100)", Surface Science **618**, 53–61 (2013).

[21] A. Krishnamoorthy, F. W. Herbert, S. Yip, K. J. Van Vliet, and B. Yildiz, "Electronic states of intrinsic surface and bulk vacancies in FeS_2", Journal of Physics: Condensed Matter **25**, 045004 (2013).

[22] M. Limpinsel, N. Farhi, N. Berry, J. Lindemuth, C. L. Perkins, Q. Lin, and M. Law, "An Inversion Layer at the Surface of n-type Iron Pyrite", Energy Environ. Sci. **7**, 1974–1989 (2014).

[23] L. Yu, S. Lany, R. Kykyneshi, V. Jieratum, R. Ravichandran, B. Pelatt, E. Altschul, H. A. S. Platt, J. F. Wager, D. A. Keszler, and A. Zunger, "Iron Chalcogenide Photovoltaic Absorbers", Advanced Energy Materials **1**, 748–753 (2011).

[24] C. Wadia, Y. Wu, S. Gul, S. K. Volkman, J. Guo, and A. P. Alivisatos, "Surfactant-Assisted Hydrothermal Synthesis of Single phase Pyrite FeS2 Nanocrystals", Chemistry of Materials **21**, 2568–2570 (2009).

[25] T. Schena, G. Bihlmayer, and S. Blügel, "First-principles studies of FeS_2 using many-body perturbation theory in the G_0W_0 approximation", Phys. Rev. B **88**, 235203 (2013).

[26] P. Lazić, R. Armiento, F. W. Herbert, R. Chakraborty, R. Sun, M. K. Y. Chan, K. Hartman, T. Buonassisi, B. Yildiz, and G. Ceder, "Low intensity conduction states in FeS_2 : implications for absorption, open-circuit voltage and surface recombination", Journal of Physics: Condensed Matter **25**, 465801 (2013).

[27] P. Cervantes, Z. Slanic, F. Bridges, E. Knittle, and Q. Williams, "The band gap and electrical resistivity of FeS_2-pyrite at high pressures", Journal of Physics and Chemistry of Solids **63**, 1927 –1933 (2002).

[28] J. Luck, A. Hartmann, and S. Fiechter, "Stoichiometry and impurity concentration in synthetically grown iron pyrite crystals and their constituents", Fresenius' Zeitschrift für analytische Chemie **334**, 441–446 (1989).

[29] R. Sun, M. K. Y. Chan, and G. Ceder, "First-principles electronic structure and relative stability of pyrite and marcasite: Implications for photovoltaic performance", Phys. Rev. B **83**, 235311 (2011).

[30] J. Hu and Y. Zhang and M. Law and R. Wu, "First-principles studies of the electronic properties of native and substitutional anionic defects in bulk iron pyrite", Phys. Rev. B **85**, 085203 (2012).

[31] J. Hu, Y. Zhang, M. Law, and R. Wu, "Increasing the Band Gap of Iron Pyrite by Alloying with Oxygen", Journal of the American Chemical Society **134**, 13216–13219 (2012).

[32] M. Jagadeesh and M. S. Seehra, "Electrical resistivity and band gap of marcasite (FeS2)", Physics Letters A **80**, 59 –61 (1980).

[33] S. Seefeld, M. Limpinsel, Y. Liu, N. Farhi, A. Weber, Y. Zhang, N. Berry, Y. J. Kwon, C. L. Perkins, J. C. Hemminger, R. Wu, and M. Law, "Iron Pyrite Thin Films Synthesized from an $Fe(acac)_3$ Ink", Journal of the American Chemical Society **135**, 4412–4424 (2013).

[34] I. Ferrer, D. Nevskaia, C. de las Heras, and C. Sánchez, "About the band gap nature of FeS_2 as determined from optical and photoelectrochemical measurements", Solid State Communications **74**, 913 –916 (1990).

[35] V. Eyert and K.-H. Höck and S. Fiechter and H. Tributsch, "Electronic structure of FeS_2: The crucial role of electron-lattice interaction", Phys. Rev. B **57**, 6350–6359 (1998).

[36] S. G. Choi, J. Hu, L. S. Abdallah, M. Limpinsel, Y. N. Zhang, S. Zollner, R. Q. Wu, and M. Law, "Pseudodielectric function and critical-point energies of iron pyrite", Phys. Rev. B **86**, 115207 (2012).

[37] T. A. Bither, R. J. Bouchard, W. H. Cloud, P. C. Donohue, and W. J. Siemons, "Transition metal pyrite dichalcogenides. High-pressure synthesis and correlation of properties", Inorganic Chemistry **7**, 2208–2220 (1968).

[38] A. Ennaoui, S. Fiechter, H. Goslowsky, and H. Tributsch, "Photoactive Synthetic Polycrystalline Pyrite (FeS_2)", Journal of The Electrochemical Society **132**, 1579–1582 (1985).

[39] P. Hohenberg and W. Kohn, "Inhomogeneous Electron Gas", Phys. Rev. **136**, B864–B871 (1964).

[40] W. Kohn and L. J. Sham, "Self-Consistent Equations Including Exchange and Correlation Effects", Phys. Rev. **140**, A1133–A1138 (1965).

[41] D. M. Ceperley and B. J. Alder, "Ground State of the Electron Gas by a Stochastic Method", Phys. Rev. Lett. **45**, 566–569 (1980).

[42] S. H. Vosko, L. Wilk, and M. Nusair, "Accurate spin-dependent electron liquid correlation energies for local spin density calculations: a critical analysis", Canadian Journal of Physics **58**, 1200–1211 (1980).

[43] J. P. Perdew, K. Burke, and M. Ernzerhof, "Generalized Gradient Approximation Made Simple", Phys. Rev. Lett. **77**, 3865–3868 (1996).

[44] R. O. Jones, "Density Functional Theory for Emergents", in *Emergent Phenomena in Correlated Matter*, edited by E. Pavarini, E. Koch, and U. Schollwöck (Schriften des Forschungszentrum Jülich, 2013).

[45] D. W. Bullett, "Electronic structure of 3d pyrite- and marcasite-type sulphides", Journal of Physics C: Solid State Physics **15**, 6163 (1982).

[46] S. Lauer, A. X. Trautwein, and F. E. Harris, "Electronic-structure calculations, photoelectron spectra, optical spectra, and Mössbauer parameters for the pyrites MS_2 (M=Fe, Co, Ni, Cu, Zn)", Phys. Rev. B **29**, 6774–6783 (1984).

[47] W. Folkerts, G. A. Sawatzky, C. Haas, R. A. de Groot, and F. U. Hillebrecht, "Electronic structure of some 3D transition-metal pyrites", Journal of Physics C: Solid State Physics **20**, 4135 (1987).

[48] G. L. Zhao, J. Callaway, and M. Hayashibara, "Electronic structures of iron and cobalt pyrites", Phys. Rev. B **48**, 15781–15786 (1993).

[49] Y. Zeng and N. A. W. Holzwarth, "Density-functional calculation of the electronic structure and equilibrium geometry of iron pyrite (FeS_2)", Phys. Rev. B **50**, 8214–8220 (1994).

[50] I. Opahle, K. Koepernik, and H. Eschrig, "Full-potential band-structure calculation of iron pyrite", Phys. Rev. B **60**, 14035–14041 (1999).

[51] W. Paszkowicz and J. Leiro, "Rietveld refinement study of pyrite crystals", Journal of Alloys and Compounds **401**, 289 (2005).

[52] J. P. Perdew and M. Levy, "Physical Content of the Exact Kohn-Sham Orbital Energies: Band Gaps and Derivative Discontinuities", Phys. Rev. Lett. **51**, 1884–1887 (1983).

[53] L. J. Sham and M. Schlüter, "Density-Functional Theory of the Energy Gap", Phys. Rev. Lett. **51**, 1888–1891 (1983).

[54] L. Hedin, "New Method for Calculating the One-Particle Green's Function with Application to the Electron-Gas Problem", Phys. Rev. **139**, A796–A823 (1965).

[55] F. Aryasetiawan and O. Gunnarsson, "The GW method", Reports on Progress in Physics **61**, 237 (1998).

[56] J. Heyd, J. E. Peralta, G. E. Scuseria, and R. L. Martin, "Energy band gaps and lattice parameters evaluated with the Heyd-Scuseria-Ernzerhof screened hybrid functional", The Journal of Chemical Physics **123** (2005).

[57] B. G. Janesko, T. M. Henderson, and G. E. Scuseria, "Screened hybrid density functionals for solid-state chemistry and physics", Phys. Chem. Chem. Phys. **11**, 443–454" (2009).

[58] P. Rinke, A. Qteish, J. Neugebauer, C. Freysoldt, and M. Scheffler, "Combining GW calculations with exact-exchange density-functional theory: an analysis of valence-band photoemission for compound semiconductors", New Journal of Physics **7**, 126 (2005).

[59] A. N. Chantis, M. van Schilfgaarde, and T. Kotani, "Quasiparticle self-consistent GW method applied to localized $4f$ electron systems", Phys. Rev. B **76**, 165126 (2007).

[60] N. Marom, F. Caruso, X. Ren, O. T. Hofmann, T. Körzdörfer, J. R. Chelikowsky, A. Rubio, M. Scheffler, and P. Rinke, "Benchmark of GW methods for azabenzenes", Phys. Rev. B **86**, 245127 (2012).

[61] T. Kotani, M. van Schilfgaarde, and S. V. Faleev, "Quasiparticle self-consistent GW method: A basis for the independent-particle approximation", Phys. Rev. B **76**, 165106 (2007).

[62] S. V. Faleev, M. van Schilfgaarde, and T. Kotani, "All-Electron Self-Consistent GW Approximation: Application to Si, MnO, and NiO", Phys. Rev. Lett. **93**, 126406 (2004).

[63] S. W. Lehner, N. Newman, M. van Schilfgaarde, S. Bandyopadhyay, K. Savage, and P. R. Buseck, "Defect energy levels and electronic behavior of Ni-, Co-, and As-doped synthetic pyrite (FeS2)", Journal of Applied Physics **111** (2012).

[64] M. Shishkin, M. Marsman, and G. Kresse, "Accurate Quasiparticle Spectra from Self-Consistent GW Calculations with Vertex Corrections", Phys. Rev. Lett. **99**, 246403 (2007).

[65] D. J. Singh, *Planewaves, Pseudopotentials, and the LAPW method* (Kluwer Academic Publishers, 1994).

[66] *http://www.flapw.de*.

[67] M. Betzinger, C. Friedrich, and S. Blügel, "Hybrid functionals within the all-electron FLAPW method: Implementation and applications of PBE0", Phys. Rev. B **81**, 195117 (2010).

[68] M. Schlipf, M. Betzinger, C. Friedrich, M. Ležaić, and S. Blügel, "HSE hybrid functional within the FLAPW method and its application to GdN", Phys. Rev. B **84**, 125142 (2011).

[69] C. Friedrich, S. Blügel, and A. Schindlmayr, "Efficient implementation of the GW approximation within the all-electron FLAPW method", Phys. Rev. B **81**, 125102 (2010).

[70] W. Kohn, "Nobel Lecture: Electronic structure of matter-wave functions and density functionals", Rev. Mod. Phys. **71**, 1253–1266 (1999).

[71] M. Born and R. Oppenheimer, "Zur Quantentheorie der Molekeln", Annalen der Physik **389**, 457–484 (1927).

[72] M. Betzinger, "Hartree-Fock and Quantum Chemical Correlation Methods", in *Computing Solids - Models, ab initio methods and supercomputing*, Vol. 74, edited by S. Blügel, N. Helbig, V. Meden, and D. Wortmann, Schriften des Forschungszentrums Jülich, Reihe Schlüsseltechnologien / Key Technologies (Forschungszentrum Jülich GmbH, 2014).

[73] A. J. Cohen, P. Mori-Sánchez, and W. Yang, "Challenges for density functional theory", Chemical reviews **112**, 289–320 (2011).

[74] K. Burke, "Perspective on density functional theory", The Journal of Chemical Physics **136**, 150901 (2012).

[75] R. O. Jones and O. Gunnarsson, "The density functional formalism, its applications and prospects", Rev. Mod. Phys. **61**, 689–746 (1989).

[76] L. H. Thomas, "The calculation of atomic fields", Mathematical Proceedings of the Cambridge Philosophical Society **23**, 542–548 (1927).

[77] E. Fermi, "Eine statistische Methode zur Bestimmung einiger Eigenschaften des Atoms und ihre Anwendung auf die Theorie des periodischen Systems der Elemente", Zeitschrift für Physik **48**, 73–79 (1928).

[78] M. Levy, "Universal variational functionals of electron densities, first-order density matrices, and natural spin-orbitals and solution of the v-representability problem", Proceedings of the National Academy of Sciences **76**, 6062–6065 (1979).

[79] R. O. Jones, "Introduction to Density Functional Theory and Exchange-Correlation Energy Functionals", in *Computational Nanoscience: Do it yourself!*, Vol. 31, edited by J. Grotendorst, S. Blügel, and D. Marx, NIC Series (John von Neumann Institute for Computing, 2006).

[80] J. P. Perdew and A. Zunger, "Self-interaction correction to density-functional approximations for many-electron systems", Phys. Rev. B **23**, 5048–5079 (1981).

[81] O. Gunnarsson, M. Jonson, and B. I. Lundqvist, "Descriptions of exchange and correlation effects in inhomogeneous electron systems", Phys. Rev. B **20**, 3136–3164 (1979).

[82] M. Ernzerhof and G. E. Scuseria, "Assessment of the Perdew–Burke–Ernzerhof exchange-correlation functional", The Journal of chemical physics **110**, 5029–5036 (1999).

[83] M. Schlipf, "Heyd-Scuseria-Ernzerhof Screened-Exchange Hybrid Functional for Complex Materials: All-Electron Implementation and Application", PhD thesis (RWTH Aachen, 2013).

[84] E. Şaşıoğlu, "DFT+U method and *ab-initio* determination of the Coulomb interaction parameter U", in *Computing Solids - Models, ab initio methods and supercomputing*, Vol. 74, edited by S. Blügel, N. Helbig, V. Meden, and D. Wortmann, Schriften des Forschungszentrums Jülich, Reihe Schlüsseltechnologien / Key Technologies (Forschungszentrum Jülich GmbH, 2014).

[85] E. Şaşıoğlu, C. Friedrich, and S. Blügel, "Effective Coulomb interaction in transition metals from constrained random-phase approximation", Phys. Rev. B **83**, 121101 (2011).

[86] E. Şaşıoğlu, C. Friedrich, and S. Blügel, "Strength of the Effective Coulomb Interaction at Metal and Insulator Surfaces", Phys. Rev. Lett. **109**, 146401 (2012).

[87] J. P. Perdew, M. Ernzerhof, and K. Burke, "Rationale for mixing exact exchange with density functional approximations", The Journal of Chemical Physics **105**, 9982–9985 (1996).

[88] J. Heyd, G. E. Scuseria, and M. Ernzerhof, "Hybrid functionals based on a screened Coulomb potential", The Journal of Chemical Physics **118**, 8207–8215 (2003).

[89] A. V. Krukau, O. A. Vydrov, A. F. Izmaylov, and G. E. Scuseria, "Influence of the exchange screening parameter on the performance of screened hybrid functionals", The Journal of Chemical Physics **125**, 224106 (2006).

[90] M. A. L. Marques, J. Vidal, M. J. T. Oliveira, L. Reining, and S. Botti, "Density-based mixing parameter for hybrid functionals", Phys. Rev. B **83**, 035119 (2011).

[91] J. He and C. Franchini, "Screened hybrid functional applied to $3d^0 \rightarrow 3d^8$ transition-metal perovskites LaMO3 (M=Sc−Cu): Influence of the exchange mixing parameter on the structural, electronic, and magnetic properties", Phys. Rev. B **86**, 235117 (2012).

[92] S. Kümmel and L. Kronik, "Orbital-dependent density functionals: Theory and applications", Rev. Mod. Phys. **80**, 3–60 (2008).

[93] C. Friedrich, M. Betzinger, M. Schlipf, S. Blügel, and A. Schindlmayr, "Hybrid functionals and GW approximation in the FLAPW method", Journal of Physics: Condensed Matter **24**, 293201 (2012).

[94] M. Schlipf, M. Betzinger, M. Ležaić, C. Friedrich, and S. Blügel, "Structural, electronic, and magnetic properties of the europium chalcogenides: A hybrid-functional DFT study", Phys. Rev. B **88**, 094433 (2013).

[95] F. Bruneval, "Exchange and Correlation in the Electronic Structure of Solids, from Silicon to Cuprous Oxide: GW Approximation and beyond", PhD thesis (École Polytechnique, 2005).

[96] G. F. Roach, *Green's Functions* (Cambridge University Press, 1982).

[97] A. L. Fetter and J. D. Walecka, *Quantum Theory of Many-Particle Systems* (Courier Dover Publications, 2003).

[98] C. Friedrich and A. Schindlmayr, "Many-Body Perturbation Theory: The GW Approximation", in *Computing Solids - Models, ab initio methods and supercomputing*, Vol. 74, edited by S. Blügel, N. Helbig, V. Meden, and D. Wortmann, Schriften des Forschungszentrums Jülich, Reihe Schlüsseltechnologien / Key Technologies (Forschungszentrum Jülich GmbH, 2014).

[99] A. Gierlich, "All-Electron GW Calculations for Perovskite Transition-Metal Oxides", PhD thesis (RWTH Aachen, 2011).

[100] F. Aryasetiawan and O. Gunnarsson, "The GW method", Reports on Progress in Physics **61**, 237 (1998).

[101] B.-C. Shih, Y. Xue, P. Zhang, M. L. Cohen, and S. G. Louie, "Quasiparticle Band Gap of ZnO: High Accuracy from the Conventional G_0W_0 Approach", Phys. Rev. Lett. **105**, 146401 (2010).

[102] C. Friedrich, M. C. Müller, and S. Blügel, "Band convergence and linearization error correction of all-electron GW calculations: The extreme case of zinc oxide", Phys. Rev. B **83**, 081101 (2011).

[103] H. Jiang, P. Rinke, and M. Scheffler, "Electronic properties of lanthanide oxides from the GW perspective", Phys. Rev. B **86**, 125115 (2012).

[104] I. Aguilera, C. Friedrich, G. Bihlmayer, and S. Blügel, "GW study of topological insulators Bi_2Se_3, Bi_2Te_3, and Sb_2Te_3: Beyond the perturbative one-shot approach", Phys. Rev. B **88**, 045206 (2013).

[105] G. Onida, L. Reining, and A. Rubio, "Electronic excitations: density-functional versus many-body Green's-function approaches", Rev. Mod. Phys. **74**, 601–659 (2002).

[106] W. E. Pickett, "Pseudopotential methods in condensed matter applications", Computer Physics Reports **9**, 115 –197 (1989).

[107] N. Troullier and J. L. Martins, "Efficient pseudopotentials for plane-wave calculations", Phys. Rev. B **43**, 1993–2006 (1991).

[108] F. Nogueira, C. Fiolhais, J. He, J. P. Perdew, and A. Rubio, "Transferability of a local pseudopotential based on solid-state electron density", Journal of Physics: Condensed Matter **8**, 287 (1996).

[109] V. Blum, R. Gehrke, F. Hanke, P. Havu, V. Havu, X. Ren, K. Reuter, and M. Scheffler, "Ab initio molecular simulations with numeric atom-centered orbitals", Computer Physics Communications **180**, 2175 –2196 (2009).

[110] B. Delley, "An all-electron numerical method for solving the local density functional for polyatomic molecules", The Journal of Chemical Physics **92**, 508–517 (1990).

[111] K. Koepernik and H. Eschrig, "Full-potential nonorthogonal local-orbital minimum-basis band-structure scheme", Phys. Rev. B **59**, 1743–1757 (1999).

[112] T. Schena, "Tight-Binding Treatment of Complex Magnetic Structures in Low-Dimensional Systems", MA thesis (RWTH Aachen, 2010).

[113] V. Kashid, T. Schena, B. Zimmermann, Y. Mokrousov, S. Blügel, V. Shah, and H. G. Salunke, "Dzyaloshinskii-Moriya interaction and chiral magnetism in $3d$-$5d$ zigzag chains: Tight-binding model and ab initio calculations", Phys. Rev. B **90**, 054412 (2014).

[114] O. K. Andersen, "Linear methods in band theory", Phys. Rev. B **12**, 3060–3083 (1975).

[115] D. D. Koelling and G. O. Arbman, "Use of energy derivative of the radial solution in an augmented plane wave method: application to copper", Journal of Physics F: Metal Physics **5**, 2041 (1975).

[116] E. Wimmer, H. Krakauer, M. Weinert, and A. J. Freeman, "Full-potential self-consistent linearized-augmented-plane-wave method for calculating the electronic structure of molecules and surfaces: O_2 molecule", Phys. Rev. B **24**, 864–875 (1981).

[117] M. Ležaić, "Spin-gap Materials from First Principles: Properties and Applications of Half-metallic Ferromagnets", PhD thesis (RWTH Aachen, 2005).

[118] H. Krakauer, M. Posternak, and A. J. Freeman, "Linearized augmented plane-wave method for the electronic band structure of thin films", Phys. Rev. B **19**, 1706–1719 (1979).

[119] S. Blügel and G. Bihlmayer, "Full-Potential Linearized Augmented-Plane-Wave Method", in *Computational Nanoscience: Do it yourself!*, Vol. 31, edited by J. Grotendorst, S. Blügel, and D. Marx, NIC Series (John von Neumann Institute for Computing, 2006).

[120] D. Singh, "Ground-state properties of lanthanum: Treatment of extended-core states", Phys. Rev. B **43**, 6388–6392 (1991).

[121] G. Michalicek, M. Betzinger, C. Friedrich, and S. Blügel, "Elimination of the linearization error and improved basis-set convergence within the FLAPW method", Computer physics communications **184**, 2670 –2679 (2013).

[122] C. Friedrich, A. Schindlmayr, and S. Blügel, "Efficient calculation of the Coulomb matrix and its expansion around within the FLAPW method", Computer Physics Communications **180**, 347 –359 (2009).

[123] G. Michalicek, "Development of an efficient Full-Potential Linearized Augmented Plane Wave Method", PhD thesis (RWTH Aachen, 2013).

[124] J. Hüpkes, S.-E. Pust, W. Böttler, A. Gordijn, N. Wyrsch, D. Güttler, A.-N. Tiwari, L. Gordon, and Y. Qiu, "Light scattering and trapping in different thin film photovoltaic device", in *Proceeding of the 24th EU Photovoltaic Solar Energy Conference* (2009).

[125] M. A. Green, K. Emery, Y. Hishikawa, W. Warta, and E. D. Dunlop, "Solar cell efficiency tables (version 43)", Progress in Photovoltaics: Research and Applications **22**, 1–9 (2014).

[126] K. W. Boer and A. Rothwarf, "Materials for Solar Photovoltaic Energy Conversion", Annual Review of Material Science **6**, 303–333 (1976).

[127] X. Deng and E. A. Schiff, "Amorphous Silicon-based Solar Cells", in *Handbook of Photovoltaic Science and Engineering*, edited by A. Luque and S. Hegedus (John Wiley & Sons, 2003).

[128] T. Tinoco, C. Rincón, M. Quintero, Pérez, and G. Sánchez, "Phase Diagram and Optical Energy Gaps for $CuIn_yGa_{1-y}Se_2$ Alloys", physica status solidi (a) **124**, 427–434 (1991).

[129] L. E. Chaar, L. Lamont, and N. E. Zein, "Review of photovoltaic technologies", Renewable and Sustainable Energy Reviews **15**, 2165 –2175 (2011).

[130] K. Momma and F. Izumi, "*VESTA3* for three-dimensional visualization of crystal, volumetric and morphology data", Journal of Applied Crystallography **44**, 1272–1276 (2011).

[131] C. Bradley and A. Cracknell, *The Mathematical Theory of Symmetry in Solids* (Oxford University Press, 2009).

[132] J. Harris, "Simplified method for calculating the energy of weakly interacting fragments", Phys. Rev. B **31**, 1770–1779 (1985).

[133] W. M. C. Foulkes and R. Haydock, "Tight-binding models and density-functional theory", Phys. Rev. B **39**, 12520–12536 (1989).

[134] F. Freimuth, Y. Mokrousov, D. Wortmann, S. Heinze, and S. Blügel, "Maximally localized Wannier functions within the FLAPW formalism", Phys. Rev. B **78**, 035120 (2008).

[135] F. Freimuth, "An efficient Full-Potential Linearized Augmented-Plane-Wave Electronic Structure Method for Charge and Spin Transport through realistic Nanoferroic Junctions", PhD thesis (RWTH Aachen, 2010).

[136] M. Betzinger, C. Friedrich, A. Görling, and S. Blügel, "Precise response functions in all-electron methods: Application to the optimized-effective-potential approach", Phys. Rev. B **85**, 245124 (2012).

[137] M. Betzinger, C. Friedrich, S. Blügel, and A. Görling, "Local exact exchange potentials within the all-electron FLAPW method and a comparison with pseudopotential results", Phys. Rev. B **83**, 045105 (2011).

[138] K. Sato, "Pyrite type compounds — With particular reference to optical characterization", Progress in Crystal Growth and Characterization **11**, 109 –154 (1985).

[139] I. Ferrer and C. Sánchez, "Photoelectrochemical response and optical absorption of pyrite (FeS_2) natural single crystals", Solid State Communications **81**, 371 –374 (1992).

[140] L. Vadkhiya and B. Ahuja, "Electronic and optical properties of iron pyrite", Journal of Alloys and Compounds **509**, 3042 –3047 (2011).

[141] V. N. Antonov, L. P. Germash, A. P. Shpak, and A. N. Yaresko, "Electronic structure, optical and X-ray emission spectra in FeS_2", physica status solidi (b) **246**, 411–416 (2009).

[142] A. Schlegel and P. Wachter, "Optical properties, phonons and electronic structure of iron pyrite (FeS_2)", Journal of Physics C: Solid State Physics **9**, 3363 (1976).

[143] S. Suga, K. Inoue, M. Taniguchi, S. Shin, M. Seki, K. Sato, and T. Teranishi, "Vacuum Ultraviolet Reflectance Spectra and Band Structures of Pyrites (FeS_2, CoS_2 and NiS_2) and NiO Measured with Synchrotron Radiation", Journal of the Physical Society of Japan **52**, 1848–1856 (1983).

[144] J. Vidal, S. Botti, P. Olsson, J. F. Guillemoles, and L. Reining, "Strong Interplay between Structure and Electronic Properties in $CuIn(S,Se)_2$: A First-Principles Study", Physical Review Letters **104**, 056401 (2010).

[145] E. Engel and R. N. Schmid, "Insulating Ground States of Transition-Metal Monoxides from Exact Exchange", Phys. Rev. Lett. **103**, 036404 (2009).

[146] A. Marini, G. Onida, and R. Del Sole, "Quasiparticle Electronic Structure of Copper in the GW Approximation", Phys. Rev. Lett. **88**, 016403 (2001).

[147] T. Rangel, D. Kecik, P. E. Trevisanutto, G.-M. Rignanese, H. Van Swygenhoven, and V. Olevano, "Band structure of gold from many-body perturbation theory", Phys. Rev. B **86**, 125125 (2012).

[148] P. Umari and S. Fabris, "Importance of semicore states in GW calculations for simulating accurately the photoemission spectra of metal phthalocyanine molecules", J. Chem. Phys. **136**, 174310 (2012).

[149] A. M. Karguppikar and A. G. Vedeshwar, "Transport properties of thin iron pyrite films", physica status solidi (a) **95**, 717–720 (1986).

[150] G. Brostigen and A. Kjekshus, "Compounds with the marcasite type crystal structure V. The Crystal Structures of FeS_2, $FeTe_2$, and $CoTe_2$", Acta Chemica Scandinavia **24**, 1925 (1970).

[151] G. Brostigen, A. Kjekshus, and C. Romming, "Compounds with the marcasite type crystal structure VIII. Redetermination of the prototype.", Acta Chemica Scandinavia **27**, 2791 (1973).

[152] F. Grønvold and E. F. Westrum Jr., "Heat capacities of iron disulfides Thermodynamics of marcasite from 5 to 700 K, pyrite from 300 to 780 K, and the transformation of marcasite to pyrite", The Journal of Chemical Thermodynamics **8**, 1039 –1048 (1976).

[153] R. Sutarno, O. O. Knop, and K. I. G. Reid, "Chalcogenides of the transition elements. V. Crystal structures of the disulfides and ditellurides of ruthenium and osmium", Canadian Journal of Chemistry **45**, 1391–1400 (1967).

[154] P. C. Donohue, T. A. Bither, and H. S. Young, "High-pressure synthesis of pyrite-type nickel diphosphide and nickel diarsenide", Inorganic Chemistry **7**, 998–1001 (1968).

[155] J. Pickardt, B. Reuter, E. Riedel, and J. Söchtig, "On the formation of FeSe2 single crystals by chemical transport reactions", Journal of Solid State Chemistry **15**, 366 –368 (1975).

[156] W. Jaegermann and H. Tributsch, "Interfacial properties of semiconducting transition metal chalcogenides", Progress in Surface Science **29**, 1 –167 (1988).

[157] T. Harada, "Transport Properties of Iron Dichalcogenides FeX_2 (X=S, Se and Te)", Journal of the Physical Society of Japan **67**, 1352–1358 (1998).

[158] R. Sun and G. Ceder, "Feasibility of band gap engineering of pyrite FeS_2", Phys. Rev. B **84**, 245211 (2011).

[159] A. N. Mariano and R. M. Beger, "Cleavage in Pyrite and Cobaltite", American Mineralogist **56**, 1867 (1971).

[160] D. R. Alfonso, "Computational Investigation of FeS2 Surfaces and Prediction of Effects of Sulfur Environment on Stabilities", The Journal of Physical Chemistry C **114**, 8971–8980 (2010).

[161] J. Cai and M. R. Philpott, "Electronic structure of bulk and (001) surface layers of pyrite FeS2", Computational Materials Science **30**, 358 –363 (2004).

[162] A. Hung, J. Muscat, I. Yarovsky, and S. P. Russo, "Density-functional theory studies of pyrite FeS2(100) and (110) surfaces", Surface Science **513**, 511 –524 (2002).

[163] A. Hung, J. Muscat, I. Yarovsky, and S. P. Russo, "Density-functional theory studies of pyrite FeS2 (111) and (210) surfaces", Surface Science **520**, 111 –119 (2002).

[164] G. Qiu, Q. Xiao, Y. Hu, W. Qin, and D. Wang, "Theoretical study of the surface energy and electronic structure of pyrite FeS2 (100) using a total-energy pseudopotential method, CASTEP", Journal of Colloid and Interface Science **270**, 127 –132 (2004).

[165] G. Smestad, A. Ennaoui, S. Fiechter, H. Tributsch, W. Hofmann, M. Birkholz, and W. Kautek, "Photoactive thin film semiconducting iron pyrite prepared by sulfurization of iron oxides", Solar Energy Materials **20**, 149 –165 (1990).

[166] V. I. Anisimov, F. Aryasetiawan, and A. I. Lichtenstein, "First-principles calculations of the electronic structure and spectra of strongly correlated systems: the LDA + U method", Journal of Physics: Condensed Matter **9**, 767 (1997).

[167] D. N. Batchelder and R. O. Simmons, "X-Ray Lattice Constants of Crystals by a Rotating-Camera Method: Al, Ar, Au, CaF2, Cu, Ge, Ne, Si", Journal of Applied Physics **36**, 2864–2868 (1965).

[168] B. J. Skinner, "The thermal expansions of thoria, periclase and diamond", American Mineralogist **42** (1957).

[169] Z. Feng, V. S. Babu, J. Zhao, and M. S. Seehra, "Effect of magnetic dilution on magnetic ordering in $Ni_pMg_{1-p}O$", Journal of Applied Physics **70**, 6161–6163 (1991).

[170] S. C. Abrahams and J. L. Bernstein, "Accuracy of an automatic diffractometer. Measurement of the sodium chloride structure factors", Acta Crystallographica **18**, 926–932 (1965).

[171] R. E. Nahory, M. A. Pollack, and J. C. DeWinter, "Growth and continuous compositional grading of $GaAs_{1-x-z}Sb_xP_z$ by liquid phase epitaxy", Journal of Applied Physics **48**, 320–323 (1977).

[172] J. E. Ortega and F. J. Himpsel, "Inverse-photoemission study of Ge(100), Si(100), and GaAs(100): Bulk bands and surface states", Phys. Rev. B **47**, 2130–2137 (1993).

[173] R. Hulthén and N. G. Nilsson, "Investigation of the second indirect transition of silicon by means of photoconductivity measurements", Solid State Communications **18**, 1341–1343 (1976).

[174] K.-H. Hellwege, O. Madelung, M. Schulz, and H. Weiss, eds., *Vol. 17 & 22 of Landolt-Börnstein Group III Condensed Matter: Numerical Data and Functional Relationships in Science and Technology* (Springer Verlag, New York, 1982).

[175] R. J. Magyar, A. Fleszar, and E. K. U. Gross, "Exact-exchange density-functional calculations for noble-gas solids", Phys. Rev. B **69**, 045111 (2004).

[176] S. Adachi, *Optical Properties of Crystalline and Amorphous Semiconductors: Numerical Data and Graphical Information* (Kluwer Academic, Dordrecht, 1999).

[177] R. T. Poole, J. Liesegang, R. C. G. Leckey, and J. G. Jenkin, "Electronic band structure of the alkali halides. II. Critical survey of theoretical calculations", Phys. Rev. B **11**, 5190–5196 (1975).

[178] H. Gebrehiwet, "Absorption Coefficient and Dielectric Function of Direct Band Gap Silicon Nanocrystallites", MA thesis (Addis Ababa University, 2007).

[179] F. Rana, *Semiconductor Optoelectronics*, Lecture Cornell University.

[180] X.-G. Wang, W. Weiss, S. K. Shaikhutdinov, M. Ritter, M. Petersen, F. Wagner, R. Schlögl, and M. Scheffler, "The Hematite (α-Fe_2O_3) (0001) Surface: Evidence for Domains of Distinct Chemistry", Phys. Rev. Lett. **81**, 1038–1041 (1998).

[181] S. J. Jenkins, "Ternary half-metallics and related binary compounds: Stoichiometry, surface states, and spin", Phys. Rev. B **70**, 245401 (2004).

List of Figures

List of Tables

Acknowledgements/Danksagung

Die etwas mehr als drei Jahre, die ich an dieser Doktorarbeit gearbeitet habe, wären ohne die Hilfe und Anwesenheit folgender Personen sicherlich deutlich schwieriger und nicht so angenehm gewesen. Ich werde zunächst den Personen die mir fachlich zur Seite standen danken und schließlich jenen die auch abseits der Arbeit zu einer angenehmen Atmosphäre beitrugen.

Zuerst einmal gehört mein Dank Herrn Prof. Dr. Stefan Blügel, der es mir ermöglichte diese Arbeit in seiner großen Arbeitsgruppe anzufertigen. Ich habe selten einen energischeren Menschen erlebt, welcher es beherrscht seine Mitarbeiter bis ins Höchste zu motivieren. Seine Bürotür stand mir immer offen, was bei seinem Tätigkeitsfeld keine Selbstverständlichkeit darstellt. Die Diskussionen mit ihm haben mir meist noch eine andere Perspektive eröffnet.

Ich danke auch Herrn Prof. Dr. Matthias Wuttig für die freundliche Übernahme des Zweitgutachtens dieser Arbeit.

Vielen Dank auch an Dr. Gustav Bihlmayer für die hervorragende Betreuung. Für offene Fragen stand seine Tür stets offen und sein ruhiger Charakter war ein guter Gegenpol zu meinem.

Ich danke auch Herrn Prof. Dr. Reinhard Carius für die Organisation der NADNuM Projekttreffen und dem Projektträger selber (NADNuM 03SF0402A), welcher die finanzielle Unterstützung gewährleistete.

Besonderer Dank geht an Dr. Martin Schlipf für die Berechnung der Hybridfunktionalergebnisse der einfachen Halbleitermaterialien, als auch an Dr. Markus Betzinger, welcher freundlicherweise die EXX-OEP Kalkulation für das Pyrit durchführte. Euch beiden auch vielen Dank für die zahlreichen fachlichen Diskussionen.

Eine ganze Reihe von anderen Personen haben mir auch durch kleinere und größere Fachgespräche weitergeholfen. Vielen Dank an Dr. Irene Aguilera, Dr. David Bauer, Dr. Christoph Friedrich, Dr. Gregor Michalicek, Dr. Ersoy Şaşıoğlu, Benedikt Schweflinghaus, Dr. Pengxiang Xu und Dr. Bernd Zimmermann.

Danke an Dr. Gustav Bihlmayer, Dr. Gregor Michalicek, Philipp Rüssmann, Benedikt Schweflinghaus und Dr. Irene Aguilera für das Korrekturlesen der Arbeit.

Danke auch an unsere Sekretärin Ute Winkler für die Hilfe bei administrativen und organisatorischen Angelegenheiten.

Zudem danke ich meinen (ehemaligen) Bürokollegen Dr. David Bauer, Dr. Daria Popova, Siebe Rossen und Kerstin Dörr für eine angenehme Atmosphäre im Büro.

Aber das Leben besteht nicht nur aus Arbeit, daher möchte ich im Folgenden auch den Personen des Instituts danken, mit welchen ich viele vergnügliche Stunden in der Freizeit verbringen durfte. Dabei werde ich von einer eher formalen Ansprache zum "Du" wechseln.

Acknowledgements/Danksagung

Ich bedanke mich bei der Brettspielegruppe und dabei vor allem bei Aaron und Martin für die Organisation. Vielen Dank auch an die Fussballgruppe, organisiert von Benedikt. Der freitäglichen Laufgruppe auch ein Danke, insbesondere an Philipp und Mathias. Insbesondere auch danke an Markus und Bernd, welche sich in spannenden Badminton und Squash Duellen mit mir gemessen haben. Ihr seid alle toll und ich hoffe auf weiteren Kontakt in der Zukunft.

Tiefgehender Dank geht an meinen Vater und meine Mutter, welche sich nun wohl sehr gefreut hätte. Durch euch wurde mir all dies erst ermöglicht. Meiner Lebensgefährtin Christa danke ich ganz herzlich für ihren Beistand in schwierigen Zeiten und die geteilte Freude in guten Zeiten.

Band / Volume 241
Spannungsinduziertes Versagen in Hochtemperaturschichtsystemen
C. Nordhorn (2014), v, 118 pp
ISBN: 978-3-95806-016-6

Band / Volume 242
Änderungsdetektion digitaler Fernerkundungsdaten mittels objekt-basierter Bildanalyse
C. Listner (2014), 176 pp
ISBN: 978-3-95806-017-3

Band / Volume 243
Räumlich hoch aufgelöste Modellierung des Spaltprodukt-verhaltens in einem HTR-Core mit kugelförmigen oder prismatischen Brennelementen
A. Xhonneux (2014), viii, 239 pp
ISBN: 978-3-95806-020-3

Band / Volume 244
Effects of Cercospora leaf spot disease on sugar beet genotypes with contrasting disease susceptibility
S. Schmittgen (2015), 121 pp
ISBN: 978-3-95806-021-0

Band / Volume 245
Light scattering and trapping in thin film silicon solar cells with an n-i-p configuration
W. Böttler (2015), 132 pp
ISBN: 978-3-95806-023-4

Band / Volume 246
Nanostructured Si-alloys for silicon solar cells
K. Ding (2015), 210 pp
ISBN: 978-3-95806-024-1

Band / Volume 247
Electrochemical Texturing and Deposition of Transparent Conductive Oxide Layers for the Application in Silicon Thin-Film Solar Cells
J.-P. Becker (2015), ix, 156, XXIV pp
ISBN: 978-3-95806-027-2

Band / Volume 248
Stoffliche Charakterisierung radioaktiver Abfallprodukte durch ein Multi-Element-Analyseverfahren basierend auf der instrumentellen Neutronen-Aktivierungs-Analyse – MEDINA –
A. W. Havenith (2015), 311 pp
ISBN: 978-3-95806-033-3

Band / Volume 249
Quantitative Two-Layer Inversion and Customizable Sensor-Array Instrument for Electromagnetic Induction based Soil Conductivity Estimation
A. T. Mester (2015), viii, 119 pp
ISBN: 978-3-95806-035-7

Band / Volume 250
Partial Neutron Capture Cross Sections of Actinides using Cold Neutron Prompt Gamma Activation Analysis
C. Genreith (2015), vii, 166, XXXII pp
ISBN: 978-3-95806-036-4

Band / Volume 251
Long Term Aerosol Composition Measurements at the CESAR Tower at Cabauw, NL
P. Schlag (2015), iii, 228 pp
ISBN: 978-3-95806-037-1

Band / Volume 252
Modellbasierte Spezifikationsmethodik zur effizienten Systementwicklung von Brennstoffzellenantrieben
R. Biurrun Sotelo (2015), 255 pp
ISBN: 978-3-95806-038-8

Band / Volume 253
Three-dimensional ray-tracing simulations of convective gravity waves
S. Kalisch (2015), iii, 183 pp
ISBN: 978-3-95806-040-1

Band / Volume 254
First-Principles Study on Pyrites and Marcasites for Photovoltaic Application
T. Schena (2015), 206 pp
ISBN: 978-3-95806-041-8

Energie & Umwelt /
Energy & Environment
Band / Volume 254
ISBN 978-3-95806-041-8